Methodological development and implementation of fast quantitative hard X-ray fluorescence multi-length-scale tomography for next-generation X-ray imaging at the NANOSCOPIUM beamline of SOLEIL synchrotron and its application to study physico-chemical processes involved in the pathologic calcifications

Ruiqiao Guo

THESE DE DOCTORAT

NNT : 2023UPASP167

université PARIS-SACLAY

Methodological development and implementation of fast quantitative hard X-ray fluorescence multi-length-scale tomography for next-generation X-ray imaging at the NANOSCOPIUM beamline of SOLEIL synchrotron and its application to study physico-chemical processes involved in the pathologic calcifications

Tomographie quantitative et multi-échelle par fluorescence X sur la ligne NANOSCOPIUM du synchrotron SOLEIL : Développements méthodologiques et mise en application pour l'étude des processus physico-chimiques impliqués dans les calcifications pathologiques

Thèse de doctorat de l'université Paris-Saclay

École doctorale n°576, particules, hadrons, énergie et noyau : instrumentation, imagerie, cosmos et simulation (PHENIICS)
Spécialité de doctorat : Physique pour l'imagerie médicale
Graduate School : Physique. Référent : Faculté des sciences d'Orsay

Thèse préparée dans l'unité de recherche **Synchrotron SOLEIL** (Université Paris-Saclay), sous la direction de **Kadda MEDJOUBI**, scientifique de ligne

Thèse soutenue à Paris-Saclay, le 28 novembre 2023, par

Ruiqiao GUO

Composition du jury

Membres du jury avec voix délibérative

Sophie KAZAMIAS Professeure des universités, Université Paris-Saclay	Présidente
Karim BENZERARA Directeur de recherche, Sorbonne Université, CNRS	Rapporteur & Examinateur
Ina REICHE Directrice de recherche, Chimie ParisTech - PSL, CNRS	Rapporteur & Examinatrice
Hester COLBOC Maître de conférence, Sorbonne Université, Hôpital Rothschild	Examinatrice
Patricia WILS Ingénieur de recherche, Muséum national d'Histoire naturelle	Examinatrice

université PARIS-SACLAY

ÉCOLE DOCTORALE
Particules, hadrons, énergie et noyau : instrumentation, imagerie, cosmos et simulation (PHENIICS)

Titre : Tomographie quantitative et multi-échelle par fluorescence X sur la ligne NANOSCOPIUM du synchrotron SOLEIL : Développements méthodologiques et mise en application pour l'étude des processus physico-chimiques impliqués dans les calcifications pathologiques

Mots clés : Tomographie clairsemée, Calcification pathologique, Tomographie quantitative, Fluorescence X, Rayonnement synchrotron

Résumé : La ligne de lumière NANOSCOPIUM au synchrotron SOLEIL est dédiée à l'imagerie X-dur (5-20 keV) multi-modale et multi-échelle par balayage rapide et à haute résolution spatiale. Depuis son ouverture en septembre 2018, la ligne a accueilli un grand nombre d'utilisateurs dans des domaines variés tels que la médecine, la biologie, la science de la terre et de l'environnement, ainsi que la science des matériaux.

L'imagerie non invasive en 2D est régulièrement proposée aux utilisateurs, offrant une grande sensibilité analytique et la possibilité de sonder en profondeur les échantillons. L'imagerie multi-technique par balayage rapide permet d'obtenir des informations simultanées de fluorescence X, de contraste d'absorption, de phase et de diffusé à une résolution spatiale allant de 50 nm à 1 μm. La micro-tomographie X plein champ rapide a également été intégrée pour fournir des informations morphologiques en 3D avec une résolution d'environ 1 μm^3.

Pour aller plus loin dans l'imagerie 3D quantitative de systèmes complexes, un aspect majeur de cette thèse est de développer une nouvelle modalité basée sur la tomographie par fluorescence X par balayage. Cette technique permettra d'obtenir de manière non-invasive des informations quantitatives sur la distribution élémentaire 3D dans des objets de quelques centaines de micromètres d'épaisseur avec une haute résolution spatiale.

Ces développements méthodologiques sont appliqués à l'étude de l'urolithiase dans le cadre de la collaboration entre NANOSCOPIUM, l'APHP (Assistance publique-Hôpitaux de Paris) et l'ICP (Institut de Chimie Physique). L'urolithiase est une pathologie croissante affectant près de 10 % de la population. Une grande proportion de ces calculs se développe sur une calcification spécifique composée de phosphate de calcium qui se forme dans les papilles rénales, appelées Randall's plaque (RP). On sait peu de choses sur les mécanismes impliqués dans la formation des RP, mais des observations récentes suggèrent que plusieurs mécanismes pourraient être impliqués dans la pathogenèse de ces plaques. Des études récentes à l'échelle mésoscopique ont montré le possible lien entre des éléments traces tels que le zinc et la formation de ce minéral, suggérant que les dépôts calcifiés sont un processus pathologique impliquant une réaction tissulaire.

Afin de clarifier le rôle du zinc et d'approfondir notre compréhension de ce mécanisme, une étude en 3D avec une résolution de quelques centaines de nanomètres sur la variation de la concentration en zinc est cruciale pour comprendre les variations de la composition chimique dès les premiers stades de la calcification des RP. La tomographie XRF quantitative rapide développée est une technique non invasive unique qui permettra, pour la première fois, d'investiguer un nombre statistiquement significatif d'échantillons et d'approfondir notre compréhension des relations entre les processus physico-chimiques et la pathologie.

université PARIS-SACLAY

ÉCOLE DOCTORALE
Particules, hadrons, énergie et noyau : instrumentation, imagerie, cosmos et simulation (PHENIICS)

Title : Methodological development and implementation of fast quantitative hard X-ray fluorescence multi-length-scale tomography for next-generation X-ray imaging at the NANOSCOPIUM beamline of SOLEIL synchrotron and its application to study physico-chemical processes involved in the pathologic calcifications

Keywords : Sparse tomography, Pathological calcification, Quantitative tomography, X-ray fluorescence, Synchrotron radiation

Abstract : The NANOSCOPIUM beamline at the SOLEIL synchrotron is dedicated to high-energy X-ray (5-20 keV) multi-modal and multi-scale nano-imaging using fast and high spatial resolution scanning techniques. Since its opening in September 2018, the beamline has welcomed a large number of users from various fields, including medicine, biology, earth and environmental science, and materials science.

One of the key features of this beamline is its capability for non-invasive 2D imaging, which provides high analytical sensitivity and enables the depth probing of samples. Moreover, the beamline offers fast multi-technique scanning imaging, allowing for the simultaneous acquisition of X-ray fluorescence, absorption-, phase-, and dark-field contrast images. These images can be obtained with spatial resolutions ranging from 50 nm to 1 μm.

Recently, the beamline has integrated rapid full-field micro-tomography, offering 3D morphological information with resolutions of about 1 μm^3. To further extend its 3D quantitative imaging capabilities for complex systems, a major aspect of this thesis is to develop a new technique for scanning X-ray fluorescence tomography. This non-invasive method will enable quantitative information on 3D elemental distribution in samples of a few hundred microns in thickness with high spatial resolution down to a few hundred nanometers. As an application of the developed method, we focus on the study of urolithiasis in the framework of the collaboration between NANOSCOPIUM, APHP (Assistance publique-Hôpitaux de Paris), and the ICP (Institut de Chimie Physique). The urolithiasis is an increasing pathology affecting almost 10 % of the population. A great proportion of these stones develop on a specific calcification made of calcium phosphate which grows in renal papillae, named Randall's plaques (RP). Little is known about the mechanisms involved in RP formation but recent observations support the idea that several mechanisms may be involved in the pathogenesis of these plaques. Recent studies in the mesoscale have shown the possible relationship between trace elements such the Zinc and the formation of this mineral suggesting that calcified deposits are a pathological process involving a tissue reaction. In order to clarify the role of Zn and go further in the understanding of this mechanism, a few-hundred-nanometer resolution 3D study of the Zn concentration variation is crucial in the function of chemical composition variation from the early stage of the calcification of the RP. The developed fast quantitative XRF tomography is a unique non-invasive technique, which, for the first time, will permit the investigation of a statistically significant number of samples and provide a deeper understanding of the physico-chemical processes-pathology relationships.

ACKNOWLEDGMENTS

I wish to express my gratitude to Synchrotron SOLEIL and the doctoral school PHENIICS for enabling me to undertake this Ph.D. study, conducted at the NANOSCOPIUM beamline. Financial support from Synchrotron SOLEIL and the doctoral school PHENIICS at Université Paris-Saclay is acknowledged.

My deepest gratitude goes to my supervisor, Dr. Kadda Medjoubi, whose unwavering support, encouragement and guidance have been integral to this Ph.D. journey. He has not only walked me through all the stages of writing this thesis but has also provided consistent and illuminating instruction during this academic journey, without which this thesis would not have reached its present form.

Additionally, my appreciation extends to the group leader of the NANOSCOPIUM beamline, Dr. Andrea Somogyi, for her invaluable contributions. I am thankful for her numerous suggestions and the time dedicated to my research. Her insights have been instrumental in refining my work and providing inspiration.

My sincere thanks go to my thesis committee members – Dr. Karim Benzerara, Dr. Hester Colboc, Prof. Sophie Kazamias, Dr. Ina Reiche, and Dr. Patricia Wils – for their constructive feedback, significantly contributing to the refinement of this work.

Special acknowledgment is given to collaborators: Dr. Dominique Bazin, Dr. Elise Bouderlique, Dr. Emilie Chouzenoux, Dr. Marie-Pierre Isaure, Dr. Emmanuel Letavernier, and Ellie Tang. Their collaboration, expertise, and enthusiasm have enriched my research experience and broadened this study's scope over the past three years.

To my wonderful friends and colleagues, thank you all for the enriching discussions, and delightful shared moments that not only added a touch of joy to this academic pursuit but also made it a truly enjoyable journey.

My heartfelt thanks go to my family for their unwavering support, encouragement, and understanding during the ups and downs of the doctoral journey. Their love and belief in me have been my pillars of strength.

In closing, I would like to express my deep appreciation to everyone who played a role, directly or indirectly, in bringing this thesis to fruition. As I step into the next chapter of my journey, I carry with me not only the valuable lessons learned but also the vibrant connections forged during this Ph.D. experience. Here's to the enduring memories that have made this endeavor not just fulfilling but genuinely joyful.

RÉSUMÉ DÉTAILLÉ

Les progrès dans les techniques analytiques constituent depuis longtemps un objectif majeur au sein de la communauté scientifique. À mesure que les défis scientifiques deviennent plus complexes, il est de plus en plus crucial de disposer de méthodes d'imagerie 3D par balayage rapides, efficaces et quantitatives à haute résolution. Parmi ces méthodes, la technique de tomographie par fluorescence X offre des perspectives sur la distribution tridimensionnelle des éléments dans les échantillons. Sa grande profondeur de pénétration et sa sensibilité analytique élevée la rendent particulièrement adaptée à l'étude de systèmes complexes et hétérogènes.

La ligne de lumière NANOSCOPIUM du synchrotron SOLEIL (Somogyi et al., 2015) est dédiée à l'imagerie X-dur (5-20 keV) multi-modale et multi-échelle par balayage rapide et à haute résolution spatiale. La ligne propose des techniques d'imagerie 2D/3D par nano-sonde à rayons X à la pointe de l'innovation. Depuis son ouverture à la communauté scientifique, en septembre 2018, la ligne a accueilli un très grand nombre d'utilisateurs qui ont pu réaliser des expériences dans des domaines extrêmement variés couvrant la médecine, la biologie, la science de la terre et de l'environnement et plus récemment la science des matériaux.

La demande croissante pour une exploration quantitative et multi-échelle de la composition chimique et de la morphologie de systèmes complexes est observée dans ces divers domaines de recherche. L'imagerie non invasive en 2D est régulièrement proposée à la communauté des utilisateurs de NANOSCOPIUM, offrant une grande sensibilité analytique et la possibilité de sonder en profondeur un échantillon. Grâce à une fonctionnalité unique de zoom, elle permet également d'imager des régions d'intérêt de taille millimétrique avec une résolution micrométrique, pour ensuite les analyser à l'échelle déca-nanométrique.

Le développement de l'imagerie multi-technique par balayage rapide sur la ligne (Medjoubi et al., 2013) permet l'obtention simultanée de techniques d'analyses complémentaires telles que la fluorescence X, le contraste d'absorption, de phase et de diffusion, couvrant une plage de résolution spatiale de 50 nm à 1 μm.

D'autre part, l'imagerie par diffraction cohérente et par balayage (Ptychographie) (Medjoubi et al., 2018), également accessible aux utilisateurs, fournit des informations morphologiques avec une plus grande finesse, i.e. avec une résolution spatiale de 30 nm. A cet éventail de modalité d'imagerie 2D, la micro-tomographie X plein champ rapide (1 minute 30 par tomographie) a été récemment intégrée et permet d'ajouter des informations morphologiques en 3D avec une résolution de l'ordre de 1 μm^3.

Pour faciliter la manipulation complète des expériences sur NANOSCOPIUM, des outils de séquencement et de traitement simples et rapides ont été développés et déployés sur la ligne (Bergamaschi, 2017). En combinant l'ensemble de ces informations, il est possible d'obtenir une distribution élémentaire 2D semi-quantitative au sein de systèmes très hétérogènes.

Cependant, les méthodes d'imagerie 2D détaillées ci-dessus fournissent des informations sur les compositions chimiques/morphologiques intégrées le long de la trajectoire du faisceau de rayons X à travers une épaisseur d'échantillon de l'ordre de quelques dizaines ou centaines de micromètres. Pour des échantillons dont la structure et la composition interne sont complexe et hétérogène, cela représente une limitation réelle pour réaliser une interprétation et une quantification dépourvue de toute ambiguïté. Afin de résoudre cette problématique, il est nécessaire d'aller méthodologiquement et techniquement plus loin en exploitant pleinement le fort potentiel des nano-sondes à rayons X durs. Dans le cadre de cette thèse, notre objectif est donc d'étendre les méthodes d'imagerie 2D déjà établies vers une nouvelle génération d'imagerie 3D basée sur la technique de tomographie par fuorescence X par balayage. L'objectif est d'obtenir de manière non-invasive des informations quantitatives sur la distribution élémentaire 3D au sein d'objets de quelques centaines de micromètres d'épaisseur avec une sensibilité analytique élevée.

Cependant, la mise en application de cette modalité de tomographie par fluorescence X, bien que puissante et très fortement demandée par une vaste communauté d'utilisateurs du synchrotron, est limitée par les longues durées d'acquisition (généralement plus de 10 heures par tomographie) notamment imposées par le flux de photons accessibles, par la complexité du séquencement des acquisitions et par la disponibilité de ressources informatiques permettant la réalisation de calculs intensifs sur des grands volumes de données. Cela explique

pourquoi seules quelques lignes de lumière à travers le monde offrent aux utilisateurs la possibilité de réaliser, de manière occasionnelle, des mesures de tomographie par fluorescence X.

Des expériences récentes de preuve de principe, menées par l'équipe de NANOSCOPIUM, ont démontré la faisabilité de la micro-tomographie semi-quantitative par fluorescence X sur la ligne.

La prochaine étape consiste à réaliser les développements méthodologiques et instrumentaux nécessaires. D'une part, la résolution spatiale 3D est étendue vers la gamme de quelques centaines de nanomètres. D'autre part, l'acquisition et la reconstruction tomographique sont accélérées. Enfin, et surtout, des analyses quantitatives de l'abondance élémentaire en 3D sont fournies.

Dans le cadre d'une collaboration entre NANOSCOPIUM et une équipe médicale, ces méthodes innovantes est appliquées pour l'étude du rôle des métaux dans les calcifications pathologiques. A la suite de ce travail de thèse, cette nouvelle modalité d'imagerie quantitative pourra être appliquée à un large éventail d'applications scientifiques réalisées sur la ligne. L'ensemble des études qui pourra être mené contribuera à renforcer notre compréhension de l'interaction entre différents processus et phénomènes intervenant dans des systèmes complexes depuis l'échelle méso vers l'échelle nano et cela pour beaucoup de domaines de la science. Les retombées de ce travail de thèse sont donc extrêmement riches et importantes.

Les travaux couvrent la théorie de l'interaction rayons X–matière, la conception d'expériences sur ligne synchrotron, l'acquisition et l'analyse de données liées à la tomographie par fluorescence X quantitative et par balayage rapide. Des algorithms adaptés pour la reconstruction tomographique clairsemée (sparse tomography), c'est-à-dire basée sur un très faible nombre de projections, sont implementés et évalués. Ce sont des méthodes prometteuses, non encore implémentées pour la tomographie par fluorescence X, qui participent également à accélérer les séquences d'acquisition. Plusieurs techniques de reconstruction numérique sont donc étudiées, telles que des algorithmes itératifs (statistiques et algébriques) dans l'espace réel ou dans l'espace de Fourier. Une méthode est développée afin d'évaluer chaque technique et de sélectionner la mieux adaptée à la tomographie clairsemée par fluorescence X et à son application en sciences médicales.

Le développement méthodologique permettant de fournir des concentrations élémentaires précises en 3D avec une résolution spatiale de quelques centaines de nanomètres constitue l'une des parties majeures de cette thèse. Les méthodes développées sont appliquées, lors d'expériences sur la ligne, à l'étude de l'urolithiase dans le cadre de la collaboration menée entre NANOSCOPIUM, APHP (Assistance publique-Hôpitaux de Paris) et ICP (Institut de Chimie Physique).

L'urolithiase, maladie qui se caractérise par la formation de calculs dans les voies urinaires, est une pathologie croissante qui affecte près de 10 % de la population. Une grande proportion de ces calculs se développe sur une calcification spécifique à base de phosphate de calcium qui pousse dans les papilles rénales, dénommées plaques de Randall (RP). On en sait peu sur les mécanismes impliqués dans la formation de ces RP, mais des observations récentes soutiennent l'idée que plusieurs mécanismes peuvent être impliqués dans la pathogenèse de ces plaques.

Des études récentes à l'échelle méso ont montrées la relation possible entre des éléments de trace de type métallique tels que le zinc et la formation de ce minéral, suggérant que les dépôts calcifiés sont un processus pathologique impliquant une réaction tissulaire (Carpentier et al., 2011). Afin de clarifier le rôle du Zn et d'aller plus loin dans la compréhension de ce mécanisme, une étude permettant de suivre en 3D l'évolution de la concentration du Zn dans un environnement structural et chimique connu, et cela depuis le début de la calcification des RP, est donc cruciale. La tomographie quantitative par fluorescence X développée est une technique unique et non invasive qui permet d'étudier un nombre, statistiquement significatif, d'échantillons et fournira une compréhension plus profonde des relations entre les processus physico-chimiques et la pathologie.

Ce manuscrit se structure en 6 chapitres:

* Le Chapitre 1 introduit le contexte de la recherche doctorale, offrant un bref aperçu des calcifications pathologiques et des méthodes analytiques actuelles pour explorer les problématiques liées aux calculs rénaux. De plus, les techniques d'imagerie par rayons X y seront présentées.

* Le Chapitre 2 propose une description approfondie des interactions de la matière avec les rayons X. Ce chapitre inclut également l'instrumentation et la méthodologie des techniques analytiques à la ligne de lumière NANOSCOPIUM du synchrotron SOLEIL, où les expériences ont été menées.

* Le Chapitre 3 se concentre sur la reconstruction d'images en tomographie, abordant les algorithmes de reconstruction et les artefacts présents dans le tomogramme.

* Le Chapitre 4 traite des développements méthodologiques et de la mise en œuvre du flux de travail. Les graines d'*Arabidopsis thaliana* ont été utilisées pour illustrer la performance du flux de travail.

* Le Chapitre 5 explore l'application du flux de travail développé dans les calcifications pathologiques. Ce chapitre présente une étude de cas sur la papille rénale à l'aide du flux de travail d'imagerie/tomographie parfluorescence X développé et déployé à la ligne de lumière NANOSCOPIUM.

* Le Chapitre 6 conclut le manuscrit. Il résume le travail de doctorat et esquisse les perspectives de recherche future.

References

A. Bergamaschi. *Développements méthodologiques et logiciels pour l'imagerie X multimodale par balayage sur la ligne de lumière Nanoscopium*. phdthesis, Université Paris-Saclay, Mar. 2017. URL https://tel.archives-ouvertes.fr/tel-01534173.

X. Carpentier, D. Bazin, C. Combes, A. Mazouyes, S. Rouzière, P. A. Albouy, E. Foy, and M. Daudon. High Zn content of Randall's plaque: A -X-ray fluorescence investigation. *Journal of Trace Elements in Medicine and Biology*, 25(3):160–165, July 2011. ISSN 0946672X. doi: 10.1016/j.jtemb.2011.05.004. URL https://linkinghub.elsevier.com/retrieve/pii/S0946672X11000769.

K. Medjoubi, N. Leclercq, F. Langlois, A. Buteau, S. Lé, S. Poirier, P. Mercère, M. C. Sforna, C. M. Kewish, and A. Somogyi. Development of fast, simultaneous and multi-technique scanning hard X-ray microscopy at Synchrotron Soleil. *J Synchrotron Rad*, 20(2):293–299, Mar. 2013. ISSN 0909-0495. doi: 10.1107/S0909049512052119. URL http://scripts.iucr.org/cgi-bin/paper?S0909049512052119.

K. Medjoubi, G. Baranton, and A. Somogyi. Fast full-field micro-tomography at the Nanoscopium multitechnique nanoprobe beamline of Synchrotron Soleil. *Microscopy and Microanalysis*, 24(S2):252–253, Aug. 2018. ISSN 1431-9276, 1435-8115. doi: 10.1017/S1431927618013612.

A. Somogyi, K. Medjoubi, G. Baranton, V. Le Roux, M. Ribbens, F. Polack, P. Philippot, and J.-P. Samama. Optical design and multi-length-scale scanning spectro-microscopy possibilities at the Nanoscopium beamline of Synchrotron Soleil. *Journal of Synchrotron Radiation*, 22:1118–1129, July 2015. doi: 10.1107/S1600577515009364.

Contents

INTRODUCTION

Advancements in analytical techniques have been a long-standing objective within the scientific community. As scientific problems become more challenging, there is a growing need for fast, efficient, and quantitative high-resolution 3D scanning imaging methods. Among these, the scanning hard X-ray fluorescence tomography technique provides unique insights into the 3D elemental distribution of samples. Its large penetration depth and high analytical sensitivity make it especially suitable for investigating heterogeneous complex systems. However, the lengthy acquisition time it requires hinders its comprehensive utilization.

The NANOSCOPIUM beamline at SOLEIL synchrotron, dedicated to 2D/3D multimodal and multi-length scale hard X-ray imaging, aims to align with the evolving scientific needs and extend its imaging capabilities to scanning X-ray fluorescence tomography. However, deploying this imaging modality presents certain challenges. Apart from the mentioned long acquisition time, the resource-intensive computations for data reconstruction complicate its implementation.

This thesis focuses on methodological improvements adapted for X-ray fluorescence tomography. The objective is to tackle these challenges and ensure its successful implementation at the beamline. A pivotal part of this strategy is optimizing the methodology to utilize a reduced projection dataset for reconstruction, while preserving the quality of the reconstructed tomograms.

Furthermore, the application of the XRF tomography technique is directed toward the pathogenesis of kidney stones, with a special focus on investigating the Randall's plaque located at the tip of the renal papilla. Through the implemented XRF tomography technique, this work aims to provide a detailed 3D quantitative elemental distribution within samples with high resolution, enhancing our knowledge of the roles trace elements have in the development of pathological calcifications.

The thesis is organized into 6 chapters:

* In Chapter 1, I will introduce the context of the PhD research, including a brief overview of pathological calcifications and current analytical methods for studying the questions associated with kidney stones. In addition, X-ray imaging techniques will be introduced.

* Chapter 2 gives a detailed description of X-ray matter interactions. This chapter also includes the instrumentation and methodology of analytical techniques at the NANOSCOPIUM beamline of the SOLEIL synchrotron, where I carried out the experiments.

* Chapter 3 focuses on tomography image reconstruction, including reconstruction algorithms and artifacts present in the tomogram.

* Chapter 4 discusses the methodological developments and implementation of the workflow. *Arabidopsis thaliana* seeds were used to demonstrate the performance of the workflow.

* Chapter 5 explores the application of the developed workflow in pathological calcifications. This chapter presents a case study on renal papilla with the developed and implemented XRF imaging/tomography workflow at the NANOSCOPIUM beamline.

* Chapter 6 concludes the thesis. It summarizes the PhD work and presents an outlook for future research.

CHAPTER 1
CONTEXT

1.1. Brief overview of pathological calcifications

In healthy individuals, mineral formation is limited to primarily skeletal components. These compounds, known as physiological calcification, are strictly controlled during growth and development. The formation of minerals is encouraged in desirable locations, while it is inhibited in soft tissues and other unwanted areas (Bazin et al., 2016; Tsolaki and Bertazzo, 2019; Vidavsky et al., 2021). While physiological calcifications' mechanisms have been extensively studied, the biochemical processes underlying pathological calcifications remain less understood (Bazin et al., 2012; Bazin and Daudon, 2012; Mulay and Anders, 2016).

Pathological calcifications refer to abnormal mineral deposits found in tissues or organs in medical terms (Bazin et al., 2012; Bazin and Daudon, 2012; Bazin et al., 2022a). There are three predominant types of pathological calcifications (see Figure 1.1). The first type involves hard, solid masses that are present inside a cavity or duct and can be found in organs such as the kidneys, pancreas, biliary, and salivary. The second comprises ectopic calcifications in soft tissues, which can be indicative of diseases like breast, thyroid, testicular, or prostate cancer. Lastly, the third type includes physiological calcifications that may transform into pathological forms due to illness or changes in physiological systems, as seen in conditions like osteoporosis impacting bone tissue (Bazin et al., 2012, 2014).

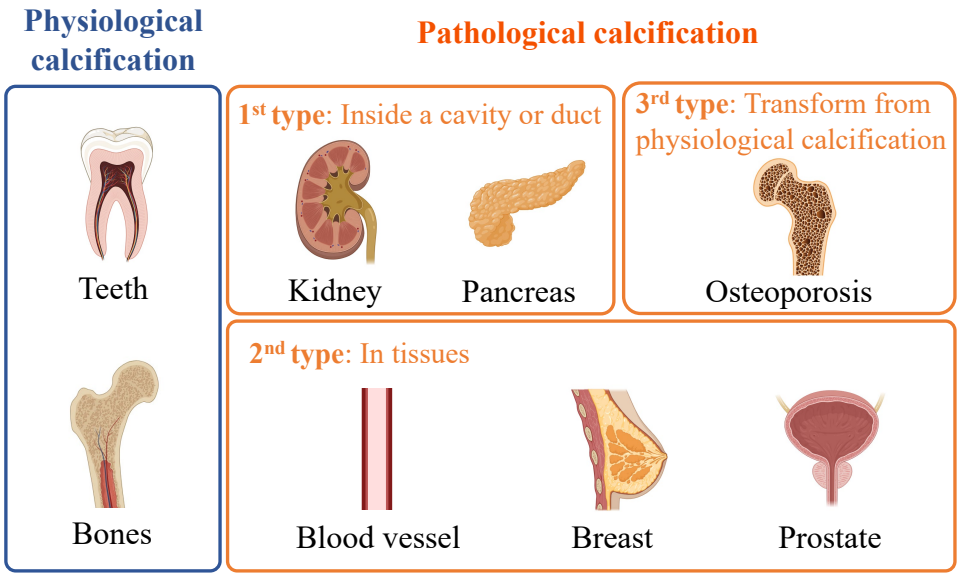

Figure 1.1: Physiological and pathological calcifications in the human body.

Consequently, a range of diseases, including infections, cancers, genetic and environmental disorders, are associated with pathological calcifications. The rising prevalence of conditions like obesity and diabetes, combined with lifestyle changes such as dietary habits, further complicates the understanding of pathological calcifications. As a result, traditional characterization methods like staining often prove insufficient (Bazin et al., 2022a,b,c).

The following sections outline the physicochemical properties of kidney stones and various analytical methods employed in the studies. In Chapter 5, we will focus on the 2D and 3D scanning X-ray fluorescence imaging and tomography of ectopic calcifications present in the kidney, specifically those which are related to Randall's plaque (Randall, 1936; Perre et al., 2022).

1.2. Kidney stones introduction

Nephrolithiasis, commonly known as kidney stones (KS), is a notable example of pathological calcification, commonly found in the renal calyces and pelvis either freely or attached to the renal papillae (Khan et al., 2016). It has risen as a significant global health concern, affecting more than 10 % of the world's population nowadays and this percentage appears to be increasing (Sorokin et al., 2017). The public healthcare costs associated with kidney stones have also risen, with the United States alone spending more than $ 2 billion (in 2000) to $ 10 billion (in 2006) annually to address this condition (Litwin and Saigal, 2007).

Initially asymptomatic, kidney stones can progress into a painful and critical medical condition. They are formed by the accumulation of tiny mineral crystals within the kidneys.

1.2.1. Kidney stone types and causes

The approach of analyzing the composition of urinary calculi dates back to the late 18^{th} century. Following the pioneering work of M. Daudon (Daudon et al., 1993, 2016), it is widely recognized that kidney stones can be categorized based on their morphology and their chemical composition, associating them with specific diseases. Around 80 % of stones are composed of calcium oxalate (CaOx) or calcium phosphate (CaP). The remaining stone types include struvite (10 %), uric acid (9 %), and cystine (1 %) stones.

The stone types are named based on their predominant compositions. Among these stone types, calcium oxalates are the most prevalent. They usually come in two chemical forms: calcium oxalate monohydrate (known as whewellite, with chemical formula $CaC_2O_4{\cdot}H_2O$, see Figure 1.2 for a representative view of subtypes of calcium oxalate monohydrate stones) and calcium oxalate dihydrate (referred to as weddellite, with chemical formula $CaC_2O_4{\cdot}2H_2O$). It is important to note that whewellite stones are related to hyperoxaluria while weddellite stones are related to hypercalciuria (Daudon et al., 1993; Bazin et al., 2022c). Calcium phosphates are primarily present as apatite, brushite, and whitlockite (Daudon et al., 2010).

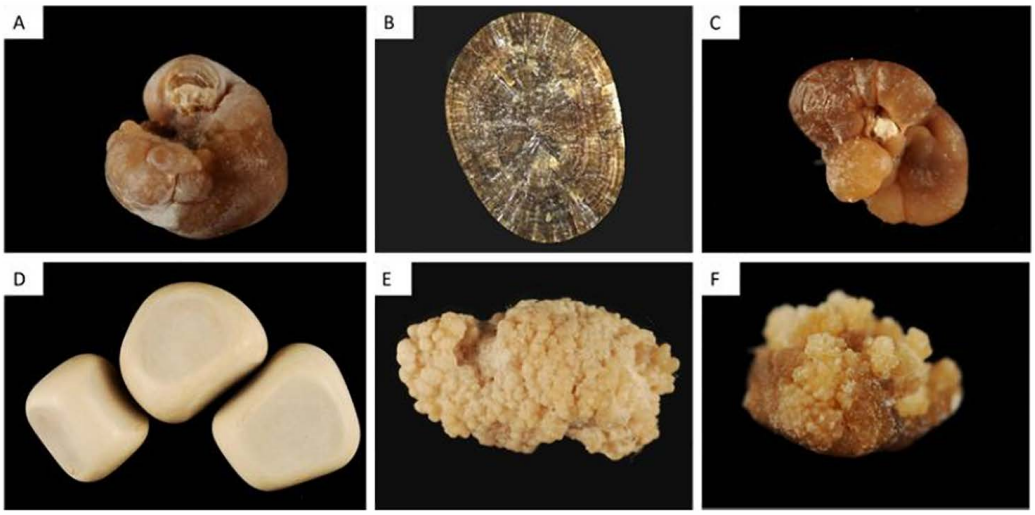

Figure 1.2: Varieties of calcium oxalate monohydrate (considered as Type I) stones. (**A**) Type Ia stone featuring a papillary umbilication, with a gray veil on the surface indicating recent crystalline deposits and thus stone activity. (**B**) Cross-section of a Type Ia stone, revealing its concentric and radial internal organization. (**C**) Type Ia stone showing a remnant of Randall's plaque (visible as a whitish deposit in the umbilication). (**D**) Type Id stones characterized by a smoothed appearance, resulting from stasis and chronic contact with other stones. (**E**) Type Ic stone exhibiting a whitish and budding structure, commonly found in cases of primary hyperoxaluria. (**F**) Type Ie stone, often associated with enteric hyperoxaluria. Adapted from (Letavernier et al., 2022).

Struvite stones are also called infection stones (Gettman and Segura, 1999; Daudon et al., 2022). They are composed of magnesium ammonium phosphate and are typically formed due to the increased production of ammonia secondary to infection with urease-producing organisms, such as *Proteus* or *Klebsiella*. The subsequent elevated urinary pH leads to the formation of struvite stones. Struvite crystals, along with associated carbonate apatite crystals, have the potential to rapidly grow into large stones known as staghorn calculi, a name reflecting their horn-like projections (Figure 1.3).

Figure 1.3: Complex stone sample consists of carbonated apatite mixed with other calcium phosphates or struvite. Struvite stones in general have a heterogeneous, and rough textured surface, and they can vary in color from clear to dark brown (Letavernier et al., 2022).

Uric acid stone formation is closely linked to decreased urinary uric acid levels, low urine pH, and limited urine volume (Daudon et al., 2005). Metabolic disorders such as diabetes and obesity contribute to the formation of uric acid stones. Diets rich in animal proteins also elevate the uric acid load and precipitation. Moreover, uric acid stone formation is associated with gout and chronic diarrhea (Ma et al., 2018).

Uric acid stones often have a compact yellow-orange appearance similar to pebbles (see Figure 1.4-A). When examined internally, they reveal the presence of orange concentric rings (see Figure 1.4-B). Occasionally, these stones may also feature a compact outer layer that encloses a porous and friable interior (Figure 1.4-C & D) (Khan et al., 2016; Letavernier et al., 2022).

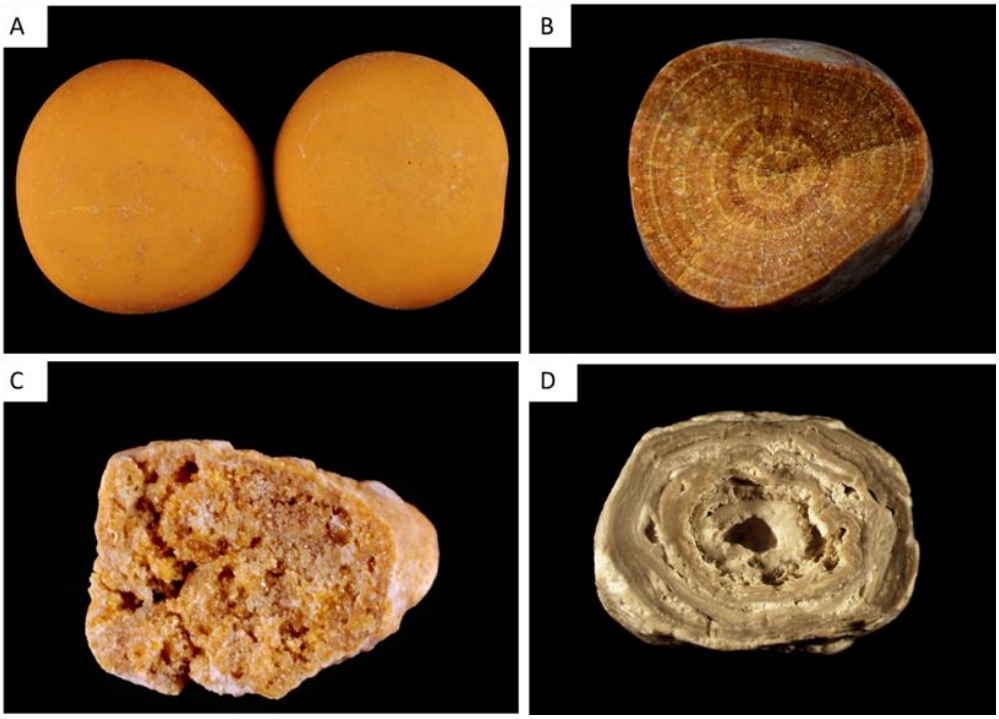

Figure 1.4: Stones that are made of uric acid or urates. The stone in **A** has a pebble-like appearance with an orange surface. **B**: In most cases, the uric acid stone's internal structure shows concentric rings. Some stones have a friable (**C**) and porous (**D**) interior structure (Letavernier et al., 2022).

Cystine stones are usually found in children and adolescents (Thakore and Liang, 2023). They occur due to congenital diseases that cause mutations in two genes, SLC3A1 and SLC7A9. These mutations lead to defects in the transport of certain amino acids, including cystine. Cystine stones have a compact, amber-colored appearance with a mild opacity (see Figure 1.5).

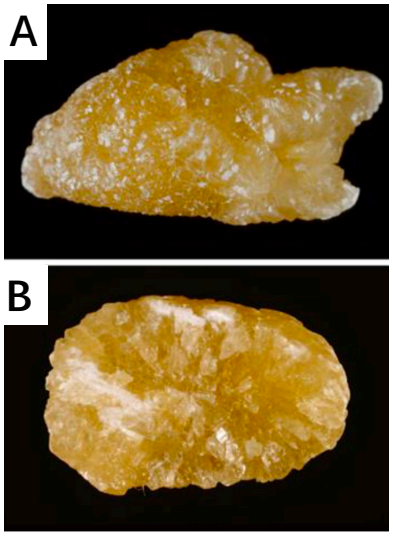

Figure 1.5: A cystine stone sample with a yellowish color, rough surface texture (**A**) featuring hexagonal crystallites, and a disorganized internal structure (**B**) (Letavernier et al., 2022).

1.2.2. Kidney stones formation

Kidney stone formation is a complex physicochemical process that remains incompletely understood despite centuries of research efforts. It involves a balance between factors that either promote or inhibit crystallization and aggregation within the urinary environment. While the specific details of these processes may vary among different types of kidney stones, the fundamental principles of nucleation and crystal growth remain the same.

According to the widely accepted theory (Aggarwal et al., 2013), the formation of kidney stones begins with the precipitation of calcium salts from a supersaturated urine solution, a step known as nucleation, resulting in the formation of crystals. These crystals then grow and aggregate, eventually forming a crystal nidus. When this aggregate of crystals attaches to the tubular epithelium and becomes exposed to urine due to epithelial sloughing, it undergoes further epitaxial growth. This process leads to the formation of a detectable renal stone.

Nucleation is the initial stage in crystallization where free ions in solution associate to form microscopic particles and start the process of stone development. Primary nucleation can be differentiated based on its origin. Homogeneous nucleation happens within the solution when the urine becomes supersaturated with respect to the tiny crystals that compose the stones, while heterogeneous nucleation is initiated by the influence of external particles, when seed crystals or certain macromolecules provide the foundation for nucleation, supporting crystal growth and facilitating the formation of kidney stones (Bazin et al., 2012; Khan et al., 2016; Rouzière et al., 2016).

In addition, considering that calcium phosphate is a frequently occurring crystal in human urine and is a commonly found crystal in stones (Khan et al., 2016), especially mixed calcium oxalate/calcium phosphate stones, it is suggested that calcium phosphate can induce the nucleation of calcium oxalate crystals (Daudon et al., 2015). This will be discussed in detail in Section 1.2.4.

1.2.3. Trace elements in kidney stones

Over the past decades, significant research efforts have been dedicated to the identification of calculi constituents that could be measured and possibly altered to mitigate stone formation. These include matrix proteins, organic acids, and polysaccharides (Fleisch, 1978; Grover et al., 1992; Bazin et al., 2007; Vasinova Galiova et al., 2015; Letavernier et al., 2022). The chemical diversity present in stones underscores the complex mechanisms that contribute to the formation of stones.

A comprehensive explanation for the origins of urolithiasis and a plan of effective preventive strategies are still elusive. In fact, a profound investigation of kidney stone elemental composition has great significance due to the potential relationships between the elements present within stones and the roles they play in stone formation. Nonetheless, only a few amounts of research have been documented to study the contents of elements (Ramaswamy et al., 2015), and their impact on the formation of kidney stones remains uncertain and under debate.

Studies show that trace elements can combine with phosphate and oxalate ions to create poorly soluble salts, indicating that they may play a distinct role in the formation of kidney stones (Singh and Rai, 2014). Among the possible hypotheses, one suggestion is that specific trace elements function as catalysts. Several research highlights the potential influence of elements such as Mg (Oka et al., 1987), Al (Sutor, 1969), Mo (Deosthale and Gopalan, 1974) or Fe citrate complexes (Muñoz and Valiente, 2005) acting as either promotors or inhibitors of the crystallization.

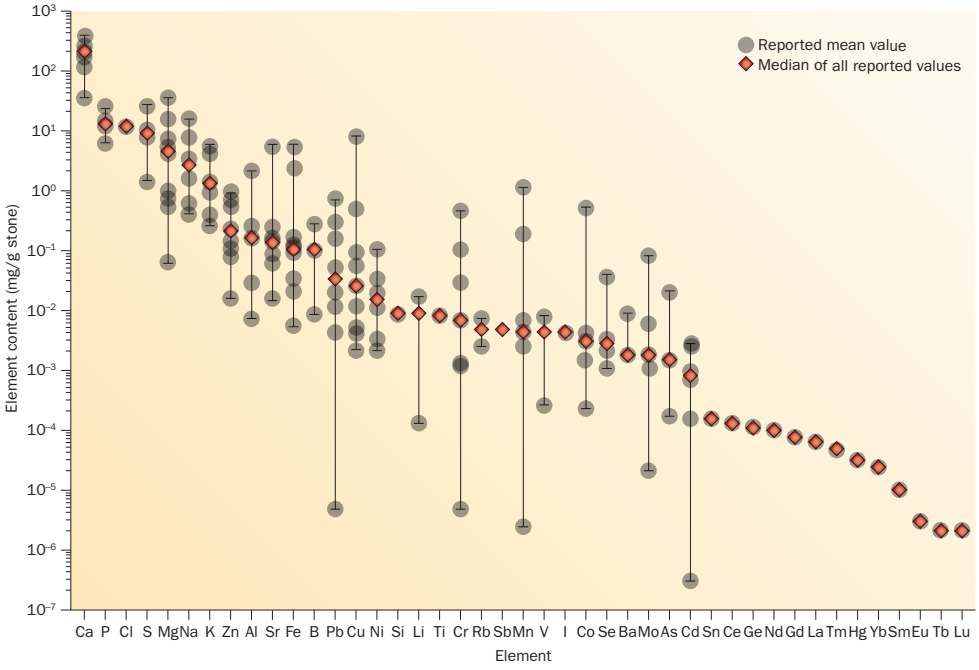

Figure 1.6: Comparison of element content in calcium-based stones from various published studies (unit: mg/g stone) (Ramaswamy et al., 2015).

Several published studies have explored the elemental composition of common calcium-based kidney stones. Concentrations of both major and trace elements are illustrated in Figure 1.6 (Ramaswamy et al., 2015). As depicted in the figure, there is a large variation in element content in calcium-based stones from various published studies, especially for elements like Fe, Pb, Cu, Mn, Co, and Cd, which span varying ranges. This variability could arise from differences in sample biological variations, or variations in the analytical techniques used.

Considering a previous study dedicated to kidney stones analysis by synchrotron-based X-ray fluorescence technique (Bazin et al., 2007) and the experimental conditions (i.e. only photons with energy higher than 3 keV were detectable), the authors have classified the different elements found in the kidney stone specimen as follows: first, the major element involved in the crystalline mineral phases, i.e. Ca, then trace elements such as Sr (Sr is in the same column of the periodic table as Ca), a group of transition elements including Fe, Cu, and also Zn. And lastly certain pathological elements such as Pb. Most of the Fe present in KS probably results from residual blood at the surface or within layers of the stones.

1.2.4. Some pathogenesis mechanisms

There are two pathways for stone formation. As shown in Figure 1.7, one involves calcium phosphate deposits creating renal interstitial plaques exposed to urine, leading to the erosion of the overlying urothelium. The other pathway, which is less common, results in the deposition of plugs in the collecting ducts. The formation of CaOx stones requires a complex interaction involving nucleation processes for both CaP and CaOx, followed by subsequent aggregation and growth (see Figure 1.8).

In both scenarios, calcium phosphate plays a crucial role in initiating a heterogeneous nucleation process for calcium oxalate crystals, leading to kidney stone formation (see Figure 1.7). Over the past two decades, observations of these deposits have provided validation for these two models (Evan et al., 2003; Matlaga et al., 2006; Linnes et al., 2013). While they can cover most of the hypothetical stone formation scenarios, no single model can fully explain the observed evidence across all stone formers, likely due to multiple contributing factors involved in the process (Khan et al., 2016).

Randall's plaque formation is a multistep physiochemical process. As the first step urine becomes supersaturated with respect to CaP within the renal tubules located at the end of the loop of Henle. This triggers the deposition of CaP in the basement membrane of the thin descending loop of Henle, representing the initiation of plaque formation.

Subsequently, collagen fibers and membranous vesicles get calcified as well. As the mineralization front progresses, it reaches the renal papillary surface, where a subepithelial plaque takes shape. Meanwhile, the epithelium covering the papillary surface is disrupted, exposing the CaP crystals to the pelvic urine, which typically maintains a metastable condition in relation to CaOx. Urinary macromolecules are deposited onto the exposed CaP crystals. This facilitates the subsequent deposition of CaOx crystals onto the CaP base.

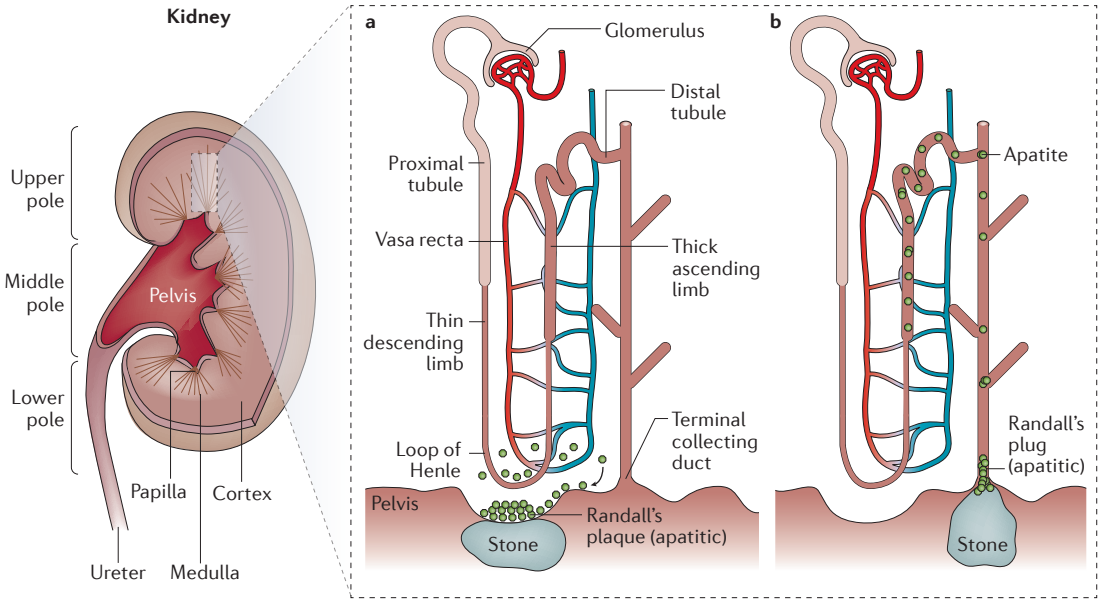

Figure 1.7: Schematic diagram of two pathways for renal stone formation. In the first pathway (**a**), the process initiates with the deposition of CaP, primarily in the form of apatite, within the renal interstitium. The overgrowth of CaP reaches the renal papillary surface, where they are exposed to pelvic urine. These CaP deposits termed Randall's plaques act as nucleus forms, facilitating the development of CaOx stones anchored to the plaque base. In the second lesion (**b**), CaP crystals originate within the renal tubules. These crystals migrate with the urine flow, aggregating and ultimately occluding the terminal collecting ducts. These plugs are also exposed to pelvic urine. In both cases, the formation of the CaP nucleus is the critical step leading to the genesis of CaOx kidney stones. Adapted from (Khan et al., 2016).

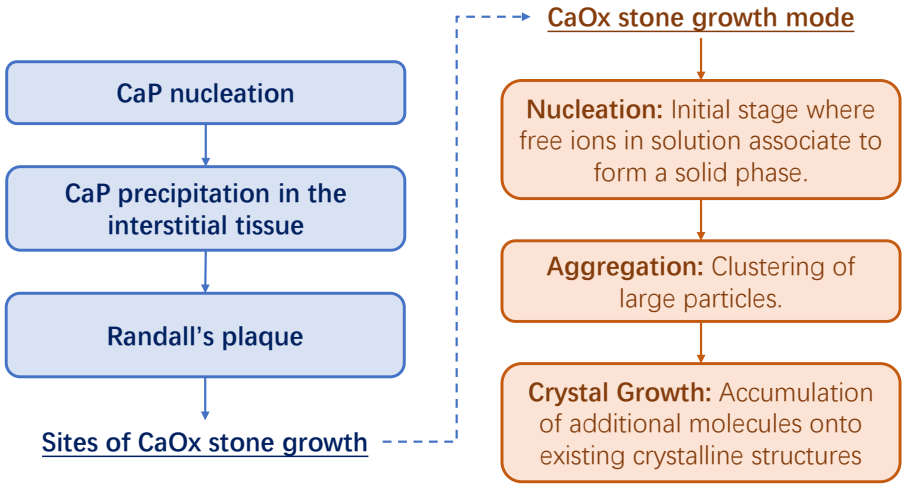

Figure 1.8: CaOx stone formation on Randall's plaque.

Over the past 20 years, there has been an increasing interest in studying Randall's plaque. This can be attributed to two factors: the increased capabilities of urologic endoscopy, which enables direct visualization of Randall's plaque at the tip of renal papillae. Additionally, the growing incidence of kidney stones

associated with Randall's plaque leads to a resurgence in interest in Randall's plaque study (Letavernier et al., 2016; Van de Perre et al., 2021). Understanding the mechanisms involved in the formation of Randall's Plaque is therefore crucial for implementing effective preventive and management strategies for kidney stones and developing new drugs. However, the analysis of Randall's Plaque poses significant challenges, primarily due to the small size of the early-stage calcifications (characterized by tiny crystallites less than half a micron (Prien, 1975)) and the complex mechanisms underlying plaque formation. Additionally, in clinical practice, the frequent use of fragmentation techniques leads to the loss of plaque fragments originally attached to the stone, thereby hindering the identification of the origin of fragmented stones. (Letavernier et al., 2016)

1.3. Analytical techniques for kidney stones

Numerous approaches have been used to analyze renal stones. These investigations are focused on understanding the morphology, composition, microstructure, and potential mechanisms involved in the formation of these stones.

1.3.1. Polarized light microscopy

Polarized light microscopy is a conventional imaging technique for kidney stone analysis. The stones are fractured to expose their internal structure and then examined and identified under a polarizing microscope (Figure 1.9). While the fast examinations offer valuable insights into the internal characteristics structure and composition of kidney stones, it is challenging to identify small amounts of crystalline material within complex mixtures, and its effectiveness often relies heavily on the expertise of the operator.

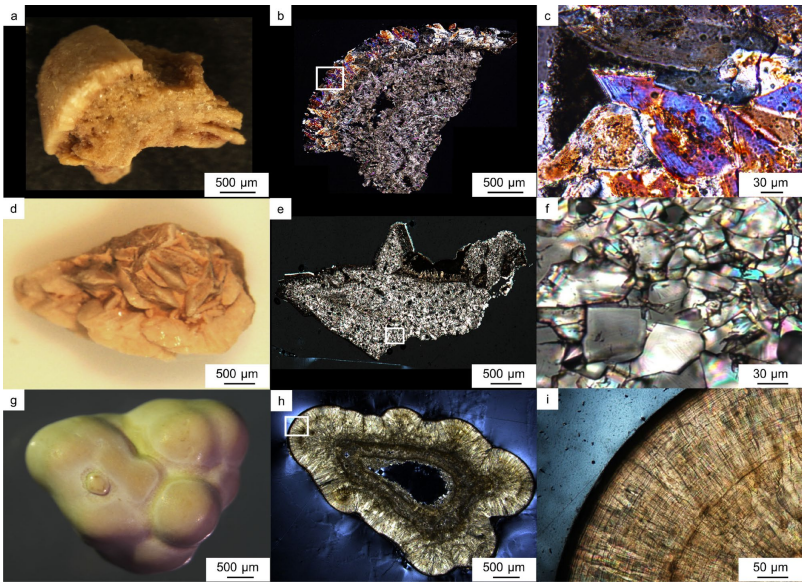

Figure 1.9: Polarized light microscopy analysis of various kidney stone samples. The left column displays the morphology of the samples. The middle column shows polarized light microscopy images of thin sections in the samples. The right column presents enlarged images of the selected white box area in the thin sections (Tanaka et al., 2021).

1.3.2. Electron microscopy

Electron microscopy, which uses accelerated electrons, has been widely used in kidney stone analysis. Electron microscopy can achieve higher spatial resolution than light microscopy, making it possible to observe structures at the nanometer scale.

Scanning electron microscopy (SEM), energy dispersive X-ray spectroscopy (EDX)

Scanning electron microscopy (SEM) is a powerful imaging technique that utilizes an electron beam to generate a high-resolution surface image of a sample. This method enables the analysis of stone characteristics with spatial resolution down to some nms. In combination with SEM, energy dispersive X-ray spectroscopy (EDX) complements the analysis by providing elemental information about the sample. When the sample is hit by electrons, it emits characteristic X-ray photons. Through EDX analysis of the collected spectrum, elements present in the stone samples, such as Ca, Mg, and P, can be then identified (see Figure 1.10), providing detailed information about the major composition of the stones.

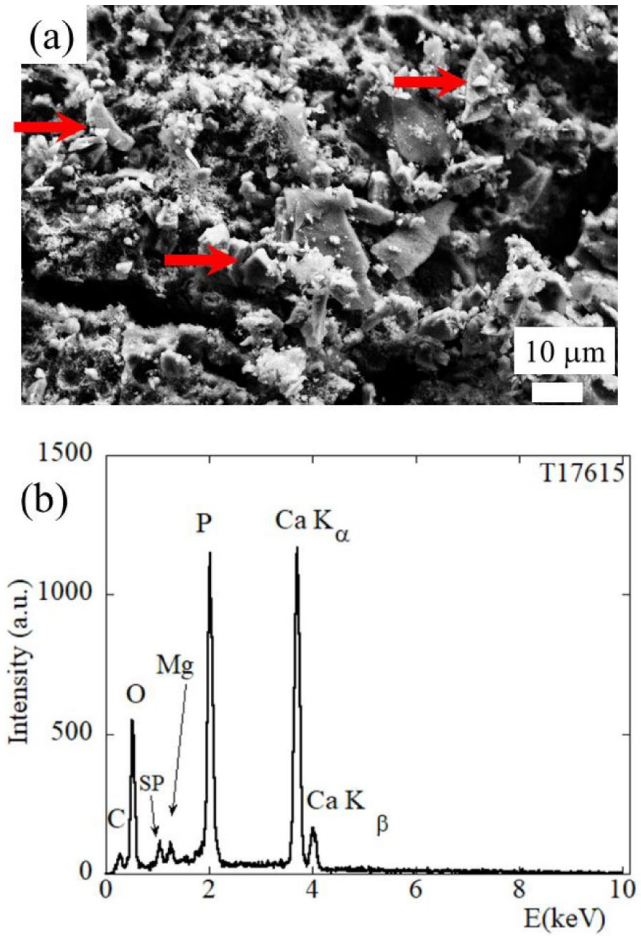

Figure 1.10: Scanning electron microscopy (SEM) combined with energy dispersive X-ray spectroscopy (EDX) spectrum. The image displays the trigonal morphology of the stone sample containing whitlockite as captured by SEM (**a**), alongside the corresponding EDX spectrum (**b**) providing elemental information (Bazin et al., 2022d).

1.3.3. Infrared spectroscopy

Infrared (IR) spectroscopy, initially applied to stone analysis by Beischer in 1955 (Beischer, 1955), has become a popular method for *in vitro* quantitative stone analysis (Singh and Rai, 2014). In this technique, an IR source irradiates the sample, inducing atomic vibrations, and the resulting absorption spectra (see Figure 1.11) are recorded and analyzed to determine the stone's composition (Nguyen and Daudon, 1997; Singh and Rai, 2014). This method can identify non-crystalline substances, such as amorphous fatty materials, and can be helpful in identifying the organic components of stones (Kasidas et al., 2004).

Fourier transform infrared spectroscopy (FTIR) is a common form of IR spectroscopy, widely used for identifying organic and inorganic components (Singh et al., 2020). In kidney stone analysis, FTIR is frequently used to identify the kidney stone constituents by the percent mass present in the stone samples.

Attenuated total internal reflectance infrared spectroscopy (ATR-FTIR) is a more recent technique of IR spectroscopy. The measured spectra are independent of sample thickness because the IR light only interacts with the sample surface within the evanescent field. This surface-sensitive method does not require grinding, pressing, or mixing the sample with an IR inactive material before analysis, making it more convenient in sample preparation than traditional methods (Singh and Rai, 2014; Gulley-Stahl et al., 2009).

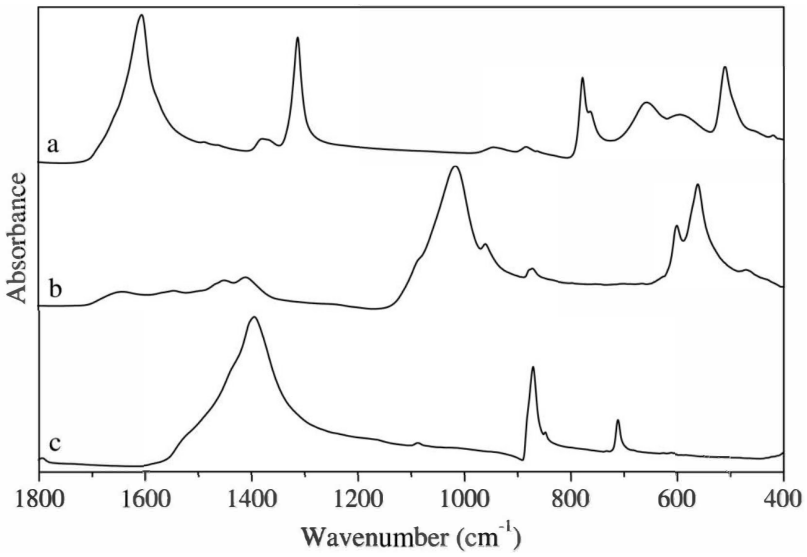

Figure 1.11: Pure infrared spectra of reference samples calcium oxalate monohydrate (**a**), hydroxylapatite (**b**) and $CaCO_3$ (**c**) collected with a Harrick Split-pea ATR microscope interfaced to a Perkin Elmer 2000 Fourier transform infrared spectrometer (Gulley-Stahl et al., 2009).

1.3.4. Laser ablation inductively coupled plasma-mass spectrometry (LA-ICP-MS)

Laser ablation inductively coupled plasma-mass spectrometry (LA-ICP-MS) is a destructive analytical method for the determination of element abundances and elemental and isotopic compositions (Durrant, 1999). This technique uses a focused laser beam directed onto the sample surface, causing it to be ablated into

fine particles, which are then transported to the ICP torch. The sample particles are instantly ionized and carried in a steam of argon and/or helium gas to an ICP-MS detector. LA-ICP-MS allows for the accurate and simultaneous determination of a wide range of elements in the kidney stone sample as shown in Figure 1.12.

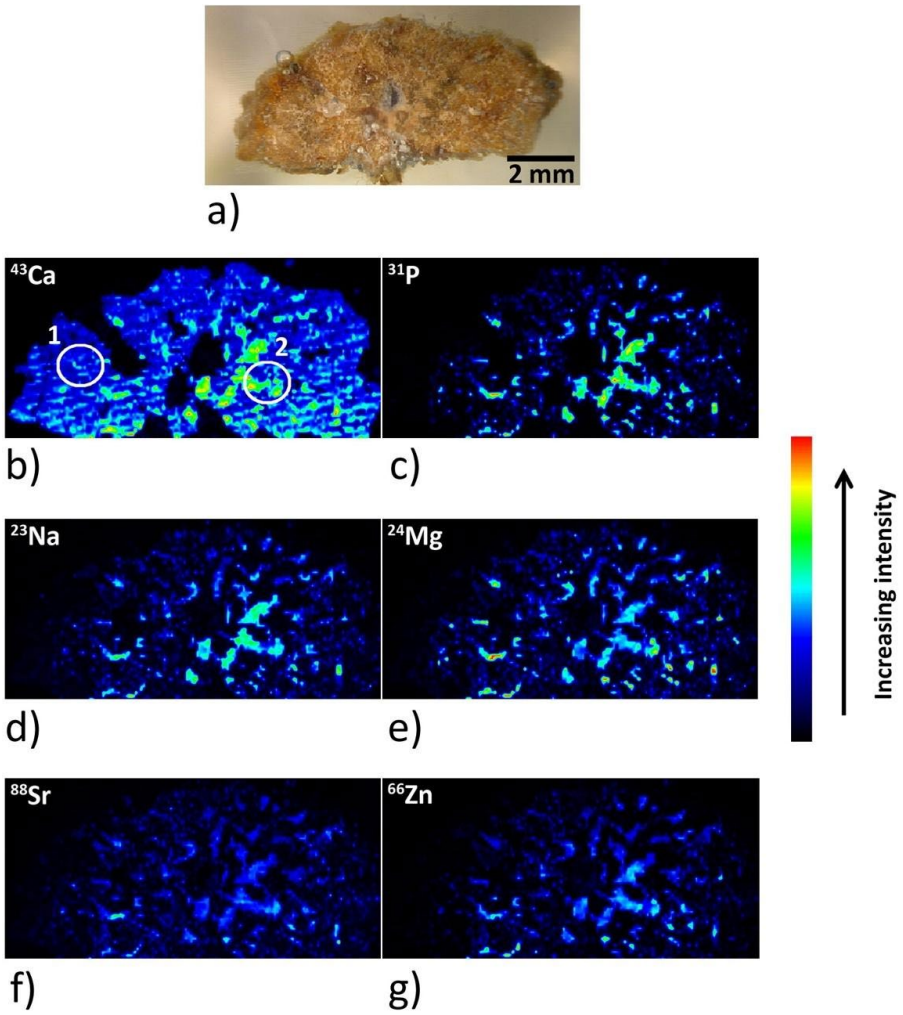

Figure 1.12: Distribution of different elements on the surface of a kidney stone sample using the LA-ICP-MS method (Vašinová Galiová et al., 2014).

1.3.5. Raman spectroscopy

Raman spectroscopy provides information about the chemical composition and structure characterization of the sample. In a Raman spectroscopy experiment, molecules in the sample are excited using a high-intensity laser beam. The resulting scattered light is passed through a spectrometer for the measurement of the Raman spectrum. As shown in Figure 1.13, in a urinary deposit study, the laser used for Raman spectra has a near-infrared wavelength of 1064 nm. This helps with Raman scattering excitation in biological samples and suppressing fluorescence background contamination (Tamosaityte et al., 2022).

(Nguyen and Daudon, 1997) used IR and Raman spectroscopy in their analysis of kidney stones, determining that this combination of spectroscopic techniques provided an effective approach for kidney stone identification.

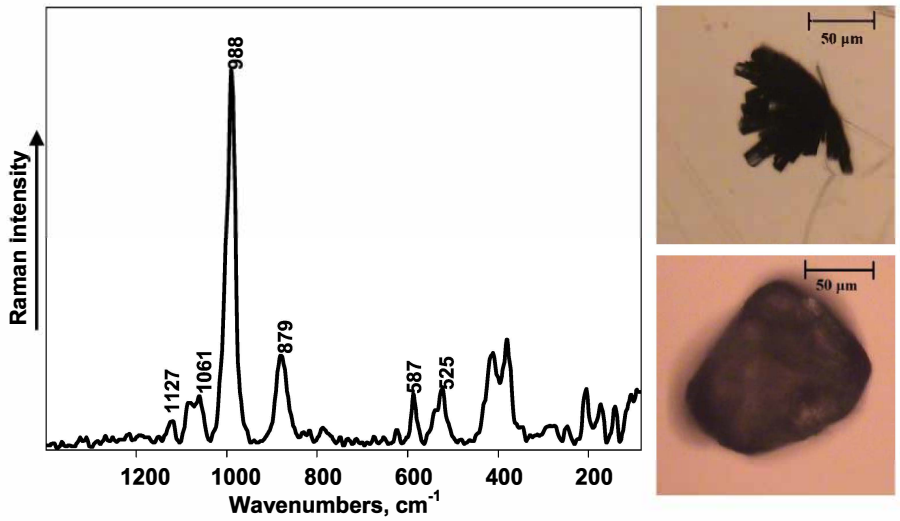

Figure 1.13: Raman spectrum of brushite crystal present in the urinary deposit, measured with a Fourier transform Raman spectrometer (Tamosaityte et al., 2022).

1.3.6. X-ray diffraction

The X-ray diffraction (XRD) method uses a monochromatic X-ray beam to identify the crystalline components of the sample. When an X-ray beam is diffracted by the crystalline sample, unique XRD patterns are produced. In practice, the angular position, and intensities of the diffraction peaks permit the identification of the various crystalline phases (Figure 1.14). This technique can measure and differentiate all various major crystalline phases present in a stone sample (Kasidas et al., 2004).

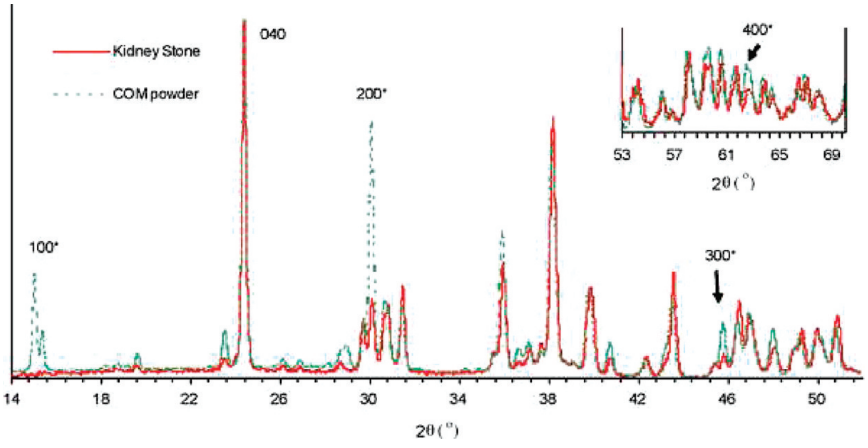

Figure 1.14: X-ray diffraction pattern of calcium oxalate monohydrate (COM) powder and the section of kidney stone. Adapted with permission from (Al-Atar et al., 2010). Copyright 2023 American Chemical Society.

1.3.7. X-ray tomography

X-ray tomography serves as a pivotal imaging modality in my thesis, enabling the acquisition of non-invasive, cross-sectional representations of kidney stones. By using high-energy X-ray beams to penetrate samples, this technique facilitates the detailed visualization of intricate sample morphology, microscale features, and

internal structures. Within the scope of this work, synchrotron-based X-ray computed tomography (SR CT) offers many advantages over conventional micro-CT. The synchrotron source used provides a high-flux and high-intensity X-ray beam. This results in the measurement of quantitative high-resolution 3D tomograms with a high signal-to-noise ratio. SR CT plays a crucial role in kidney stone research, aiding in the detailed identification of stone sample morphology and microstructure. It guides the selection of relevant cross-sections in samples, facilitating subsequent multi-modal analyses (Kaiser et al., 2011). As shown in Figure 1.15, a full-field micro-CT experiment was conducted on a calcium oxalate monohydrate stone sample, achieving an effective voxel size of 2.25 μm.

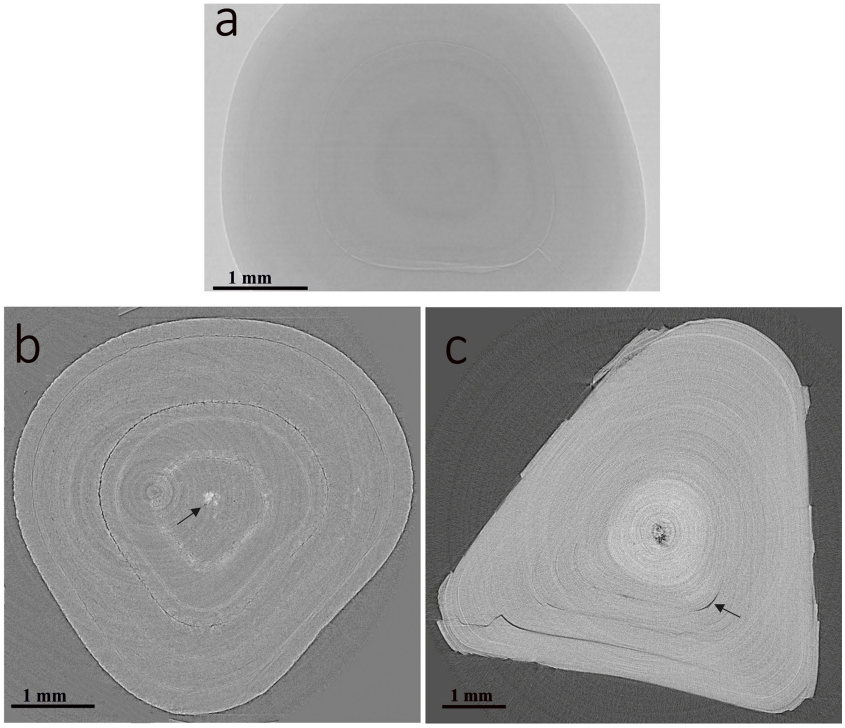

Figure 1.15: Micro-CT slice of a pure calcium oxalate monohydrate (COM) stone. The reconstructed μCT slice shows concentric layers of organization in **a**. The denser region of the reconstructed slice indicated by an arrow in **b** is an apatite nucleus in the central. Another SR-μCT slice (**c**) shows multiple layers of organization, with visible internal cracks marked by an arrow (Kaiser et al., 2011).

1.3.8. X-ray fluorescence

X-ray fluorescence (XRF) is a well-established non-destructive analytical technique for elemental analysis in various scientific fields. When a sample is exposed to an X-ray beam, the ionization and transitions of inner-shell electrons within the atoms result in the emission of characteristic X-ray fluorescence photons, with energies specific to the excited elements present in the sample. By analyzing the emitted XRF signal, we can quantify the intensity of the different elements present in the stone sample, such as Ca, P, S, K, Zn, Cu, Fe, and Sr (Bazin et al., 2007). This method enables the determination of trace elements in kidney stones (Srivastava et al., 2014). Figure 1.16 shows the in-lab XRF experimental set-up and a typical XRF spectrum measured for a kidney stone.

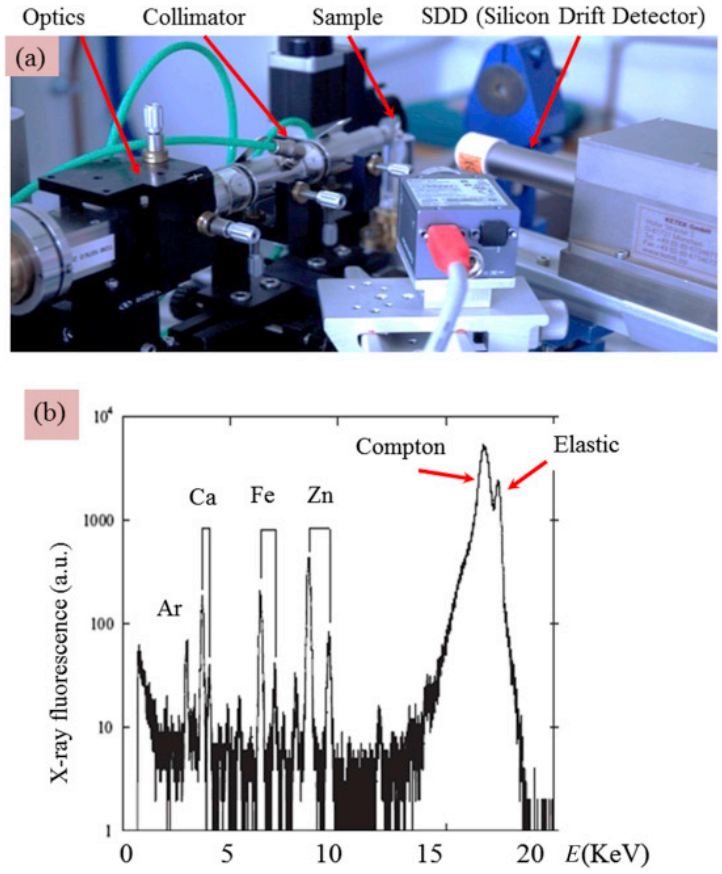

Figure 1.16: In-lab XRF experimental set-up and XRF spectrum clearly shows the contributions of elements such as Ca, Fe and Zn in the stone sample. The focused monochromatic beam is generated using an in-lab X-ray source (Rouzière et al., 2016).

1.4. Analytical techniques for Randall's plaque

The analysis of incipient Randall's plaque still poses several challenges due to the localization of the plaques, and the sub-micron-sized characteristics of these calcifications.

In the investigation of incipient Randall's plaques, achieving high spatial resolution is essential for effectively visualizing the morphology and micro-features of these tiny mineral deposits. Non-destructive methods are preferred to ensure the preservation of sample integrity. Additionally, analytical techniques with high sensitivity to investigate the roles of trace elements are also necessary in the study. All these requirements demand multi-modal imaging techniques for comprehensive characterization.

Undoubtedly, multiple analytical techniques discussed in Section 1.3 can be effectively employed to study Randall's Plaque. For example, in a recently published paper, researchers used a multimodal method including the combination of laboratory X-ray micro–CT and Fourier transform infrared spectroscopy (Figure 1.17), in order to gain a comprehensive understanding of the mineral and organic components of Randall's plaque (Winfree et al., 2021).

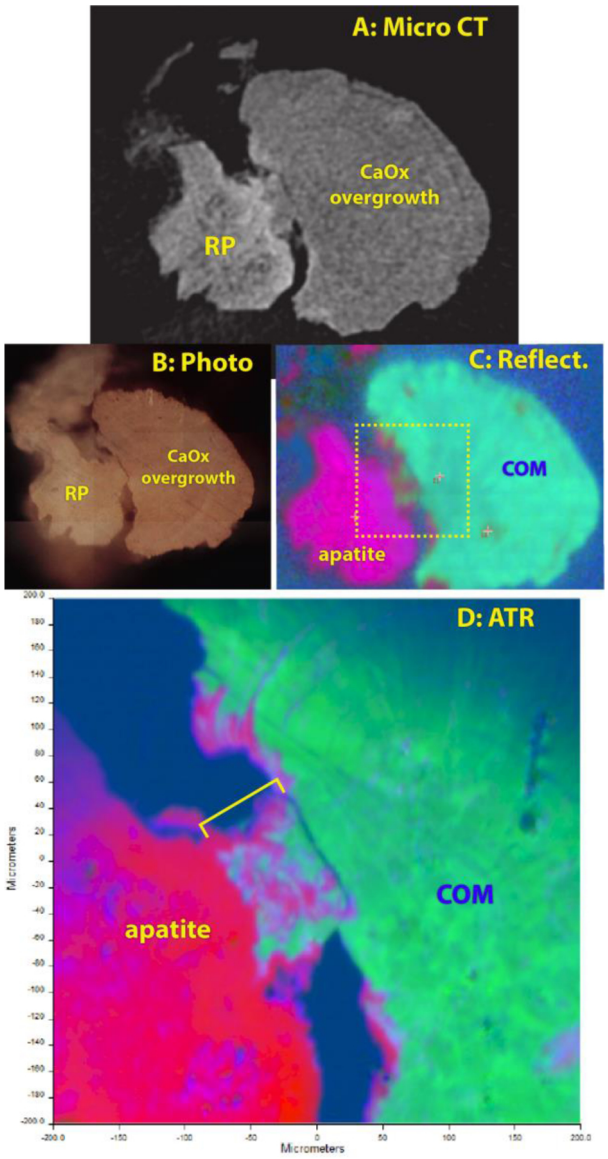

Figure 1.17: A kidney stone polished to expose Randall's plaque and the stone overgrowth region. **A**. Micro-CT slice displaying the polished stone. **B**. Photographic montage captured on an infrared microscope. **C**. Reflectance-mode FT-IR microscopy results. **D**. Attenuated total reflection (ATR) mode FT-IR microscopy results (Winfree et al., 2021).

Several studies have revealed the diversity and complexity of chemical components in Randall's plaque (Khan et al., 2012; Williams et al., 2015; Carpentier et al., 2010; Bouderlique et al., 2019).

In a prior research conducted by (Carpentier et al., 2011), trace elements, including zinc, were detected in the plaque by X-ray fluorescence technique. Notably, the concentration of zinc was found to be higher in Randall's plaque compared to the reference kidney stone. Given the established association of zinc with inflammation in various studies (Bao et al., 2008; Haase et al., 2008), it is indicated that these calcified deposits are a pathological process involving a tissue reaction.

To better understand the pathology and early-stage kidney stone formation, a high-resolution 3D study of Zn concentration variations is needed, as it will shed light on the roles of Zn and other trace elements, offering insights into the spatial distribution of Zn within Randall's plaque and its potential role in stone formation.

Addressing this challenge requires the development of a rapid quantitative XRF tomography method. The development of fast sparse quantitative X-ray fluorescence imaging and tomography offers a non-invasive way to explore the spatial elemental distribution in RP. Understanding the roles of trace elements in the pathological process paves the way toward efficient prevention and medical treatment of kidney stone disease.

1.5. X-ray imaging

1.5.1. X-ray imaging history

X-ray imaging began in 1895 with Wilhelm Conrad Roentgen's discovery of X-rays. Working with a cathode ray tube called a Crooke's tube, he uncovered a new form of invisible rays that could penetrate materials: X-rays (Figure 1.18). Röntgen's groundbreaking discovery earned him the first Nobel Prize in Physics in 1901, and its application quickly expanded to the field of medicine for the non-invasive identification and diagnosis of internal diseases.

Figure 1.18: Röntgen used X-ray to take pictures of the left hand of his wife, showing the skeletal structure of the hand (Haase et al., 1997).

Since Roentgen's discovery, X-ray imaging has evolved significantly during the first half of the 20th century, and progress in specialized instrument development paved the way for various high-resolution X-ray microscopy techniques. In 1913, P. Goby introduced the microradiography method (Goby, 1913) to study the structural details of objects by enlargement of X-ray radiographs with micron-level resolution. Further enhancements in X-ray microscopy have been made since the late 1940s. A. Engstrom developed the quantitative elemental imaging technique (Engström, 1946). P. Kirkpatrick

improved the resolution of X-ray microscopy by using focusing X-ray mirrors (Kirkpatrick and Baez, 1948). Subsequently, Fresnel zone plates were employed for X-ray focusing (Baez, 1952). In parallel, Cosslett and Nixon first carried out work in the development of the projection X-ray microscope, involving producing a small X-ray source using an electron beam focused on a thin target (Cosslett, 1959). During this period, the early X-ray microscopy work reached a peak.

Prior to the 1970s, the size and intensity of available X-ray sources were limited. However, the emergence of synchrotron radiation, once considered a byproduct in high-energy physics accelerators, brought significant improvements in X-ray capabilities in microscopy. Horowitz and Howell (in 1972) designed the first transmission and fluorescence X-ray microscope at the Massachusetts Institute of Technology accelerator, which marked a crucial milestone in the field.

Following this development, scanning X-ray imaging advanced further, driven by the utilization of intense sources like 3rd generation synchrotrons, improved X-ray optics, fast scanning strategies, and precise sample positioning. These technological improvements have made X-ray imaging more appealing, allowing for higher spatial resolutions, faster image acquisition, and the realization of multimodal imaging techniques.

SOLEIL Synchrotron is one of the existing 3rd generation synchrotron sources. It provides high-brilliance synchrotron radiation across a broad spectral range, from far infrared to hard X-rays. NANOSCOPIUM beamline is the scanning hard X-ray nano-probe beamline at SOLEIL. It is dedicated to 2D/3D multimodal scanning X-ray imaging techniques in the energy range of 5 to 20 keV energy range, which is ideal for imaging a wide range of samples from biological samples to advanced materials.

1.5.2. X-ray microscopy techniques

X-ray microscopy (XRM) covers multiple experimental techniques aimed at imaging samples using X-rays as a non-invasive probing tool. Due to the inherent penetrating nature of X-rays, XRM is well-suited for investigating the internal properties of samples. It offers higher resolution when compared to optical microscopy and offers larger information depth compared to electron microscopy. Depending on the specific research needs of the imaging modalities for a study, measurements can be carried out using either full-field or scanning methods. Full-field microscopy at a synchrotron radiation source employs projection imaging with a parallel beam (Figure 1.19-A). With the help of X-ray focusing optics, scanning X-ray microscopy uses a small and intense beam to scan the sample. The resolution of the scanning method is determined by the beam size at the focal plane.

Essentially, in most cases of scanning XRM, the sample is mounted and supported on a translation and/or rotation stage and raster-scanned with a stationary focused X-ray beam. The transmitted beam and/or secondary emission are recorded at each scanning position of the sample. (Figure 1.19-B).

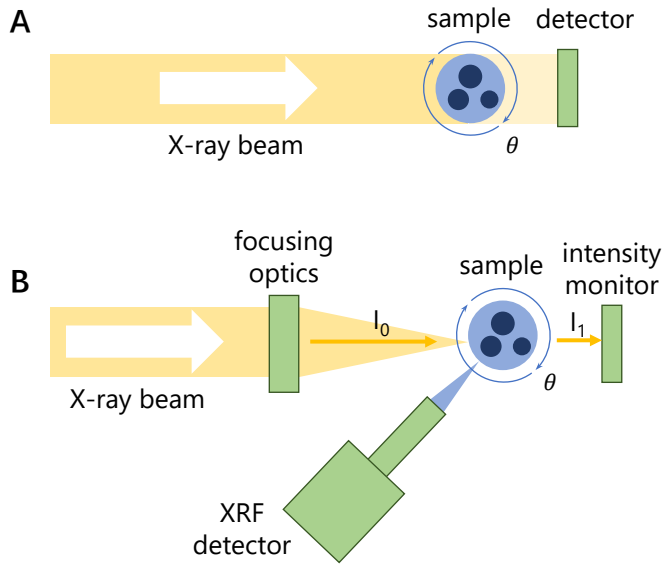

Figure 1.19: Schematic view of the full-field transmission X-ray tomography (**A**) and scanning X-ray fluorescence tomography (**B**).

Scanning X-ray microscopy can include several modalities, including X-ray absorption, X-ray fluorescence, X-ray diffraction, and coherent diffractive imaging. These spatially resolved techniques in scanning XRM provide a broad range of capabilities when compared to full-field XRM (Brueckner, 2021). However, scanning XRM measurements typically require more time than full-field XRM measurements. This is due to the necessity of raster scanning during the data acquisition process. For 3D tomography datasets, the time will be further extended due to the additional dimension. Therefore, the development of rapid and effective data acquisition and processing strategies, such as sparse-angle scanning tomography experiments combined with appropriate reconstruction algorithms, is important to optimize the efficiency of scanning XRM methodologies.

1.5.2.1. X-ray absorption microscopy

The transmission of an X-ray beam through the sample is measured by a detector placed directly behind the sample. Scanning X-ray tomography can be performed in the absorption mode and the contrast is obtained owing to the difference in X-ray absorption of elements in the sample (Baruchel, 2000). The transmitted intensity can be normalized to the incident beam intensity measured by a detector placed before the sample.

1.5.2.2. X-ray fluorescence microscopy

Scanning X-ray fluorescence imaging involves the scanning of a sample to analyze its elemental composition. The emitted X-ray fluorescence signals from the sample are captured by dedicated XRF detector(s) (Figure 1.19-B) and the resulting XRF spectra are subsequently fitted to identify elements present within the scanned area. This fitting process also enables the determination of the intensity of the XRF photons emitted by these elements. This method generates spatially resolved elemental maps of the sample. The concentration of each element can be further quantified by using a reference standard.

1.5.2.3. Scanning X-ray diffraction

Unlike conventional X-ray diffraction, which provides bulk information, Scanning X-ray diffraction offers the advantage of spatial-resolved structural variations on the microscale. By scanning the sample and recording diffraction patterns at each point, this method enables researchers to construct a detailed map of crystalline structures and their orientations in a sample. Particularly useful for heterogeneous samples. It can be combined with X-ray fluorescence imaging to identify the crystallographic phases and element distribution in the sample simultaneously (Figure 1.20).

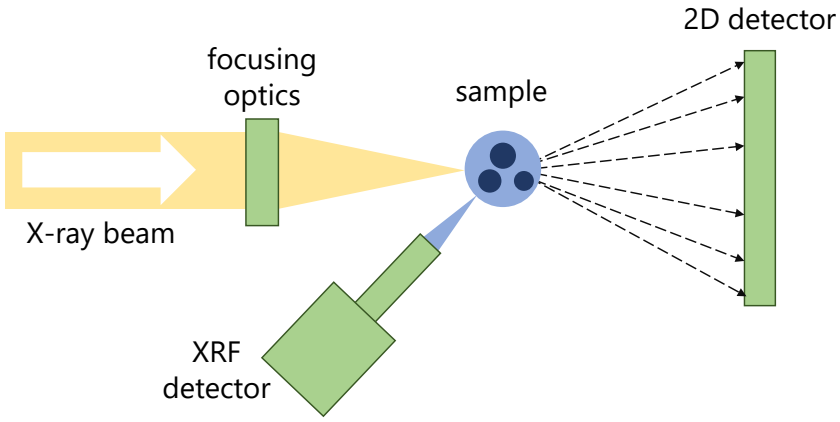

Figure 1.20: Schematic view of the scanning X-ray diffraction combined with X-ray fluorescence technique.

1.5.2.4. X-ray phase contrast imaging

Phase-contrast X-ray imaging techniques have received much attention in recent years. They can offer contrast based on the phase shifts introduced by the sample. It can provide enhanced morphological information in cases when the sample is weakly absorbing compared to conventional absorbing techniques (Figure 1.21). In fact, phase contrast imaging demonstrates sensitivities to light elements that are 10 to 100 times larger than those achieved by absorption contrast methods.

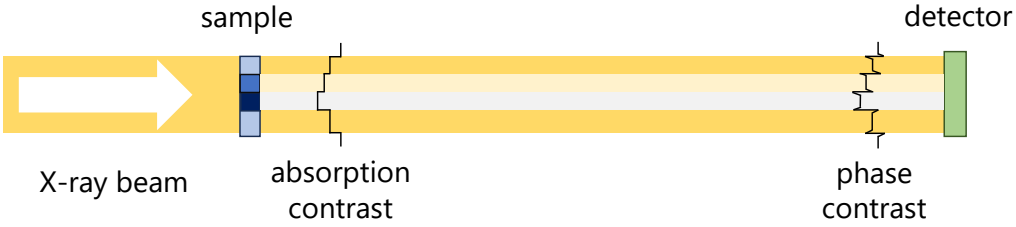

Figure 1.21: A schematic comparison of absorption and phase contrast projections. Phase contrast projection emphasizes the internal sample boundaries. Adapted from (Bertrand et al., 2012).

1.5.3. Scanning XRF tomography

Recent developments in fast continuous scanning, data acquisition (Deng et al., 2018; Kopittke et al., 2018; Medjoubi et al., 2013; Wang et al., 2001), and the high flux obtained at modern synchrotron-based hard X-ray nanoprobes have opened routine access to scanning 2D multimodal imaging. Scanning hard X-ray imaging and tomography techniques are ideally suited to provide complementary information on the elemental distribution, morphology, crystalline structure, and chemical speciation that can be obtained simultaneously. Moreover, these non-invasive scanning techniques provide straightforward access to multiple-length scale experiments.

Amongst the scanning techniques, the high analytical sensitivity of X-ray Fluorescence (XRF) imaging provides unique possibilities in several scientific fields to study the role and fate of trace elements (Chaurand et al., 2018; Dean et al., 2018; Figon et al., 2021; Kosior et al., 2012; Serpell et al., 2016; Sforna et al., 2014; Wolf et al., 2017; Xie et al., 2020; Yan et al., 2016). However, the unambiguous interpretation of 2D elemental distribution maps is not always straightforward or feasible and is especially problematic in the case of thick, complex samples. As such, the scientific community is highly demanding the extension of XRF imaging and other complementary scanning techniques to 3D tomography. Scanning XRF and multimodal tomography, where measuring projection images at different projection angles permits the reconstruction of the internal features by adapted reconstruction methods, provides unambiguous internal information about the sample (Deng et al., 2018; Gao et al., 2021; Gürsoy et al., 2015; Helliwell et al., 2013; Hong et al., 2015; Parsons et al., 2017; Punshon et al., 2012; Somogyi et al., 2015a; Suuronen and Sayab, 2018).

Up to now, the lengthy acquisition time necessary for these experiments (Deng et al., 2018) at 3rd generation synchrotrons has been one of the practical difficulties to its comprehensive utilization. Indeed, even if emerging sparse tomography techniques permit boosting the measurement throughput (Bourassa et al., 2016; Gao et al., 2021; Villarraga-Gómez and Smith, 2020) by compromising spatial resolution, overcoming the time constraint remains a challenge at 3rd generation synchrotrons.

Meanwhile, at the dawn of 4th generation synchrotron sources, routine 3D scanning X-ray tomography is becoming within reach. Indeed, the two orders of magnitude larger flux available at 4th generation hard X-ray nanoprobes boosts the speed of scanning tomography measurements proportionally, paving the way towards high-throughput scanning X-ray tomography of mesoscale samples (Li et al., 2022). Hence, the implementation of a robust, user-friendly scanning tomography workflow is crucial for the routine application of these techniques, similarly as has been published recently for high-throughput electron tomography (Schwartz et al., 2022).

Such workflow imposes flexible and fast on-site data processing and tomographic reconstruction adapted to the different number of projections (sparse and high-resolution tomography), diverse data quality (e.g., high and low-level elemental abundances, missing wedge), different imaging modalities (e.g., XRF, X-ray absorption, X-ray diffraction), and the possibility of adapting the field of

view and spatial resolution to the examined phenomenon by using multi-scale or local tomography.

Some recent developments tackle part of these requirements by sample-type specific processing of multimodal tomography data sets (Gao et al., 2021; Suuronen and Sayab, 2018), also in a semi-automatic way in the case of similar processing requirements (Atwood et al., 2015; Parsons et al., 2017). A sparse sampling approach followed by sophisticated data treatment has also been reported (Gao et al., 2021; Liu et al., 2020). However, according to our knowledge, a robust, holistic approach addressing all requirements of flexible multi-scale and multimodal scanning 2D/3D X-ray tomography does not exist yet.

Chapter 4 of the thesis introduces sparse tomography and a robust workflow for scanning multi-length scale XRF-tomography and complementary modalities. It has been developed and implemented at the NANOSCOPIUM beamline (Somogyi et al., 2015a) of SOLEIL Synchrotron and includes semi-automatic data reconstruction. The proposed reconstruction algorithm yields good reconstruction data quality for diverse scientific fields with no need for parameter readjustment depending on the sample type. As the first step of this approach, sparse tomography provides a 3D overview of the entire meso- or microscale sample. The reconstructed sparse tomograms, containing relevant information to the investigated scientific problem, are used to choose pertinent regions for high spatial resolution single slice tomography, projection imaging, and local tomography. This approach permits optimizing the scanning tomography experiments and obtaining relevant information from pertinent sample regions in 2D or 3D during a user project. Thanks to recent developments (Bourassa et al., 2016; Chu et al., 2020; Kopittke et al., 2018; Somogyi et al., 2015b), this method paves the way towards statistically significant 3D studies, similar to those already available in full-field X-ray tomography (Odstrcil et al., 2019), and electron tomography (Schwartz et al., 2022).

References

K. P. Aggarwal, S. Narula, M. Kakkar, and C. Tandon. Nephrolithiasis: molecular mechanism of renal stone formation and the critical role played by modulators. *Biomed Res Int*, 2013:292953, 2013. ISSN 2314-6141. doi: 10.1155/2013/292953.

U. Al-Atar, A. A. Bokov, D. Marshall, J. M. H. Teichman, B. D. Gates, Z.-G. Ye, and N. R. Branda. Mechanism of calcium oxalate monohydrate kidney stones formation: Layered spherulitic growth. *Chemistry of Materials*, 22(4):1318–1329, 2010. doi: 10.1021/cm901751g. URL https://doi.org/10.1021/cm901751g.

R. C. Atwood, A. J. Bodey, S. W. T. Price, M. Basham, and M. Drakopoulos. A high-throughput system for high-quality tomographic reconstruction of large datasets at Diamond Light Source. *Phil. Trans. R. Soc. A.*, 373(2043):20140398, June 2015. ISSN 1364-503X, 1471-2962. doi: 10.1098/rsta.2014.0398. URL https://royalsocietypublishing.org/doi/10.1098/rsta.2014.0398.

A. V. Baez. Resolving Power in Diffraction Microscopy with Special Reference to X-Rays. *Nature*, 169(4310):963–964, June 1952. ISSN 0028-0836, 1476-4687. doi: 10.1038/169963b0. URL https://www.nature.com/articles/169963b0.

B. Bao, A. S. Prasad, F. W. Beck, D. Snell, A. Suneja, F. H. Sarkar, N. Doshi, J. T. Fitzgerald, and P. Swerdlow. Zinc supplementation decreases oxidative stress, incidence of infection, and generation of inflammatory cytokines in sickle cell disease patients. *Translational Research*, 152(2):67–80, Aug. 2008. doi: 10.1016/j.trsl.2008.06.001. URL https://doi.org/10.1016/j.trsl.2008.06.001.

J. Baruchel. *X-ray tomography in material science*. Hermes Science, Paris, 2000. ISBN 978-2-7462-0115-6.

D. Bazin and M. Daudon. Pathological calcifications and selected examples at the medicine–solid-state physics interface. *J. Phys. D: Appl. Phys.*, 45(38):383001, Sept. 2012. ISSN 0022-3727. doi: 10.1088/0022-3727/45/38/383001. URL https://dx.doi.org/10.1088/0022-3727/45/38/383001.

D. Bazin, P. Chevallier, G. Matzen, P. Jungers, and M. Daudon. Heavy elements in urinary stones. *Urol Res*, 35(4):179–184, Aug. 2007. ISSN 1434-0879. doi: 10.1007/s00240-007-0099-z. URL https://doi.org/10.1007/s00240-007-0099-z.

D. Bazin, M. Daudon, C. Combes, and C. Rey. Characterization and some physicochemical aspects of pathological microcalcifications. *Chem Rev*, 112(10): 5092–5120, Oct. 2012. ISSN 1520-6890. doi: 10.1021/cr200068d.

D. Bazin, J.-P. Haymann, L. Emmanuel, J. Rode, and M. Daudon. Pathological calcifications: a medical diagnosis based on their physicochemical properties. *La Presse medicale*, 43(2):135–48, Feb. 2014. doi: 10.1016/j.lpm.2013.02.333. URL https://hal.sorbonne-universite.fr/hal-00996294.

D. Bazin, E. Letavernier, and J.-P. Haymann. Biomineralization versus microcrystalline pathologies: Beauty and the beast. *Comptes Rendus Chimie*, 19(11):1395–1403, Nov. 2016. ISSN 1631-0748. doi: 10.1016/j.crci.2015.12.012. URL https://www.sciencedirect.com/science/article/pii/S1631074816300145.

D. Bazin, M. Daudon, V. Frochot, J.-P. Haymann, and E. Letavernier. Foreword to microcrystalline pathologies: combining clinical activity and fundamental research at the nanoscale. *Comptes Rendus. Chimie*, 25(S1):11–35, 2022a. ISSN 1878-1543. doi: 10.5802/crchim.200. URL https://comptes-rendus.academie-sciences.fr/chimie/articles/10.5802/crchim.200/.

D. Bazin, E. Foy, S. Reguer, S. Rouzière, B. Fayard, H. Colboc, J.-P. Haymann, M. Daudon, and C. Mocuta. The crucial contribution of X-ray fluorescence spectroscopy in medicine. *Comptes Rendus. Chimie*, 25(S1):165–188, 2022b. ISSN 1878-1543. doi: 10.5802/crchim.103. URL https://comptes-rendus.academie-sciences.fr/chimie/item/CRCHIM_2022__25_S1_165_0/.

D. Bazin, I. T. Lucas, S. Rouzière, E. Elkaim, C. Mocuta, S. Réguer, D. G. Reid, J. Mathurin, A. Dazzi, A. Deniset-Besseau, M. Petay, V. Frochot, J.-P. Haymann, E. Letavernier, M.-C. Verpont, E. Foy, E. Bouderlique, H. Colboc, and M. Daudon. Profile of an "at cutting edge" pathology laboratory for pathological human deposits: from nanometer to in vivo scale analysis on large scale facilities. *Comptes Rendus. Chimie*, 25(S1):219, July 2022c. doi: 10.5802/crchim.199. URL https://cea.hal.science/cea-03741948.

D. Bazin, R. J. Papoular, E. Elkaim, R. Weil, D. Thiaudière, C. Pisapia, B. Ménez, N. S. Hwang, F. Tielens, M. Livrozet, E. Bouderlique, J.-P. Haymann, E. Letavernier, L. Hennet, V. Frochot, and M. Daudon. Whitlockite structures in kidney stones indicate infectious origin: a scanning electron microscopy and Synchrotron Radiation investigation. *Comptes Rendus. Chimie*, 25(S1):343–354, Sept. 2022d. ISSN 1878-1543. doi: 10.5802/crchim.80. URL https://comptes-rendus.academie-sciences.fr/chimie/articles/10.5802/crchim.80/.

D. E. Beischer. Analysis of renal calculi by infrared spectroscopy. *J Urol*, 73(4):653–659, Apr. 1955. ISSN 0022-5347. doi: 10.1016/S0022-5347(17)67449-4.

L. Bertrand, M. Cotte, M. Stampanoni, M. Thoury, F. Marone, and S. Schöder. Development and trends in synchrotron studies of ancient and historical materials. *Physics Reports*, 519(2):51–96, Oct. 2012. ISSN 0370-1573. doi: 10.1016/j.physrep.2012.03.003. URL https://www.sciencedirect.com/science/article/pii/S0370157312000865.

E. Bouderlique, E. Tang, J. Perez, A. Coudert, D. Bazin, M.-C. Verpont, C. Duranton, I. Rubera, J.-P. Haymann, G. Leftheriotis, L. Martin, M. Daudon, and E. Letavernier. Vitamin D and Calcium Supplementation Accelerates Randall's Plaque Formation in a Murine Model. *The American Journal of Pathology*, 189(11):2171–2180, Nov. 2019. ISSN 0002-9440. doi: 10.1016/j.ajpath.2019.07.013. URL https://www.sciencedirect.com/science/article/pii/S0002944019306698.

D. Bourassa, S.-C. Gleber, S. Vogt, C. H. Shin, and C. J. Fahrni. MicroXRF tomographic visualization of zinc and iron in the zebrafish embryo at the onset of the hatching period. *Metallomics*, 8(10):1122–1130, 2016. ISSN 1756-5901, 1756-591X. doi: 10.1039/C6MT00073H. URL https://academic.oup.com/metallomics/article/8/10/1122-1130/6012998.

D. B. Brueckner. *Self-Absorption Corrected X-Ray Microtomography with Structural and Elemental Contrast*. PhD thesis, Deutsches Elektronen-Synchrotron, DESY, Hamburg, 2021. URL https://bib-pubdb1.desy.de/record/475080.

X. Carpentier, D. Bazin, P. Jungers, S. Reguer, D. Thiaudière, and M. Daudon. The pathogenesis of Randall's plaque: a papilla cartography of Ca compounds through an *ex vivo* investigation based on XANES spectroscopy. *J Synchrotron Rad*, 17(3): 374–379, May 2010. ISSN 0909-0495. doi: 10.1107/S0909049510003791. URL https://scripts.iucr.org/cgi-bin/paper?S0909049510003791.

X. Carpentier, D. Bazin, C. Combes, A. Mazouyes, S. Rouzière, P. A. Albouy, E. Foy, and M. Daudon. High Zn content of Randall's plaque: A -X-ray fluorescence investigation. *Journal of Trace Elements in Medicine and Biology*, 25(3):160–165, July 2011. ISSN 0946672X. doi: 10.1016/j.jtemb.2011.05.004. URL https://linkinghub.elsevier.com/retrieve/pii/S0946672X11000769.

P. Chaurand, W. Liu, D. Borschneck, C. Levard, M. Auffan, E. Paul, B. Collin, I. Kieffer, S. Lanone, J. Rose, and J. Perrin. Multi-scale X-ray computed tomography to detect and localize metal-based nanomaterials in lung tissues of in vivo exposed mice. *Sci Rep*, 8(1):4408, Dec. 2018. ISSN 2045-2322. doi: 10.1038/s41598-018-21862-4. URL http://www.nature.com/articles/s41598-018-21862-4.

Y. S. Chu, W.-K. Lee, R. Tappero, M. Ge, X. Huang, X. Xiao, H. Yan, P. Northrup, J. Thieme, A. M. Kiss, G. J. Williams, Y. Yang, S. L. Nicholas, A. Pattammattel, R. Smith, P. Ilinski, and Y. Du. Multimodal, Multidimensional, and Multiscale X-ray Imaging at the National Synchrotron Light Source II. *Synchrotron Radiation News*, 33(3):29–36, June 2020. ISSN 0894-0886, 1931-7344. doi: 10.1080/08940886.2020.1751520. URL https://www.tandfonline.com/doi/full/10.1080/08940886.2020.1751520.

V. E. Cosslett. X-Ray Microscopy and X-Ray Microanalysis. *Nature*, 184(4690):860–862, Sept. 1959. ISSN 0028-0836, 1476-4687. doi: 10.1038/184860a0. URL https://www.nature.com/articles/184860a0.

M. Daudon, C. A. Bader, and P. Jungers. Urinary calculi: review of classification methods and correlations with etiology. *Scanning Microsc*, 7(3):1081–1104; discussion 1104–1106, Sept. 1993. ISSN 0891-7035.

M. Daudon, B. Lacour, and P. Jungers. High prevalence of uric acid calculi in diabetic stone formers. *Nephrology Dialysis Transplantation*, 20(2):468–469, Feb. 2005. ISSN 0931-0509. doi: 10.1093/ndt/gfh594. URL https://doi.org/10.1093/ndt/gfh594.

M. Daudon, H. Bouzidi, and D. Bazin. Composition and morphology of phosphate stones and their relation with etiology. *Urological research*, 38:459–67, Oct. 2010. doi: 10.1007/s00240-010-0320-3.

M. Daudon, D. Bazin, and E. Letavernier. Randall's plaque as the origin of calcium oxalate kidney stones. *Urolithiasis*, 43(1):5–11, Jan. 2015. ISSN 2194-7236. doi: 10.1007/s00240-014-0703-y. URL https://doi.org/10.1007/s00240-014-0703-y.

M. Daudon, A. Dessombz, V. Frochot, E. Letavernier, J.-P. Haymann, P. Jungers, and D. Bazin. Comprehensive morpho-constitutional analysis of urinary stones improves etiological diagnosis and therapeutic strategy of nephrolithiasis. *Comptes Rendus Chimie*, 19(11):1470–1491, Nov. 2016. ISSN 1631-0748. doi: 10.1016/j.crci.2016.05.008. URL https://www.sciencedirect.com/science/article/pii/S163107481630128X.

M. Daudon, M. Petay, S. Vimont, A. Deniset, F. Tielens, J.-P. Haymann, E. Letavernier, V. Frochot, and D. Bazin. Urinary tract infection inducing stones: some clinical and chemical data. *Comptes Rendus. Chimie*, 25(S1):315–334, 2022. ISSN 1878-1543. doi: 10.5802/crchim.159. URL https://comptes-rendus.academie-sciences.fr/chimie/articles/10.5802/crchim.159/.

C. Dean, A. Le Cabec, K. Spiers, Y. Zhang, and J. Garrevoet. Incremental distribution of strontium and zinc in great ape and fossil hominin cementum using synchrotron X-ray fluorescence mapping. *J. R. Soc. Interface.*, 15(138): 20170626, Jan. 2018. ISSN 1742-5689, 1742-5662. doi: 10.1098/rsif.2017.0626. URL https://royalsocietypublishing.org/doi/10.1098/rsif.2017.0626.

J. Deng, Y. H. Lo, M. Gallagher-Jones, S. Chen, A. Pryor, Q. Jin, Y. P. Hong, Y. S. G. Nashed, S. Vogt, J. Miao, and C. Jacobsen. Correlative 3D x-ray fluorescence and ptychographic tomography of frozen-hydrated green algae. *Sci. Adv.*, 4(11): eaau4548, Nov. 2018. ISSN 2375-2548. doi: 10.1126/sciadv.aau4548. URL https://www.science.org/doi/10.1126/sciadv.aau4548.

Y. G. Deosthale and C. Gopalan. The effect of molybdenum levels in sorghum (*Sorghum vulgare* Pers.) on uric acid and copper excretion in man. *Br J Nutr*, 31(3):351–355, May 1974. ISSN 0007-1145, 1475-2662. doi: 10.1079/BJN19740043. URL https://www.cambridge.org/core/product/identifier/S0007114574000444/type/journal_article.

S. F. Durrant. Laser ablation inductively coupled plasma mass spectrometry: achievements, problems, prospects. *J. Anal. At. Spectrom.*, 14(9):1385–1403, 1999. ISSN 02679477, 13645544. doi: 10.1039/a901765h. URL http://xlink.rsc.org/?DOI=a901765h.

A. Engström. *Quantitative micro-and histochemical elementary analysis by roentgen absorption spectrography*, volume 63. PA Norstedt, 1946.

A. P. Evan, J. E. Lingeman, F. L. Coe, J. H. Parks, S. B. Bledsoe, Y. Shao, A. J. Sommer, R. F. Paterson, R. L. Kuo, and M. Grynpas. Randall's plaque of patients with nephrolithiasis begins in basement membranes of thin loops of Henle. *J Clin Invest*, 111(5):607–616, Mar. 2003. ISSN 0021-9738. doi: 10.1172/JCI17038. URL https://www.jci.org/articles/view/17038. Publisher: American Society for Clinical Investigation.

F. Figon, I. Hurbain, X. Heiligenstein, S. Trépout, A. Lanoue, K. Medjoubi, A. Somogyi, C. Delevoye, G. Raposo, and J. Casas. Catabolism of lysosome-related organelles in color-changing spiders supports intracellular turnover of pigments. *Proc. Natl. Acad. Sci. U.S.A.*, 118(35):e2103020118, Aug. 2021. ISSN 0027-8424, 1091-6490. doi: 10.1073/pnas.2103020118. URL https://pnas.org/doi/full/10.1073/pnas.2103020118.

H. Fleisch. Inhibitors and promoters of stone formation. *Kidney International*, 13 (5):361–371, May 1978. ISSN 00852538. doi: 10.1038/ki.1978.54. URL https://linkinghub.elsevier.com/retrieve/pii/S0085253815318913.

X. Gao, Y. Yang, S. Yang, Y. Ma, and M. Chen. Microstructure evolution of chalcopyrite agglomerates during leaching – A synchrotron-based X-ray CT approach combined with a data-constrained modelling (DCM). *Hydrometallurgy*, 201:105586, May 2021. ISSN 0304386X. doi: 10.1016/j.hydromet.2021.105586. URL https://linkinghub.elsevier.com/retrieve/pii/S0304386X21000359.

M. T. Gettman and J. W. Segura. Struvite stones: diagnosis and current treatment concepts. *J Endourol*, 13(9):653–658, Nov. 1999. ISSN 0892-7790. doi: 10.1089/end.1999.13.653.

P. Goby. New Application of the X-rays: Micro-radiography. *Journal of the Royal Microscopical Society*, 33(4):373–375, Aug. 1913. ISSN 03683974. doi: 10.1111/j.1365-2818.1913.tb01033.x. URL https://onlinelibrary.wiley.com/doi/10.1111/j.1365-2818.1913.tb01033.x.

P. K. Grover, R. L. Ryall, and V. R. Marshall. Calcium oxalate crystallization in urine: Role of urate and glycosaminoglycans. *Kidney International*, 41(1): 149–154, Jan. 1992. ISSN 00852538. doi: 10.1038/ki.1992.20. URL https://linkinghub.elsevier.com/retrieve/pii/S0085253815574413.

H. J. Gulley-Stahl, J. A. Haas, K. A. Schmidt, A. P. Evan, and A. J. Sommer. Attenuated Total Internal Reflectance Infrared Spectroscopy (ATR-FTIR): A Quantitative Approach for Kidney Stone Analysis. *Appl Spectrosc*, 63(7):759–766, July 2009. ISSN 0003-7028. doi: 10.1366/000370209788701044. URL https://www.ncbi.nlm.nih.gov/pmc/articles/PMC3309560/.

D. Gürsoy, T. Biçer, A. Lanzirotti, M. G. Newville, and F. De Carlo. Hyperspectral image reconstruction for x-ray fluorescence tomography. *Opt. Express*, 23(7): 9014, Apr. 2015. ISSN 1094-4087. doi: 10.1364/OE.23.009014. URL https://opg.optica.org/abstract.cfm?URI=oe-23-7-9014.

A. Haase, G. Landwehr, E. Umbach, W. C. Röntgen, and J.-M.-U. Würzburg, editors. *Röntgen Centennial: X-rays in natural and life sciences*. World Scientific, Singapore, 1997. ISBN 978-981-02-3085-2.

H. Haase, J. L. Ober-Blöbaum, G. Engelhardt, S. Hebel, A. Heit, H. Heine, and L. Rink. Zinc Signals Are Essential for Lipopolysaccharide-Induced Signal Transduction in Monocytes1. *The Journal of Immunology*, 181(9):6491–6502, Nov. 2008. ISSN 0022-1767. doi: 10.4049/jimmunol.181.9.6491. URL https://doi.org/10.4049/jimmunol.181.9.6491.

J. R. Helliwell, C. J. Sturrock, K. M. Grayling, S. R. Tracy, R. J. Flavel, I. M. Young, W. R. Whalley, and S. J. Mooney. Applications of X-ray computed tomography for examining biophysical interactions and structural development in soil systems: a review: X-ray computed tomography for soil physical properties. *Eur J Soil Sci*, 64(3):279–297, June 2013. ISSN 13510754. doi: 10.1111/ejss.12028. URL https://onlinelibrary.wiley.com/doi/10.1111/ejss.12028.

Y. P. Hong, S. Chen, and C. Jacobsen. A new workflow for x-ray fluorescence tomography: X-Ray Nanoimaging: Instruments and Methods II. *X-Ray Nanoimaging*, 2015. doi: 10.1117/12.2194162. URL http://www.scopus.com/inward/record.url?scp=84951038388&partnerID=8YFLogxK.

J. Kaiser, M. Holá, M. Galiová, K. Novotný, V. Kanický, P. Martinec, J. Š u ka, F. Brun, N. Sodini, G. Tromba, L. Mancini, and T. Ko istková. Investigation of the microstructure and mineralogical composition of urinary calculi fragments by synchrotron radiation X-ray microtomography: a feasibility study. *Urol Res*, 39 (4):259–267, Aug. 2011. ISSN 1434-0879. doi: 10.1007/s00240-010-0343-9. URL https://doi.org/10.1007/s00240-010-0343-9.

G. P. Kasidas, C. T. Samuell, and T. B. Weir. Renal stone analysis: why and how? *Ann Clin Biochem*, 41(2):91–97, Mar. 2004. ISSN 0004-5632. doi: 10.1258/000456304322879962. URL https://doi.org/10.1258/000456304322879962.

S. R. Khan, D. E. Rodriguez, L. B. Gower, and M. Monga. Association of Randall Plaque With Collagen Fibers and Membrane Vesicles. *The Journal of Urology*, 187(3):1094–1100, Mar. 2012. ISSN 0022-5347. doi: 10.1016/j.juro.2011.10.125. URL https://www.sciencedirect.com/science/article/pii/S0022534711054486.

S. R. Khan, M. S. Pearle, W. G. Robertson, G. Gambaro, B. K. Canales, S. Doizi, O. Traxer, and H.-G. Tiselius. Kidney stones. *Nat Rev Dis Primers*, 2(1):1–23, Feb. 2016. ISSN 2056-676X. doi: 10.1038/nrdp.2016.8. URL https://www.nature.com/articles/nrdp20168.

P. Kirkpatrick and A. V. Baez. Formation of Optical Images by X-Rays. *J. Opt. Soc. Am.*, 38(9):766, Sept. 1948. ISSN 0030-3941. doi: 10.1364/JOSA.38.000766. URL https://opg.optica.org/abstract.cfm?URI=josa-38-9-766.

P. M. Kopittke, T. Punshon, D. J. Paterson, R. V. Tappero, P. Wang, F. P. C. Blamey, A. van der Ent, and E. Lombi. Synchrotron-Based X-Ray Fluorescence Microscopy as a Technique for Imaging of Elements in Plants. *Plant Physiol.*, 178(2):507–523, Oct. 2018. ISSN 0032-0889, 1532-2548. doi: 10.1104/pp.18.00759. URL https://academic.oup.com/plphys/article/178/2/507-523/6116539.

E. Kosior, S. Bohic, H. Suhonen, R. Ortega, G. Devès, A. Carmona, F. Marchi, J. F. Guillet, and P. Cloetens. Combined use of hard X-ray phase contrast imaging and X-ray fluorescence microscopy for sub-cellular metal quantification. *Journal of Structural Biology*, 177(2):239–247, Feb. 2012. ISSN 10478477. doi: 10.1016/j.jsb.2011.12.005. URL https://linkinghub.elsevier.com/retrieve/pii/S1047847711003510.

E. Letavernier, D. Bazin, and M. Daudon. Randall's plaque and kidney stones: Recent advances and future challenges. *Comptes Rendus Chimie*, 19(11):1456–1460, Nov. 2016. ISSN 1631-0748. doi: 10.1016/j.crci.2014.12.005. URL https://www.sciencedirect.com/science/article/pii/S1631074814002987.

E. Letavernier, D. Bazin, and M. Daudon. Description of Stone Morphology and Crystalluria Improve Diagnosis and Care of Kidney Stone Formers. *Healthcare*, 11:2, Dec. 2022. doi: 10.3390/healthcare11010002.

P. Li, M. Allain, T. A. Grünewald, M. Rommel, A. Campos, D. Carbone, and V. Chamard. 4th generation synchrotron source boosts crystalline imaging at the nanoscale. *Light Sci Appl*, 11(1):73, Dec. 2022. ISSN 2047-7538. doi: 10.1038/s41377-022-00758-z. URL https://www.nature.com/articles/s41377-022-00758-z.

M. P. Linnes, A. E. Krambeck, L. Cornell, J. C. Williams, M. Korinek, E. J. Bergstralh, X. Li, A. D. Rule, C. M. McCollough, T. J. Vrtiska, and J. C. Lieske. Phenotypic characterization of kidney stone formers by endoscopic and histological quantification of intrarenal calcification. *Kidney International*, 84 (4):818–825, Oct. 2013. ISSN 0085-2538. doi: 10.1038/ki.2013.189. URL https://www.sciencedirect.com/science/article/pii/S0085253815560328.

M. S. Litwin and C. S. Saigal. *Urologic diseases in America*. Number 7 in NIH publication. National Institute of Diabetes & Digestive & Kidney Diseases, National Institutes of Health, 2007. URL https://books.google.it/books?id=N_5PAQAAIAAJ.

Z. Liu, T. Bicer, R. Kettimuthu, D. Gursoy, F. De Carlo, and I. Foster. TomoGAN: low-dose synchrotron x-ray tomography with generative adversarial networks: discussion. *J. Opt. Soc. Am. A*, 37(3):422, Mar. 2020. ISSN 1084-7529, 1520-8532. doi: 10.1364/JOSAA.375595. URL https://opg.optica.org/abstract.cfm?URI=josaa-37-3-422.

Q. Ma, L. Fang, R. Su, L. Ma, G. Xie, and Y. Cheng. Uric acid stones, clinical manifestations and therapeutic considerations. *Postgrad Med J*, 94(1114):458–462, Aug. 2018. ISSN 1469-0756. doi: 10.1136/postgradmedj-2017-135332.

B. R. Matlaga, J. C. Williams, S. C. Kim, R. L. Kuo, A. P. Evan, S. B. Bledsoe, F. L. Coe, E. M. Worcester, L. C. Munch, and J. E. Lingeman. Endoscopic Evidence of Calculus Attachment to Randall's Plaque. *The Journal of Urology*, 175(5):1720–1724, May 2006. ISSN 0022-5347. doi: 10.1016/S0022-5347(05)01017-7. URL https://www.sciencedirect.com/science/article/pii/S0022534705010177.

K. Medjoubi, N. Leclercq, F. Langlois, A. Buteau, S. Lé, S. Poirier, P. Mercère, M. C. Sforna, C. M. Kewish, and A. Somogyi. Development of fast, simultaneous and multi-technique scanning hard X-ray microscopy at Synchrotron Soleil. *J Synchrotron Rad*, 20(2):293–299, Mar. 2013. ISSN 0909-0495. doi: 10.1107/S0909049512052119. URL http://scripts.iucr.org/cgi-bin/paper?S0909049512052119.

S. R. Mulay and H.-J. Anders. Crystallopathies. *N Engl J Med*, 374(25):2465–2476, June 2016. ISSN 1533-4406. doi: 10.1056/NEJMra1601611.

J. A. Muñoz and M. Valiente. Effects of trace metals on the inhibition of calcium oxalate crystallization. *Urol Res*, 33(4):267–272, Aug. 2005. ISSN 1434-0879. doi: 10.1007/s00240-005-0468-4. URL https://doi.org/10.1007/s00240-005-0468-4.

Q. D. Nguyen and M. Daudon. *Infrared and Raman spectra of calculi*. Elsevier, Paris Amsterdam Oxford [etc.], 1997. ISBN 978-2-84299-003-9.

M. Odstrcil, M. Holler, J. Raabe, A. Sepe, X. Sheng, S. Vignolini, C. G. Schroer, and M. Guizar-Sicairos. Ab initio nonrigid X-ray nanotomography. *Nat Commun*, 10 (1):2600, Dec. 2019. ISSN 2041-1723. doi: 10.1038/s41467-019-10670-7. URL http://www.nature.com/articles/s41467-019-10670-7.

T. Oka, T. Yoshioka, T. Koide, M. Takaha, and T. Sonoda. Role of magnesium in the growth of calcium oxalate monohydrate and calcium oxalate dihydrate crystals. *Urol Int*, 42(2):89–93, 1987. ISSN 0042-1138. doi: 10.1159/000281861.

A. D. Parsons, S. W. T. Price, N. Wadeson, M. Basham, A. M. Beale, A. W. Ashton, J. F. W. Mosselmans, and P. D. Quinn. Automatic processing of multimodal tomography datasets. *J Synchrotron Rad*, 24(1):248–256, Jan. 2017. ISSN 1600-5775. doi: 10.1107/S1600577516017756. URL http://scripts.iucr.org/cgi-bin/paper?S1600577516017756.

E. V. d. Perre, D. Bazin, V. Estrade, E. Bouderlique, K. M. Wissing, M. Daudon, and E. Letavernier. Randall's plaque as the origin of idiopathic calcium oxalate stone formation: an update. *Comptes Rendus. Chimie*, 25(S1):373–391, 2022. ISSN 1878-1543. doi: 10.5802/crchim.102. URL https://comptes-rendus.academie-sciences.fr/chimie/articles/10.5802/crchim.102/.

E. L. Prien. The Riddle of Randall's Plaques. *Journal of Urology*, 114(4):500–507, Oct. 1975. ISSN 0022-5347, 1527-3792. doi: 10.1016/S0022-5347(17)67068-X. URL http://www.jurology.com/doi/10.1016/S0022-5347%2817%2967068-X.

T. Punshon, K. Hirschi, J. Yang, A. Lanzirotti, B. Lai, and M. L. Guerinot. The Role of CAX1 and CAX3 in Elemental Distribution and Abundance in Arabidopsis Seed. *Plant Physiology*, 158(1):352–362, Jan. 2012. ISSN 1532-2548. doi: 10.1104/pp.111.184812. URL https://academic.oup.com/plphys/article/158/1/352/6109135.

K. Ramaswamy, D. W. Killilea, P. Kapahi, A. J. Kahn, T. Chi, and M. L. Stoller. The elementome of calcium-based urinary stones and its role in urolithiasis. *Nat Rev Urol*, 12(10):543–557, Oct. 2015. ISSN 1759-4812, 1759-4820. doi: 10.1038/nrurol.2015.208. URL https://www.nature.com/articles/nrurol.2015.208.

A. Randall. An Hypothesis for the Origin of Renal Calculus. *N Engl J Med*, 214(6):234–242, Feb. 1936. ISSN 0028-4793, 1533-4406. doi: 10.1056/NEJM193602062140603. URL http://www.nejm.org/doi/abs/10.1056/NEJM193602062140603.

S. Rouzière, D. Bazin, and M. Daudon. In-lab X-ray fluorescence and diffraction techniques for pathological calcifications. *Comptes Rendus Chimie*, 19(11):1404–1415, Nov. 2016. ISSN 1631-0748. doi: 10.1016/j.crci.2015.05.013. URL https://www.sciencedirect.com/science/article/pii/S1631074815001459.

J. Schwartz, C. Harris, J. Pietryga, H. Zheng, P. Kumar, A. Visheratina, N. A. Kotov, B. Major, P. Avery, P. Ercius, U. Ayachit, B. Geveci, D. A. Muller, A. Genova, Y. Jiang, M. Hanwell, and R. Hovden. Real-time 3D analysis during electron tomography using tomviz. *Nat Commun*, 13(1):4458, Dec. 2022. ISSN 2041-1723. doi: 10.1038/s41467-022-32046-0. URL https://www.nature.com/articles/s41467-022-32046-0.

C. J. Serpell, R. N. Rutte, K. Geraki, E. Pach, M. Martincic, M. Kierkowicz, S. De Munari, K. Wals, R. Raj, B. Ballesteros, G. Tobias, D. C. Anthony, and B. G. Davis. Carbon nanotubes allow capture of krypton, barium and lead for multichannel biological X-ray fluorescence imaging. *Nat Commun*, 7(1):13118, Dec. 2016. ISSN 2041-1723. doi: 10.1038/ncomms13118. URL http://www.nature.com/articles/ncomms13118.

M. C. Sforna, P. Philippot, A. Somogyi, M. A. van Zuilen, K. Medjoubi, B. Schoepp-Cothenet, W. Nitschke, and P. T. Visscher. Evidence for arsenic metabolism and cycling by microorganisms 2.7 billion years ago. *Nature Geosci*, 7(11):811–815, Nov. 2014. ISSN 1752-0894, 1752-0908. doi: 10.1038/ngeo2276. URL http://www.nature.com/articles/ngeo2276.

V. K. Singh and P. K. Rai. Kidney stone analysis techniques and the role of major and trace elements on their pathogenesis: a review. *Biophys Rev*, 6(3):291–310, Dec. 2014. ISSN 1867-2469. doi: 10.1007/s12551-014-0144-4. URL https://doi.org/10.1007/s12551-014-0144-4.

V. K. Singh, B. S. Jaswal, J. Sharma, and P. K. Rai. Analysis of stones formed in the human gall bladder and kidney using advanced spectroscopic techniques. *Biophys Rev*, 12(3):647–668, June 2020. ISSN 1867-2469. doi: 10.1007/s12551-020-00697-2. URL https://doi.org/10.1007/s12551-020-00697-2.

A. Somogyi, K. Medjoubi, G. Baranton, V. Le Roux, M. Ribbens, F. Polack, P. Philippot, and J.-P. Samama. Optical design and multi-length-scale scanning spectro-microscopy possibilities at the Nanoscopium beamline of Synchrotron Soleil. *Journal of Synchrotron Radiation*, 22:1118–1129, July 2015a. doi: 10.1107/S1600577515009364.

A. Somogyi, C. Mocuta, and Synchrotron Soleil, BP 48, Saint-Aubin, Gif sur Yvette, 91192, France. Possibilities and Challenges of Scanning Hard X-ray Spectro-microscopy Techniques in Material Sciences. *AIMS Materials Science*, 2(2):122–162, 2015b. ISSN 2372-0484. doi: 10.3934/matersci.2015.2.122. URL http://www.aimspress.com/article/10.3934/matersci.2015.2.122.

I. Sorokin, C. Mamoulakis, K. Miyazawa, A. Rodgers, J. Talati, and Y. Lotan. Epidemiology of stone disease across the world. *World J Urol*, 35(9):1301–1320, Sept. 2017. ISSN 1433-8726. doi: 10.1007/s00345-017-2008-6. URL https://doi.org/10.1007/s00345-017-2008-6.

A. Srivastava, B. J. Heisinger, V. Sinha, H.-K. Lee, X. Liu, M. Qu, X. Duan, S. Leng, and C. H. McCollough. Determination of minor and trace elements in kidney stones by x-ray fluorescence analysis. In *Medical Imaging 2014: Physics of Medical Imaging*, volume 9033, pages 1562–1569. SPIE, Mar. 2014. doi: 10.1117/12.2043733. URL https://www.spiedigitallibrary.org/conference-proceedings-of-spie/9033/90335R/Determination-of-minor-and-trace-elements-in-kidney-stones-by/10.1117/12.2043733.full.

D. J. Sutor. Growth studies of calcium oxalate in the presence of various ions and compounds. *Br J Urol*, 41(2):171–178, Apr. 1969. ISSN 0007-1331. doi: 10.1111/j.1464-410x.1969.tb09919.x.

J.-P. Suuronen and M. Sayab. 3D nanopetrography and chemical imaging of datable zircons by synchrotron multimodal X-ray tomography. *Sci Rep*, 8(1):4747, Dec. 2018. ISSN 2045-2322. doi: 10.1038/s41598-018-22891-9. URL http://www.nature.com/articles/s41598-018-22891-9.

S. Tamosaityte, M. Pucetaite, A. Zelvys, S. Varvuolyte, V. Hendrixson, and V. Sablinskas. Raman spectroscopy as a non-destructive tool to determine the chemical composition of urinary sediments. *Comptes Rendus. Chimie*, 25(S1):73–82, 2022. ISSN 1878-1543. doi: 10.5802/crchim.121. URL https://comptes-rendus.academie-sciences.fr/chimie/articles/10.5802/crchim.121/#body-html-1.

Y. Tanaka, M. Maruyama, A. Okada, Y. Furukawa, K. Momma, Y. Sugiura, R. Tajiri, K. P. Sawada, S. Tanaka, K. Takano, K. Taguchi, S. Hamamoto, R. Ando, K. Tsukamoto, M. Yoshimura, Y. Mori, and T. Yasui. Multicolor imaging of calcium-binding proteins in human kidney stones for elucidating the effects of proteins on crystal growth. *Sci Rep*, 11(1):16841, Aug. 2021. ISSN 2045-2322. doi: 10.1038/s41598-021-95782-1. URL https://www.nature.com/articles/s41598-021-95782-1.

P. Thakore and T. H. Liang. Urolithiasis. In *StatPearls*. StatPearls Publishing, Treasure Island (FL), 2023. URL http://www.ncbi.nlm.nih.gov/books/NBK559101/.

E. Tsolaki and S. Bertazzo. Pathological Mineralization: The Potential of Mineralomics. *Materials (Basel)*, 12(19):3126, Sept. 2019. ISSN 1996-1944. doi: 10.3390/ma12193126. URL https://www.ncbi.nlm.nih.gov/pmc/articles/PMC6804219/.

E. Van de Perre, D. Bazin, V. Estrade, E. Bouderlique, K. M. Wissing, M. Daudon, and E. Letavernier. Randall's plaque as the origin of idiopathic calcium oxalate stone formation: an update. *Comptes Rendus. Chimie*, 24(S2):1–19, Aug. 2021. ISSN 1878-1543. doi: 10.5802/crchim.102. URL https://comptes-rendus.academie-sciences.fr/chimie/articles/10.5802/crchim.102/.

M. Vasinova Galiova, K. Stepankova, R. opjaková, J. Kuta, L. Prokes, J. Kynicky, and V. Kanický. Preparation and testing of phosphate, oxalate and uric acid matrix-matched standards for accurate quantification of 2D elemental distribution in kidney stone sections using 213 nm nanosecond laser ablation inductively coupled plasma mass spectrometry. *J. Anal. At. Spectrom.*, 30, Mar. 2015. doi: 10.1039/C4JA00347K.

M. Vašinová Galiová, R. opjaková, R. Škoda, K. Št pánková, M. Va ková, J. Kuta, L. Prokeš, J. Kynický, and V. Kanický. 2D elemental mapping of sections of human kidney stones using laser ablation inductively-coupled plasma-mass spectrometry: Possibilities and limitations. *Spectrochimica Acta Part B: Atomic Spectroscopy*, 100:105–115, Oct. 2014. ISSN 0584-8547. doi: 10.1016/j.sab.2014.08.024. URL https://www.sciencedirect.com/science/article/pii/S0584854714001992.

N. Vidavsky, J. A. Kunitake, and L. A. Estroff. Multiple Pathways for Pathological Calcification in the Human Body. *Adv Healthc Mater*, 10(4):e2001271, Feb. 2021. ISSN 2192-2640. doi: 10.1002/adhm.202001271. URL https://www.ncbi.nlm.nih.gov/pmc/articles/PMC8724004/.

H. Villarraga-Gómez and S. T. Smith. Effect of the number of projections on dimensional measurements with X-ray computed tomography. *Precision Engineering*, 66:445–456, Nov. 2020. ISSN 01416359. doi: 10.1016/j.precisioneng.2020.08.006. URL https://linkinghub.elsevier.com/retrieve/pii/S0141635920302944.

Y. Wang, F. De Carlo, D. C. Mancini, I. McNulty, B. Tieman, J. Bresnahan, I. Foster, J. Insley, P. Lane, G. von Laszewski, C. Kesselman, M.-H. Su, and M. Thiebaux. A high-throughput x-ray microtomography system at the Advanced Photon Source. *Review of Scientific Instruments*, 72(4):2062–2068, Apr. 2001. ISSN 0034-6748, 1089-7623. doi: 10.1063/1.1355270. URL http://aip.scitation.org/doi/10.1063/1.1355270.

J. C. Williams, J. E. Lingeman, F. L. Coe, E. M. Worcester, and A. P. Evan. Micro-CT imaging of Randall's plaques. *Urolithiasis*, 43(0 1):13–17, Jan. 2015. ISSN 2194-7228. doi: 10.1007/s00240-014-0702-z. URL https://www.ncbi.nlm.nih.gov/pmc/articles/PMC4285664/.

S. Winfree, C. Weiler, S. B. Bledsoe, T. Gardner, A. J. Sommer, A. P. Evan, J. E. Lingeman, A. E. Krambeck, E. M. Worcester, T. M. El-Achkar, and J. C. Williams. Multimodal imaging reveals a unique autofluorescence signature of Randall's plaque. *Urolithiasis*, 49(2):123–135, Apr. 2021. ISSN 2194-7236. doi: 10.1007/s00240-020-01216-4.

M. Wolf, B. M. May, and J. Cabana. Visualization of Electrochemical Reactions in Battery Materials with X-ray Microscopy and Mapping. *Chem. Mater.*, 29(8):3347–3362, Apr. 2017. ISSN 0897-4756, 1520-5002. doi: 10.1021/acs.chemmater.6b05114. URL https://pubs.acs.org/doi/10.1021/acs.chemmater.6b05114.

R. Xie, J. Zhao, L. Lu, P. Brown, X. Lin, S. M. Webb, J. Ge, O. Antipova, L. Li, and S. Tian. Seasonal Zinc Storage and a Strategy for Its Use in Buds of Fruit Trees. *Plant Physiol.*, 183(3):1200–1212, July 2020. ISSN 0032-0889, 1532-2548. doi: 10.1104/pp.19.01563. URL https://academic.oup.com/plphys/article/183/3/1200-1212/6116384.

H. Yan, E. Nazaretski, K. Lauer, X. Huang, U. Wagner, C. Rau, M. Yusuf, I. Robinson, S. Kalbfleisch, L. Li, N. Bouet, J. Zhou, R. Conley, and Y. S. Chu. Multimodality hard-x-ray imaging of a chromosome with nanoscale spatial resolution. *Sci Rep*, 6(1):20112, Apr. 2016. ISSN 2045-2322. doi: 10.1038/srep20112. URL http://www.nature.com/articles/srep20112.

CHAPTER 2
FOUNDATIONS AND INSTRUMENTATION

This chapter provides an overview of the fundamentals and instrumental setups used to carry out the PhD work. In the first section of this chapter, the basic interactions of X-rays with matter are presented. Subsequent sections outline the characteristics of synchrotron radiation techniques and the analytical tools in place at the NANOSCOPIUM beamline.

2.1. X-ray matter interactions

X-rays, classified as high-energy electromagnetic radiation, have a strong penetrating capability. X-rays typically have wavelengths in the range of 0.1 to 100 angstroms, allowing them to efficiently penetrate a wide range of materials. The relationship between X-ray photon energy (E) and its wavelength (λ) can be described by the equation:

$$E = \frac{hc}{\lambda} \tag{2.1}$$

where h is Planck's constant and c is the speed of light. In practice, the equation is usually expressed for photon energy in keV and wavelength in $\mathring{A}$ for approximate estimation of the photon energy:

$$E(keV) \approx \frac{12.398}{\lambda(\mathring{A})} \tag{2.2}$$

When directing X-ray photons toward a sample, several processes can occur simultaneously. The X-ray could pass through the sample without any interaction. Alternatively, the sample may absorb the X-ray, causing atoms to enter excited states. Furthermore, X-ray photons might scatter. In some cases, they maintain their original energy, known as elastic scattering. In other cases, they lose energy within the sample, referred to as inelastic scattering. The possibility for these interactions to occur depends on the energy of the X-ray photons and the characteristics of the sample materials.

Interactions between X-rays and matter form the foundation for various analytical techniques. An example is the X-ray fluorescence method used in my PhD study.

2.1.1. X-ray attenuation

X-rays are attenuated as they pass through materials due to photon absorption and scattering by atoms. The degree of attenuation depends on the energy of the incident X-ray, the material's density, and its thickness. The Beer-Lambert law is fundamental in determining the attenuation of X-rays. In the case of a homogeneous material with a thickness of Δx, exposed to an X-ray beam with energy E and intensity I_0, the attenuated beam intensity I follows the Beer-Lambert law:

$$I = I_0 e^{-\mu(E)\cdot\Delta x} \tag{2.3}$$

In this context, the linear attenuation coefficient $\mu(E)$ characterizes the sample's ability to attenuate X-rays and is a function of the beam energy. The attenuation μ encompasses contributions from both scattering and absorption. Therefore μ can be expressed as the sum of the linear absorption coefficient μ_a and scattering coefficient μ_s:

$$\mu = \mu_a + \mu_s \tag{2.4}$$

The mass attenuation coefficient μ/ρ is useful when comparing the attenuation properties of materials with different densities ρ.

Figure 2.1 illustrates the mass attenuation coefficients for calcium, iron and zinc. Typically, these coefficients exhibit a decreasing trend as the X-ray energy increases, except for distinct absorption edges where there is an abrupt increase in attenuation. These edges correspond to the binding energies of electrons within the atoms.

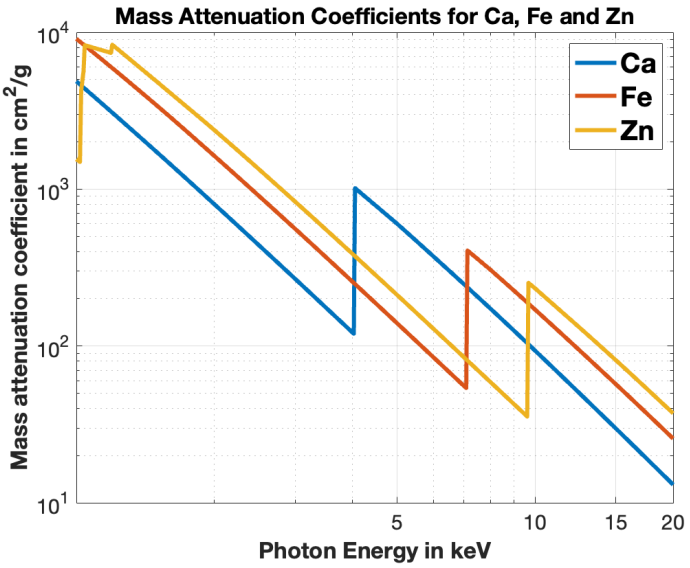

Figure 2.1: A $\log_{10}$-$\log_{10}$ plot of the mass attenuation coefficient for Ca, Fe, and Zn in the energy range between 1 keV and 20 keV.

2.1.2. X-ray absorption

When X-rays are absorbed by an atom through the photoelectric effect, a core-level electron, known as a photoelectron, is ejected. This ejection results in the creation of a "core hole" in the atom. To stabilize itself, the atom undergoes reorganization, leading to the emission of X-ray fluorescence photons or Auger electrons. These emitted particles provide valuable information for identifying the specific absorbing atom within the material.

Following X-ray absorption and the ejection of a photoelectron, as illustrated in Figure 2.2, two primary processes can occur: X-ray fluorescence and Auger electron emission. During the X-ray fluorescence process, an atom emits characteristic X-ray fluorescence uniformly in all directions (isotropically). The energy of these emitted photons is equivalent to the difference between the initial and final electron states, specifically the energy gap between the inner and outer

shells from which the electron originates to fill the core hole. This emitted characteristic X-ray fluorescence serves as an essential indicator for identifying the element present in the material.

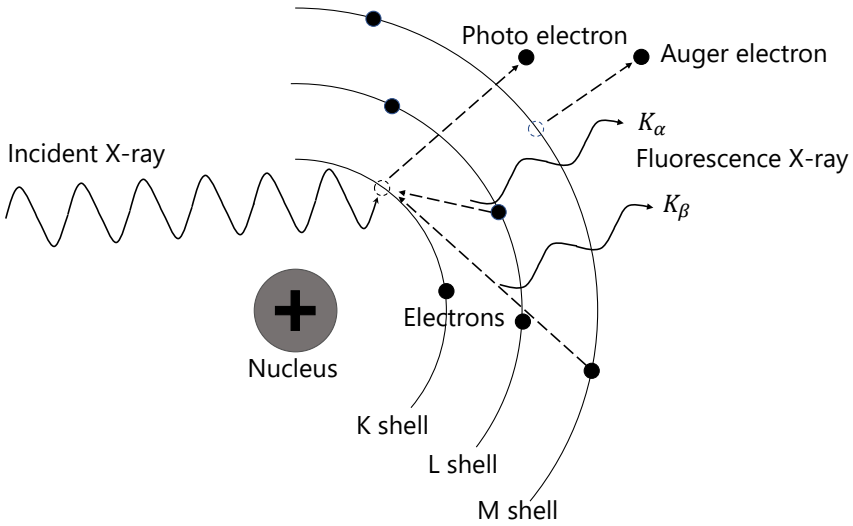

Figure 2.2: Diagram of the mechanisms of X-ray photon/matter interactions: Photoelectron emission, Auger electron, and X-ray fluorescence. Here the atom model is simplified, where the electrons are in orbits labeled K, L, and M around the nucleus.

The identification of transitions relies on understanding which primary and outer electron shells the X-ray-emitting electrons originate. For instance, as shown in Figure 2.3, when an electron from the L shell fills a vacancy in the K shell, this process is denoted as K_α. More detailed subscripts are used to represent the fine structures of these transitions.

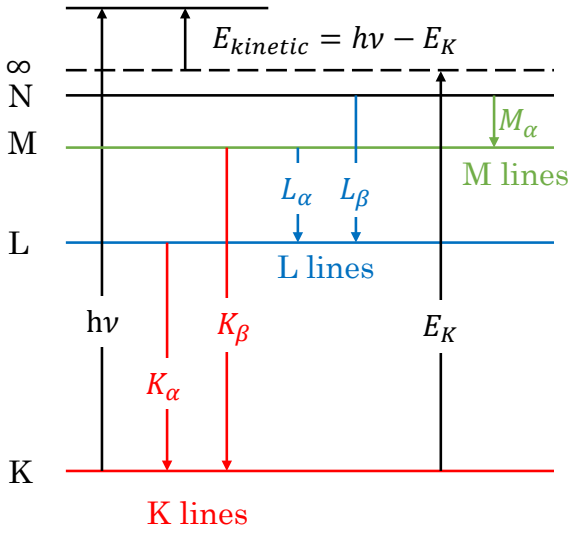

Figure 2.3: Common transitions in XRF fluorescence. $h\nu$ is the incident photon energy. The absorption edge, denoted as E_K, represents the energy required to free a bound electron. The discontinuity observed in Figure 2.1 occurs when the energy reaches the binding energy of each individual electron subshell.

Alternatively, in contrast to the radiative X-ray fluorescence process, there is a competing nonradiative process that leads to the emission of an electron from an outer shell. This is known as Auger emission and the emitted electron is termed an Auger electron.

The probability of either the Auger electron emission or X-ray fluorescence depends on the atomic number of the element. Auger electron emission is more probable for elements with lower atomic numbers. Conversely, for elements with higher atomic numbers, X-ray fluorescence becomes more dominant. This relationship is illustrated in Figure 2.4. It is also important to note that K emission lines are typically stronger than L emission lines for any given atom, making them the preferred choice for XRF analysis.

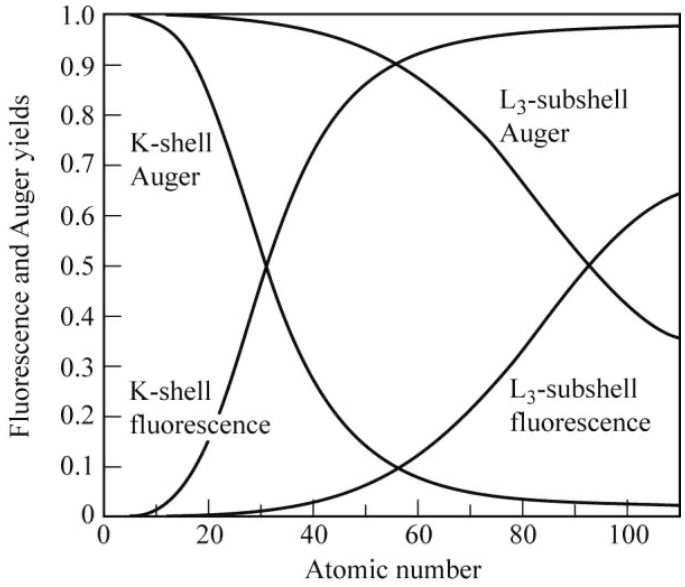

Figure 2.4: Yields of Auger electrons and fluorescence, as a function of atomic number for the K- and L_3-subshell. The yield is normalized for both Auger and XRF processes, calculated as the ratio of the number of ejected Auger electrons or XRF photons to the total number of created core holes (Attwood and Sakdinawat, 2017).

2.1.3. X-ray scattering

X-ray scattering is a phenomenon where an X-ray photon changes its direction after interacting with an electron. This interaction can either involve an exchange of energy, known as inelastic scattering, or proceed without any energy exchange, termed elastic scattering.

2.1.3.1. Rayleigh scattering

Scattering is elastic in which incident photons are scattered by bound electrons (see Figure 2.5) without any energy loss.

Taking I_0 as incoming photons per unit area per second, the scattered photons per second I_S within the solid angle $\Delta\Omega$ can be expressed as follows:

$$I_S = I_0 \frac{d\sigma}{d\Omega} \Delta\Omega \tag{2.5}$$

with the differential scattering cross section $d\sigma/d\Omega$ which indicates the probability of this process to occur:

$$\frac{d\sigma}{d\Omega} = r_e^2 P(\theta) \left| F\left(\frac{4\pi \sin\theta}{\lambda}\right) \right|^2 \tag{2.6}$$

where $P(\theta)$ is the polarization factor, F is the atomic scattering factor and $r_e = \frac{e^2}{4\pi\epsilon_0 m_e c^2} = 2.82 \times 10^{-15}\, m$ is the electron classical radius. The atomic scattering factor F represents the scattering amplitude as a function of $\frac{\sin\theta}{\lambda}$.

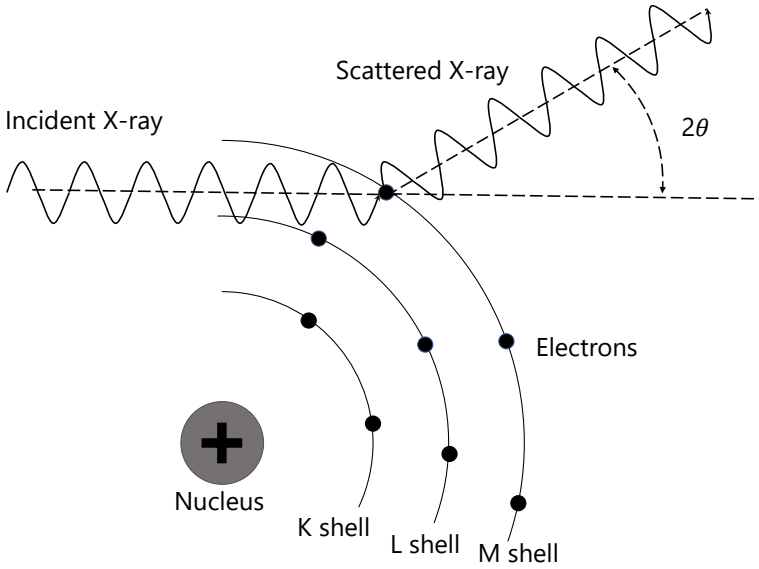

Figure 2.5: Illustration of the Rayleigh scattering. The incident photon is redirected without energy exchange with the atomic electrons.

2.1.3.2. Compton scattering

Compton scattering is an inelastic scattering process in which a photon is scattered by a free or weakly bound electron within an atom. During this interaction, the photon's kinetic energy is not conserved. Instead, a portion of its energy is transferred to the electron, as illustrated in Figure 2.6.

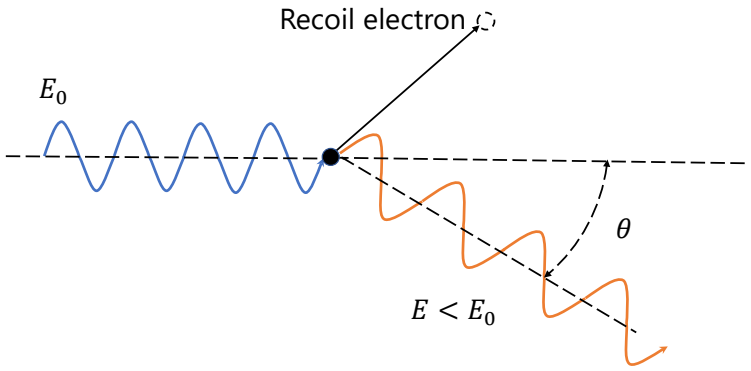

Figure 2.6: Illustration of Compton scattering. The incident photon is scattered along the angle θ with lower energy and transfers part of its energy to a recoil electron.

We assume here that the electron is free primarily due to its low binding energy compared to the incident photon energy. The conservation of both total energy and momentum leads to the following formula, which relates the angle θ with the energy of the incident photon E_0 and the energy of the scattered photon E:

$$\frac{E}{E_0} = \frac{1}{1 + \alpha(1 - \cos\theta)} \tag{2.7}$$

Here α is given by:

$$\alpha = \frac{E_0}{m_e c^2} \tag{2.8}$$

where m_e is the electron mass and c denotes the speed of light.

2.2. Synchrotron radiation

2.2.1. X-ray production

According to electromagnetic radiation theory, when a charged particle undergoes a change in its velocity, either in magnitude or direction (which can be due to influences like a nucleus's Coulomb field), it emits electromagnetic radiation. This means that an accelerated or decelerated particle will dissipate energy through the emission of electromagnetic radiation (Podgorsak, 2013). This fundamental physical phenomenon serves as the foundation for various X-ray sources, including laboratory sources and synchrotrons.

2.2.1.1. Principal characteristics of an X-ray source

An X-ray source is characterized by several key parameters:

Energy spectrum:

The energy spectrum describes the energy distribution of photons constituting the X-ray beam, and its nature depends on how the beam is generated. For many experiments, like absorption spectroscopy, a high monochromatic X-ray beam is required. The degree of monochromaticity is represented by the ratio $\frac{\Delta E}{E}$ signifying the deviation from the beam's nominal energy.

Flux and brilliance:

Flux denotes the number of photons per unit area and time, typically expressed in $photons/s/mm^2$. Brilliance serves as a critical metric for comparing different X-ray sources. It corresponds to the number of photons emitted per second, per source unit area, per unit solid angle, and within an energy bandwidth (BW) of 0.1 %. It quantifies the intensity of a source, taking into account its spectral purity and its angular aperture (Garolfi et al., 2017).

Coherence:

Coherence is another important characteristic. It enables focusing the beam down to the diffraction limit and also reveals interference effects due to the phase shift that occurs when the beam passes across a material.

The coherence is defined along two axes: longitudinal and transverse coherence.

Longitudinal Coherence L_L: Also known as temporal coherence, this metric reflects the length over which the incident X-ray wave can be considered monochromatic. It is determined by the wavelength (λ) of the beam and the deviation in wavelength ($\Delta\lambda$):

$$L_L = \frac{\lambda^2}{2\Delta\lambda} \tag{2.9}$$

For monochromatic X-ray beams, longitudinal coherence usually is not of primary concern.

Transverse Coherence L_T: Transverse coherence is often more critical. It indicates the distance over which the X-ray waves can be considered in phase. This length is determined by the wavelength (λ), the distance (D) from the source to the observation point and the source's size (S):

$$L_T = \frac{\lambda D}{S} \tag{2.10}$$

Achieving larger transverse coherence requires reducing the source size and increasing the observation distance. At the NANOSCOPIUM beamline, these criteria are met, enabling the generation of X-ray beams with significant transverse coherence lengths, which is advantageous for various experiments.

2.2.1.2. Laboratory sources

The X-ray tubes are the most commonly used laboratory X-ray sources. They operate on the principle of bremsstrahlung, a phenomenon in which X-rays are emitted as a result of the deceleration of an electron beam when it collides with a heavy material. The X-ray tube typically consists of two main components: an anode and a cathode, both encapsulated within a vacuum-sealed glass enclosure.

Made typically from a tungsten filament, the cathode is the site of electron generation. As an electric current traverses this filament, electrons are emitted via the thermionic emission process. The emitted electrons are accelerated by applying a potential difference between the cathode and the anode. The anode is typically made of dense materials such as tungsten, copper, or molybdenum. It acts as the target for the cathode's accelerated electrons. When these electrons collide with the anode, they are rapidly decelerated. This deceleration is the basis of bremsstrahlung, resulting in the emission of X-rays.

The X-ray spectrum generated by an X-ray tube has two main components: a continuous part and a line spectrum. The continuous spectrum arises from the deceleration of electrons. It has a range of energies, with the upper limit determined by the maximum kinetic energy of the electrons (denoted by eU, where e is the electron's charge, and U is the accelerating voltage between the anode and cathode).

The line spectrum is produced through X-ray fluorescence. When electrons from the cathode collide with the anode, they can ionize the constituent atoms of the anode material. This ionization process leads to the emission of characteristic X-ray lines. These lines have well-defined energies and are specific to the elements present in the anode material.

However, this emitted X-ray radiation is non-tunable because the energy values are determined by the properties of the anode material. Moreover, only a small portion of the total emitted X-rays can be effectively used for experimental purposes, as the radiation is emitted in all directions.

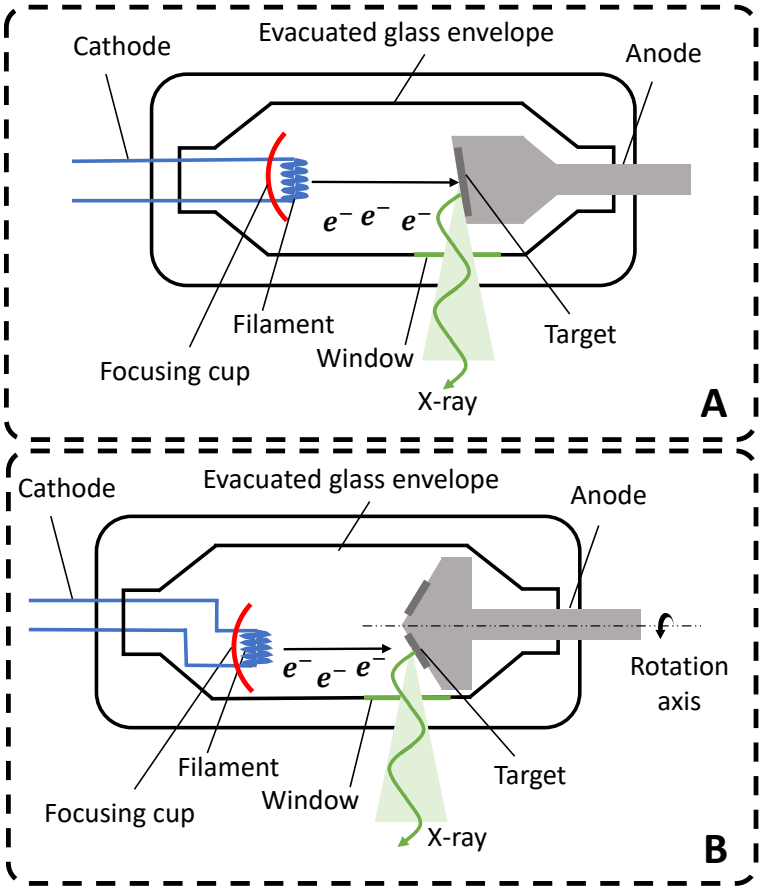

Figure 2.7: **A**: X-ray tube with a fixed anode. **B**: X-ray tube with a rotating anode.

The tubes generally used are tubes with a fixed anode. As shown in Figure 2.7-A, these tubes feature a target embedded within a copper block, serving as a thermal diffuser. Nonetheless, this design has restrictions in terms of heat transfer efficiency at the interface between the target and copper. As a result, their power output ranges are typically confined between 0.5 to 3 kW.

To overcome these limitations and access higher power levels, rotating anode tubes, as illustrated in Figure 2.7-B, employ a continuous rotation of the anode. This design facilitates varying the electron beam's impact surfaces on the anode while ensuring a consistent electron beam section. This rotational movement effectively spreads out the heat exchange over a larger surface area, enabling more efficient dissipation of absorbed heat (Van Grieken and Markowicz, 2001).

The brilliance of laboratory sources using this type of tube can reach 10^8-10^{10} ph/s/mm^2/mrad^2/0.1%BW. More advanced technologies based on the use of liquid metal as an anode have improved the brilliance of laboratory sources (~3-4 $\times$ 10 ^{11} ph/s/mm^2/mrad^2/0.1%BW) by overcoming the limitation associated with target heating induced by the electron beam (Hemberg et al., 2003).

In ongoing developments, larger laboratory facilities are aiming to further boost the brilliance by utilizing the inverse Compton effect to generate X-ray radiation from low-energy photons (Jacquet, 2014). This approach has more substantial brilliance improvements, with current advancements achieving brilliance levels ranging from 10^{11}-10^{13} ph/s/mm^2/mrad^2/0.1%BW.

2.2.1.3. Synchrotron sources

Synchrotron radiation is a form of electromagnetic radiation emitted when charged particles are accelerated and deviate from their trajectory due to the presence of a magnetic field. Synchrotron sources are known for their powerful brilliance (Couprie and Filhol, 2008), capable of providing up to 10^{21} ph/s/mm^2/mrad^2/0.1%BW. These facilities, such as the synchrotron SOLEIL, are the choice for a wide range of scientific investigations across the electromagnetic spectrum, spanning from the far infrared to several hundred keV.

Typically, synchrotron sources comprise three types of accelerators operating in a high vacuum environment. The process begins with a linear accelerator, which accelerates electrons to an energy level on the order of a hundred MeV (e.g., 100 MeV at the SOLEIL Synchrotron) and subsequently injects them into a booster. The booster is essentially a synchrotron that further accelerates the electrons to their target energy. Once the electrons reach a specified energy level, usually in the range of a few GeV (e.g., 2.75 GeV at SOLEIL), they are introduced into a circular accelerator known as a storage ring. This ring is where the synchrotron radiation used for experiments is produced.

To compensate for energy losses experienced by the electrons due to synchrotron radiation emission or potential collisions with residual air molecules, the storage ring incorporates accelerating cavities. These cavities serve to restore the electrons to their nominal energy (Willmott, 2019).

In current synchrotrons, known as 3rd generation (with the 1st generation representing the byproduct usage of particle accelerators for high-energy physics and the 2nd generation corresponding to the first circular machines dedicated to synchrotron radiation emitted by bending magnets), particular focus is placed on employing undulators and wigglers inserted into the straight sections of the storage ring. Unlike bending magnets, these inserts feature multiple magnetic poles, causing the electrons to follow an undulating path (Winick et al., 1981). With each acceleration or deceleration event in the electron packets, synchrotron radiation is emitted in the form of electromagnetic radiation. These elements significantly enhance photon flux production and enable the generation of a highly collimated beam.

2.2.1.4. Dosimetry

Dosimetry serves the vital function of quantitatively measuring the absorbed dose of ionizing radiation in a specific medium. It stands at the intersection of physics, biology, and medicine, making it a diverse and multi-faceted field. Within dosimetry, multiple quantities are of interest, broadly categorized into two groups: those associated with incident radiation and those linked to the radiation's effects on an object (Russo, 2017).

The absorbed dose, denoted by D, is measured in gray (Gy). It relates the energy dE (in $joules$) deposited by ionizing radiation in a volume element dV with a mass dm (in kg) as (Attix, 1986):

$$D = \frac{dE}{dm} \tag{2.11}$$

In this thesis, we simplify the dose calculation by assuming electronic equilibrium, where ionization due to photon-electron interactions from the incident beam has a significantly shorter range compared to the transverse size of the incident beam (Nicolas et al., 2019). The absorbed dose in a medium exposed to a monochromatic and parallel X-ray beam can be represented as:

$$D = \frac{\mu_{en}}{\rho} E\phi t \tag{2.12}$$

where μ_{en} is the mass energy-absorption coefficient of the medium, E stands for the beam energy, ϕ is the incident flux (number of photons per second per unit area), and t is the exposure duration. In this thesis, the absorbed dose in air will be used to quantify the incident dose.

2.2.2. Multimodal X-ray nano-imaging on the NANOSCOPIUM beamline of the SOLEIL synchrotron

2.2.2.1. The SOLEIL synchrotron

SOLEIL is a synchrotron radiation facility situated on the Plateau de Saclay in France. It operates as a non-profit civil company funded jointly by the CNRS and the CEA. Employing a staff of approximately 350 people, SOLEIL serves as an international hub for multidisciplinary scientific research.

Synchrotron radiation, with its powerful brilliance and spectral range spanning from infrared to hard X-rays, is a tool for exploring the properties of matter across an array of domains. These domains encompass biology, chemistry, materials science, environmental studies, physics, earth sciences, heritage preservation, and archaeology. The production of synchrotron radiation lies in the high-energy electrons circulating within a circular accelerator. Subsequently, this synchrotron radiation is used in beamlines, where targets (i.e. the samples under investigation) are mounted at the end of the beamline.

At SOLEIL, the circular accelerator has a circumference of 354 m, serving as the source of synchrotron radiation. SOLEIL has 29 beamlines, including NANOSCOPIUM, a unique beamline at SOLEIL dedicated to multimodal and multiscale scanning X-ray imaging (Somogyi et al., 2015).

2.2.2.2. The NANOSCOPIUM beamline

NANOSCOPIUM is a beamline dedicated to X-ray imaging techniques within the 5-20 keV energy range, offering fast multi-technique and multi-length scale scanning capabilities, with spatial resolutions reaching down to 30 nm. It provides a diverse range of complementary imaging methods, including X-ray fluorescence, spectro-microscopy (XANES), differential phase contrast, and X-ray diffraction.

X-ray fluorescence gives access to chemical composition maps with an analytical sensitivity down to the ppm or even sub-ppm level. X-ray Absorption Near Edge Structure (XANES) spectroscopy provides information on the chemical

speciation distribution of compounds, such as their degree of oxidation (Penner-Hahn, 2003). The phase contrast technique delivers morphological details with sensitivities to light elements that are notably higher (10 to 100 times) than absorption contrast. Additionally, diffraction is employed to investigate crystallographic structures, providing information on the spatial distribution of crystal phases.

NANOSCOPIUM offers an advanced scanning Coherent Diffraction Imaging (CDI) technique called Ptychography (Rodenburg et al., 2007), which excels in morphological imaging and provides extremely high spatial resolution (achieving 30 nm on the beamline). This technique relies on an X-ray beam with a high degree of transverse and longitudinal coherence. The resulting image is obtained indirectly through phase and amplitude retrieval algorithms, involving the analysis of multiple diffraction patterns while the object is moved, maintaining an overlap to reconstruct the final image.

To facilitate these diverse scanning X-ray nano-imaging methods, NANOSCOPIUM is based on a complex optical scheme compared to a standard beamline. The 155-meter-long beamline features a secondary source, which allows its size to be modulated, to guarantee the stability of the beam on the sample and to extend the transverse coherence length up to several hundred microns in the energy range of 5 to 20 keV.

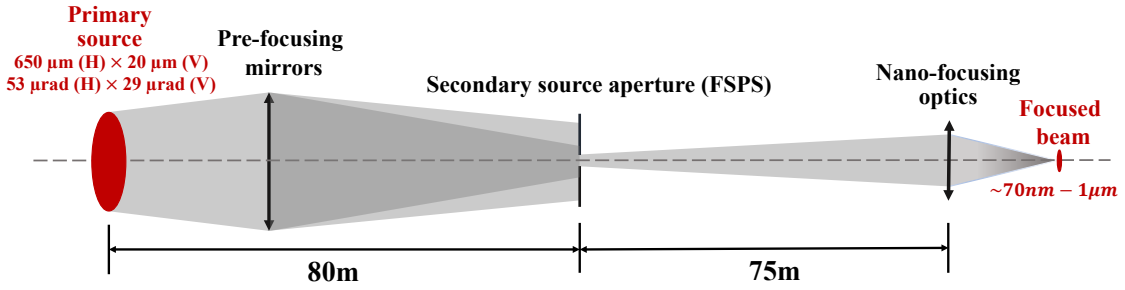

Figure 2.8: Synoptic of the NANOSCOPIUM beamline.

The source of NANOSCOPIUM is a 2-meter-long U18 undulator, offering an optimal energy range spanning from 5 keV to 20 keV. The primary source exhibits a beam size of 650 µm (horizontal) by 20 µm (vertical) and a divergence of 53 µrad (horizontal) by 29 µrad (vertical), as illustrated in Figure 2.8. To focus the polychromatic beam generated by the undulator onto a set of slits named FSPS (Fentes Second Point Source in French), located 58 m away, mirrors M1 and M2 are positioned at 26 m and 27.8 m from the primary source, respectively. This arrangement effectively creates the secondary source of the beamline.

The primary source image is magnified by a factor of approximately 2.6 in the vertical direction and 2.3 in the horizontal direction. For experimental flexibility, a defined slit opening allows for varying the second source point size, ranging from 20 µm × 20 µm to 150 µm × 150 µm. Before the secondary source, a double crystal Si (111) monochromator with fixed output is utilized for producing a monochromatic beam, which guarantees monochromaticity at $\Delta E/E \approx 10^{-4}$.

The beam then proceeds towards three multi-scanning nano-imaging experimental stations, namely CX1, CX2, and CX3, situated at distances of 60 m, 70 m, and 75 m from the secondary source, respectively. These experimental stations are housed within two hutches, EH1 and EH2. With an FSPS aperture of 20 μm, NANOSCOPIUM achieves transverse coherence lengths of several hundred microns, for instance (e.g., 465 μm at 10 keV). This coherence allows for coherent illumination of the focusing optics and enables focusing at the diffraction limit, thereby producing a highly precise nanobeam. Moreover, it facilitates the realization of a wide range of coherence-dependent experiments.

2.2.2.3. Multi-technique scanning X-ray nano-imaging station

The operational principle of the scanning multi-technique imaging system developed at the NANOSCOPIUM beamline is described in Figure 2.9. The incident monochromatic X-ray beam is focused onto the sample using an X-ray optic. This sample is mounted on a two-axis translation table, allowing 2D mapping.

For each scanning position on the sample, the system records chemical composition data by detecting the X-ray fluorescence signal that arises from photon absorption. Simultaneously, it captures the transmitted, scattered, or diffracted beam using a two-dimensional detector. The resulting images provide comprehensive morphological and/or crystallographic insights for every point across the sample.

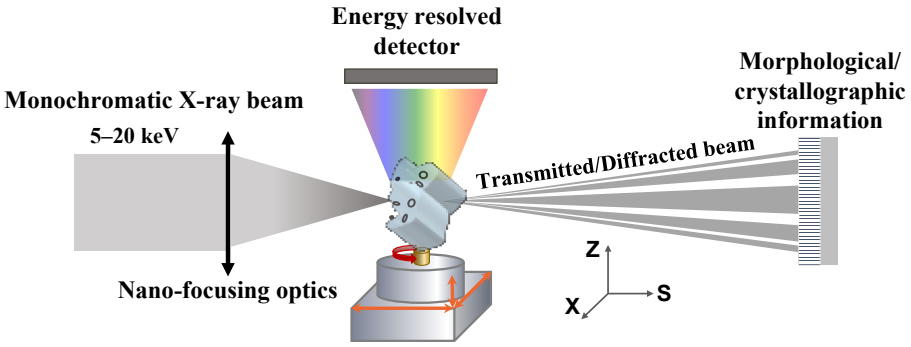

Figure 2.9: Schema of multi-technique scanning X-ray imaging.

Figure 2.10-A gives an overview of the experimental hutch EH2. The experimental station CX2 is situated on the left and the experimental station CX3 is on the right. Although both stations offer almost similar imaging techniques, their focusing optics are different. Currently in its commissioning phase, the CX2 station aims to achieve a spatial resolution of 40 to 50 nm, by using Fresnel Zone Plate focusing optics, and will be mainly dedicated to biological applications. Additionally, fast full-field micro-tomography experiments can be conducted at CX2, enabling rapid 3D morphology analysis of samples (1-2 minutes per tomography).

On the other hand, the CX3 station is fully operational and fully open to the user community. The beam can be focused down to 70 nm by using a “Kirkpatrick-Baez” (KB) mirror. Almost all the experiments done during this PhD work were done with this experimental station.

Furthermore, the CX1 station is currently under construction and, like the other stations, is based on scanning imaging but with the additional ability to offer wide-angle X-ray scanning diffraction. When operational, its primary focus will be on experiments related to material science.

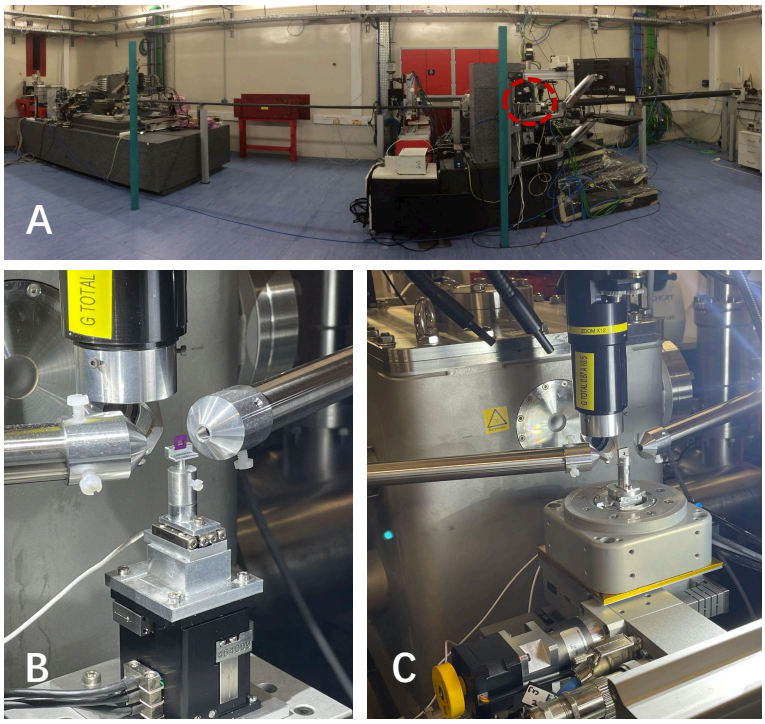

Figure 2.10: **A**: Overview of the experimental hutch EH2. **B** and **C**: Zoom in on the circled region in **A**. Sample environment of the CX3 experimental station with respectively: translation stage (**B**) and rotation stage (**C**).

The following section provides a description of the optical elements, sample environment, and detectors that are currently integrated and operational at the NANOSCOPIUM beamline.

a). Optical elements

As described above, two types of nano-focusing optics: Kirkpatrick-Baez mirrors and Fresnel Zone Plate (FZP), are used on the NANOSCOPIUM experimental stations.

FZP are diffractive optic which can be described as circular grating with decreasing periodicity towards its outer edge. Such a structure ensures that the incident beam's constructive interferences converge at a single focal point. They are chromatic optics, implying their focal length is dependent on the energy of the beam. In the hard X-ray regime, an FZP is typically composed of concentric gold rings with a thickness of a few microns deposited on a substrate like a silicon nitride membrane. The size of the focused beam is typically on the order of the FZP's smallest grating period. This can be down a few tens of nanometers, though there is a trade-off with efficiency, constrained by the feasible aspect ratio (Mohacsi et al., 2017). To ensure only the first diffraction order is selected, an FZP is combined with a central stop (CS) and an order-sorting aperture (OSA).

In order to gain familiarity with 2D XRF imaging techniques, I have been involved in several experiments at the CX2 experimental station, specifically with the alignment and characterization of the FZPs available at the NANOSCOPIUM beamline. The details of this work are not presented in this manuscript.

The CX3 station employs a Kirkpatrick-Baez (KB) system, which is an achromatic optic. This means that its focal length remains constant with varying energy. This characteristic proves advantageous for spectroscopy experiments like XANES that necessitate energy scans. The KB system consists of two orthogonal mirrors. These mirrors serve the purpose of focusing the X-ray beam horizontally and vertically. Manufactured by JTEC Corporation (JTEC CORPORATION, 2019), these mirrors have an elliptical shape and maintain a slope error that is consistently below 60 nrad. They are made of silicon and coated with platinum to increase the reflectivity of the X-ray beam.

The KB system on the CX3 station offers a nanobeam with a minimum size of 70 nm (FWHM) and a flux of approximately 10^8-10^9 ph/s under routine operation conditions. The efficiency of the KB system, measured as the beam's intensity at the focal plane relative to the intensity at the KB's entrance, is 87 %.

b). Sample Environment

The sample environment includes the translation stages to move the sample and the support on which it is mounted. The support is designed for minimal interference and contamination during the quantification process. It consists of a plastic rod that fits into a cylindrical support made of Aluminium Alloy 2017, as shown in Figure 2.10-B. This support features a magnetic base, facilitating the sample mounting process.

In the CX3 station, two sets of translations are used to scan the sample (as seen in Figure 2.11 (left)) across the beam. The first set utilizes stepper motors provided by AXMO PRECISION (Axmo, 2023)]. These motors (Tx_stepper and Tz_stepper in Figure 2.11) can map the sample in both the x and z axes over a large displacement range of approximately 10 mm. They offer a position resolution of around 400 nm. However, to maximize the precision of measurements and fully benefit from the nanobeam's performance, a second set of translations is mounted on top of the first one (Tx_piezo and Tz_piezo in Figure 2.11). These nano-positioners are based on piezoelectric motors supplied by NPOINT (Motion Solutions, accessed 06 Sept. 2023). While the x and z range of the nano-positioners are limited to 80 µm, they provide an improved resolution of 150 nm routinely used at the beamline.

For 3D scanning tomography during my PhD research, a second set-up has been used. As illustrated in Figure 2.11 (right), the rotation stage replaces the nano-positioner. The rotation stage is a high-precision compact air-bearing model (LAB Motion Systems, Leuven, Belgium (LAB Motion Systems, accessed 07 Sept. 2023)). The same model is employed at the CX2 station, enabling fast full-field micro-tomography. In this setup, the stepper motors are responsible for carrying out the 2D and 1D scans for every orientation of the sample. On the top of the rotation stage, a 2-axis translation stage (Tx_rotation and Ts_rotation in Figure 2.11) allows for the centering of the sample on the rotation axis.

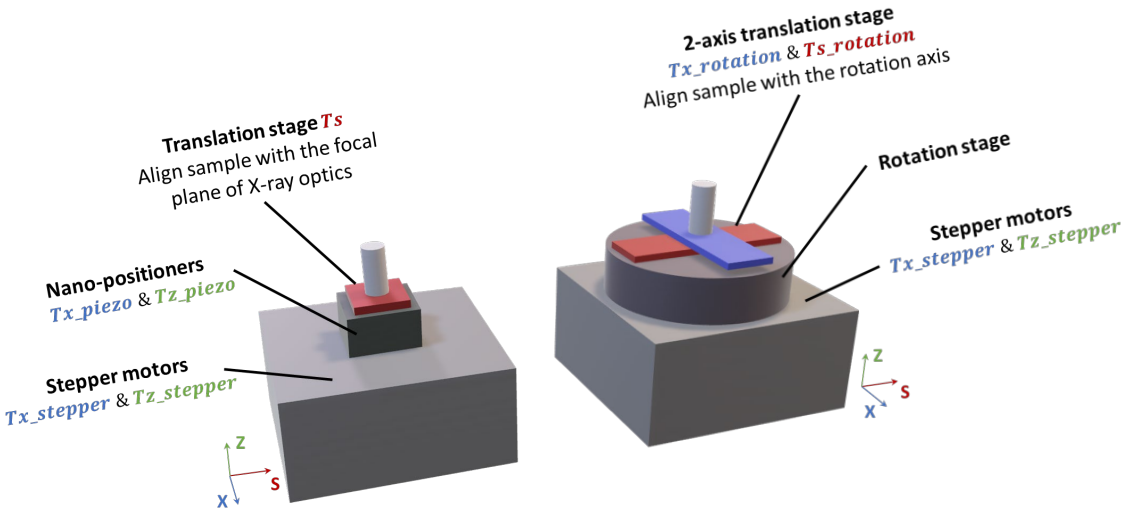

Figure 2.11: Schematic diagram illustrating two different setups for scanning 2D imaging (left) and 3D tomography (right).

Most of the scans at NANOSCOPIUM use a continuous scanning mode named Flyscan (Medjoubi et al., 2013). Unlike the step-by-step mode where the scan at a given position starts only after the completion of the previous acquisition, Flyscan allows data acquisition during the sample displacement. To minimize the dead time during mapping, scans are conducted in a bidirectional manner using raster scanning mode (refer to Figure 2.12). The motorization requirements are more demanding in continuous mode compared to step mode. In addition to the positioning resolution, the motors need to maintain a consistent speed, with variations restricted to less than 5 % of the maximum amplitude, covering speeds ranging from 1 µm/s to 1 mm/s.

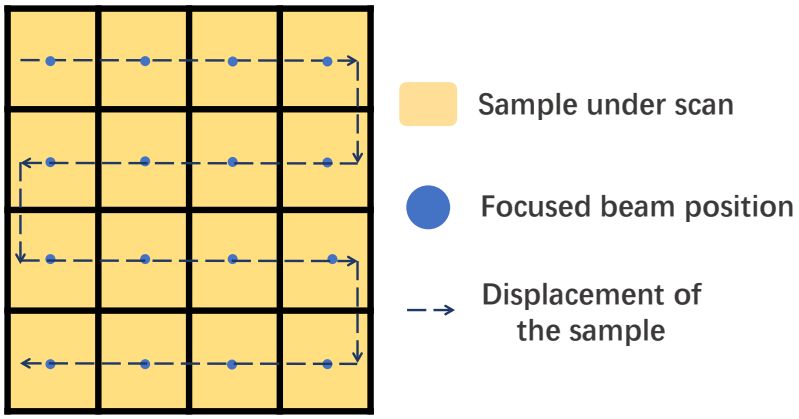

Figure 2.12: Schematic of the acquisition method. The sample is presented in yellow. The blue dots are the positions of the focused X-ray nanobeam and the black arrows represent the trajectories of the sample displacements during a mapping acquisition.

c). Detectors

In the context of multi-technique scanning imaging experiments, the choice and configuration of detectors are paramount. These detectors capture, process, and translate the interactions between the X-ray beam and the samples into data, which can then be interpreted for analysis. Here is a brief introduction to some commonly used detectors at the experimental stations:

Visible microscope The visible microscope plays a crucial role in sample positioning on the focal plane of the X-ray nano-focusing optics and in selecting areas of interest for analysis. At the CX3 station, it consists of a visible camera coupled with a variable magnification microscope objective (ranging from ×10 to ×4) mounted on a 45 ° mirror. This arrangement allows the entire system to be perpendicular to the beam axis, reducing its spatial dimensions and facilitating integration into a constrained environment. While the depth of field of such a microscope, meaning the longitudinal distance over which the image remains sharp, is only a few microns (much less than that of X-ray optics, which is ~hundred microns), even if the image is slightly blurred, the sample will still be at the focal point of the focused X-ray beam.

X-ray fluorescence detectors The X-ray fluorescence detectors used in multi-technique scanning imaging experiments are silicon drift detectors (SDDs (Gatti and Rehak, 1984)). When an X-ray photon is absorbed by the silicon in the SDD, it induces charges proportional to the photon's energy. These charges then move towards the electrodes due to an applied electric field. The resulting current, produced by the drift of the electrons and holes, is integrated and converted into a voltage, which is amplified by a pre-amplifier. The amplitude of this resultant pulse is directly proportional to the energy of the absorbed X-ray photon.

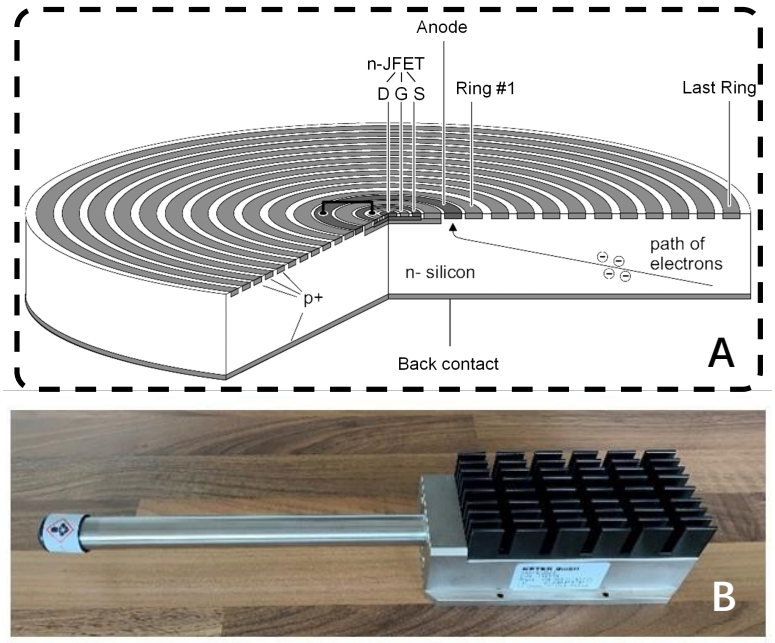

Figure 2.13: **A**. Schematic of a charge drift diode where the structure can be seen on the front side concentric ring of the electrodes. **B**. Photograph of a KETEK GmbH SDD model VITUS H50.

The SDD detectors used at the beamline are the VITUS H50 models from KETEK GmbH (KETEK GmbH, accessed 08 Sept. 2023), with a central, small anode contact, which is surrounded by a number of concentric drift electrodes (Figure 2.13-A). This design reduces the detector's capacitance and enhances its energy resolution. To analyze the X-ray fluorescence spectrum, a multichannel analyzer, the xMAP card from XIA LLC (XIA, accessed 09 Sept. 2023), is used.

At the end of the detection chain, the energy resolution is about 200 eV (FWHM) at 6 keV. The detector can handle photon rates of up to 200,000 per second with a minimal dead time of less than 10 %.

2D indirect detector In the full-field tomography experiment set-up at the CX2 station, to convert X-ray photons into visible light, an indirect imaging device is used. This 2D indirect detector is composed of a thin scintillator screen coupled with an objective microscope that magnifies the image onto a large CMOS camera (ORCA-Flash, Hamamatsu (Hamamatsu Photonics K.K., accessed 23 Sept. 2023)) as illustrated in Figure 2.14.

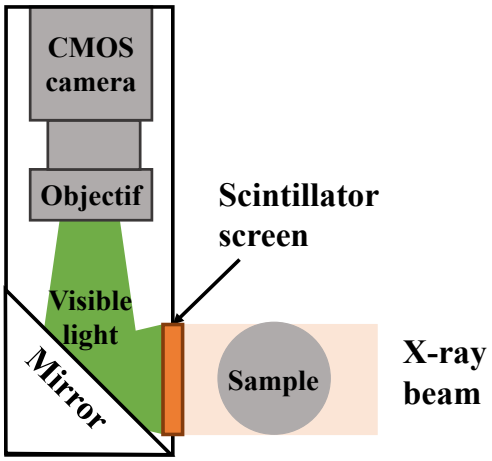

Figure 2.14: Schematic of the 2D indirect detector system based on a CMOS camera.

The scintillator is a YAG crystal and allows the absorption of X-ray photons and emission of visible light which will be collected by the camera. To prevent signal contamination from the visible light emitted by other sources inside the hutch, such as LED or exit signs, a carbon filter is placed in front of the scintillator. In order to prevent the X-ray beam radiation damage on the objective (Montaux-Lambert, 2017) and on the camera, a 45 ° tilted mirror is inserted between the screen and the objective.

Intensity monitor At CX3, the intensity of the incident X-ray beam is measured using a thin silicon photodiode supplied by Micron Semiconductor Ltd. The 8 µm thickness of the photodiode allows to limit the attenuation of the direct beam. The absorption is less than 10 % at 8 keV and only 0.8 % at 20 keV. The photo-current generated by the photodiode is directly proportional to the number of X-ray photons per second, denoted as N, and can be calculated using a specific formula:

$$N(ph/s) = \frac{Ie}{qE(1 - e^{-\mu d})} \tag{2.13}$$

with I the photo-current (unit: A) produced by the photodiode, E the energy of photons in eV, q the charge of an electron, e the energy of creation of an electron-hole pair (3.65 eV for silicon), μ the linear absorption coefficient in cm^{-1} of silicon and d the thickness of the photodiode in cm.

2.2.2.4. FLYSCAN acquisition architecture in operation

FLYSCAN (Medjoubi et al., 2013) has been developed to enable multi-technique imaging experiments through continuous scanning. Initially designed for NANOSCOPIUM, it was later adapted as a generic acquisition model for other SOLEIL beamlines. FLYSCAN is based on a distributed control system called TANGO (Tango Controls, accessed 10 Sept. 2023), which allows individual control of detectors and motors through the beamline network. A common trigger signal integrated into the architecture achieves synchronization of detector acquisition—encompassing X-ray fluorescence detectors, 2D detectors, and intensity monitors—and translation stage positions during continuous scanning. FLYSCAN also manages the data streaming and storage by accumulating individual data files produced by each detector into a single NEXUS file, organized according to a convention in HDF5 format.

To handle a high data flow of several Gb/s which can be generated for example by a 2D detector during, for example, a fast full-field tomography experiment, the architecture relies on 10 Gb/s links and a local storage area of several tens of terabytes.

The parallelization of the acquisition of all detectors as well as the continuous movement of the sample allows to significantly reduce total duration of an experiment by up to a factor of 100 compared to the “step-by-step” mode. This enables imaging experiments on many samples or some repeat mappings under different experimental conditions.

2.2.3. Data processing

The NANOSCOPIUM beamline provides a range of software tools for processing raw data, consisting of three main steps: raw data reduction, correction and/or reconstruction, and analysis. The first two steps are executed using a MATLAB toolbox that has been developed by the beamline (called the NANOSCOPIUM toolbox). They are routinely used by the user community whatever the imaging technique used.

The corrected and reduced data are typically in HDF5 format, ensuring compatibility with various analysis tools. Some examples of these tools include PyMca and ImageJ, both of which were used during this thesis, along with MATLAB algorithms specifically created for certain data reconstruction and analysis which will be detailed in Chapter 4.

2.2.3.1. Data organization

Depending on the imaging techniques and the type of scan conducted, the dimensions of data stored in a single NEXUS file can range from one to four dimensions. For instance, in a 2D scan using an X-ray fluorescence detector, the final data has 3 dimensions: two dimensions for the position and one for the spectrum.

The initial data processing step, data reduction, involves converting raw data into an easily interpretable physical quantity. This process is technique-dependent and is explained in detail for the X-ray fluorescence technique used during the PhD work.

2.2.3.2. Data reduction

Reduction of X-ray fluorescence data

The reduction of X-ray fluorescence data aims to create elemental distribution images based on the spectra associated with each position in the mapping. This involves several key steps:

Identification: The process begins with an identification step to correlate the element with its X-ray fluorescence lines in the spectrum.

Calibration: Next, the spectrum is calibrated to represent it as a function of energy. This is achieved using PyMca software (Solé et al., 2007), which enhances precision. During calibration, the elemental composition is adjusted until the simulated spectrum closely aligns with the measured spectrum.

Extraction: After identifying the elements present, images of elemental distribution are created by extracting the intensity per pixel from the measured spectrum at each position. The reduction step involves simply integrating one of the characteristic peaks of the element over a defined interval while ensuring that the chosen line does not overlap with a line of another element.

Figure 2.15 shows a measured spectrum from a renal papilla sample studied in this thesis, along with its corresponding calibrated spectrum.

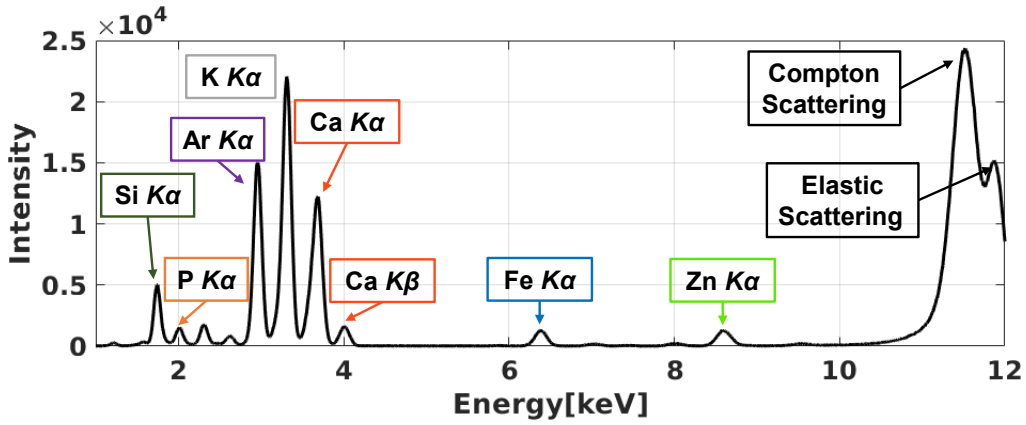

Figure 2.15: An X-ray fluorescence spectrum measured and calibrated with the PyMca software.

2.2.3.3. Position correction

Designed to align data by their acquisition time base, the NEXUS file organizes data irrespective of their dimension (1D, 2D, 3D, or 4D). However, practical factors like acceleration and deceleration phases, variable translation speeds, and alternating scan directions can introduce inaccuracies into this time base. Consequently, a realignment process is necessary to accurately position the data within an orthonormal reference frame.

In this thesis context, which addresses 2D, 3D, and 4D realigned data, such as elemental distribution images/projections and incident intensity, the MATLAB NANOSCOPIUM toolbox implements the realignment function. It relies on encoder values from the translation stages recorded during acquisition. Bicubic interpolation is employed to create a smooth, regular two-dimensional grid from the measured intensity values. This choice of interpolation method is preferred over linear, bilinear, and cubic interpolation because it results in a smoother surface. However, when analyses require to preserve the Poisson statistic in the statistics of the image, nearest neighbor interpolation is used instead.

For 3D/4D data, the interpolation operation is performed on each energy channel in X-ray fluorescence (XRF). This process yields data cubes that enable the extraction of the XRF spectrum for a region or volume of interest (ROI/VOI), which can take various shapes. The realignment and interpolation steps are essential for data processing and offer powerful capabilities for conducting analyses on these regions/volumes.

2.3. Conclusion

This chapter outlines the interactions of X-rays with matter, which are crucial to understanding the data and results generated during the work. Furthermore, it introduces the specificities of synchrotron radiation techniques and the suite of analytical tools available at the NANOSCOPIUM beamline. These instrumental setups and theoretical frameworks are not only the basis but also the enabling factors for the workflows and methodologies presented in this PhD work.

References

F. H. Attix. *Introduction to Radiological Physics and Radiation Dosimetry*. John Wiley & Sons, Ltd, Nov. 1986. ISBN 978-0-471-01146-0. doi: 10.1002/9783527617135.

D. Attwood and A. Sakdinawat. *X-Rays and Extreme Ultraviolet Radiation: Principles and Applications*. Cambridge University Press, Feb. 2017. ISBN 978-1-107-06289-4. doi: https://doi.org/10.1017/CBO9781107477629.

Axmo. Axmo Précision | Guidage linéaire, Rails & Douilles à billes, Aug. 2023. URL https://axmo.fr/.

M.-E. Couprie and J.-M. Filhol. X radiation sources based on accelerators. *Comptes Rendus Physique*, 9(5):487–506, June 2008. ISSN 1631-0705. doi: 10.1016/j.crhy.2008.04.001. URL https://www.sciencedirect.com/science/article/pii/S1631070508000571.

L. Garolfi, C. Bruni, M. El Khaldi, and C. Vallerand. Beam Dynamics for the ThomX Linac. In *8th International Particle Accelerator Conference*, page THPIK008, Copenhagen, Denmark, May 2017. doi: 10.18429/JACoW-IPAC2017-THPIK008. URL https://hal.science/hal-01646011.

E. Gatti and P. Rehak. Semiconductor drift chamber — An application of a novel charge transport scheme. *Nuclear Instruments and Methods in Physics Research*, 225(3):608–614, Sept. 1984. ISSN 0167-5087. doi: 10.1016/0167-5087(84)90113-3. URL https://www.sciencedirect.com/science/article/pii/0167508784901133.

Hamamatsu Photonics K.K. ORCA-Flash4.0 V3 Digital CMOS camera C13440-20CU | Hamamatsu Photonics, accessed 23 Sept. 2023. URL https://www.hamamatsu.com/eu/en/product/cameras/cmos-cameras/C13440-20CU.html.

O. Hemberg, M. Otendal, and H. M. Hertz. Liquid-metal-jet anode electron-impact x-ray source. *Applied Physics Letters*, 83(7):1483–1485, Aug. 2003. ISSN 0003-6951. doi: 10.1063/1.1602157. URL https://doi.org/10.1063/1.1602157.

M. Jacquet. High intensity compact Compton X-ray sources: Challenges and potential of applications. *Nuclear Instruments and Methods in Physics Research Section B: Beam Interactions with Materials and Atoms*, 331, July 2014. doi: 10.1016/j.nimb.2013.10.078.

JTEC CORPORATION. Kirkpatrick-Baez (KB) mirror, Oct. 2019. URL https://www.j-tec.co.jp/english/optical/optical-products/kb-mirror/.

KETEK GmbH. KETEK GmbH, accessed 08 Sept. 2023. URL https://www.ketek.net/.

LAB Motion Systems. RT100S Air Bearing Rotary Stage, accessed 07 Sept. 2023. URL https://www.labmotionsystems.com/product/rt100s/.

K. Medjoubi, N. Leclercq, F. Langlois, A. Buteau, S. Lé, S. Poirier, P. Mercère, M. C. Sforna, C. M. Kewish, and A. Somogyi. Development of fast, simultaneous and multi-technique scanning hard X-ray microscopy at Synchrotron Soleil. *J Synchrotron Rad*, 20(2):293–299, Mar. 2013. ISSN 0909-0495. doi: 10.1107/S0909049512052119. URL http://scripts.iucr.org/cgi-bin/paper?S0909049512052119.

I. Mohacsi, I. Vartiainen, B. Rösner, M. Guizar-Sicairos, V. A. Guzenko, I. McNulty, R. Winarski, M. V. Holt, and C. David. Interlaced zone plate optics for hard X-ray imaging in the 10 nm range. *Scientific Reports*, 7(1):43624, Mar. 2017. ISSN 2045-2322. doi: 10.1038/srep43624. URL https://doi.org/10.1038/srep43624.

A. Montaux-Lambert. *Conception d'un interféromètre large bande spectrale pour la métrologie et l'imagerie de phase sur sources synchrotron*. Theses, Université Paris Saclay (COmUE), Feb. 2017. URL https://theses.hal.science/tel-01523982.

Motion Solutions. Piezo Stages, accessed 06 Sept. 2023. URL https://www.motionsolutions.com/stages/piezo/.

J. D. Nicolas, S. Aeffner, and T. Salditt. Radiation damage studies in cardiac muscle cells and tissue using microfocused X-ray beams: experiment and simulation. *J Synchrotron Radiat*, 26(Pt 4):980–990, July 2019. ISSN 1600-5775. doi: 10.1107/S1600577519006817.

J. Penner-Hahn. X-ray Absorption Spectroscopy. In *Comprehensive Coordination Chemistry II*, pages 159–186. Elsevier, 2003. ISBN 978-0-08-043748-4. doi: 10.1016/B0-08-043748-6/01063-X. URL https://linkinghub.elsevier.com/retrieve/pii/B008043748601063X.

E. B. Podgorsak. *Compendium to Radiation Physics for Medical Physicists: 300 Problems and Solutions*. Springer Science & Business Media, Sept. 2013. ISBN 978-3-642-20186-8.

J. M. Rodenburg, A. C. Hurst, A. G. Cullis, B. R. Dobson, F. Pfeiffer, O. Bunk, C. David, K. Jefimovs, and I. Johnson. Hard-X-Ray Lensless Imaging of Extended Objects. *Phys. Rev. Lett.*, 98(3):034801, Jan. 2007. doi: 10.1103/PhysRevLett.98.034801. URL https://link.aps.org/doi/10.1103/PhysRevLett.98.034801.

P. Russo. *Handbook of X-ray imaging: physics and technology*. CRC Press, Boca Raton, 2017. ISBN 978-1-4987-4152-1. doi: https://doi.org/10.1201/9781351228251.

V. A. Solé, E. Papillon, M. Cotte, P. Walter, and J. Susini. A multiplatform code for the analysis of energy-dispersive X-ray fluorescence spectra. *Spectrochimica Acta Part B: Atomic Spectroscopy*, 62(1):63–68, Jan. 2007. ISSN 0584-8547. doi: 10.1016/j.sab.2006.12.002. URL https://www.sciencedirect.com/science/article/pii/S0584854706003764.

A. Somogyi, K. Medjoubi, G. Baranton, V. Le Roux, M. Ribbens, F. Polack, P. Philippot, and J.-P. Samama. Optical design and multi-length-scale scanning spectro-microscopy possibilities at the Nanoscopium beamline of Synchrotron Soleil. *Journal of Synchrotron Radiation*, 22:1118–1129, July 2015. doi: 10.1107/S1600577515009364.

Tango Controls. Software - TANGO Controls, accessed 10 Sept. 2023. URL https://www.tango-controls.org/developers/.

R. Van Grieken and A. Markowicz, editors. *Handbook of X-Ray Spectrometry*. CRC Press, 0 edition, Nov. 2001. ISBN 978-0-429-20827-0. doi: 10.1201/9780203908709. URL https://www.taylorfrancis.com/books/9780203908709.

P. Willmott. *An introduction to synchrotron radiation: techniques and applications*. Wiley, Hoboken, New Jersey, second edition, 2019. ISBN 978-1-119-28037-8 978-1-119-28038-5.

H. Winick, G. Brown, K. Halbach, and J. Harris. Wiggler and undulator magnets. *Physics Today*, 34(5):50–63, May 1981. ISSN 0031-9228. doi: 10.1063/1.2914568. URL https://doi.org/10.1063/1.2914568.

XIA. xMAP, accessed 09 Sept. 2023. URL https://xia.com/support/xmap/.

CHAPTER 3

TOMOGRAPHY IMAGE RECONSTRUCTION

This chapter provides a brief introduction to tomography image reconstruction, presenting an overview of the fundamental principles of computed tomography within the context of the parallel beam configuration at the NANOSCOPIUM beamline. It also introduces the algorithms that have been explored during the PhD research, as well as the artifacts that may appear in the reconstructed tomograms.

The tomographic reconstruction process starts with a collection of raw projections of the object, taken from varying angles. Following the data acquisition, the processing and reconstruction procedures enable the depiction of the object's internal structure non-destructively. This involves assembling the acquired data and using adaptive algorithms to create cross-sectional images of the sample, both in 2D and 3D.

The principles, advantages, and potential limitations of the algorithms are analyzed in this chapter. Such an analysis enables us to select the most appropriate reconstruction approach, considering raw data attributes like the signal-to-noise ratio and specific constraints such as the missing wedge condition or limited numbers of projection in X-ray tomography experiments. Furthermore, understanding the underlying principles of these algorithms allows for their optimization, especially when addressing challenges inherent to specific applications, such as sparse tomography. The adaptive reconstruction algorithms to solve the intricacies of sparse tomography are pivotal to the theme of my PhD thesis.

3.1. Background of tomography reconstruction

This section is essential for comprehending the fundamental principles of X-ray tomography. The term "tomography" originates from the Greek word "tomos", signifying "slice" or "section". Tomography is the process of imaging a sample in cross-section, i.e., as axial slices (Goldman, 2007).

As a nondestructive and multi-modal imaging technique, X-ray tomography involves acquiring multiple projections of a sample's physical properties from various angles. These projections subsequently serve as the input for the reconstruction of either a 2D slice or 3D volume illustrating the inner structure of the object. Conceptually, the reconstruction of an object can be regarded as an "inverse problem", representing the inverse of the initial acquisition process.

3.1.1. Radon transform

In tomography measurement, the projection operator is mathematically represented by the Radon transform, which sums the object function along a radial line oriented at a specified angle.

The formulation of the Radon transform differs depending on the beam modes employed, such as parallel beam, fan beam, or cone beam, during data acquisition. For scanning imaging, like that performed at the NANOSCOPIUM beamline, the acquisition geometry is parallel. Thus, our discussion here is limited to this case.

Assume an object is described by a 2D density function $f(x, y)$, indicating the distribution of its physical property (e.g., the linear attenuation coefficients or the X-ray fluorescence density emitted by the sample). The Radon transform, i.e., the projection function at angle ϕ, denoted as $p_\phi(r)$, is:

$$p_\phi(r) = \int_{-\infty}^{\infty} f(x, y) ds \tag{3.1}$$

Here s is the line at a distance r from the origin, oriented at an angle ϕ from the axis (see Figure 3.1). To facilitate the transformation, we link the $x-y$ coordinate system with the $r-s$ coordinate system through a rotation matrix:

$$\begin{bmatrix} x \\ y \end{bmatrix} = \begin{bmatrix} \cos\phi & -\sin\phi \\ \sin\phi & \cos\phi \end{bmatrix} \begin{bmatrix} r \\ s \end{bmatrix} \tag{3.2}$$

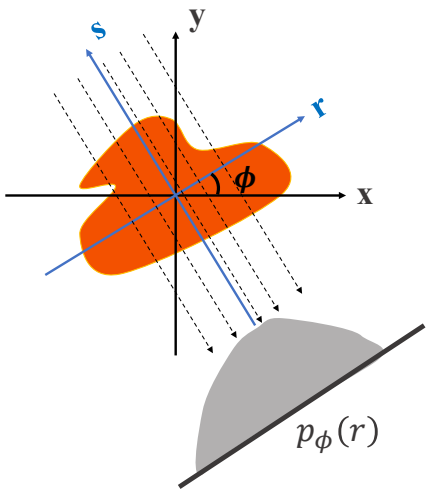

Figure 3.1: Schematic diagram of the original coordinate system and the rotated new coordinate system.

By replacing ϕ with $-\phi$, the inverse transformation is:

$$\begin{bmatrix} r \\ s \end{bmatrix} = \begin{bmatrix} \cos\phi & \sin\phi \\ -\sin\phi & \cos\phi \end{bmatrix} \begin{bmatrix} x \\ y \end{bmatrix} \tag{3.3}$$

Consequently, the projection becomes:

$$p_\phi(r) = \int_{-\infty}^{\infty} f(r\cos\phi - s\sin\phi, r\sin\phi + s\cos\phi) ds \tag{3.4}$$

This equation describes the Radon transform at angle ϕ. Often, the image function values are discrete rather than continuous, like pixel positions in an image. As a result, the Radon transform's integral becomes a sum:

$$p_\phi(r) = \sum_s f(r\cos\phi - s\sin\phi, r\sin\phi + s\cos\phi) \tag{3.5}$$

To accurately reconstruct the internal density function $f(x, y)$ of the sample, projections must be collected from various angles ϕ. The complete collection of these line integrals over the full angle range constitutes a 2D dataset typically known as the sinogram, named for the sinusoidal trajectory a point on the object traces during rotation (refer to Figure 3.2-C). In this sinogram, the vertical axis signifies the value measured at each pixel along the *r* axis, while the horizontal axis corresponds to the different projection angles.

Figure 3.2 illustrates the projection process using a phantom example. Here the forward projection dataset results from data collection ranging from $0\,^\circ$ to $180\,^\circ$, incremented by $1\,^\circ$. Of note, due to symmetry, the line integral at angle θ is identical to the line integral at angle $\theta + \pi$. This symmetry simplifies data acquisition in absorption tomography. However, it is inapplicable to X-ray fluorescence tomography, which will be discussed in Chapter 4. In X-ray fluorescence tomography experiments, the self-absorption depth of the measured element differs for two angles separated by π. Thus, data acquisition extends to 2π. This makes the data acquisition and reconstruction more time-consuming and challenging due to the absence of this symmetry property.

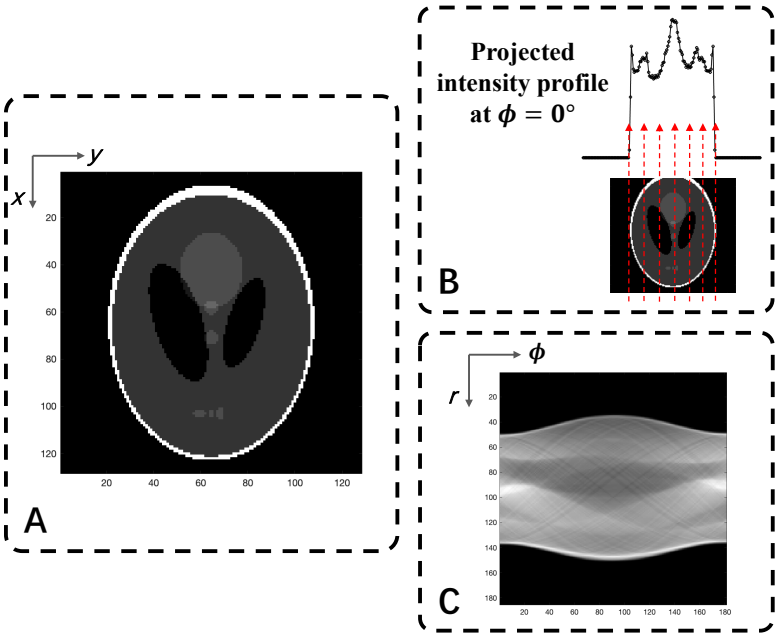

Figure 3.2: Shepp-Logan phantom example for illustration of the projection process. Considering a phantom slice represented by a density function $f(x, y)$ as shown in **A**. The projections of this phantom slice are collected from various angles ranging from $0\,^\circ$ to $180\,^\circ$ with a step size of $1\,^\circ$. In **B**, an intensity profile at $0\,^\circ$ is presented. **C** displays the corresponding sinogram, which represents the dataset obtained from the 180 forward projections. The two axes represent the measured intensity and the different projection angles.

3.1.2. Inverse Radon transform

The inverse Radon transform is the back projection operation that can be considered the inverse operation of forward projection. In back projection, each point in the object domain receives the value of the corresponding point where it projects to. This process will be formulated in detail in Section 3.3.2.

3.1.3. Central slice theorem

The central slice theorem, also known as the Fourier slice theorem or projection slice theorem, is a fundamental concept in many reconstruction methods. This theorem establishes a direct connection between the object and its projection in the spatial frequency domain. It states that the 1D Fourier transform of an object's parallel projection function at a specific angle corresponds to a "sample" (a cross-section) of the 2D Fourier transform of the object evaluated at the same angle (Kak and Slaney, 2001; Russo, 2017).

Using the notation introduced in Section 3.1.1, the 1D Fourier transform of the projection function $p_\phi(r)$ at frequency ω, denoted as $P_\phi(\omega)$, can be expressed as:

$$p_\phi(\omega) = \int p_\phi(r) e^{-i2\pi\omega r} dr = \iint_{-\infty}^{\infty} f(x,y) e^{-i2\pi\omega r} dr ds \tag{3.6}$$

Next we perform the substitution of $drds$ to $dxdy$:

$$drds = det \begin{bmatrix} \frac{\partial r}{\partial x} & \frac{\partial r}{\partial y} \\ \frac{\partial s}{\partial x} & \frac{\partial s}{\partial y} \end{bmatrix} dxdy = det \begin{bmatrix} \cos\phi & \sin\phi \\ -\sin\phi & \cos\phi \end{bmatrix} dxdy = dxdy \tag{3.7}$$

In addition, we replace $r = x\cos\phi + y\sin\phi$ obtained from the rotation matrix:

$$\begin{aligned} p_\phi(\omega) &= \iint_{-\infty}^{\infty} f(x,y) e^{-i2\pi\omega r} dxdy \\ &= \iint_{-\infty}^{\infty} f(x,y) e^{-i2\pi\omega(x\cos\phi + y\sin\phi)} dxdy \\ &= \iint_{-\infty}^{\infty} f(x,y) e^{-i2\pi(x\omega\cos\phi + y\omega\sin\phi)} dxdy \end{aligned} \tag{3.8}$$

Comparing this with the 2D Fourier transform of the complete density function $f(x,y)$:

$$F(u,v) = \iint f(x,y) e^{-i2\pi(ux+vy)} dxdy \tag{3.9}$$

We observe that these two expressions are equivalent when $u = \omega\cos\phi$ and $v = \omega\sin\phi$. This means that the values obtained by the 1D Fourier transform of the object's projection, when rotated to an angle ϕ, correspond to the values along a line forming an angle ϕ with the u-axis and passing through the origin of the 2D Fourier transform of the object (Figure 3.3).

In principle, if the data in Fourier space is sufficiently sampled, we can gradually improve our understanding of the object and the reconstruction can be done using an inverse Fourier transform of the Fourier space $F(u,v)$:

$$f(u,v) = \iint F(x,y) e^{i2\pi(ux+vy)} dudv \tag{3.10}$$

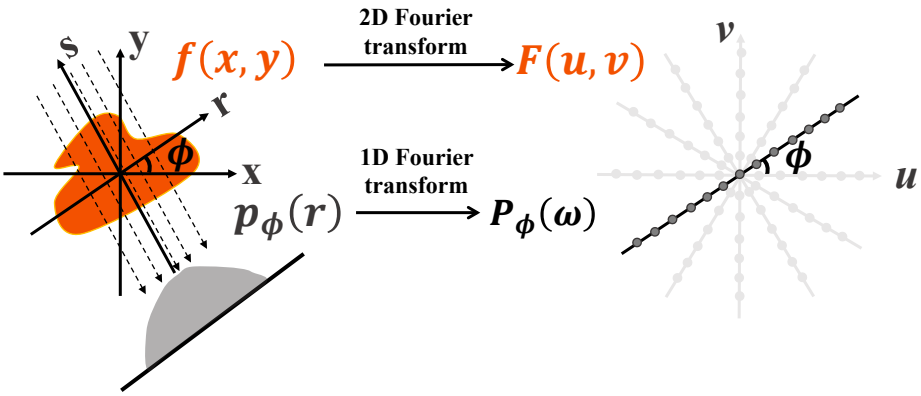

Figure 3.3: Illustration of the central slice theorem.

In practice, it is impossible to acquire an infinite number of projections for reconstruction. This situation results in gaps between two successive projections, as shown in Figure 3.4. Sampling in Fourier space is crucial for the reconstruction of images. Undersampling can be a source of reconstruction error, which can lead to the appearance of aliasing artifacts in the reconstructed image. A unique and information-preserving reconstruction is achievable when the sampling frequency of an object exceeds twice the highest frequency of its details, this critical frequency is called Nyquist frequency (f_N).

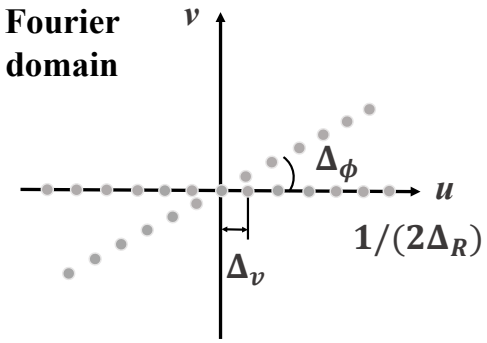

Figure 3.4: Angular sampling considerations. Adapted from (Fessler, accessed 23 Sept. 2023).

To achieve the required sampling in Fourier space, we consider an object with a length of $N_R \cdot \Delta_R$ spaced by Δ_R, where N_R is the number of pixels in reciprocal space. f_N is related to the pixel spacing Δ_R as $f_N = 1/(2\Delta_R)$. The spatial frequencies in Fourier space are then spaced by:

$$\Delta v = \frac{1}{N_R \cdot \Delta_R} \tag{3.11}$$

Consequently, the angular sampling step Δ_ϕ (see Figure 3.4) must not exceed the spatial frequency Δ_v. Thus, the maximum angular interval Δ_ϕ is given by:

$$\Delta_\phi = \frac{\Delta_v}{f_N} = \frac{\Delta_v}{1/(2\Delta_R)} = \frac{2}{N_R} \tag{3.12}$$

As a result, the number of equally spaced projections is:

$$N_{proj} = \frac{\pi}{\Delta_\phi} = \frac{\pi}{2} N_R \tag{3.13}$$

over an angular range of π rad.

In scanning X-ray tomography, fewer projections are used to avoid the substantial multiplied increase in acquisition time, and this is often referred to as "sparse tomography". However, inadequate projection numbers can lead to significant artifacts in the results using analytical algorithms, as discussed in subsequent sections, typically in the form of visible streaks, compromising the quality of the reconstructed image. Therefore, the selection of the proper reconstruction algorithm is crucial for sparse tomography.

3.2. Introduction to the reconstruction algorithms

In Section 2.2.2.3, we introduced how X-ray continuous scanning provides projections of the imaged object. The subsequent step is the reconstruction of the imaged object in 3D, which requires the tomography reconstruction algorithm that utilizes the acquired projections as its input.

Reconstruction algorithms for tomography imaging can be classified into two main categories: analytical and iterative methods. Analytical methods, like filtered back projection (FBP), use mathematical transformations and inversion techniques to efficiently reconstruct images without iteration. On the other hand, iterative methods improve the quality by iteratively refining the image estimate. This classification is illustrated in Figure 3.5.

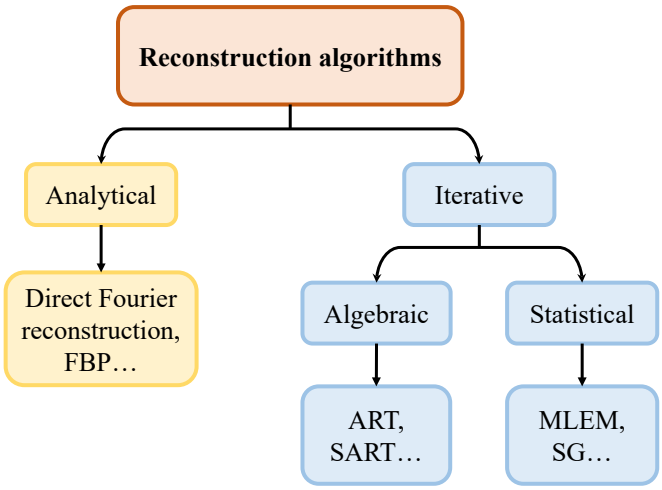

Figure 3.5: Classification of the reconstruction algorithms. The analytical algorithms, including direct Fourier reconstruction and filtered back-projection (FBP), use mathematical equations to directly compute the reconstructed image from the raw projection data. Iterative methods iteratively refine an initial estimate of the image until it converges to the best-fit reconstruction.

While analytical methods like filtered back projection are computationally fast and efficient, they may produce reconstructions with lower image quality compared

to iterative methods. On the other hand, iterative methods can produce higher-quality reconstructions by iteratively refining the image estimate, but they require more computational resources and longer processing time. The number of iterations can also significantly impact the reconstruction quality.

3.3. Analytical methods

3.3.1. Direct Fourier reconstruction

As explained in Section 3.1.3, the central slice theorem states that the 1D Fourier transform of a projection acquired at a certain angle is mathematically equivalent to a "central slice" in the 2D Fourier transform $F(u, v)$ of the original image function evaluated at the same angle (Kak and Slaney, 2001).

Intuitively, by conducting as many independent projections as possible, the reconstruction results can be obtained by applying the inverse Fourier transform. However, during tomographic acquisition, the inherent sampling characteristics in the Fourier domain of the object introduce a bias towards low frequencies. As shown in Figure 3.6, high frequencies are under-sampled, and low frequencies are over-sampled. Consequently, this results in a blurred reconstructed image. The high-frequency details like sharp edges are lost.

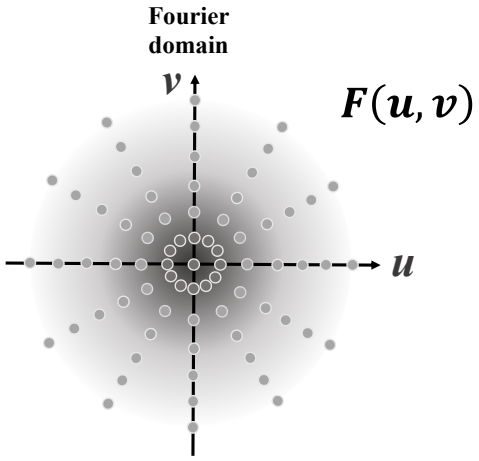

Figure 3.6: Illustration of the sampling in the Fourier domain. The available samples in Fourier space are organized in a radial grid, resulting in the low-frequency components being sampled more densely than the high-frequency ones.

Moreover, the Fourier transform of $f(x, y)$ is sampled along radial lines. To apply the discrete inverse 2D Fourier transform, it is necessary for $F(u, v)$ to be sampled on a rectangular grid. This leads to an interpolation process, often referred to as "gridding", Consequently, interpolation is used to transition from polar coordinates to a Cartesian grid, as illustrated in Figure 3.7.

Common interpolation methods include linear or nearest-neighbor interpolation, as well as higher-order techniques like cubic interpolation. Interpolation in the Fourier space may result in image artifacts when the inverse Fourier transform is applied to convert data back into real space (Russo, 2017).

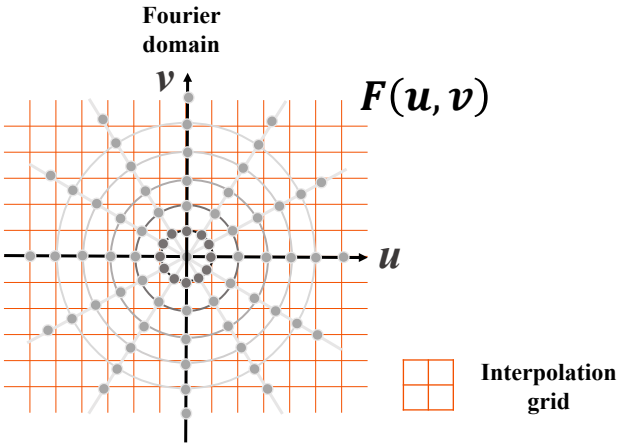

Figure 3.7: Interpolation from the polar coordinates to a Cartesian grid.

3.3.2. Filtered back projection

To overcome the blurring problem in the reconstructed image, filtering techniques are employed in the filtered back projection (FBP) algorithm. In particular, a high-pass filter is applied to the projection to attenuate the low-frequency components, thereby improving the visualization of finer details and edges in the reconstructed image.

We recall the notation used in Section 3.1.3. In tomographic imaging, a 2D density function $f(x, y)$ can be reconstructed from its Fourier transform $F(u, v)$ by:

$$\begin{aligned} f(x,y) &= \iint F(u,v) e^{i2\pi(ux+vy)} du dv \\ &= \iint F(\omega\cos\phi, \omega\sin\phi)|\omega| e^{i2\pi\omega(x\cos\phi + y\sin\phi)} d\omega d\phi \end{aligned} \tag{3.14}$$

where $dudv = |\omega| d\omega d\phi$ for the variable change from Cartesian to polar coordinates.

Replacing $F(\omega\cos\phi, \omega\sin\phi)$ with $P(\phi, \omega)$ according to the central slice theorem:

$$f(x,y) = \iint P(\phi,\omega)|\omega| e^{i2\pi\omega(x\cos\phi + y\sin\phi)} d\omega d\phi \tag{3.15}$$

$$= \int \hat{p}(\phi, x\cos\phi + y\sin\phi) d\phi \tag{3.16}$$

$$\hat{p}(\phi, r) = \mathcal{F}^{-1}(P(\phi,\omega)|\omega|) = \int P(\phi,\omega)|\omega| e^{i2\pi\omega r} d\omega \tag{3.17}$$

In Equation (3.15), we observe that in the Fourier domain, the product $P(\phi, \omega)|\omega|$ represents a filtering process, with $|\omega|$ acting as a ramp filter in the frequency domain, commonly known as the Ram-Lak filter. This filtering operation can lead to the negative components in the filtered projection (Baruchel, 2000). Then Equation (3.16) represents the back projection operation of the filtered projection into the image domain. This leads us to the formula of the filtered back projection algorithm for tomographic reconstruction.

The FBP algorithm involves the following steps:

(1). Collection of complete projections $p(\phi, r)$ and obtain the 2D sinogram.
(2). Filtering process:
  (a). Calculation of the Fourier transform $P(\phi, \omega)$ of the projections $p(\phi, r)$.
  (b). Fourier space filtering: $P(\phi, \omega)|\omega|$. The filter can be a combination of a ramp filter and other filters, such as using a sinc-function (Shepp-Logan filter), a cosine- or a Hamming filter (Russo, 2017). Some specific forms for these filters can be found in Figure 3.9.
(3). Compute the inverse Fourier transform of $P(\phi, \omega)|\omega|$ to get the filtered projection $\hat{p}(\phi, r)$.
(4). Back project the filtered projection $\hat{p}(\phi, r)$ to get the 2D density function $f(x, y)$.

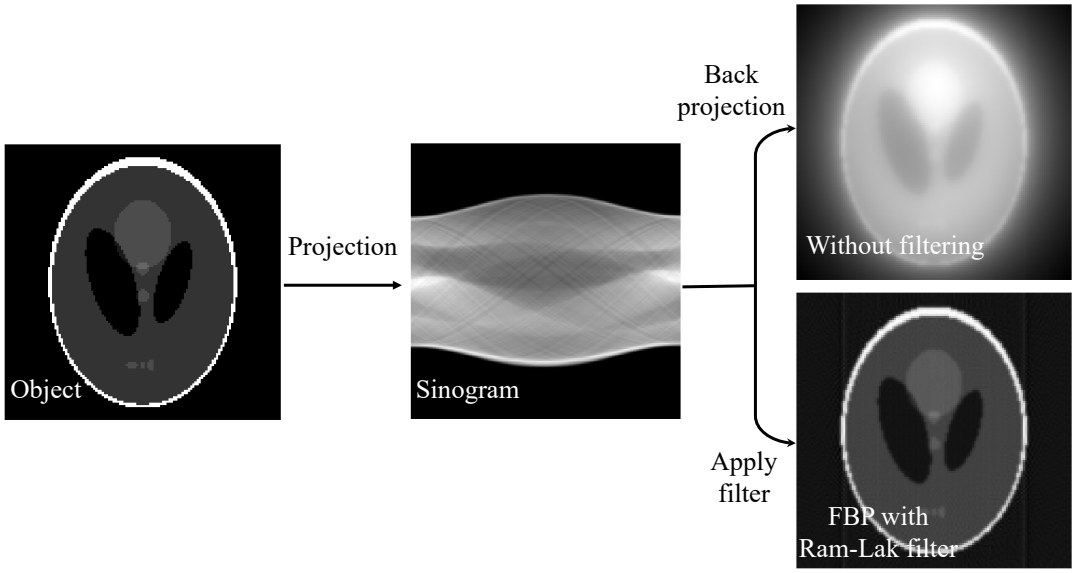

Figure 3.8: Reconstruction by FBP algorithm. Reconstruction of a Shepp-Logan phantom respectively by unfiltered back projection and FBP with Ram-Lak filter with 180 projections over 180°.

In Figure 3.8, we compare the results of the reconstructed images using the FBP algorithm with a Ram-Lak filter and back projection without filtering. As discussed in Section 3.3.1, the absence of filtering causes oversampling in the low-frequency domain. This results in a blurred reconstruction where the image values deviate from the original data.

Nonetheless, the FBP algorithm not only effectively captured the low-frequency features of the image function but also reconstructed sharp edges and preserved high-frequency details within the reconstructed phantom, such as the light gray circle features. To achieve the best compromise between spatial resolution and image noise in practical implementations, the ramp filter $|\omega|$ is frequently combined with different apodization window functions $W(\omega)$ that are tailored to match the noise characteristics:

$$f(x, y) = \iint_{-\omega_{max}}^{\omega_{max}} P(\phi, \omega) W(\omega) |\omega| e^{i2\pi\omega(x\cos\phi + y\sin\phi)} d\omega d\phi \tag{3.18}$$

The ramp filter $|\omega|$ serves as the baseline in Equation (3.18). And the window functions shown in Figure 3.9 are defined as (Velo et al., 2015):

$$Ramp: \quad W(\omega) = 1 \tag{3.19}$$

$$Shepp-Logan: \quad W(\omega) = \text{sinc}\,(\omega/2) \tag{3.20}$$

$$Cosine: \quad W(\omega) = \cos\,(\omega/2) \tag{3.21}$$

$$Hamming: \quad W(\omega) = 0.54 + 0.46\cos\,(\omega) \tag{3.22}$$

$$Hann: \quad W(\omega) = 0.5 + 0.5\cos\,(\omega) \tag{3.23}$$

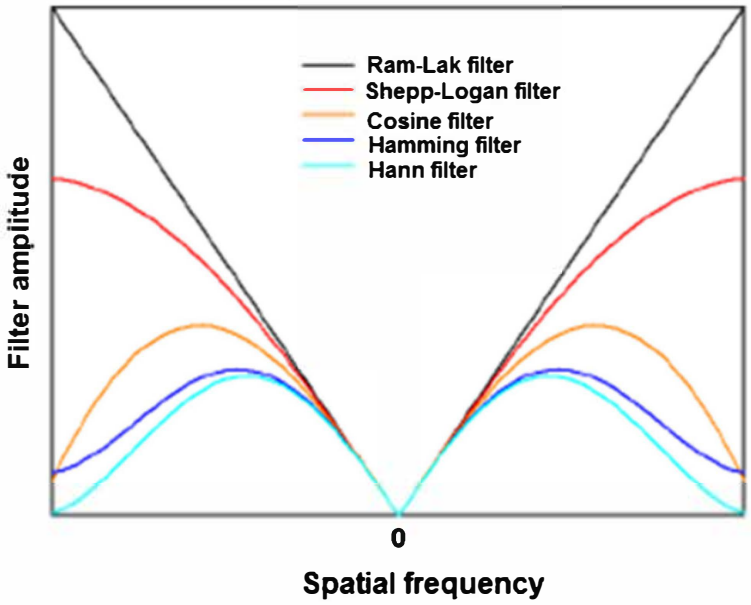

Figure 3.9: Different filters for the FBP algorithm. Ram-Lak filter serves as the standard ramp filter derived from coordinate transformation. The other filters have an increasing roll-off as they approach higher frequencies, designed for noise suppression. Adapted from (Srinivasan et al., 2014).

When using FBP for image reconstruction, one of the very few parameters we can adjust is the window type $W(\omega)$. Essentially, these windows allow us to customize the ramp filter by varying the attenuation of high frequencies to achieve noise reduction in the final image.

FBP is widely adopted in various software packages due to its rapid reconstruction process. Nonetheless, it requires a large number of projections to mitigate streak artifacts, as illustrated in Figure 3.10. Additionally, it is less proficient at handling random noise introduced into the data, as illustrated in Figure 3.11 for the example of Poisson statistical noise. Consequently, iterative methods are frequently used to tackle these challenges.

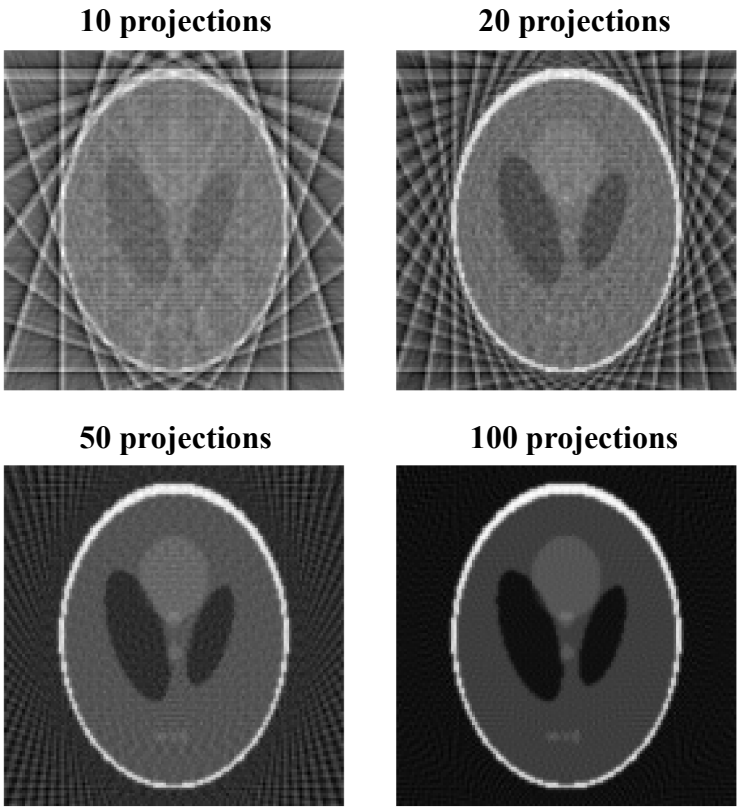

Figure 3.10: Streak artifacts caused by insufficient projections in the reconstructed phantom by FBP.

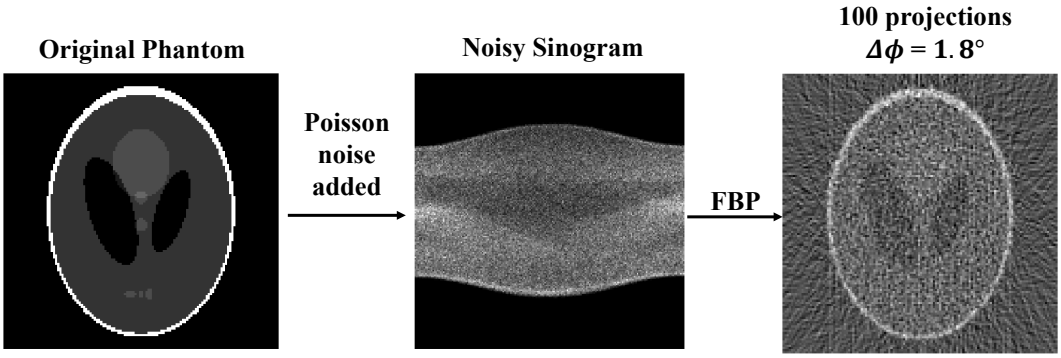

Figure 3.11: Reconstruction result using FBP when the sinogram is corrupted by Poisson noise.

3.4. Iterative methods

Iterative algorithms have gained much attention in X-ray tomography reconstruction. Unlike the analytical methods, which rely on an analytical expression for inverting the Radon transform, iterative reconstruction offers an alternative by addressing the problem through discretization, simplifying the reconstruction task into solving a set of unknown values from a set of equations (Bailey, 2014). In particular, the objective function is often constructed using the likelihood function, enabling the modeling of noise in the projection data, even in the low signal-to-noise ratio cases.

Iterative methods follow a sequential process to improve the quality of the reconstructed image as illustrated in Figure 3.12. Firstly, an initial image approximation is generated, typically consisting of pixels with uniform values. This approximation is then projected to obtain an estimated projection, which may deviate from the actual measurement. A quantifiable error is determined by comparing the projection calculated based on the estimated distribution, to the measured one. This error is then back-projected into the image space which leads to an updated estimation of the image. The updated image is then projected and compared with the measured projection in an iterative manner. As the iterations progress, the reconstructed image gradually converges toward a representation that best fits the sample.

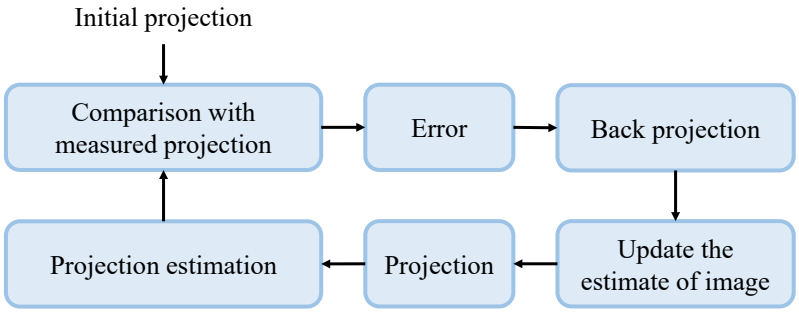

Figure 3.12: Flow chart of iterative reconstruction algorithms.

3.4.1. Algebraic reconstruction technique

The algebraic reconstruction technique (ART), also known as the Kaczmarz method, is named after the mathematician Stefan Kaczmarz (Kaczmarz, 1937). In this approach, the unknown object function $f(x, y)$ is discretized into pixels as $f(x, y) \approx \sum_{j=1}^{N} f_j \phi_j(x, y)$, with the pixel basis function ϕ defined as:

$$\phi_j(x, y) = \begin{cases} 1, & if\ (x, y) \in pixel\ j \\ 0, & otherwise \end{cases} \tag{3.24}$$

Using the discretized object function, the projection process can be mathematically expressed as:

$$p_i = \sum_{j=1}^{N} w_{ij} f_j \tag{3.25}$$

where w_{ij} represents the probability or contribution of detecting events from the pixel f_j at the i^{th} detection unit p_i (see fig. 3.13).

Also, it can be represented in matrix notation as follows:

$$\boldsymbol{p} = \boldsymbol{W}\boldsymbol{f} \tag{3.26}$$

where N is the number of pixels in the grid. M is the total number of measured data values. $\boldsymbol{W} = w_{ij} \in \mathbb{R}^{M \times N}$ denotes the projection matrix. $\boldsymbol{f} = (f_j) = [f_1, f_2, \cdots f_N]^T$ and $\boldsymbol{p} = (p_i) = [p_1, p_2, \cdots p_M]^T$ are one-dimensional vector representing respectively the pixel value in the grid and the projection value measured on each detection unit.

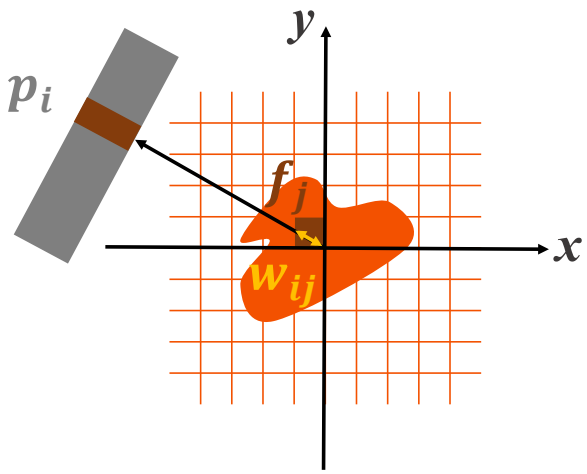

Figure 3.13: Illustration of the discretization of the projection process. The contribution w_{ij} of pixel j to the projection value p_i is illustrated as the length of intersection indicated in yellow.

Solving the Equation (3.26) directly for an accurate solution $\boldsymbol{f}$ is impractical because the presence of noise and discretization effects makes the system inconsistent and also the matrix would be too large to be numerally inversed (Bloch, 2010). Consequently, algebraic methods are typically employed to minimize the norm $\| \boldsymbol{W}\boldsymbol{f} - \boldsymbol{p} \|$.

The ART algorithm is a row-action algorithm, updating the image in a "ray-by-ray" manner. Its objective is to iteratively refine the estimated image to satisfy one "ray" equation (corresponding to one row of the equation $\boldsymbol{p} = \boldsymbol{W}\boldsymbol{f}$) during each update.

The search for the solution proceeds through an iterative process where the solution is iteratively projected onto one of the constraints. This approach ensures that at least one of the system's equations is satisfied at each step. Through the iterative process, the algorithm tries to converge progressively toward the intersection point, providing a final solution for the reconstruction.

In the example illustrated in Figure 3.14, the object only has 2 pixels $\boldsymbol{f} = [f_1, f_2]^T$ and each line represents an equation:

$$\begin{aligned} \boldsymbol{L_1} &: p_1 = w_{11}f_1 + w_{12}f_2 \\ \boldsymbol{L_2} &: p_2 = w_{21}f_1 + w_{22}f_2 \end{aligned} \tag{3.27}$$

The solution is their intersection point. $\boldsymbol{f}^{(0)}$ is the initial guess of the solution. The first step is to project this point onto line $\boldsymbol{L_1}$, and we obtain $\boldsymbol{f}^{(1)}$. Next, we project $\boldsymbol{f}^{(1)}$ onto line $\boldsymbol{L_2}$ to obtain $\boldsymbol{f}^{(0)} \cdots$ and so on: Project each point onto a line (which is one equation) once at a time. This iterative process continues until the algorithm converges to the solution of the system of equations. If the equations are not consistent, the algorithm will diverge.

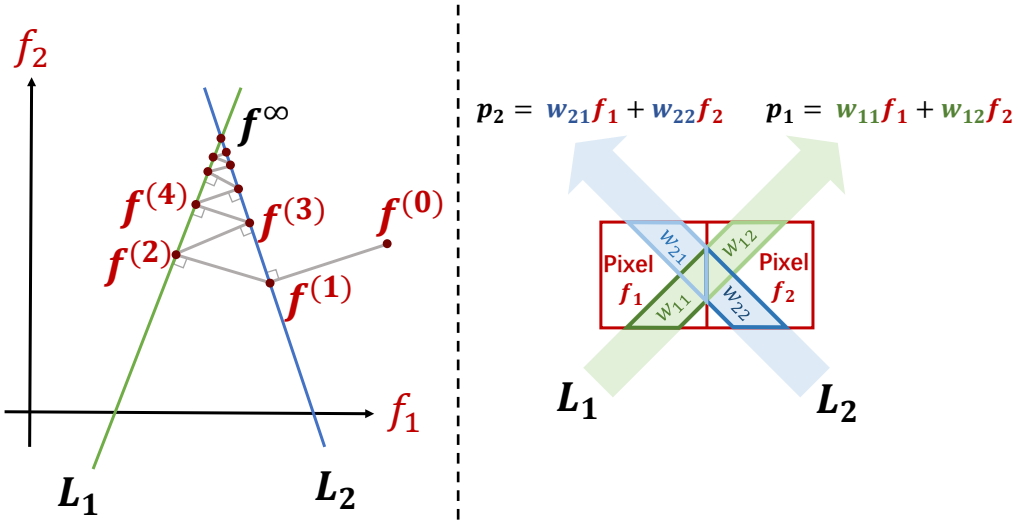

Figure 3.14: The ART algorithm procedure with 2 projection measurements. The intersection of two lines is the solution. In this example, the object only has 2 pixels $\boldsymbol{f} = [f_1, f_2]^T$.

The formula for updating the pixel values is:

$$f_j^{(k+1)} = f_j^{(k)} + w_{ij} \frac{p_i - \sum_{h=1}^{N} w_{ih} f_h^{(k)}}{\sum_{h=1}^{N} w_{ih}^2} \tag{3.28}$$

where $\boldsymbol{f}^{(k+1)}$ is the updated pixel value of the image, $\boldsymbol{f}^{(k)}$ is the current pixel value, p_i is defined in Equation (3.25) as $p_i = \sum_{j=1}^{N} w_{ij} f_j$.

For sparse angle tomography, the ART method can produce noisy results. To improve its performance, the variation method: Simultaneous Algebraic Reconstruction Technique (SART) has been introduced. In SART, all projection values within a single projection are collectively processed in a single iteration. (Andersen and Kak, 1984). The update formula for SART is then expressed as follows:

$$f_j^{(k+1)} = f_j^{(k)} + \frac{1}{\sum_{i \in I_\theta} w_{ij}} \sum_{i \in I_\theta} \frac{w_{ij}(p_i - \sum_{h=1}^{N} w_{ih} f_h^{(k)})}{\sum_{h=1}^{N} w_{ih}^2} \tag{3.29}$$

where I_θ represents the set including all indices corresponding to projection values within a single projection at angle θ (Russo, 2017).

SART can offer good performance with limited projection data. Figure 3.15 shows the evolution of the reconstruction result as a function of the number of iterations using the SART algorithm. The dataset used 20 projections spanning 180 °. In the beginning stages of iteration, the reconstruction might appear with streak artifacts (characteristic of sparse tomography). As the number of iterations increases, one can notice improvements in image clarity, resolution, and the gradual suppression of artifacts. In the final stages, while the image might appear clearer and more accurate, there is a risk of over-enhancement, which could introduce artifacts or amplify noise (not presented in this case). This emphasizes the importance of selecting an optimal iteration number to achieve a balance between image quality and noise/artifact suppression.

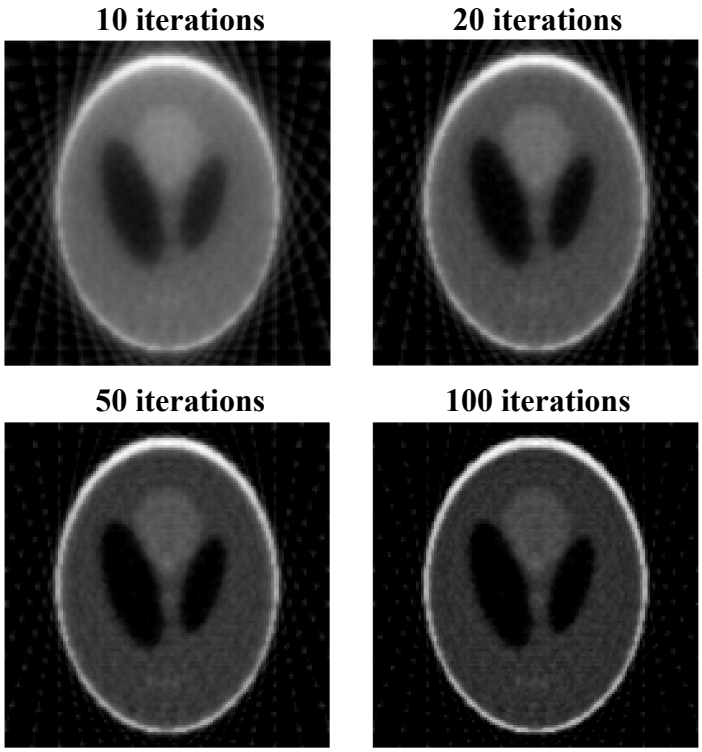

Figure 3.15: Reconstruction results obtained using the SART algorithm with different iterations. Results were obtained from a dataset consisting of 20 projections over 180°.

3.4.2. Maximum-likelihood expectation-maximization

When considering statistical modeling for image reconstruction, the Maximum Likelihood-Expectation Maximization (MLEM) algorithm emerges as a prominent and widely recognized method. It serves as the foundation for several image reconstruction algorithms that are more practical for real-world applications. For instance, the Ordered Subset Expectation Maximization (OSEM) method and other derived approaches have been developed to enhance the convergence speed and reconstruction quality.

The primary objective of the MLEM algorithm is to establish a statistical model for image reconstruction. The objective function in this algorithm can be defined as a likelihood function, representing the joint probability density function of Poisson random variables. The goal is to find a solution, i.e., the reconstructed image, that maximizes this likelihood function. Hence, the MLEM algorithm operates as a Maximum Likelihood (ML) algorithm.

In mathematical terms, when seeking to determine the maximum or minimum of a given function, such as the likelihood function in our case, it is common practice to take partial derivatives with respect to all unknowns (i.e., pixel or voxel values) These derivatives are then equated to zero to obtain the solutions for these unknowns. However, solving the Poisson likelihood function directly can be challenging. Therefore, we adopt a strategy, where we convert the problem of finding the extremum of a complex function into a series of optimizations for “simpler functions”. This is achieved by taking the conditional expectation value of the likelihood function, referred to as the “E-step”. This step

significantly simplifies the problem at hand. We then proceed with finding the maximum of the expected likelihood function to derive the corresponding image estimates. This stage is known as the "M-step", giving rise to the name "EM", representing the Expectation-Maximization algorithm.

By iteratively updating the reconstruction based on the expectation-maximization principle, the MLEM algorithm aims to converge toward an accurate estimation of the inverse Radon transform.

3.4.2.1. Mathematical derivation

The derivation of the MLEM algorithm for X-ray tomography is based on (Bruyant, 2002; Zaidi, 2005). Let $\bar{f}_j$ represent the mean number of events occurring in pixel j, and a_{ij} be the probabilities that denote bin i detecting an event from pixel j. The mean number of events $\bar{g}_i$ detected by bin i can be seen as the sum of the mean numbers of detected events from each pixel j:

$$\bar{g}_i = \sum_{j=1}^{m} a_{ij} \bar{f}_j \tag{3.30}$$

The MLEM algorithm assumes that the number of events detected by bin i is a Poisson variable. The probability (P) of detecting g_i events is:

$$P(g_i) = \frac{e^{-\bar{g}_i} \bar{g}_i^{g_i}}{g_i!} \tag{3.31}$$

Given that i is independent, the probability of measuring a vector g given an event map $\bar{f}$ is the product of probabilities for individual pixels. Hence, the likelihood function $L(\bar{f})$ is:

$$L(\bar{f}) = P(g|\bar{f}) = \prod_{i=1}^{n} P(g_i) = \prod_{i=1}^{n} \frac{e^{-\bar{g}_i} \bar{g}_i^{g_i}}{g_i!} \tag{3.32}$$

where $P(g_i)$ is the Poisson probability of detecting g_i events in bin i, as given by Equation (3.31). Maximizing $L(\bar{f})$ will yield the most likely distribution of events according to the measured projections. To simplify the problem, the logarithm of the likelihood is taken:

$$l(\bar{f}) = \ln\left(L(\bar{f})\right) = \sum_{i=1}^{n} (-\bar{g}_i + g_i \ln\left(\bar{g}_i\right) - \ln\left(g_i\right)!) \tag{3.33}$$

The maximization step identifies the image most likely to have the measured data by finding the maximum of the equation:

$$\frac{\partial l(\bar{f})}{\partial \bar{f}_j} = -\sum_{i=1}^{n} a_{ij} + \sum_{i=1}^{n} \frac{g_i}{\sum_{j=1}^{m} a_{ij} \bar{f}_j} a_{ij} = 0 \tag{3.34}$$

From which we can derive:

$$f_j^{next} = \frac{f_j^{current}}{\sum_{i=1}^{n} a_{ij}} \sum_{i=1}^{n} a_{ij} \frac{g_i}{\sum_{j=1}^{m} a_{ij} f_j^{current}} \tag{3.35}$$

In the Equation (3.35), the projection operation is represented as a summation over j, while the back projection is indicated as a summation over i. In the MLEM algorithm, the process begins by projecting the current estimated image via $\sum_{j=1}^{m} a_{ij} f_j^{current}$. This is compared with the actual image projection data by dividing each element of the vector g_i by $\sum_{j=1}^{m} a_{ij} f_j^{current}$. This correction ratio is then back-projected into the image space, which serves to update the current image estimate.

Moreover, the first summation $\sum_{i=1}^{n} a_{ij}$ in the expression serves as a normalization factor. This corresponds to the back projection of a constant value of 1 into the image domain. By dividing the correction factor by this normalization factor, the updated image is appropriately adjusted.

Essentially, the MLEM algorithm iteratively improves the image estimation (see Figure 3.16) by iteratively projecting and comparing the estimated image with the actual projection data, followed by back projecting the correction factor to update the image, while maintaining proper normalization.

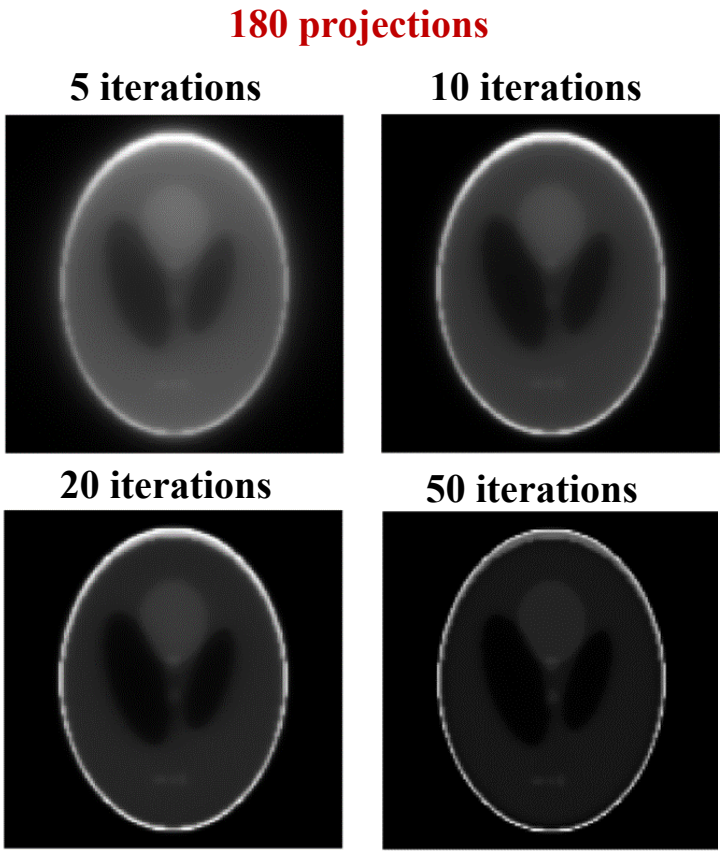

Figure 3.16: As the number of iterations increases in the MLEM algorithm, the quality of the reconstruction generally improves.

The MLEM algorithm presents several advantages over the FBP algorithm. One of the key advantages is its enhanced signal-to-noise ratio, particularly in empty regions outside of the reconstructed sample. This quality proves crucial when faced with challenges like insufficient angular sampling, as highlighted by its ability to reduce streak artifacts (see Figure 3.17).

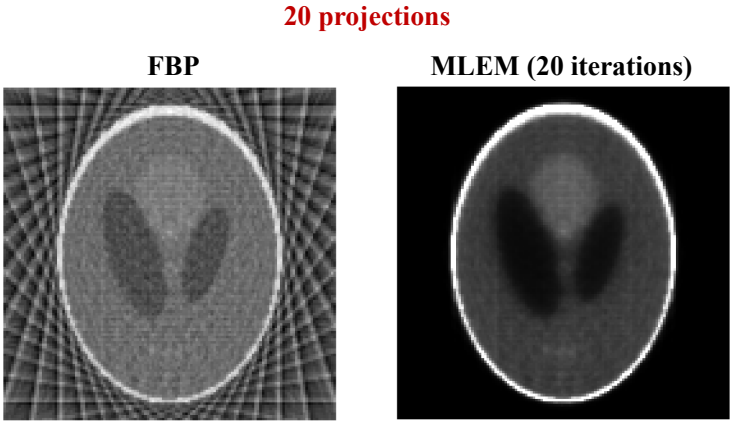

Figure 3.17: Reconstruction results obtained using the FBP algorithm and the MLEM algorithm with 20 iterations. These results were obtained from a dataset consisting of 20 projections over 180 °.

Furthermore, MLEM algorithm offers a distinct advantage in X-ray tomography. This advantage stems from the algorithm's explicit accounting for noise affecting the data (see Figure 3.18), as well as its inherent assumption that the data are positive. As a result of its multiplicative nature, MLEM consistently ensures that the results of reconstruction are non-negative. On the other hand, FBP does not explicitly exclude non-physical negative values, which can occur as part of the noise or reconstruction artifacts.

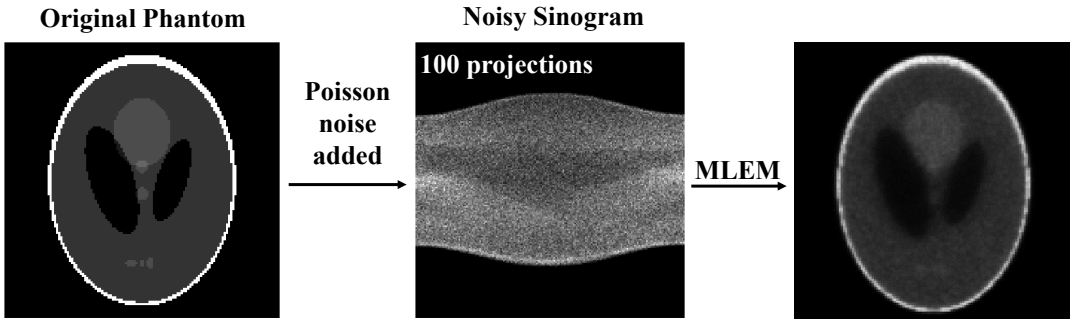

Figure 3.18: Reconstruction results using MLEM when the sinogram is corrupted by Poisson noise.

When we compare MLEM with ART and SART, each exhibits unique merits and drawbacks. While ART and SART are rooted in algebraic methods and can be more straightforward and are often easier to implement, their proficiency in handling noise, especially in sparse datasets or when the signal-to-noise ratio may not be as effective as MLEM. Moreover, to achieve non-negative results comparable to those of MLEM, ART and SART might sometimes demand modifications or the incorporation of additional constraints (Sanz et al., 2013).

For the sparse tomography in our workflow, detailed in Chapter 4, we chose MLEM for reconstruction. However, there are some challenges to consider when implementing MLEM. Its iterative nature implies that the reconstruction time scales with the number of iterations, making it computationally demanding compared to one-step algorithms like FBP.

Additionally, like many iterative tomographic reconstruction algorithms, MLEM poses the risk of noise amplification with increasing iterations. This can make it challenging to define appropriate termination criteria for the iterative process. Nevertheless, applying strategies such as defining optimal stopping points, utilizing filters, or integrating penalizing priors can effectively mitigate this challenge.

Figure 3.19 illustrates these differences between the reconstructions obtained using different iteration numbers in the MLEM algorithm. The MLEM reconstructions show improved signal-to-noise levels, indicating better noise suppression compared to the FBP reconstruction in Figure 3.19. The 20-iteration MLEM reconstruction has a slightly worse resolution. This implies that the MLEM algorithm, with a smaller number of iterations, may result in a loss of fine details or blurring in the reconstructed image.

The 100-iteration MLEM reconstruction has higher resolution, but it also comes with higher noise levels at the features in the phantom (edges, and internal elliptical features).

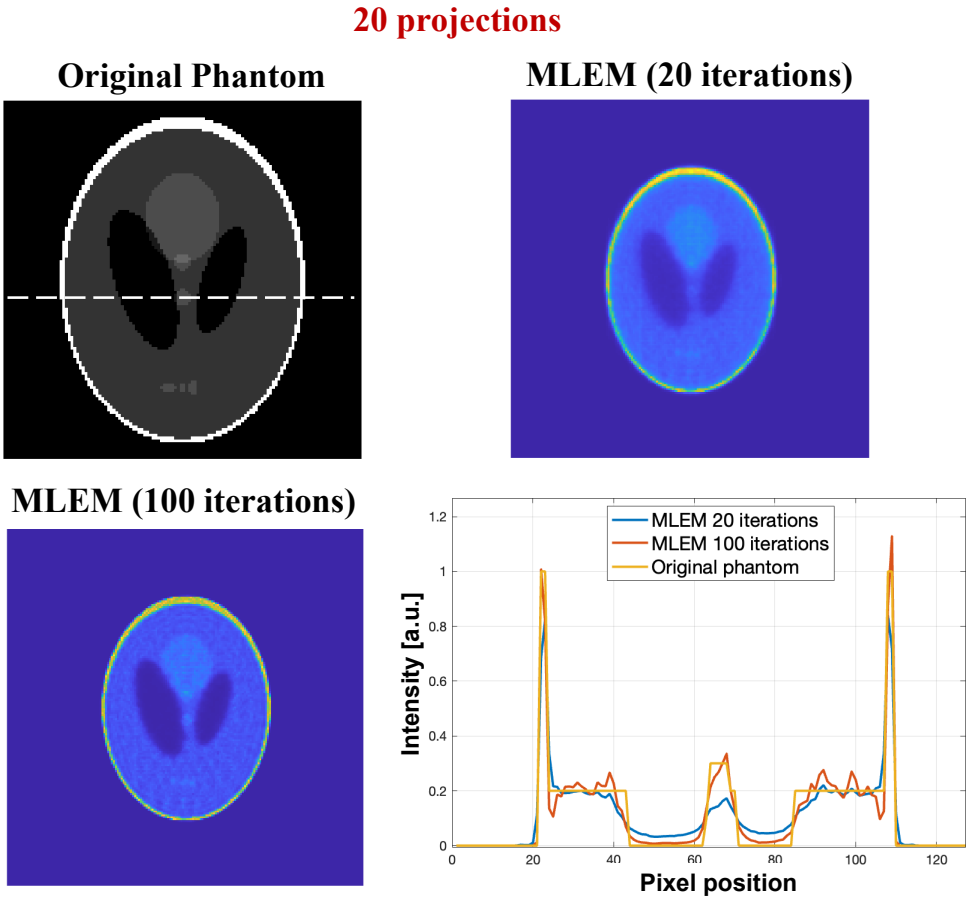

Figure 3.19: Reconstruction results obtained using the MLEM algorithm with 20 and 100 iterations. These results were obtained from a dataset consisting of 20 projections over 180 ° to simulate sparse tomography conditions. The line profiles along the dotted line in the original phantom are shown for results with different iteration numbers in MLEM.

These observations emphasize the trade-offs and characteristics of the MLEM algorithm in terms of noise suppression and resolution. The choice of the number of iterations in the MLEM algorithm should be carefully considered, taking into account the desired level of noise reduction, resolution, and the presence of artifacts in the reconstructed image.

3.5. Reconstruction artifacts

Another crucial aspect to consider when interpreting tomographic images is the presence of artifacts. These represent features that appear in the image but don't physically exist within the actual object. They can originate from various sources and strongly compromise the quality and accuracy of reconstructed images.

Several types of artifacts can occur, with the primary ones observed in the case study of this thesis being: ring artifacts (found in full-field tomography), errors from the rotation stage, missing wedge artifacts, and artifacts due to a limited number of projections.

3.5.1. Ring artifacts

Ring artifacts appear as concentric rings or circular patterns in the reconstructed image, as shown in Figure 3.20. In this thesis, these artifacts are specifically associated with the full-field tomography technique. They can emerge due to imperfections in the X-ray detector or irregularities in the data acquisition process. These artifacts can lead to distortions and inaccuracies in the reconstructed image, complicating subsequent data segmentation.

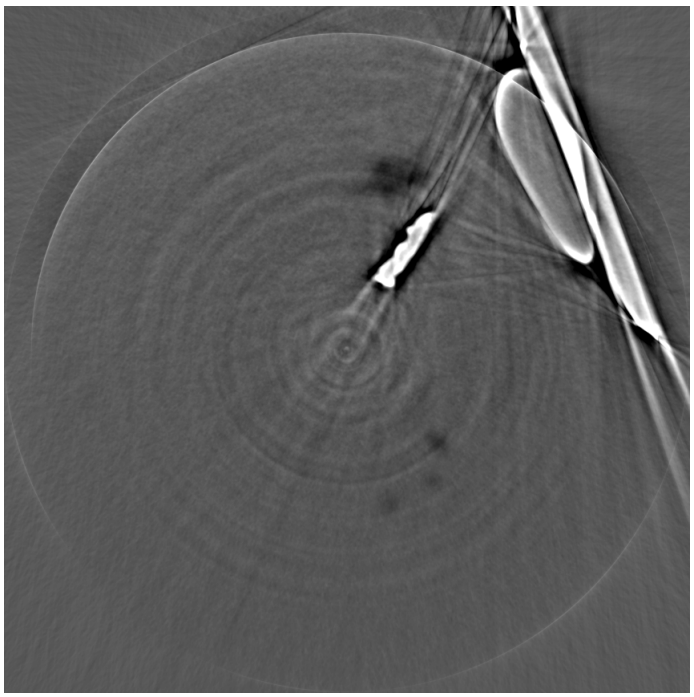

Figure 3.20: Ring artifacts present and superimposed on the reconstructed tomogram.

One way to mitigate ring artifacts is through flat-field correction, particularly relevant for full-field tomography. This method involves capturing images without the sample, either before or after the main data acquisition. These "flat-field" images capture irregularities such as the non-uniform sensitivity of the CCD camera pixels, the non-uniform response of the scintillator screen, and variations in the incident X-ray beam. However, even after applying this correction, some artifacts might persist, especially when camera elements exhibit nonlinear, intensity-dependent response functions or when the incident beam has time-dependent irregularities (Boin and Haibel, 2006).

Another method involves utilizing image processing techniques to identify and reduce the ring artifacts. Employing filtering and smoothing methods (Münch et al., 2009), these techniques target either the sinogram or the reconstructed image directly. With the application of these image processing techniques, the visibility of the ring artifacts can be substantially reduced or eliminated.

3.5.2. Rotation stage errors

Errors in the rotation stage's motion in tomography can impact the measurements, thereby reducing the quality of the reconstruction. The main sources of discrepancies between the actual and ideal positions over one revolution include axial error, radial error, and tilt error. These motion errors are presented in Figure 3.21.

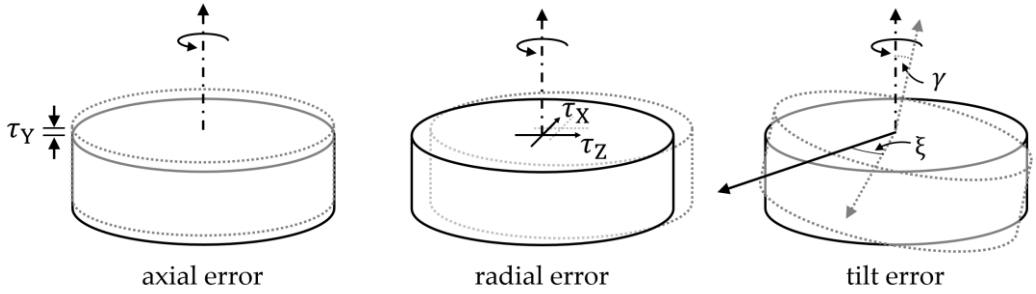

Figure 3.21: Rotation stage errors refer to unintentional deviations in the sample rotation stage's position. From left to right: axial error, radial error motions, and tilt error. Adapted from (Ferrucci et al., 2018).

The tilt error, also known as the "Wobble", refers to the tilt of the rotation axis compared to the ideal axis (see Figure 3.21 (right)). As the distance between the tilted axis and the ideal one increases with altitude, the wobble can quickly become the most significant source of error in submicronic tomography (tomography with a voxel size smaller than one micrometer). Figure 3.22 displays the artifacts caused by the wobble in a simulated image. Even with a shift of just $\pm$ 3 pixels from the ideal sinogram, the tilt error causes shape distortion in the reconstructed image, resulting in the inner structures blending and becoming unrecognizable.

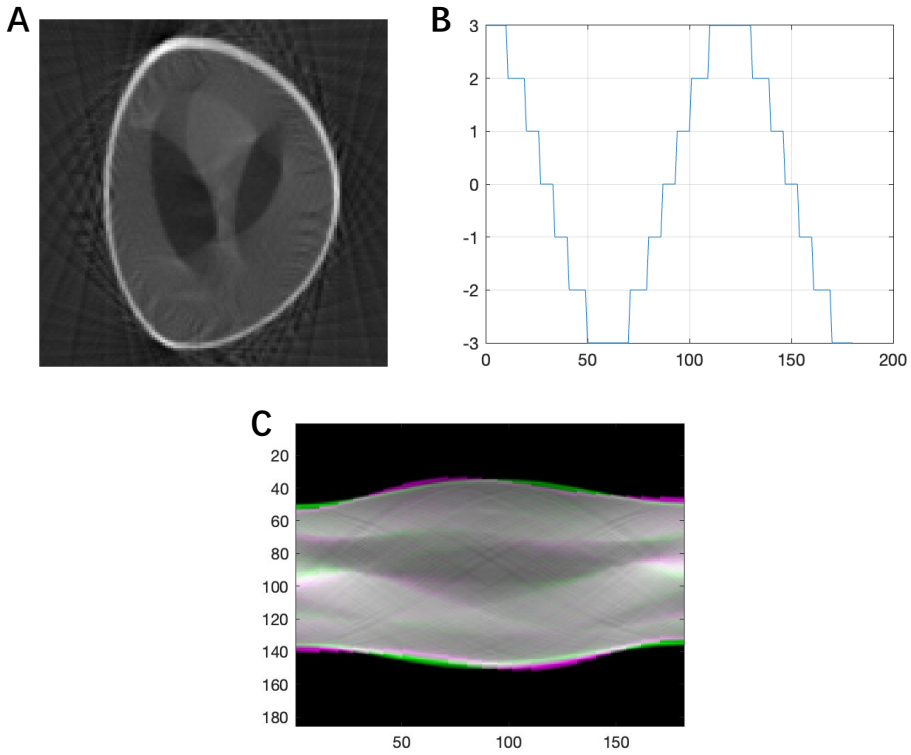

Figure 3.22: Illustration of the tilt error in the simulated phantom. **A**: Reconstruction result of the object influenced by the tilt axis error. **B**: Model of the tilt error represented by a cosine function relative to the rotation angle. **C**: Overlay of the ideal sinogram and sinogram impacted by the tilt error. Magenta and green areas highlight regions where the intensities differ.

3.5.3. Missing wedge artifacts

In X-ray tomography, "missing wedge" artifacts can occur in the reconstructed image due to practical limitations during the acquisition process, which might lead to certain regions or angles being inadequately sampled. Such as limitations on hardware conditions of the experimental set-up or the supporting membrane on which the sample is placed, making measurements at certain projections angles impossible. Based on analytical reconstruction theories, this incomplete sampling manifests as a "wedge-shaped" region in the Fourier space, where data is either missing or underrepresented.

These missing wedge artifacts appear as distortions or inaccuracies in the reconstructed image, particularly in areas corresponding to the unsampled data. Such artifacts can take various forms, such as streaking, elongation, ghost tails, or incomplete structural information (see Figure 3.23). As a result, there is risk of misinterpretation the data or inaccuracies in the sample analysis.

While enhancing data acquisition conditions can mitigate some of these issues, effectively addressing missing wedge artifacts necessitates advanced reconstruction techniques or correction methods during data processing. Approaches such as iterative reconstruction algorithms (MLEM, SART and also a Fourier-based iterative algorithm from (Pryor et al., 2017)), or the incorporation of prior knowledge using deep neural network (Pelt and Batenburg, 2013; Zhu et al., 2018), can help reduce the impact of these artifacts.

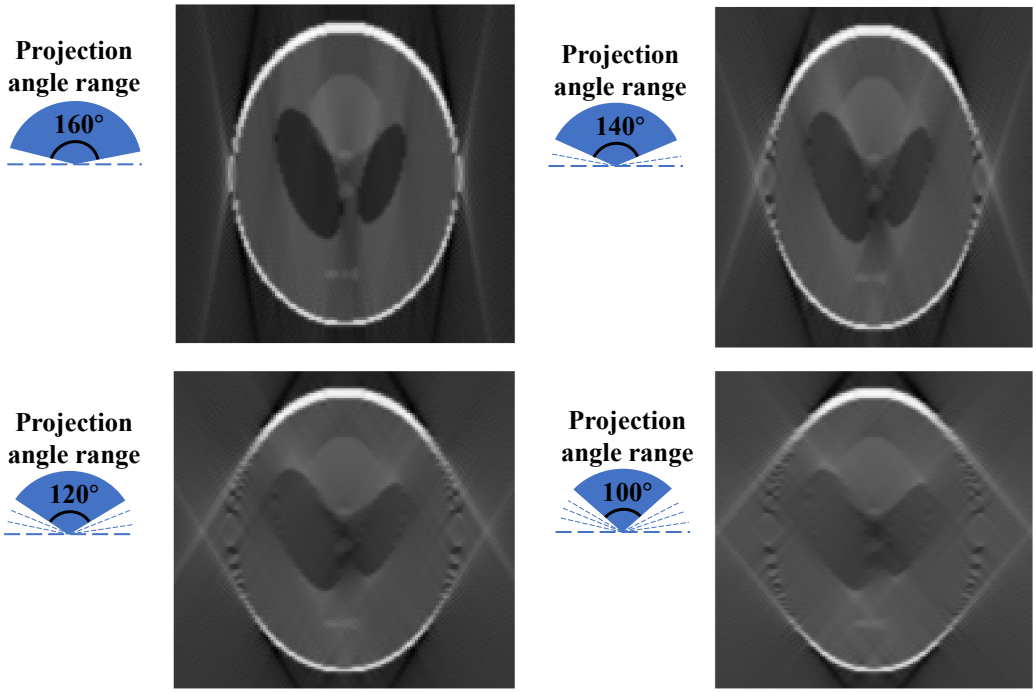

Figure 3.23: With the increase of the missing angle, the images reconstructed by the FBP algorithm have obvious missing wedge artifacts. The increasing area of missing wedge information introduces elongation and ghost-tail artifacts in the reconstructed images. The original internal elliptical structure is also distorted.

3.5.4. Limited numbers of projection artifact

During the data acquisition process, if the angular sampling of the X-ray projections is limited to a few projections or sparse in the whole sample rotation, particularly in certain regions or orientations, streak artifacts can arise (see Figure 3.24).

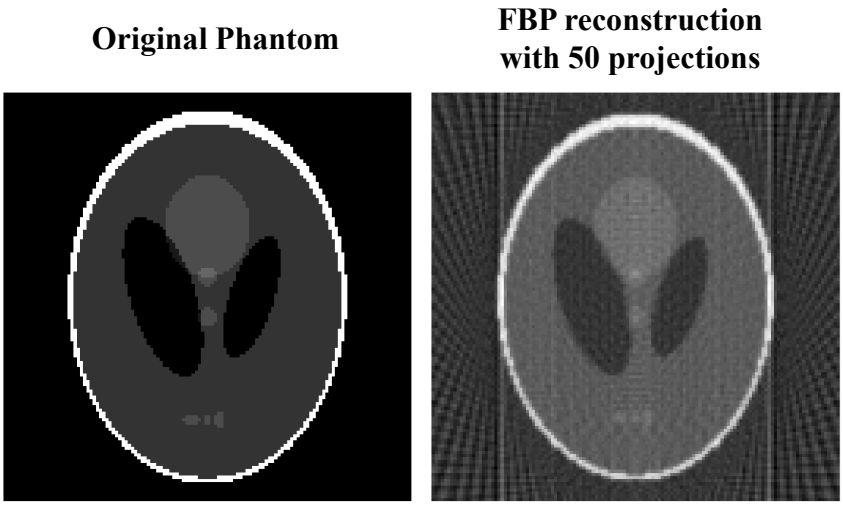

Figure 3.24: Illustration of the streak artifacts caused by limited angle projections.

This is because the missing projection data can result in incomplete information during the reconstruction process. Although increasing angular coverage is one of the most effective ways to reduce the artifacts, it is not always a good option for scanning X-ray tomography in practice due to the lengthy acquisition time per projection. There are still several strategies to reduce these artifacts:

(1). Regularization techniques: Various regularization methods can be employed to compensate for the limited angle data. These techniques impose constraints on the reconstruction process to promote smoothness and reduce artifacts. For example, Total Variation (TV) regularization encourages sparsity and piecewise constant solutions (Behrooz et al., 2012).

(2). Prior knowledge incorporation: Utilizing prior knowledge about the object being imaged can help alleviate limited angle artifacts. This can involve some structural information, such as known boundaries or interior domain constraints, in the reconstruction process (Bridges et al., 2020).

(3). Advanced reconstruction algorithms: Iterative algorithms like MLEM are commonly used in limited-angle cases. Their iterative nature allows for gradual improvement in image quality and can help mitigate artifacts. Recently, the development in some deep learning-based reconstructions like Convolutional neural networks (CNNs) can also be trained to directly learn the mapping between limited-angle projection data and the corresponding artifact-free reconstructions. By training the network on a large dataset of paired limited-angle projections and high-quality reconstructions, the network can learn to generalize and produce artifact-free images from limited-angle data (Buccino et al., 2023; Yang et al., 2018).

(4). Post-processing techniques: Additional post-processing steps can be applied to further reduce limited angle artifacts. These can include noise filtering, deconvolution, etc.

3.6. Conclusion

In this chapter, we introduced the principles of tomography and different tomography reconstruction algorithms. In addition, artifacts related to different situations are also discussed.

Analytical methods offer the advantages of computational efficiency and easy implementation. These methods rely on mathematical transformations and direct inversion techniques. Their ability to reconstruct images quickly makes them well-suited for applications that require real-time imaging or fast analysis. In addition, their straightforward implementation simplifies their integration with existing tomographic systems.

In more realistic biomedical imaging scenarios, where challenges like incomplete data or the use of a limited number of projection angles are common, iterative reconstruction methods demonstrate better performance when compared to conventional approaches. By iteratively refining the reconstructed image, the iterative methods can mitigate the effects of data imperfections and converge to a

more accurate representation of the imaged object. It's crucial to note that this improved performance often requires additional computational resources and longer processing times. Maximum Likelihood Expectation Maximization (MLEM), as one of the iterative methods, is well suited for scanning XRF tomography, especially when dealing with a limited number of projections (sparse tomography) and a low signal-to-noise ratio. This is especially advantageous when dealing with trace elements.

X-ray tomography reconstruction is susceptible to various artifacts, that arise from factors such as limited angles, rotation stage's motion, system imperfections, etc. Techniques such as advanced reconstruction algorithms, regularization, filtering, and hardware improvements can be employed to reduce or remove these artifacts.

Understanding the trade-offs associated with reconstruction algorithms is critical for us to make the decision depending on the specific requirements of the application, such as reconstruction speed, accuracy, noise robustness, or availability of a priori information.

References

A. H. Andersen and A. C. Kak. Simultaneous Algebraic Reconstruction Technique (SART): A superior implementation of the ART algorithm. *Ultrasonic Imaging*, 6 (1):81–94, Jan. 1984. ISSN 0161-7346. doi: 10.1016/0161-7346(84)90008-7. URL https://www.sciencedirect.com/science/article/pii/0161734684900087.

D. L. Bailey. *Nuclear medicine physics: a handbook for teachers and students*. International Atomic Energy Agency, Vienna, 2014. ISBN 978-92-0-143810-2. URL https://www.iaea.org/publications/10368/nuclear-medicine-physics.

J. Baruchel. *X-ray tomography in material science*. Hermes Science, Paris, 2000. ISBN 978-2-7462-0115-6.

A. Behrooz, H.-M. Zhou, A. A. Eftekhar, and A. Adibi. Total variation regularization for 3D reconstruction in fluorescence tomography: experimental phantom studies. *Appl. Opt., AO*, 51(34):8216–8227, Dec. 2012. ISSN 2155-3165. doi: 10.1364/AO.51.008216. URL https://opg.optica.org/ao/abstract.cfm?uri=ao-51-34-8216.

I. Bloch. Reconstruction d'images de tomographie. *École Nationale Supérieure des Télécommunications, département Traitement du Signal et des Images*, 2010.

M. Boin and A. Haibel. Compensation of ring artefacts in synchrotron tomographic images. *Opt. Express*, 14(25):12071–12075, Dec 2006. doi: 10.1364/OE.14.012071. URL https://opg.optica.org/oe/abstract.cfm?URI=oe-14-25-12071.

E. Bridges, G. Ambartsoumian, and L. Florescu. Improving interior tomography reconstruction based on prior knowledge. In *AIP Conference Proceedings*, volume 2302, Albena, Bulgaria, 2020. doi: 10.1063/5.0033674. URL https://pubs.aip.org/aip/acp/article/755032.

P. P. Bruyant. Analytic and iterative reconstruction algorithms in spect. *Journal of Nuclear Medicine*, 43(10):1343–1358, 2002. ISSN 0161-5505. URL https://jnm.snmjournals.org/content/43/10/1343.

F. Buccino, I. Aiazzi, A. Casto, B. Liu, M. C. Sbarra, G. Ziarelli, G. Banfi, and L. M. Vergani. The synergy of synchrotron imaging and convolutional neural networks towards the detection of human micro-scale bone architecture and damage. *Journal of the Mechanical Behavior of Biomedical Materials*, 137: 105576, Jan. 2023. ISSN 1751-6161. doi: 10.1016/j.jmbbm.2022.105576. URL https://www.sciencedirect.com/science/article/pii/S1751616122004817.

M. Ferrucci, E. Ametova, G. Probst, T. Craeghs, and W. Dewulf. Sensitivity of CT dimensional measurements to rotation stage errors. In *Proceedings of the 8th Conference on Industrial Computed Tomography*, 2018.

J. Fessler. Analytical tomographic image reconstruction methods. In *Image reconstruction: Algorithms and analysis*. Book draft, accessed 23 Sept. 2023. URL https://web.eecs.umich.edu/~fessler/book/c-tomo.pdf.

L. W. Goldman. Principles of CT and CT Technology. *Journal of Nuclear Medicine Technology*, 35(3):115–128, Sept. 2007. ISSN 0091-4916. doi: 10.2967/jnmt.107.042978. URL http://tech.snmjournals.org/cgi/doi/10.2967/jnmt.107.042978.

S. Kaczmarz. Angenaherte auflosung von systemen linearer gleichungenti bulletin international de lacademie polonaise des sciences et des lettres. *Séries A*, 60: 596–599, 1937.

A. C. Kak and M. Slaney. *Principles of Computerized Tomographic Imaging*. Society for Industrial and Applied Mathematics, 2001. doi: 10.1137/1.9780898719277. URL https://epubs.siam.org/doi/abs/10.1137/1.9780898719277.

B. Münch, P. Trtik, F. Marone, and M. Stampanoni. Stripe and ring artifact removal with combined wavelet - fourier filtering. *Opt. Express*, 17(10):8567–8591, May 2009. doi: 10.1364/OE.17.008567. URL https://opg.optica.org/oe/abstract.cfm?URI=oe-17-10-8567.

D. M. Pelt and K. J. Batenburg. Fast tomographic reconstruction from limited data using artificial neural networks. *IEEE Trans Image Process*, 22(12):5238–5251, Dec. 2013. ISSN 1941-0042. doi: 10.1109/TIP.2013.2283142.

A. Pryor, Y. Yang, A. Rana, M. Gallagher-Jones, J. Zhou, Y. H. Lo, G. Melinte, W. Chiu, J. A. Rodriguez, and J. Miao. GENFIRE: A generalized Fourier iterative reconstruction algorithm for high-resolution 3D imaging. *Sci Rep*, 7(1):10409, Sept. 2017. ISSN 2045-2322. doi: 10.1038/s41598-017-09847-1. URL https://www.nature.com/articles/s41598-017-09847-1.

P. Russo. *Handbook of X-ray imaging: physics and technology*. CRC Press, Boca Raton, 2017. ISBN 978-1-4987-4152-1. doi: https://doi.org/10.1201/9781351228251.

J. Sanz, E. Hinkle, and A. Jain. *Radon and Projection Transform-Based Computer Vision: Algorithms, A Pipeline Architecture, and Industrial Applications*, volume 16 of *Springer Series in Information Sciences*. Springer Berlin Heidelberg, 2013. ISBN 9783642730122.

K. Srinivasan, M. Mohammadi, and J. Shepherd. Investigation of effect of reconstruction filters on cone-beam computed tomography image quality. *Australas Phys Eng Sci Med*, 37(3):607–614, Sept. 2014. ISSN 1879-5447. doi: 10.1007/s13246-014-0291-8. URL https://doi.org/10.1007/s13246-014-0291-8.

A. F. Velo, J. F. Martins, A. S. Oliveira, D. V. Carvalho, F. S. Faria, M. M. Hamada, and C. H. Mesquita. Filter assessment applied to analytical reconstruction for industrial third-generation tomography. In *2015 International Nuclear Atlantic Conference - INAC 2015*, Brazil, 2015. ISBN 978-85-99141-06-9. URL http://inis.iaea.org/search/search.aspx?orig_q=RN:47032105.

X. Yang, V. De Andrade, W. Scullin, E. L. Dyer, N. Kasthuri, F. De Carlo, and D. Gürsoy. Low-dose x-ray tomography through a deep convolutional neural network. *Sci Rep*, 8(1):2575, Feb. 2018. ISSN 2045-2322. doi: 10.1038/s41598-018-19426-7. URL https://www.nature.com/articles/s41598-018-19426-7.

H. Zaidi. *Quantum analysis in nuclear medicine imaging*. Springer, New York, NY, 2005. ISBN 9780387254449.

B. Zhu, J. Z. Liu, S. F. Cauley, B. R. Rosen, and M. S. Rosen. Image reconstruction by domain-transform manifold learning. *Nature*, 555(7697):487–492, Mar. 2018. ISSN 1476-4687. doi: 10.1038/nature25988.

CHAPTER 4

METHODOLOGICAL DEVELOPMENTS AND IMPLEMENTATION OF THE WORKFLOW

The chapter is based on the published paper: Guo, R., Somogyi, A., Bazin, D. *et al*. Towards routine 3D characterization of intact mesoscale samples by multi-scale and multimodal scanning X-ray tomography. *Sci Rep* **12**, 16924 (2022).

This chapter outlines the workflow developed and implemented at the NANOSCOPIUM beamline of the SOLEIL synchrotron. The workflow covers the complete process, from data acquisition to data processing and analysis, detailing each step involved in the experiment. Two types of *Arabidopsis thaliana* seeds serve as demonstration samples to showcase the workflow's performance. Notably, the proposed workflow is both robust and efficient, enabling real-time data analysis during the beamtime period.

4.1. Introduction

Scanning XRF and multimodal tomography techniques are highly effective for studying mesoscale samples, offering a comprehensive understanding of their internal features by reconstructing the projection images from various angles. These methods provide clear insights into the spatial distribution of elemental constituents, enabling analysis of sample morphology, crystalline structure, chemical speciation, and more. At NANOSCOPIUM, all user projects apply for XRF multi-scale imaging, often supplemented with additional modalities such as absorption- or phase-contrast imaging/tomography, XANES, or XRD, to address specific scientific challenges. In this methodology section, we have selected scanning XRF imaging and the implemented scanning XRF tomography method during this PhD work to demonstrate our workflow.

Scanning XRF tomography is a powerful technique used to investigate the elemental composition and distribution within a sample. It involves acquiring projections of X-ray fluorescence signals emitted by the sample from different angles. Utilizing a focused X-ray beam to irradiate the sample, this technique permits the analysis of spectra from individual pixels on each projection.

Processing the acquired projection data enables the creation of the reconstruction of a three-dimensional representation of the sample. This further facilitates the generation of elemental maps and concentration profiles, providing valuable insights into the spatial distribution of elements and their relative quantities within the material.

Scanning XRF tomography has diverse applications in fields such as materials science, geology, biology, archaeology, and environmental studies, offering a non-destructive means of studying the composition and structure of various materials. However, its implementation in synchrotron beamlines is limited, primarily due to the extended acquisition time it demands. This remains a significant obstacle to its comprehensive utilization.

While enhancements have been made in essential components like XRF detectors–resulting in expanded active area ranges, higher count rates, and consistent energy resolution regardless of input photon counts–these improvements may not be a solution for reducing lengthy acquisition time. The complexity of the samples being analyzed often necessitates additional methodological approaches to get high-resolution images.

To illustrate the challenge, let us consider a practical example. We'll assume that we need to reconstruct the 3D tomogram of a sample with a scanning area of approximately $300\,\mu m \times 300\,\mu m$, utilizing a pixel size of $2\,\mu m$. This implies that we will need to scan a total of 22,500 points, and for each of these points, a dwell time of 20 ms is estimated. Consequently, the completion time for each projection would be around 7.5 minutes. To ensure compliance with the Nyquist sampling condition (see Section 3.1.3), a fundamental requirement for traditional algorithms like Filtered Back Projection (FBP), we need to have more than 470 projections over a 360° rotation. This is crucial to prevent streak artifacts from appearing in the reconstructed image. However, based on these parameters, it becomes apparent that the acquisition time would exceed 60 hours.

In scanning XRF tomography, several challenges persist, one of which is the timely delivery of results to users. The processing and analysis of large volumes of multidimensional experimental data can often take up a large part of the available beamtime. This delay can inhibit users from making informed decisions in a timely manner, such as identifying the next areas for scanning based on the ongoing results. Consequently, there is a pressing need for smart and efficient data processing methods that can deliver results to users promptly, enabling them to adapt their experimental strategies on-the-fly during the beamtime session.

Another crucial aspect of scanning XRF tomography is the need to make decisions regarding experimental strategies while on-site at the beamline. Different users have unique objectives for their studies, with varying priorities in terms of spatial resolution, or elemental identification within the 3D volume. This underscores the necessity for a flexible experimental approach that can address the specific research questions posed by individual users.

All the aforementioned challenges highlight the need for a fast, robust, and flexible workflow in scanning XRF tomography (see Figure 4.1). This workflow optimizes the data processing and analysis stages, enabling users to obtain results promptly. Moreover, it provides the necessary flexibility to adapt experimental strategies in real-time during beamtime, allowing users to make informed decisions and gain valuable insights from their samples in a more efficient manner. Eventually, this enhanced workflow contributes to the broader advancement and widespread application of scanning XRF tomography in various scientific disciplines.

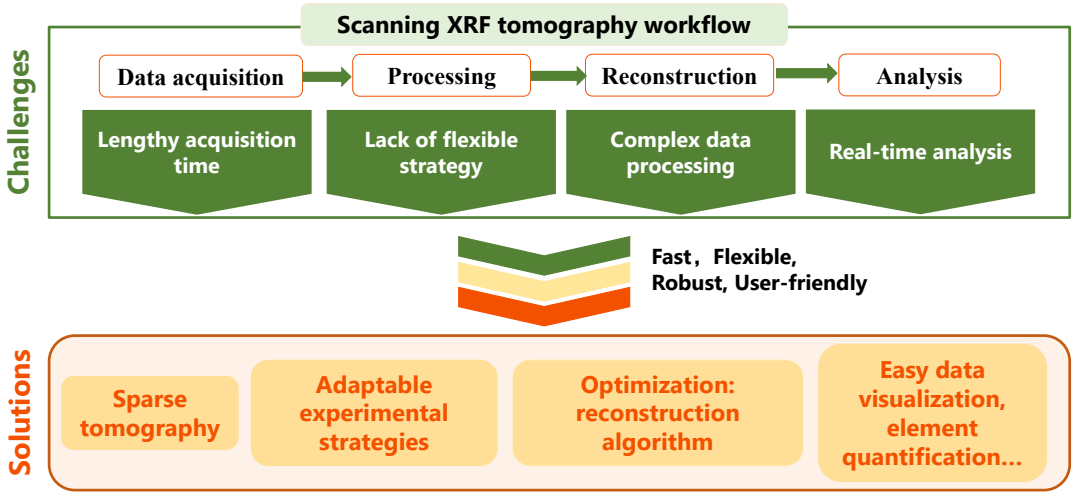

Figure 4.1: Challenges in scanning XRF tomography and proposed solutions. By integrating these proposed solutions into a coherent workflow, users can effectively overcome the challenges, making the technique more accessible and efficient for scientific applications.

4.2. Description of developed and implemented workflow on NANOSCOPIUM

In this section, we introduce the developed and implemented workflow for scanning multi-length scale XRF-tomography and complementary modalities at the NANOSCOPIUM beamline. The implementation of quantitative XRF sparse tomography in the workflow constitutes a significant component of the PhD work. To demonstrate the performances of the workflow, *Arabidopsis thaliana* seeds–provided by a collaborator of NANOSCOPIUM, Marie-Pierre ISAURE, from IPREM, Pau–were used as demonstration samples.

The workflow, as illustrated in Figure 4.2, begins with sample mounting and alignment to guarantee accurate positioning of the sample within the imaging setup. This step is essential for achieving reliable and high-quality imaging data. The next step involves the acquisition of sparse tomographic data of the entire sample. This preliminary scan offers a comprehensive overview, facilitating the identification of regions of interest for further investigation. The acquired data is then reconstructed in medium-resolution tomograms, serving as a basis for subsequent high-resolution measurements.

A strategy is developed for the high-resolution measurements, based on the information obtained from the medium-resolution results. This strategy allows users to focus their efforts on specific regions or features of interest, thereby optimizing the efficiency of data collection. This high-resolution measurement can be 2D projection imaging, 2D single slice tomography, local scanning 3D tomography, or any combination of these. A careful balance needs to be struck between acquisition time, spatial resolution, and the number of samples to be investigated. Users must make a reasonable trade-off to optimize these factors.

Following a high-resolution experiment, an approximation of the achievable spatial resolution for different projection numbers can be obtained using Fourier ring correlation (FRC) calculations, as described in Section 4.2.5.2. This analysis deepens our understanding of the expected spatial resolution in sparse tomography by examining multiple datasets. It allows us to assess whether the achieved resolution aligns with the specific requirements.

If the initial sparse tomography results do not meet the user's expectations for resolution, a second sparse tomography measurement can be performed. In this case, the angular offset is adjusted to half the angular step employed in the first sparse tomography experiment. The second sparse tomography, with the same number of projections as the first, effectively doubles the total number of projections and improves the spatial resolution accordingly. This approach provides users with the flexibility to fine-tune spatial resolution in accordance with their specific research goals.

As illustrated in Figure 4.2, all these imaging modalities can be reconstructed semi-automatically on-site during the beamtime, using predefined and pre-parameterized reconstruction algorithms. This enables users, including those unfamiliar with X-ray imaging and tomography, to effectively guide their experiments and refine scientific objectives based on real-time results obtained on-site.

Moreover, the reconstructed tomograms are stored in the HDF5 data format, which is fully interoperable with widely used cross-platform freeware and open-source data analysis tools. Well-known tools such as PyMca for XRF data processing (Solé et al., 2007), Fiji (Schindelin et al., 2012), and Chimera (Pettersen et al., 2004) for imaging/tomography data visualization can be seamlessly used with the reconstructed data. The use of the HDF5 simplifies data management with the best-adapted software for further processing both on-site and post-experiment, such as extracting mean XRF spectra, quantification, and combining different imaging modalities. This approach also broadens the scope for multivariate statistical analysis such as Principal Component Analysis (PCA) and Cluster Analysis. These analyses can be performed straightforwardly on any identified 2D features from the projection images or the reconstructed 3D tomograms, facilitating comprehensive data exploration and interpretation.

Although scanning XRF tomography has been chosen as the primary focus to illustrate the developed workflow during this PhD work, it is worth mentioning that the workflow can be flexibly adapted and applied to various other imaging and tomographic modalities. This multimodal approach enables a comprehensive characterization of the sample, thereby facilitating a deeper understanding of its composition, structure, and elemental distribution.

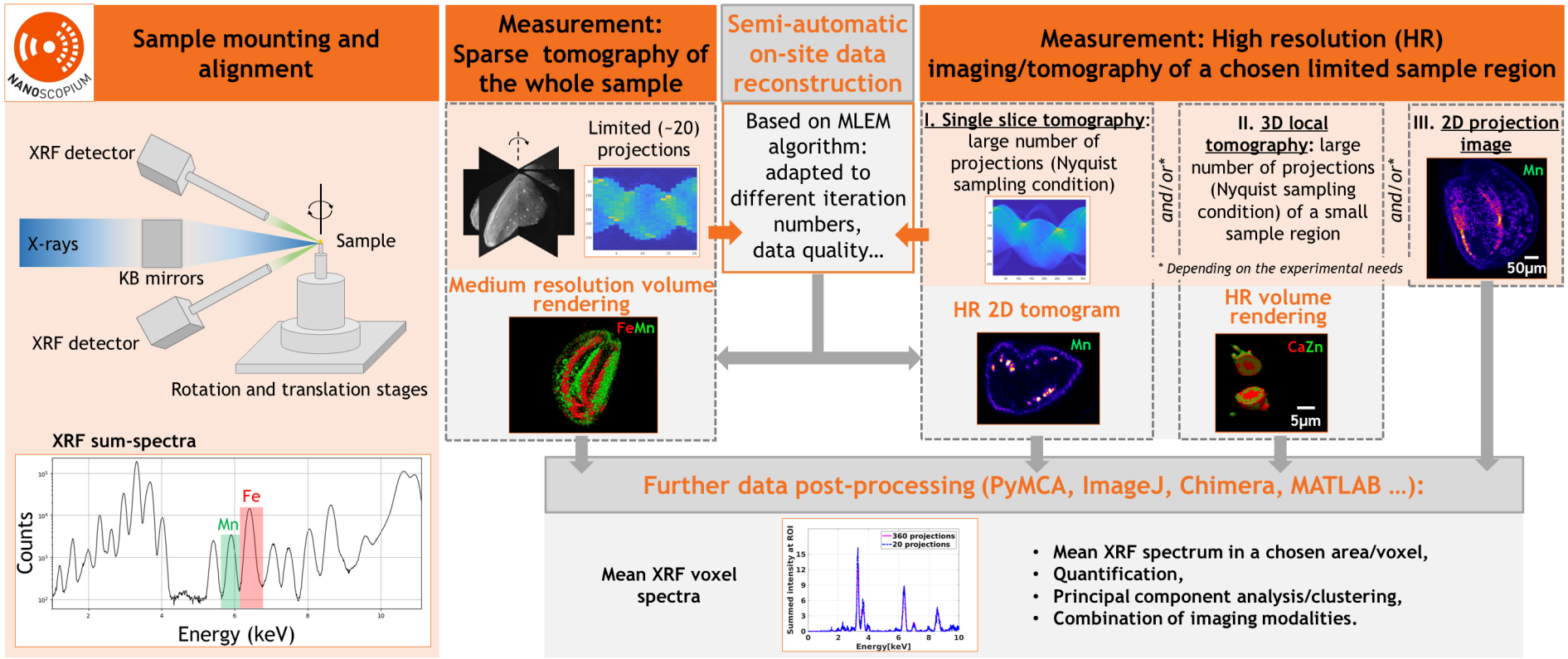

Figure 4.2: Multi-scale and multimodal scanning imaging and tomography workflow developed and implemented at NANOSCOPIUM (Guo et al., 2022).

4.2.1. Data acquisition

4.2.1.1. Experimental set-up

The experiments were conducted at the CX3 station at the NANOSCOPIUM beamline of synchrotron SOLEIL, where KB mirrors are used for effective beam focusing. Prior to scanning, a microscope is temporarily placed to visually assess the sample and align it precisely on the focal plane of the KB mirrors, defining the region of interest (see Figure 4.3). XRF signals are recorded by two energy-dispersive detectors situated at a 120 ° angle to the beam, and incident and transmitted beams are monitored using Si diodes.

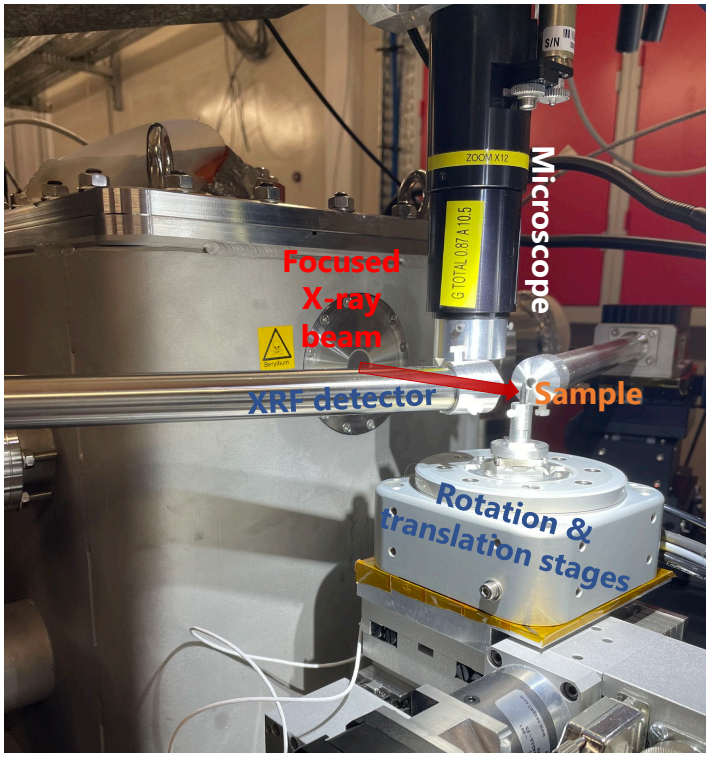

Figure 4.3: Experimental set-up for XRF tomography experiment.

To generate the angular projections required for tomographic analysis, we employed an RT100-type rotation stage with controlled settings, operated through a dedicated control panel. This setup is integrated into the Flyscan architecture for efficient, continuous data collection. The rotation stage exhibits minimal wobble, ensuring high-precision measurements and is complemented by two-axis translation stages for additional sample alignment with the rotation axis, as detailed in the following section.

4.2.1.2. Sample alignment

Alignment of the sample with rotation stage

Indeed, the rotation axis is pre-positioned at the focal plane of the KB mirror by using a transversal translation stage positioned under the granite. For precise alignment, it is crucial to align the sample axis with the rotation stage's axis. This involves both transversal and longitudinal adjustments using two perpendicular translation stages (Tx_rotation and Ts_rotation) situated under the sample.

The procedure begins with the alignment of the sample with the rotation axis of the rotation stage. The sample is rotated to a position where Tx_rotation is aligned with the transversal plane relative to the beam, and this position is marked. It is then rotated 180 ° and marked again. The sample is then carefully repositioned by using Tx_rotation at the midpoint between these two marked positions. A similar procedure is followed with Ts_rotation after rotating the sample by 90 °. We are in the process of developing an automated solution to expedite this sequence and enhance its accuracy.

Alignment of sample with beam

Following the alignment with the rotation stage, the subsequent step is to designate the suitable Region of Interest (ROI) for all the projections measured during the sparse tomography acquisition.

Since the image collected by the microscope (also shown in Figure 4.3) is pre-calibrated by the beamline team, the ROI coordinates can be directly input into the FLYSCAN control panel (see Figure 4.4). Within this control panel, users can specify the ROI coordinates, pixel size, angular steps, and integration time. A key distinction between 3D tomography (Figure 4.4-A) and high-resolution single-slice tomography (Figure 4.4-B) lies in the additional definition of the dimension along the z-axis.

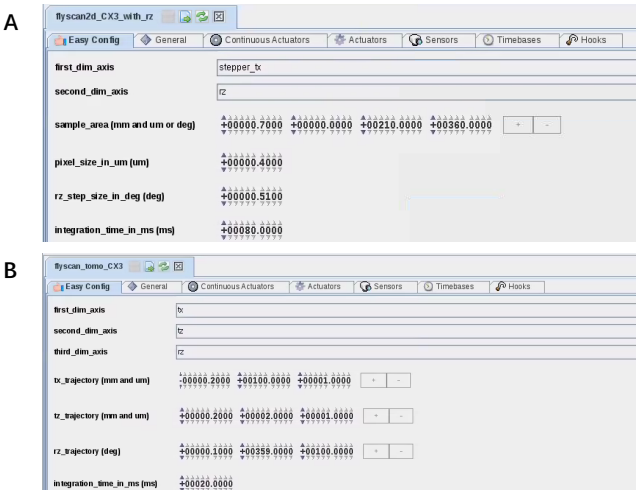

Figure 4.4: FLYSCAN control panel for scanning tomography experiments, featuring settings for 3D tomography (**A**) and high-resolution single-slice tomography (**B**).

4.2.1.3. Projection number of tomography

In the workflow, sparse tomography serves as the initial experiment. We have chosen a configuration of 20 projections at 18 ° intervals covering a total 360 ° rotation by default. These scanning parameters are proposed as the default settings for sparse tomography in our workflow because, based on our experience with multiple samples and imaging modalities, they have been found to be the best-balanced parameters for almost all experimental conditions. Most XRF tomography processes will typically require no more than one shift (1 shift = 8 hours), allowing for ample time to conduct high-resolution measurements on various samples during the remaining 14 shifts of beamtime.

For high-resolution slice tomography, the selection of the projection number for the analytical reconstruction methods follows the Nyquist sampling condition to ensure the preservation of spatial resolution along the x-axis in the reconstructed tomograms (see Figure 4.5). The projection number over 180 ° n_{proj} satisfying Nyquist sampling condition is defined as:

$$n_{proj} = \frac{\pi N}{2} \tag{4.1}$$

with N the pixel number along the scanning direction. For XRF tomography, the number of projections needs to be doubled because the self-absorption depth of the element being measured varies at two angles that differ by π. This consideration is crucial for achieving accurate elemental mapping. As a point of reference, the estimated spatial resolution for a configuration with 20 projections is around 10 µm.

4.2.2. Data processing

4.2.2.1. Data preprocessing

The elements present in the investigated samples are identified by analyzing the sum XRF spectra obtained from all angular projections. PyMca software is used for fitting the sum spectra, enabling the identification of elements within the sample. Subsequently, elemental distribution maps and sinograms are extracted from the raw dataset by integrating spectral regions of interest corresponding to the detected elements. To obtain sample absorption maps and sinograms, the ratio of transmitted and incident beam intensities was calculated at each pixel.

4.2.2.2. Data alignment

A crucial processing step is data alignment before the reconstruction. This contains two different steps for the tomography dataset: the correction for positions, which is the common one, and the correction for the measured sinogram, which is specific to the tomography dataset due to its volume characteristic.

(1). Position correction: This follows the same procedure as explained in Section 2.2.3.3.

(2). Sinogram correction: In order to ensure precise alignment of the center-of-rotation, an essential step is the alignment of the sinogram along the x-axis (see Figure 4.5-C). The objective of this step is to correct the shift between the rotation axis and the horizontal symmetry axis (aligned with the angle axis) of the sinogram image. Failure to address this shift can lead to undesirable artifacts, which be observed as crescent or round-shaped blurs and can obscure the sample's microstructural details (see Figure 4.5 for the uncorrected result).

To accomplish this alignment, we employ a correction algorithm described by (Azevedo et al., 1990). This algorithm is based on the relationship between the center of mass of a sample and the center of mass of its projections. Custom MATLAB code is utilized to execute the necessary sinogram shifts, thereby ensuring accurate alignment of the center of rotation.

To achieve precise sinogram correction of XRF datasets, we employ the signal with the highest signal-to-noise ratio such as the sum-spectra signal as a reliable reference. The correction factor identified using the sum-spectra signal is then automatically applied to the remaining XRF datasets.

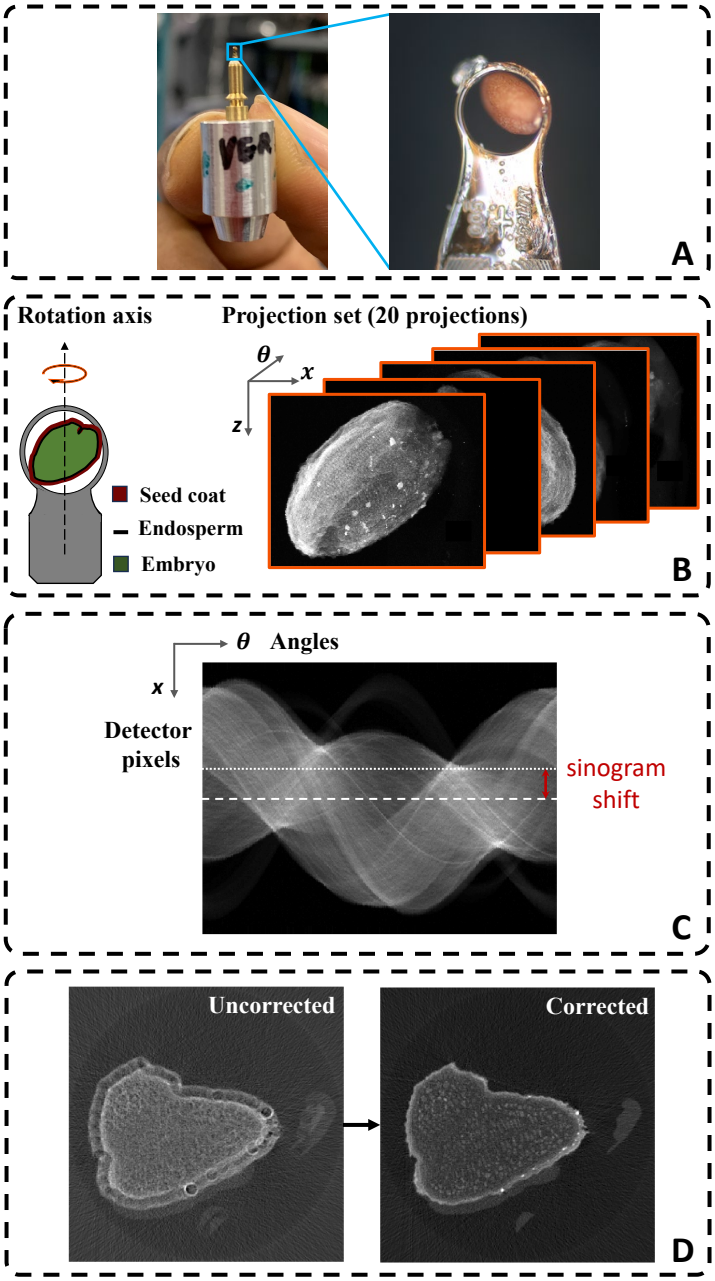

Figure 4.5: Sample Sinogram Alignment. **A**: The sample is fixed on a loop mounted in a pin (not shown here) for a 360° rotation data acquisition. **B**: In a mature *Arabidopsis* seed sample, the embryo is enveloped by the endosperm, which is further protected by the surrounding seed coat, and this entire structure is what is being imaged. The sample is then rotated to collect the necessary projection data for subsequent analysis and visualization. **C**: The alignment process focuses on aligning the sinogram on the x-axis. **D**: The impact of misalignment of the sum-spectra sinogram with the center line, comparing the results reconstructed by FBP before and after correction. The reconstruction of the corrected sinogram presents a clear inner structure of the seed.

The reconstructed volumetric data, exported as 16-bit z-stacks from MATLAB, are further analyzed using ImageJ and visualized in Chimera for three-dimensional volume rendering. The overall data processing is performed on

a workstation equipped with an Intel® Xeon® Processor E5-2630 v3 operating at 2.40 GHz, featuring 32 CPUs and 125.8 GB of system RAM. This computational setup provided the necessary resources for efficient data analysis and visualization.

4.2.3. Tomographic reconstruction

In this section, we provide a brief recapitulation of the two reconstruction algorithms employed in the workflow: Filtered Back Projection (FBP) and Maximum Likelihood Expectation Maximization (MLEM).

The utilization of these two algorithms is motivated by the objectives of simplifying the reconstruction process and enhancing user-friendliness.

As these algorithms are introduced in detail in Chapter 3, here we aim to outline their functions within the workflow and highlight their respective characteristics and limitations.

The FBP algorithm is under the category of analytical methods and is widely employed for routine tomographic dataset reconstruction. It offers simplicity and speed, making it the most commonly used method. FBP exploits fast Fourier transforms and does not require extensive parameter tuning. However, its robustness is compromised when dealing with sparse, low-contrast, or noisy measurements (Kazantsev et al., 2017; Bergamaschi et al., 2016), which are frequently encountered in XRF tomography. Consequently, it is implemented for high-resolution imaging and single-slice tomography reconstruction in the workflow when the Nyquist condition is satisfied.

MLEM, an iterative algorithm, plays an important role in the workflow due to its ability to explicitly account for noise in the data and enforce pixel positivity in the estimated image (Dempster et al., 1977). Initially developed for positron emission tomography (PET) data analysis, MLEM assumes a Poisson distribution of acquired photon statistics, making it more tolerant to noise compared to FBP (Bourassa et al., 2016). It is categorized under majorization-minimization algorithms (Hunter and Lange, 2004), characterized by a monotonic decrease in the negative log-likelihood of the estimated image based on the given data. Moreover, MLEM employs simple multiplicative updates, ensuring that the estimated image has positive pixel values as long as the starting assumption image also contains positive pixels. Notably, the MLEM algorithm exhibits good performance when dealing with sparse tomography datasets in the workflow, and streak artifacts can be reduced when combined with an appropriate early stopping strategy, as described subsequently.

4.2.3.1. Determination of the number of iterations: automatic early stopping strategy for MLEM

In the previous section, we discussed the efficiency of the MLEM algorithm, particularly in the context of limited projection number datasets. The MLEM algorithm exhibits noise tolerance, making it a suitable choice for various data conditions. However, it does suffer from a drawback: as the iteration increases beyond a certain number, it introduces additional noise into the reconstructed tomogram. This noise accumulation is unpredictable and varies with different data conditions.

While this problem is of less concern for datasets with a large number of projections, it becomes more obvious in sparse tomography. In sparse tomography, the signal-to-noise ratio in the reconstructed tomogram is already compromised due to reduced acquisition time (or statistics) and lower resolution. Consequently, this significantly impacts the accuracy of the final reconstruction results.

Therefore, it is imperative to develop a method that can strike a balance between achieving satisfactory results and preventing unnecessary iterations that introduce excessive noise (Pafilis et al., 2011). It is crucial to integrate an early stopping strategy with a well-tuned criterion into the MLEM reconstruction. The early stopping strategy enables the automatic termination of the MLEM iteration, providing satisfactory results while avoiding premature termination that could hinder the refinement of resolution.

In this Ph.D. work, I propose an appropriate early-stop criterion for the MLEM reconstruction algorithm, specifically designed for sparse tomography datasets. The criterion is based on a widely adopted figure of merit known as the normalized root-mean-square error deviation (NRMSED). The NRMSED serves as an indicator of the reconstruction quality, capturing the deviation between the reconstructed and measured data. It is defined as:

$$NRMSED = \sqrt{\frac{\sum_{i=1}^{N}(x(i) - \tilde{x}(i))^2}{\sum_{i=1}^{N} x(i)^2}} \tag{4.2}$$

where $x(i)$ is the measured sinogram, $\tilde{x}(i)$ is the reconstructed estimation by MLEM and N is the total pixel number in the sinogram.

To continuously track the differences throughout the reconstruction process, it is essential to compare the change in NRMSED dynamically, i.e., considering its connection with the previous reconstruction result. It becomes particularly necessary as small differences between successive reconstructions indicate the optimal time to stop the algorithm. To facilitate this dynamic evaluation, we introduce the derivative of NRMSED, and the ratio, denoted as R, which quantifies the change in NRMSED between two consecutive iterations:

$$R = \frac{\Delta NRMSED}{NRMSED} \tag{4.3}$$

where $\Delta NRMSED = NRMSED^{(i)} - NRMSED^{(i-1)}$ is the derivative of NRMSED.

The similarity increases monotonically between successive iterations, as indicated by R, guiding the termination decision. To establish a threshold, we have set $R \geqslant -0.15\%$ based on extensive testing across multiple datasets and imaging modalities, ensuring robust and efficient results. To limit the maximum reconstruction time, a predetermined large number of iterations (e.g., 200) is initially set. The MLEM algorithm reconstructs the tomograms slice by slice, calculating the R ratio for each slice after each iteration. Once the threshold is reached, the algorithm automatically terminates for that particular slice and proceeds to reconstruct the next one. Optionally, the reconstruction could perform a few additional iterations after reaching $R_{threshold}$.

According to our experience, the algorithm generally reaches the $R \geqslant R_{threshold}$ condition around 20 iterations, well before the preset 200 iteration steps.

The stopping strategy for the iteration number i can be summarized as follows:

(1). For all the slices, set the threshold to $-0.15\,\%$ and the initial number of iterations to a relatively large value, around 200.
(2). Reconstruction process begins for the first slice using the MLEM algorithm, and the ratio R is calculated for each iteration.
(3). The iteration is stopped when the condition $R \geqslant R_{threshold}$ is satisfied.
(4). Repeated for all the slices in the dataset.

This robust and automated reconstruction process can generate reliable results even when working with a minimal number of angular projections, such as five, as demonstrated in Section 4.3.3. Its effectiveness enables inexperienced users in synchrotron-based imaging and tomography to confidently reconstruct their tomographic datasets directly on-site.

4.2.3.2. 3D volume visualization

The reconstructed volumes are visualized using the freely available software, Chimera (Pettersen et al., 2004). With the user-friendly interface, users of all skill levels can easily navigate and utilize its features. Chimera facilitates users to explore volumes by providing interactive tools for 3D visualization.

4.2.4. Data quantification

The technique of 2D scanning XRF imaging is frequently utilized as a semi-quantitative approach in elemental analysis. The spectra obtained per scanning pixel provide information on the number of characteristic X-ray fluorescence photons recorded within a specific dwell time. However, to obtain absolute element concentrations within the sample, it is necessary to compare these spectra with the spectrum of a reference standard sample that possesses known element concentrations. The integration of elemental concentration quantification into the workflow is of utmost importance. It enables users to determine precise amounts of elements present in the sample and facilitates the observation of changes in elemental concentrations in different areas within the sample. Moreover, quantitative analysis plays a crucial role in enabling meaningful comparisons between diverse samples or datasets during the experiments, thereby completing the on-site data analysis step in the workflow.

Elements	**Group**	**Areal mass (ng/mm ^{2})**	**Reference areal mass (ng/mm ^{2})**
Ca	K	147.6	152.5 ± 41.5
Fe	K	36.38	37.9 ± 4.9
Cu	K	21.75	21.8 ± 2.2

Table 4.1: Quantified areal mass of some of the elements covered in the reference standard sample, compared to the known reference areal mass.

In practice, the quantification of element concentrations in the sample under investigation involves the use of a thin-film reference sample provided by AXO DRESDEN GmbH. This reference sample is comprised of several elements with known areal mass densities in the unit of ng/mm ^{2} (see Table 4.1).

The process of concentration quantification that I have implemented during the PhD work is illustrated in Figure 4.6. To ensure accuracy, the reference sample is scanned under identical experimental conditions. This includes factors such as the beam energy, angle of incidence for the beam, exit angle of XRF signals, distance between the sample and XRF detector, and the environmental conditions proximate to the sample area. It is crucial to note that the data obtained from the reference sample must be normalized using the same incident flux as employed during the sample scan.

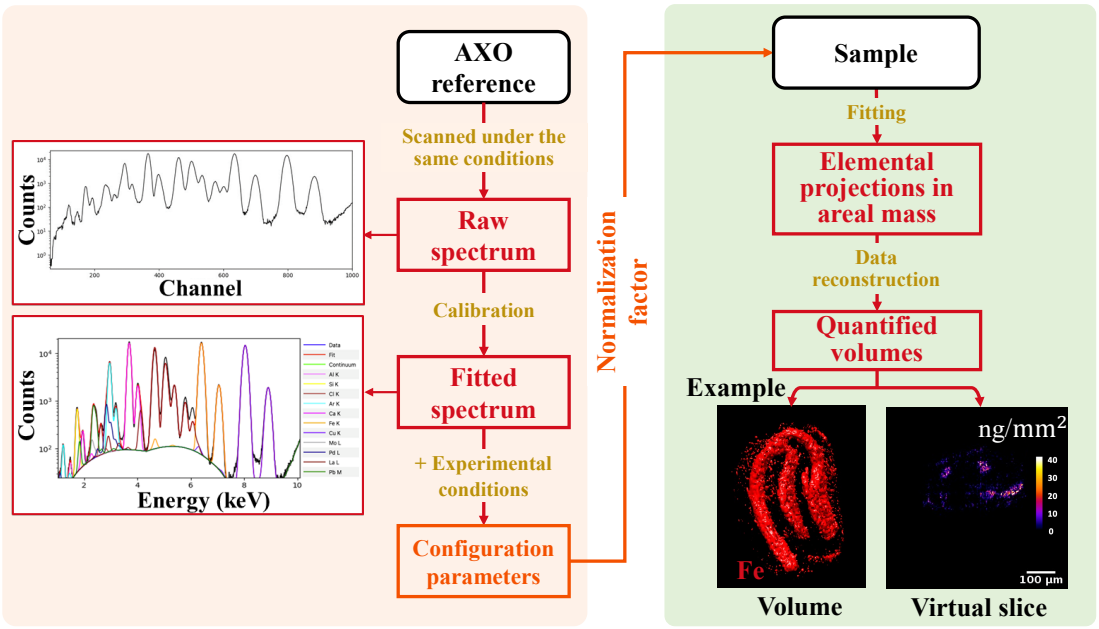

Figure 4.6: Scheme of the concentration quantification process in the implemented workflow.

The calibration process is performed using PyMca software (Solé et al., 2007). Initially, the obtained standard spectrum is fitted to identify the peaks corresponding to different elements in the standard. The software then requires providing the input of the experimental conditions to fit the XRF signal attenuation process occurring before and after reaching the XRF detector. This includes considering attenuators such as the silicon membrane of the standard sample, the air path between the sample and the XRF detector, the Beryllium window and the silicon absorption depth of the silicon drift detector, etc.

PyMca can provide results in the form of mass fractions. For each element, it converts the number of photon counts into the mass of the element, taking into consideration the distinct fluorescence yields of various elements. The mass fraction provided by PyMca can be considered as an equivalent representation of areal mass. When using a standard sample with a known areal mass, we adjust the photon flux

value in the panel to achieve mass fraction values shown in the software that match the known areal mass concentrations of the reference standard.

Of note, this flux value represents a normalization factor and not the actual photon flux on the sample. This normalization factor acts as a link, connecting the measured element intensities to their concentrations. Subsequently, this derived normalization factor is applied to the sample scans for a quantitative comparison between different elements.

In the workflow, the quantification procedure can be applied to various scan modalities in 2D and 3D. If the sample scan is a high-resolution 2D XRF imaging, the scan file can be directly quantified. The resulting concentration maps can be saved as a series of $.tif$ files, which can be further analyzed using ImageJ software. Alternatively, if the sample scans consist of a set of tomographic projections, each projection is quantified individually using the normalization factor mentioned earlier. The quantified projections are then reconstructed using the MLEM algorithm with an appropriate stopping criterion, as discussed in Section 4.2.3.1.

4.2.5. Spatial resolution evaluation

4.2.5.1. Nyquist angular sampling condition

During the experiment, it is crucial to strike a balance between acquisition time and spatial resolution. When using analytical reconstruction methods, it is necessary to ensure that the number of projections fulfills the Nyquist angular sampling condition (Epstein, 2003). As explained in Section 4.2.1.3, the projection number over 180 ° n_{proj} satisfying Nyquist sampling condition is defined as:

$$n_{proj} = \frac{\pi}{2} N \tag{4.4}$$

where n_{proj} is the number of projections over 180 °, and N is the number of pixels along the scanning direction.

The corresponding maximum resolvable spatial frequency f_{res} in the Fourier domain can be written as:

$$f_{res} = \frac{1}{\pi} \frac{n_{proj}}{PN} \tag{4.5}$$

where P is the pixel size.

The resolution limit R in direct space is then:

$$R = \frac{\pi}{2} \frac{PN}{n_{proj}} \tag{4.6}$$

This resolution limit decreases with an increasing number of projections.

4.2.5.2. Fourier ring correlation for spatial resolution estimation

To estimate the achievable spatial resolution in the context of iterative reconstruction methods, the Fourier ring correlation (FRC) approach is commonly employed (Koho et al., 2019; van Heel and Schatz, 2005; Banterle et al., 2013). Unlike the knife-edge technique, which can be challenging for highly heterogeneous samples, FRC offers a more general approach to resolution estimation.

The FRC method involves measuring the normalized cross-correlation of two independent datasets of the sample. In the frequency domain, spatial frequency elements at different radii are integrated circularly. The FRC formula, denoted as $FRC_{12}(r)$, calculates the correlation between the Fourier transforms of the two reconstructed tomograms, F_1 and F_2:

$$FRC_{12}(r) = \frac{\sum_{r_i \in r} F_1(r_i) \cdot F_2(r_i)^*}{\sqrt{\sum_{r_i \in r} |F_1(r_i)|^2 \cdot \sum_{r_i \in r} |F_2(r_i)|^2}} \tag{4.7}$$

Here, r_i is the i^{th} frequency element at radius r. The FRC curve is then analyzed by setting a specified cut-off threshold. When the curve falls below the established threshold, it signifies the resolution level at which sufficient information has been gathered for meaningful interpretation, thus defining the spatial resolution (van Heel and Schatz, 2005).

Ideally, the two datasets used for FRC calculation should be obtained from independent measurements (de Jonge et al., 2017). However, in practice, this can be impractical, particularly in high-resolution scanning experiments that involve several hours of acquisition time at 3rd generation synchrotrons. To overcome this limitation, two subsets are extracted from the high-resolution tomography sinogram, and independent tomographic images of the same slice are reconstructed from these subsets. This method is primarily applied to 2D high-resolution datasets for estimating resolution.

4.3. Proof of principle test measurements

We present a demonstration example to show the performance of our workflow using two types of *Arabidopsis thaliana* seeds. These seeds denoted as wild-type and mutant, were chosen to evaluate the effectiveness of our workflow in characterizing elemental distributions within intact mesoscale biological samples.

4.3.1. *Arabidopsis thaliana* seeds

Arabidopsis thaliana, commonly known as thale cress or mouse-ear cress, is a weed that is native to Eurasia and Africa. This plant has a relatively short life cycle ($\geqslant$ 6 weeks) and holds great significance as a model organism in plant biology research. This is primarily due to its well-characterized genome resources and the availability of a wide range of mutants.

The wild-type *Arabidopsis thaliana* strain, commonly known as Col-0, has become a staple in plant biology laboratory experiments and even in space experiments to study genetics, evolution, and flowering plant development. As a model plant, *Arabidopsis thaliana* also serves as a powerful tool to investigate metal homeostasis and nutrient distribution, relevant questions about the world's food production, and the agriculture industry.

In this context, the presence of essential trace elements like iron (Fe) and manganese (Mn) assumes critical significance. Mn, in particular, is an indispensable micronutrient for plants and is involved in many cellular processes including photosynthesis (functioning of photosystem II within the chloroplast) and respiration. It is also particularly crucial for seeds and germinating plants,

but the processes of Mn loading in the seeds are still poorly documented. Mn availability in soils is generally limited, necessitating plants to employ specific adaptive mechanisms to cope with Mn deficiency. One such mechanism involves the synthesis of a high-affinity Mn transporter derived from the Natural Resistance Associated Macrophage Protein (NRAMP) family, which facilitates efficient uptake of Mn at the root surface. The disruption of *NRAMP3/4* does not alter Mn distribution in the seed (Schnell Ramos et al., 2013) but the role of other NRAMPs transporters has not been investigated, particularly the role of NRAMP2 that can transport Mn from intracellular compartments. For this reason, we would like to understand in detail the role of NRAMP2 and explore the Mn allocation in different seed compartments.

On the other hand, Fe is indispensable for various metabolic processes including also both respiration and photosynthesis. However, these two elements, Fe and Mn, possess unique physiological functions and follow different transporter pathways, leading to expected differences in their distribution and concentration within the seed (see Figure 4.7 for the distribution in detail). Element mapping within the *Arabidopsis thaliana* wild-type seed reveals that Fe is primarily associated with the provascular system throughout the embryo. On the other hand, Mn is predominantly localized in the cortex of the root and in the abaxial side of the cotyledons.

2D scanning XRF imaging has emerged as a powerful technique for precisely locating trace elements in plants. However, accurately attributing the measured metal distribution to specific grain ultrastructure can be challenging due to the information depth (several hundreds of microns) of Mn and Fe. Moreover, studying the internal elemental distribution through 2D scanning XRF imaging often requires sample sectioning, which can be destructive for small and hard samples such as *Arabidopsis thaliana* seeds. The process of sample sectioning itself can induce tissue alterations and artifacts, further complicating the analysis.

XRF and multimodal tomography techniques are useful complementary approaches for analyzing metal concentrations and distribution in intact seeds, requiring minimal sample preparation (Eroglu et al., 2017; Kim et al., 2006; Punshon et al., 2012). These methods enable non-destructive investigations, preserving the integrity of the seed and providing insights into the spatial distribution of metals.

In this section, we chose wild-type and *NRAMP2* mutant *Arabidopsis thaliana* seeds as demonstration examples to underscore the capabilities of the workflow we have implemented. While we will not delve into the detailed biology of the mutant seed in this chapter, it functions as a comparison for quantification evaluation purposes alongside the wild-type. The investigative techniques employed on the seeds included sparse XRF tomography, scanning X-ray absorption tomography, high-resolution 2D tomography of specific virtual slices, and high-resolution 2D projection imaging.

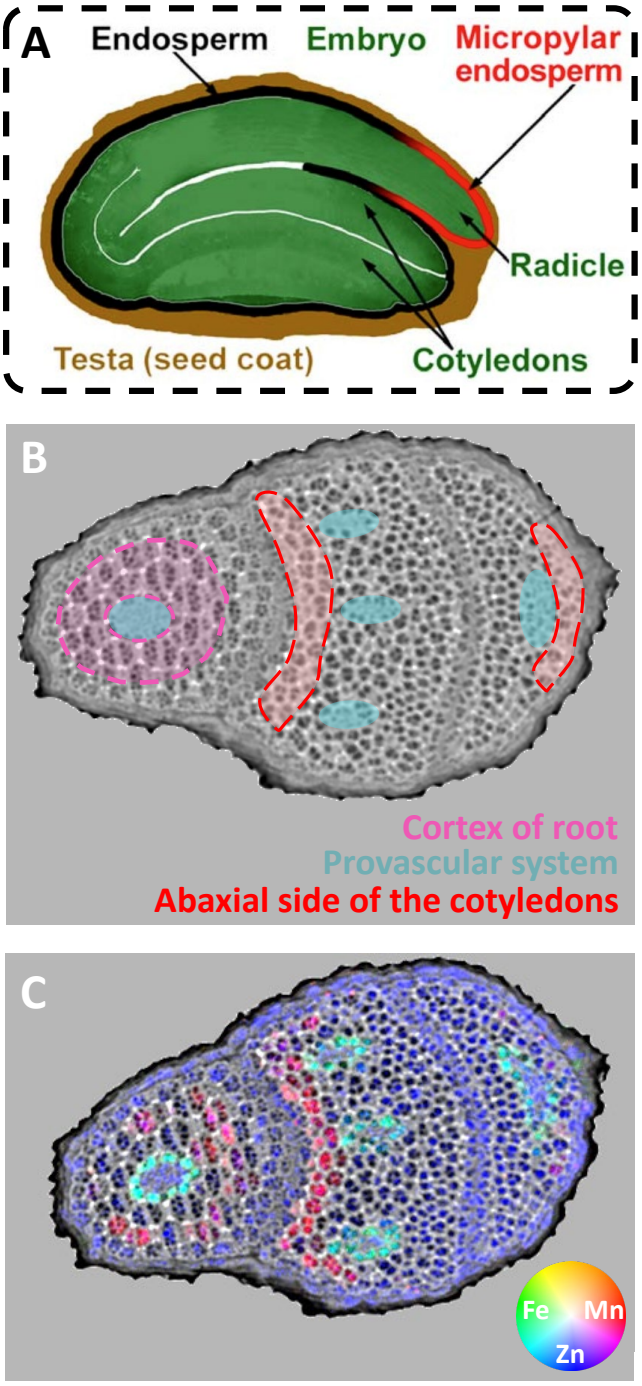

Figure 4.7: Seed structure and elemental distribution of wild-type *Arabidopsis thaliana* seed. **A**. Schematic representation of a seed structure (Gerhard Leubner Lab, accessed 16 Sept. 2023). Previous findings from a research project conducted at the NANOSCOPIUM beamline have revealed the distribution of zinc, manganese, and iron in a virtual cross-section of a wild-type *Arabidopsis thaliana* seed, using a combination of fast full-field tomography and 2D XRF scanning tomography. **B**. A cross-sectional view of a wild-type *Arabidopsis thaliana* seed showing the provascular system (shown in blue) and the cortex of the root (in magenta) along with the abaxial side of the cotyledons (in red). **C**. Fe is predominantly present in the cells surrounding the provascular bundles in the roots and cotyledons while Mn is located in the cortex of the root and the abaxial side of the cotyledons.

4.3.2. Data acquisition

4.3.2.1. 3D sparse XRF and X-ray absorption tomography

The medium-resolution 3D elemental distribution of the *Arabidopsis* seeds was acquired through sparse XRF tomography using incident beam energy at 11 keV. A total of 20 projections were collected at 18 ° angular intervals over 360 ° for two seed samples respectively.

For wild-type seed, each projection angle involved scanning a total area of $581 \times 445\,\mu m^2$ with a pixel size of 2 µm and a dwell time of 20 ms in continuous scanning mode. The complete collection of the sparse XRF tomography dataset required a total time of 8 hours and 40 minutes.

The *NRAMP2* mutant seed required scanning a total area of $622 \times 335\,\mu m^2$ for each projection angle. The scanning was performed with a pixel size of 2 µm and a dwell time of 20 ms in continuous scanning mode. The complete collection of the sparse XRF tomography dataset for the *NRAMP2* mutant seed took a total time of 7 hours.

Simultaneously scanning X-ray absorption tomography was performed during the data acquisition process.

4.3.2.2. High-resolution 2D tomography

For high-resolution single-slice tomography, we performed measurements of 360 angular projections spanning 360 °. The lateral step size between each measurement was set to 2 µm, and the dwell time per pixel was 20 ms. The entire measurement typically took 30-50 minutes, depending on the specific sample being investigated.

4.3.2.3. High-resolution 2D projection imaging

For the wild-type seed, the high-resolution 2D projection imaging involved scanning a field of view measuring $375 \times 434\,\mu m^2$. The scanning process had a step size of 500 nm and a dwell time of 40 ms per pixel. The total acquisition time was 7 hours and 30 minutes. The high-resolution 2D projection imaging of *NRAMP2* mutant involved scanning a field of view measuring $320 \times 278\,\mu m^2$ with a step size of 500 nm and a dwell time of 30 ms per pixel. The total duration for data acquisition took 3 hours and 15 minutes.

4.3.3. Results and validation

4.3.3.1. Sparse scanning X ray tomography

In order to capture a comprehensive overview of elemental distribution in mesoscale seeds–specifically the wild-type seed with dimensions of 700 µm and the mutant seed with dimensions of 400 µm–a sparse XRF and absorption scanning tomography experiment was executed for both seed types following the developed workflow. The primary objective was to identify the distribution of elements, particularly Mn and Fe, within different seed compartments.

As explained in Section 4.2, the advantage of using a limited number of projections in the tomography experiment is the ability to identify features of interest within an acceptable measurement time. By reducing the number of angular projections, the total measurement time and potential radiation damage to the sample can be significantly minimized. However, it is crucial to choose the

reduced number of projections in a way that does not compromise the quality of the resulting 3D mesoscale tomograms.

The reconstructed sparse 3D tomograms of Ca, Mn, and Fe for the two types of seeds, obtained using MLEM from 20 measured angular projections, are presented in Figure 4.8. It is evident from the visual inspection that there are distinctive differences in the Mn distribution patterns between the two seeds.

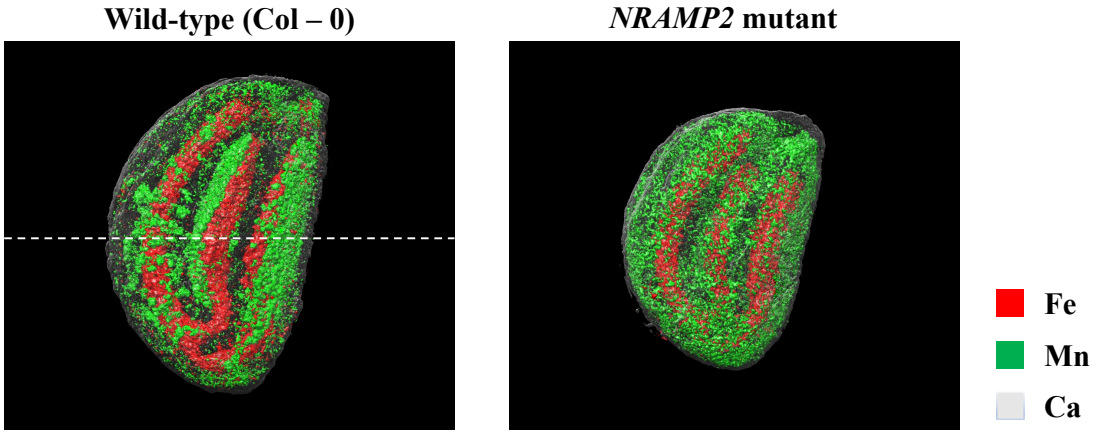

Figure 4.8: Reconstruction of scanning XRF tomography of *Arabidopsis thaliana* seeds, comparing the wild-type (left) and mutant (right).

The reconstructed tomograms reveal distinct elemental distribution patterns. In the wild-type seed (Col-0), Fe is predominantly located in the provascular systems, while Mn is primarily distributed in the abaxial area of both cotyledons at the subepidermal level, as well as in the cortex area of the hypocotyl.

In the reconstructed tomograms of the *NRAMP2* mutant seed, we observed a different Mn distribution inside the seed. Our initial observations from the sparse tomograms were qualitative and require further quantitative analysis to confirm. However, they do offer preliminary evidence of the substantial influence of the *NRAMP2* mutation on the distribution of Mn within the seed. For a comprehensive characterization of these seeds, further element concentration quantification is requisite, using the standard sample as a reference (see Section 4.3.3.4).

To optimize the measurement conditions and reconstruction parameters of sparse tomography, we conducted a comparative analysis between two reconstruction algorithms: FBP and MLEM. The comparison aimed to assess the performance of these algorithms with different numbers of measured angular projections (5, 10, and 20). The evaluation was carried out using a virtual slice in the reconstructed volumes of wild-type seed, indicated by a white dashed line in Figure 4.8, and the results are presented in Figure 4.9. This virtual slice provides visualization of the elemental distribution within the seed with medium resolution, allowing for further analysis and interpretation.

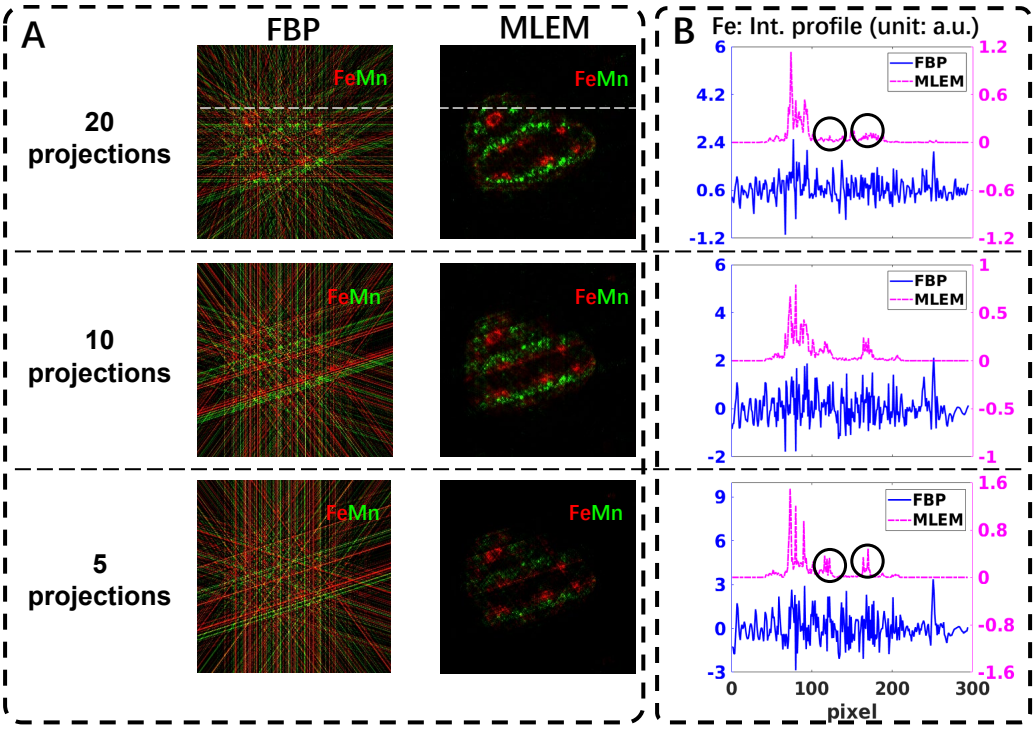

Figure 4.9: A virtual slice from the reconstructed sparse 3D tomograms of wild-type seed, displaying the internal distributions of Fe and Mn. **A**: Comparison of the reconstructed results obtained using FBP and MLEM, with varying numbers of angular projections. Each column represents a specific algorithm, while the lines correspond to 20, 10, and 5 angular projections. In **B** we present a comparison of the intensity profiles obtained using FBP and MLEM. The Fe intensity profiles were extracted along the white dashed line highlighted in **A**.

The FBP algorithm is commonly employed for 3D tomography reconstruction due to its fast execution time and ease of implementation. However, it exhibits limitations when dealing with noisy datasets and highly under-determined measurement conditions, such as those involving a small number of projections (as shown in Chapter 3). This is evident from the first column in Figure 4.9-A, where all sparse tomograms obtained from 5, 10, and 20 projections exhibit a low signal-to-noise ratio. Notably, the FBP reconstructions display strong streak artifacts caused by the limited number of projections, thereby obscuring the elemental distributions. With 20 angular projections, the Mn and Fe distributions are barely discernible. These streak artifacts, as circled in Figure 4.9-B representing the Fe intensity profiles, not only impair the visibility of Fe variations within the sample but also lead to negative intensity values. As expected, the FBP method is not well-suited for the reconstruction of sparse tomography datasets. This is primarily due to its inability to effectively mitigate streak artifacts when the number of projections is low, which aligns with our expectations given the undersampling in this case.

MLEM algorithm (second column of Figure 4.9-A) is superior to FBP in handling noisy datasets. Moreover, it includes the non-negativity constraint assumption. In our workflow, we implemented a simple automatic stopping criterion for the MLEM algorithm, using the smallest possible noise as a measure

of quality (as described in Section 4.2.3.1). This criterion allows for terminating the reconstruction process at a low number of iterations, resulting in a short reconstruction time and minimal introduction of weak artifacts in the reconstructed tomograms. The tomograms shown in Figure 4.9 highlight the robustness of the MLEM algorithm in handling a limited number of projections. Furthermore, as the number of projections increases, the reconstruction artifacts in MLEM become less pronounced. This is exemplified by the purple Fe profiles in Figure 4.9-B, where the strongest reconstruction artifacts, indicated by black circles in the 5-projection tomogram (last line in Figure 4.9-B), diminish in the 20-projection tomogram (first line in Figure 4.9-B).

Simultaneous scanning X-ray absorption tomography was performed alongside the XRF data acquisition process. Figure 4.10-A displays the reconstruction result of the wild-type seed using the MLEM algorithm. The seed coat is well-reconstructed, providing valuable information about the seed's morphology. It is important to note that absorption tomography is just one of the complementary modalities.

Figure 4.10-B shows a cut-off view inside the seed, revealing that the inner structure is not clearly visible or well-resolved. The information we can extract from the X-ray absorption tomogram of the seed's interior is limited because the X-ray probe is lightly attenuated as it passes through the sample. Therefore, the small structures within the seed are not well contrasted.

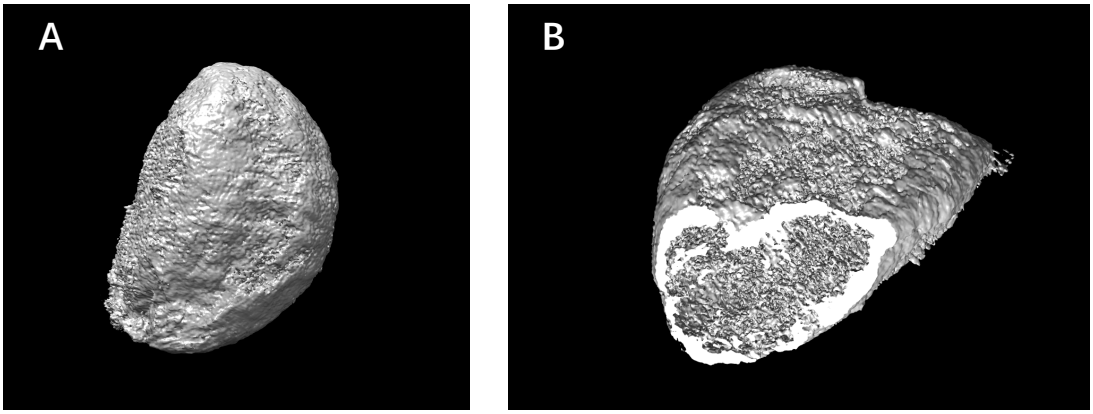

Figure 4.10: Reconstruction of the scanning X-ray absorption tomography of the wild-type *Arabidopsis thaliana* seeds. **A**: 3D volume rendering of X-ray absorption reconstructed from the 20-projection dataset with the MLEM algorithm. **B**: Cut-off view of the reconstructed tomogram.

4.3.3.2. High resolution single slice tomography

In this section, we used the results from the scanning 3D sparse tomography to optimize the selection of angular positions for high-resolution 2D projection imaging and the determination of altitudes for high-resolution single-slice tomography. These techniques allowed us to gain valuable insights into the internal distribution of Mn and Fe within subcellular features of intact seeds.

For high-resolution single-slice XRF tomography, we focused on the altitude in the wild-type sample indicated by the dashed line in Figure 4.11-A, and the reconstructed 2D Mn distribution using both FBP and MLEM algorithms can be observed in Figure 4.11-B and Figure 4.11-C respectively. Additionally, we included a sparse tomogram of Mn with medium resolution obtained by MLEM in the same virtual slice for comparison (Figure 4.11-D).

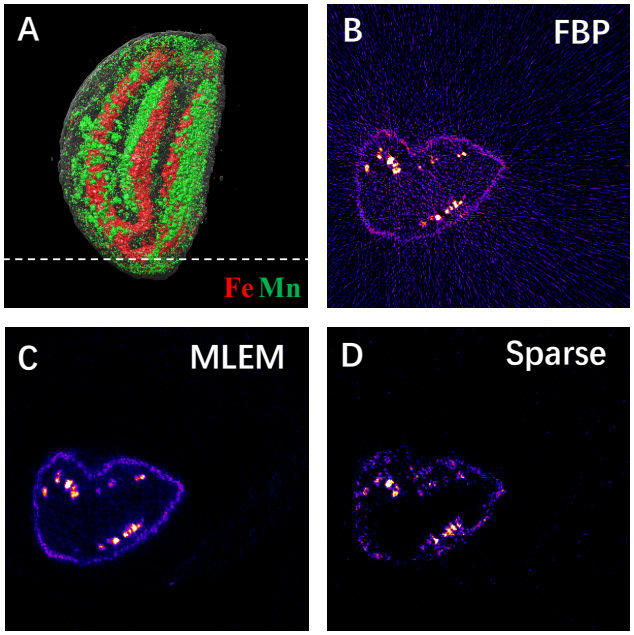

Figure 4.11: High-resolution 2D scanning XRF tomography of the wild-type *Arabidopsis* seed. **A**: Reconstruction of Fe and Mn tomogram in sparse tomography, the white dashed line indicated the altitude for the high-resolution 2D tomography. **B**, **C**: Reconstructed high-resolution single slice of the Mn tomogram obtained by the FBP algorithm (**B**) and by the MLEM algorithm (**C**). **D**: Mn sparse tomography reconstruction at the same slice obtained by MLEM.

The results from both sparse and high-resolution tomography exhibit good agreement in terms of the reconstructed features. As expected, high-resolution tomography unveils finer details with improved spatial resolution that are not easily detectable or distinguishable in sparse tomography. For high-resolution tomography, the FBP algorithm (Figure 4.11-B) offers a straightforward and fast reconstruction approach, with computation time proportional to the number of projections. Nonetheless, even with 360 angular positions, noticeable streak artifacts remain due to insufficient angular projections compared to the number of scanned pixels in this mesoscale sample, as indicated by the Nyquist sampling condition (see Section 4.2.1.3). The MLEM algorithm (Figure 4.11-C) yields better contrast in the reconstructed result.

Moreover, the computation time of < 2 s/sinogram is significantly faster than the measurement time of some hours (and will be comparable with the measurement time of some minutes/sparse tomography at a 4th generation synchrotron). As such, the MLEM algorithm proved to be the best compromise for image reconstruction for both 3D sparse tomography and 2D high-resolution single-slice tomography experiments.

4.3.3.3. High resolution 2D XRF imaging

The selection of a high-resolution 2D XRF imaging angle is determined based on the results obtained from the sparse tomography reconstruction. Users have the flexibility to choose the desired projection angle for conducting further high-resolution imaging. This standard experimental procedure is routinely followed at the NANOSCOPIUM beamline.

Figure 4.12 shows two examples of high-resolution 2D imaging, focusing on the chosen angle, and presenting the Fe and Mn distributions in both the wild-type and mutant seed samples.

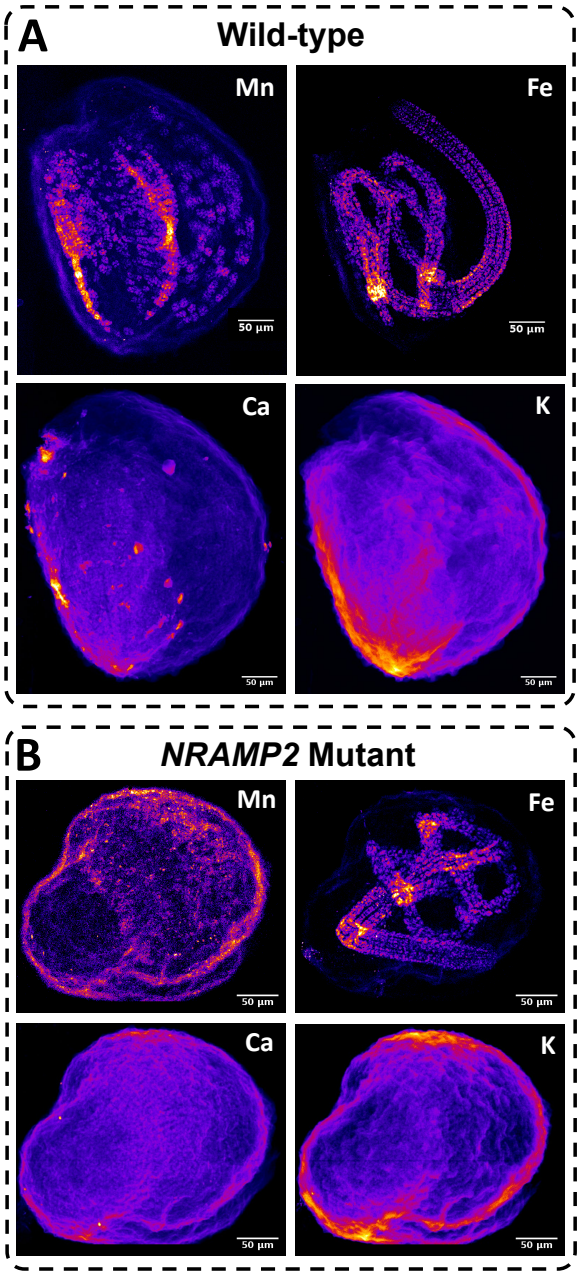

Figure 4.12: High-resolution 2D XRF imaging of wild-type (**A**) and *NRAMP2* mutant (**B**) *Arabidopsis* seed. In the element maps, a noticeable difference in the distribution of Mn between the wild-type and *NRAMP2* mutant seeds was observed visually.

Visually, there is a noticeable difference in the distribution of Mn between the wild-type and *NRAMP2* mutant seeds in the element maps. In the wild-type seeds, high Mn concentration is distributed on the abaxial side of the cotyledons and the hypocotyl.

In contrast, the *NRAMP2* mutant seeds exhibit a distinct pattern. Mn appears to be more evenly distributed throughout the seed and looks more concentrated in the seed coat. In any case, the most enriched parts are not the abaxial cells of the subepidermis, in contrast to the wild type. This disparity suggests that the mutation in *NRAMP2* has a significant impact on Mn uptake and distribution within the seeds, potentially affecting their overall nutritional content. Further analysis is needed to elucidate the molecular mechanisms underlying this observed difference.

4.3.3.4. Element concentration quantification

In this section, the element concentration quantification in the reconstructed tomograms of the wild-type and *NRAMP2* mutant seeds obtained from the sparse tomography experiment was performed using the freeware PyMca (Solé et al., 2007). The purpose of this analysis is to accurately determine the elemental content in both seeds and investigate the impact of the *NRAMP2* mutation on the distribution of Mn within the seeds.

Quantification of the element area concentrations (areal masses) (initially in the unit of ng/mm^2) was carried out using a fitting procedure applied to the recorded fluorescence spectra of the reference standard sample provided by AXO Dresden, as shown in Figure 4.13. The spectrum is further calibrated based on elements with known concentrations in the reference standard spectra.

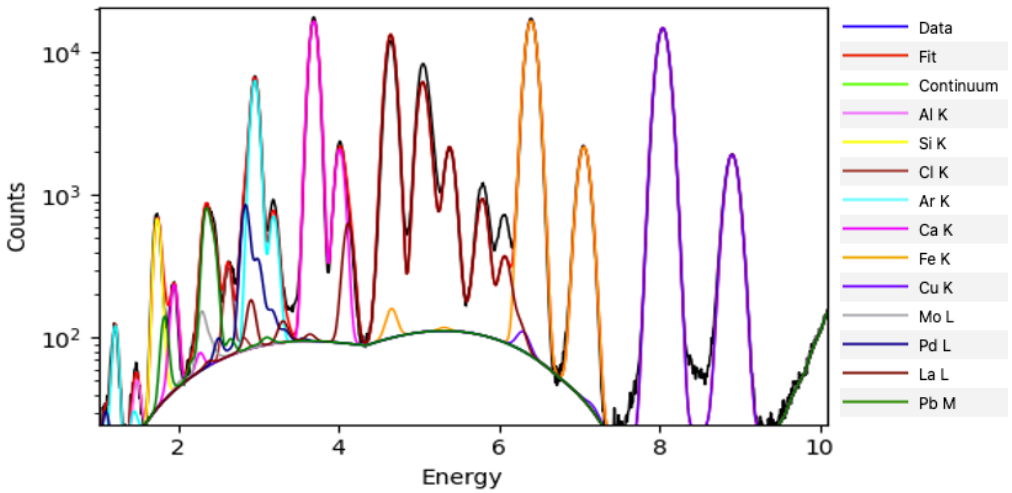

Figure 4.13: Fitted spectra of AXO standard by PyMca software scanned under the same experimental condition as the sample scan.

The quantified concentrations of selected elements, measured under the same experimental geometry as the sample, were compared to the tabulated reference values and are presented in Table 4.1. This allows for interpolation and extrapolation (West et al., 2017) of the relative XRF signal for elements not covered by the reference standard. The quantification analysis was performed

pixel by pixel in each collected projection, resulting in an elemental projection set in units of areal mass. The concentration values were measured in units of ng/mm^2.

For high-resolution 2D imaging, the projection data is quantified using the method described above. An example of the quantified result can be observed in Figure 4.14, which displays the element mass distribution map of Fe and Mn in both wild-type and *NRAMP2* mutant seeds. Notably, we observe that the areal mass of Fe and Mn in the wild-type seed is approximately double that of the mutant seed.

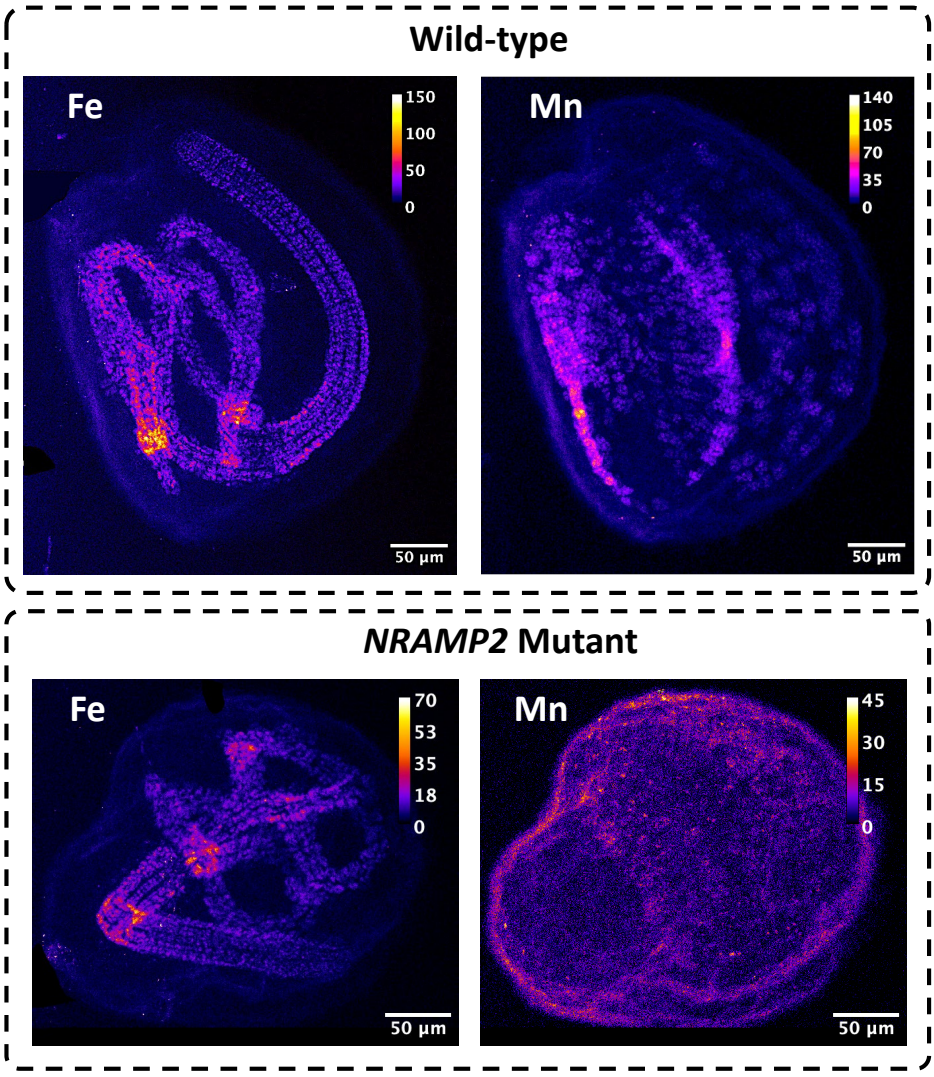

Figure 4.14: Illustration of the element quantification (Fe, Mn) obtained from high-resolution scanning XRF 2D imaging of *Arabidopsis* seeds, presented in ng/mm^2.

Upon further processing and analysis of the data, we calculated the total mass for the projections in Figure 4.14. For Mn, the mass recorded in the wild-type seed is 0.113 ng, which exceeds the mutant's mass of 0.083 ng, indicating a reduced Mn accumulation in the mutant. Similarly, the mass of Fe in the wild-type seed is registered at 1.002 ng, higher than the 0.744 ng noted in the mutant seed.

This difference in elemental mass suggests potential disparities in nutrient uptake or metabolism between the two seed types. Furthermore, the involvement of NRAMP2 in the Mn nutritional pathway in *Arabidopsis* is supported by these observations, in agreement with previous literature publications (Kim et al., 2006; Eroglu et al., 2017).

In high-resolution single-slice tomography, the quantified dataset is reconstructed using either the FBP algorithm or the optimized MLEM algorithm with the developed early stopping strategy. Figure 4.15 shows the virtual slices obtained from the sinograms at specific altitudes, as indicated by the red lines in the figure. The quantified mass distributions of Fe and Mn in these virtual slices are consistent with the findings from the 2D high-resolution imaging presented in Figure 4.14. This agreement in mass ranges further reinforces the reliability and accuracy of our quantification approach across different imaging modalities.

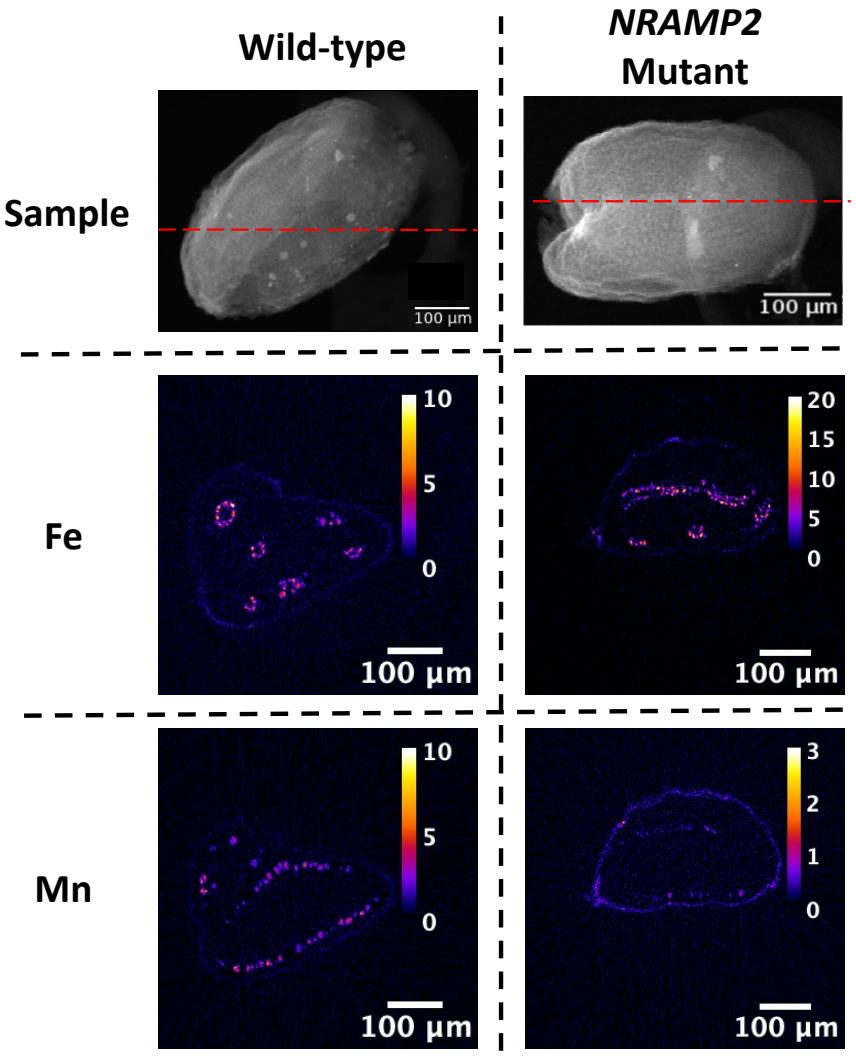

Figure 4.15: Illustration of the element quantification (Fe, Mn) obtained from high-resolution scanning XRF 2D single-slice tomography of *Arabidopsis* seeds, presented in ng/mm^2.Here for instance we see a clear location of Mn in the seed coat that is not obvious in the reconstruction in Figure 4.8.

The precise characterization and quantification of elemental mass distribution provide valuable insights into the elemental composition of the seeds, particularly regarding the distribution of Mn. By comparing the wild-type and *NRAMP2* mutant seeds, we can observe significant differences in Mn distribution, indicating potential variations in physiological processes and genetic factors related to plant development and nutrient homeostasis.

The quantification of elemental mass distribution, as demonstrated in this case study, serves as a powerful tool for unraveling the complex interplay between genetic factors, nutrient uptake, and plant growth, ultimately advancing our knowledge of plant biology and aiding in the development of strategies for improving crop productivity and nutrient management.

4.3.3.5. Mean XRF voxel-spectrum

Next to the elemental distribution maps, obtaining complete local XRF spectral information is crucial for detailed chemical composition analysis of specific sample locations. This is particularly important for identifying rare characteristics that may only appear in certain voxels ("needle in the haystack problem"). By collecting the full XRF spectrum in each pixel during data acquisition, it is possible to reconstruct the full XRF spectrum for each voxel in the tomogram, adding a spectral dimension to the dataset. This hyperspectral tomography reconstruction was performed for each energy channel, resulting in 1000 sinograms per virtual slice. However, due to the increased computational complexity, the reconstruction process becomes time-consuming, taking approximately 1 hour for the high-resolution hyperspectral XRF tomogram of an *Arabidopsis* seed using the MLEM iterative method and around 10 minutes for the FBP method.

In Figure 4.16, a virtual slice of the *Arabidopsis* seed reconstructed from the sum-XRF spectra of the dataset with 360 projections is presented. The mean XRF spectra extracted from the area marked by a red circle in Figure 4.16-A using FBP and MLEM are shown in Figure 4.16-B and C, respectively. Comparatively, the mean XRF spectra obtained by FBP and MLEM exhibit no significant difference, with the total intensities agreeing within 5 %. Hence, for high-resolution tomography, FBP serves as a suitable compromise to obtain local spectral information within a reasonable reconstruction time.

To investigate the influence of the projection number in sparse tomography, we selected 20 equiangular projections out of the 360 to simulate sparse tomography under identical experimental conditions. As already demonstrated, due to the low number of projections, FBP cannot be employed for data reconstruction in this case. Instead, we reconstructed the sparse tomogram for each energy channel using the MLEM algorithm. The mean XRF spectrum of the same region as before (red circle in Figure 4.16-A) was derived from this sparse tomography dataset. Figure 4.16-C demonstrates good agreement between the two mean XRF spectra, highlighting the reliable hyperspectral tomograms and mean XRF spectra obtained even with a severely limited number of projections using the MLEM algorithm.

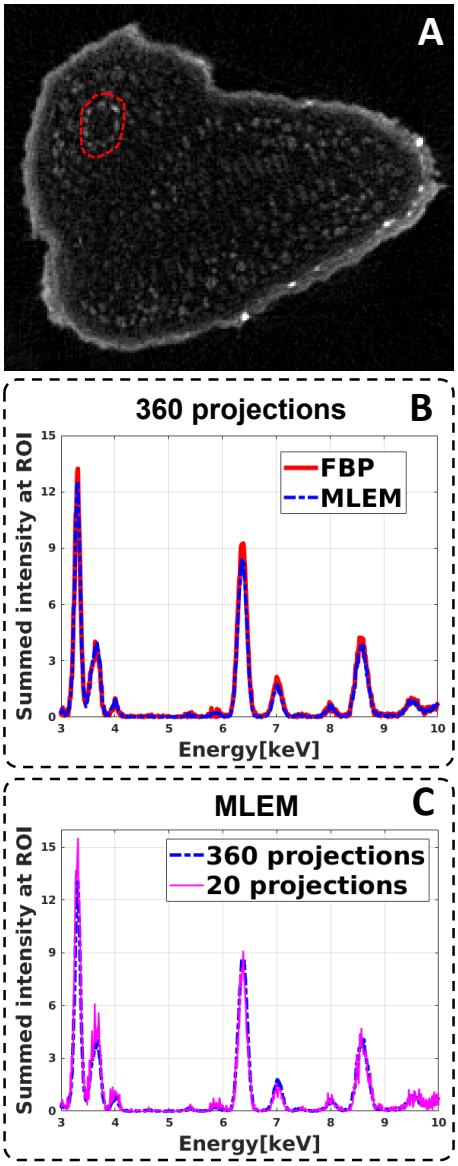

Figure 4.16: Extraction of the mean XRF spectra of a chosen area in a virtual slice of the *Arabidopsis* seed. **A**: Reconstructed high-resolution virtual slice of the sum XRF spectra of the *Arabidopsis* seed. **B**: Comparison of the mean XRF spectra of the selected area, marked by a red dashed circle in **A**, obtained by FBP (red curve) and MLEM (blue curve) algorithm. **C**: The mean XRF spectra of the selected area obtained by MLEM from 360 projections (blue curve) and from 20 projections (fuchsine curve).

4.3.3.6. Tomogram spatial resolution with MLEM

To assess the spatial resolution of the tomograms reconstructed using the MLEM algorithm, we conducted an analysis using two subsets of the 2D high-resolution dataset. These subsets were obtained by dividing the full projection dataset, which had 360 projections, into two subsets with an equal number of projections. Each subset was independently reconstructed using the MLEM algorithm with automatically determined iteration numbers. The resulting tomograms from the two subsets were then subjected to Fourier ring correlation (FRC) analysis.

In Figure 4.17, we present the FRC curves depicting the comparison between the two tomograms reconstructed using different numbers of projections from the same 2D high-resolution sinogram. The spatial resolution was determined by identifying the intersection point of the FRC curve with a fixed 0.5 threshold (van Heel and Schatz, 2005). Table 4.2 provides the spatial resolution values determined using the 0.5 threshold criterion for different numbers of projections. As anticipated, the spatial resolution improves with an increasing number of projections. Notably, a resolution estimate of 8.4 μm was obtained for the tomogram reconstructed from 20 projections. This signifies a significant improvement in resolution achieved by the MLEM iterative method compared to the spatial resolution determined by the Nyquist sampling condition.

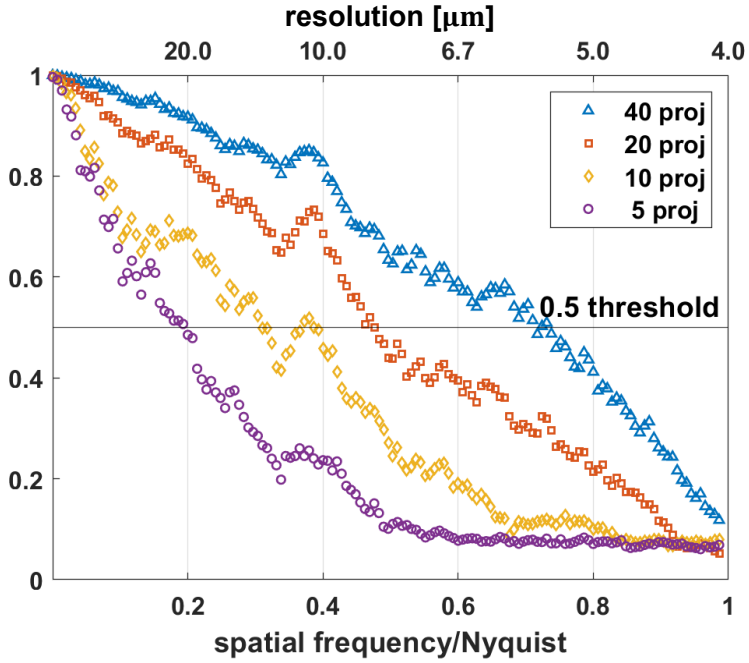

Figure 4.17: Spatial resolution estimation by Fourier ring correlation (FRC) method. Estimation of spatial resolution for tomograms reconstructed by MLEM from different numbers of projections chosen from the measured 360 angular projection Fe dataset. The fixed 0.5 threshold was used for FRC analysis. The Nyquist frequency is 0.25 μm^{-1}.

Number of projections	**FRC analysis: resolution (μm)**	**Nyquist sampling condition: resolution (μm)**
5	20.5	184.7
10	12.9	92.4
20	8.4	46.2
40	5.6	23.1

Table 4.2: Estimation of the spatial resolution of sparse tomograms (reconstructed by the MLEM algorithm) by FRC analysis in the function of the measured number of projections. The spatial resolution defined by the Nyquist sampling condition is included in the 3rd column for comparison.

4.3.3.7. Dose evaluation

In this study, the estimation of radiation dose was a critical component of our analysis. As discussed in Section 2.2.1.4. The incident photon flux was calculated in photons per second and factored in the efficiency of the KB system (87.5 %). We used the absorbed dose in air to quantify the incident dose. Subsequently, we calculated the dose rates for different scans, including sparse tomography on wild-type (WT) and mutant samples, as well as high-resolution (HR) 2D imaging and single-slice tomography scans. It is worth noting that the integrated dose for a given scan type is computed as the product of the dose rate, dwell time per pixel, and, in the case of tomography, the number of projections. The specific dose rate and integrated dose for each type of scan are detailed in the Table 4.3 below.

Of note, a future avenue of investigation should also focus on the quantification of the integrated dose within the sample during the scanning process. This is imperative for optimizing the number of projections utilized in sparse tomography, thereby achieving a balance between data fidelity and radiation exposure.

	Scan type	**Dose rate (Gy/s)**	**Integrated dose (Gy)**
Figure 4.8	Sparse tomography (WT)	3.4×10^5	1.4×10^5
	Sparse tomography (mutant)	3.1×10^5	1.2×10^5
Figure 4.11	HR single slice (WT)	3.2×10^5	2.3×10^6
Figure 4.14	HR 2D (WT)	5.1×10^6	2.0×10^5
	HR 2D (mutant)	4.6×10^6	1.3×10^5
Figure 4.15	HR single slice (WT)	3.3×10^5	2.3×10^6
	HR single slice (mutant)	3.2×10^5	2.3×10^6

Table 4.3: Dose estimation for different scans in this chapter.

4.4. Discussion

At the NANOSCOPIUM beamline, a holistic multi-scale and multimodal scanning X-ray tomography workflow was implemented and has been successfully tested on mesoscale samples, specifically *Arabidopsis thaliana* seeds. The best compromise for semi-automatic on-site tomography reconstruction for sparse-, and high-resolution scanning X-ray tomography is proved to be the MLEM algorithm if it is benefited from the apt early stopping strategy. On the other hand, the FBP algorithm was found to be generally unsuitable for reconstructing sparse tomography due to the failure to meet the optimal Nyquist sampling criterion. When dealing with high-resolution hyperspectral tomography and its associated large datasets, a trade-off between data quality and reconstruction time becomes necessary. In this context, FBP emerged as a viable option, enabling the extraction of reliable mean XRF spectra from selected regions or volumes within a reasonable reconstruction time frame.

By implementing the above-detailed conditions and using the two algorithms in a semi-automatic manner, our workflow offers flexibility and enables

high-quality on-site reconstruction for various samples under diverse experimental conditions. This adaptability makes it particularly suitable for progressively studying features of interest at different length scales during an experiment. However, it is important to acknowledge that scanning XRF imaging is susceptible to the self-absorption phenomenon. The XRF signals emitted by the sample traverse a complex structure before reaching the detector, which can affect the accuracy of quantification if not corrected (Ge et al., 2023).

In our current implementation, we presented the quantification of element concentrations in 2D and 3D (in units of areal mass) without accounting for self-absorption. In future work, a self-absorption correction method has to be integrated into the semi-automatic and user-friendly data-processing pipeline. This will be applied for all scanning XRF tomography experiments. The correction process will involve simultaneous scanning X-ray absorption tomography, which will correct for self-absorption in each voxel of the tomogram for every reconstructed element. By incorporating this correction, we will significantly improve the accuracy and analysis derived from the scanning XRF tomography experiments.

The robust scanning tomography method implemented at the NANOSCOPIUM beamline allows non-expert users to perform routine non-destructive multi-length-scale characterization of complex samples within a standard beam-time of 3-5 days. The reconstructed tomograms can be easily handled using widely used software tools such as ImageJ and Chimera, facilitating data analysis for users during and after their experiments. The workflow allows the study of relevant 3D micro-features of several mesoscale samples during a routine user experiment, even at 3rd generation synchrotrons. Additionally, this approach can be straightforwardly applied to XANES tomography, which can be considered a variant of hyperspectral tomography.

Such a robust, semi-automatic, and flexible scanning multimodal tomography workflow will be a game-changer in scientific fields by enabling the simultaneous exploration of multiple sample characteristics with high analytical sensitivity at hierarchical length scales in 3D. It will provide valuable insights in a statistically significant manner for meso- and micro-scale samples. Furthermore, it complements existing state-of-the-art multi-scale and fast full-field X-ray tomography techniques, acting as a unique and powerful addition. These high-throughput scanning X-ray imaging techniques will also complement emerging laboratory scanning charged-particle microscopy and tomography, as well as other conventional laboratory microscopy techniques that provide 2D/3D elemental and morphology information with nanometer resolution. For instance, scanning electron microscopy has limited analytical sensitivity (around 0.1-1%) for heavy elements, and its shallow depth of information restricts its non-invasive application to surface studies of large samples or the 3D analysis of light, major, and minor components of tiny, micrometer-sized samples. Due to sample radiation damage caused by charged-particle microscopies, multiple measurements on the very same sample region are often problematic. Scanning hard XRF imaging and tomography has high analytical sensitivity (with trace, $\leqslant$ ppm detection limit) for transition metals and heavier elements. Moreover, their large information depth of several tens/hundreds of microns permits the non-invasive multilength-scale 3D

study of mesoscale samples. Multiple measurements and hence, multi-scale and local tomography are readily available by scanning X-ray imaging techniques, where radiation damage is smaller than by charged particle microscopies.

4.5. Conclusion

In this section, we showcased the capabilities of our implemented multi-scale and multimodal scanning X-ray tomography workflow by selecting wild-type and *NRAMP2* mutant *Arabidopsis thaliana* seeds as demonstration examples. Our experimental setup involved medium-resolution scanning of the seeds using XRF sparse tomography, followed by the reconstruction of tomographic slices using the MLEM algorithm with an optimized iteration number. The reconstructed sparse tomograms provided coherent spatial information on the elemental distribution within the seeds, enabling us to observe variations between the wild-type and mutant seeds.

To gain further insights, we employed additional investigative strategies on the seeds, including high-resolution 2D tomography of specific virtual slices and high-resolution 2D projection imaging. The acquired XRF results in both 2D and 3D were processed and quantified using a reference standard scan.

Subsequent analysis and comparison of the elemental concentrations were conducted at specific altitudes within the seeds. These altitudes were chosen based on morphological features and prior knowledge of element localization in the samples. We quantified and compared the concentrations of elements such as calcium (Ca), iron (Fe), and manganese (Mn) between the two types of seeds. The results unveiled significant variations in elemental composition, suggesting potential differences in nutrient uptake, metabolism, or genetic factors between the wild-type and mutant seeds.

The ability of our workflow to accurately quantify element concentrations in biological samples is crucial for understanding the physiological processes and elemental homeostasis within organisms. These findings highlight the potential applications of our workflow in plant biology research and provide a foundation for further investigations into the elemental composition of various mesoscale samples.

In addition, the successful application of our workflow to *Arabidopsis thaliana* seeds serves as a compelling demonstration of its effectiveness in characterizing mesoscale samples. By integrating synchrotron-based imaging, optimized MLEM reconstruction, and rigorous quantification, we have comprehensively characterized the samples, encompassing their morphology, element spatial distribution, and concentrations. This holistic and robust multi-scale and multimodal workflow helps users gain valuable insights into complex biological systems. The capabilities of the workflow open up possibilities for routine multimodal 3D characterization of intact samples, enabling the extraction of crucial information from specific regions of interest. The potential impact of this approach extends across a range of scientific fields, including biology, geology, and materials sciences.

References

S. Azevedo, D. Schneberk, J. Fitch, and H. Martz. Calculation of the rotational centers in computed tomography sinograms. *IEEE Transactions on Nuclear Science*, 37(4):1525–1540, 1990. doi: 10.1109/23.55866.

N. Banterle, K. H. Bui, E. A. Lemke, and M. Beck. Fourier ring correlation as a resolution criterion for super-resolution microscopy. *Journal of Structural Biology*, 183(3):363–367, Sept. 2013. ISSN 10478477. doi: 10.1016/j.jsb.2013.05.004. URL https://linkinghub.elsevier.com/retrieve/pii/S1047847713001184.

A. Bergamaschi, K. Medjoubi, C. Messaoudi, S. Marco, and A. Somogyi. *MMX-I* : data-processing software for multimodal X-ray imaging and tomography. *J Synchrotron Rad*, 23(3):783–794, May 2016. ISSN 1600-5775. doi: 10.1107/S1600577516003052. URL http://scripts.iucr.org/cgi-bin/paper?S1600577516003052.

D. Bourassa, S.-C. Gleber, S. Vogt, C. H. Shin, and C. J. Fahrni. MicroXRF tomographic visualization of zinc and iron in the zebrafish embryo at the onset of the hatching period. *Metallomics*, 8(10):1122–1130, 2016. ISSN 1756-5901, 1756-591X. doi: 10.1039/C6MT00073H. URL https://academic.oup.com/metallomics/article/8/10/1122-1130/6012998.

M. D. de Jonge, A. M. Kingston, N. Afshar, J. Garrevoet, R. Kirkham, G. Ruben, G. R. Myers, S. J. Latham, D. L. Howard, D. J. Paterson, C. G. Ryan, and G. McColl. Spiral scanning X-ray fluorescence computed tomography. *Opt. Express*, 25(19):23424, Sept. 2017. ISSN 1094-4087. doi: 10.1364/OE.25.023424. URL https://opg.optica.org/abstract.cfm?URI=oe-25-19-23424.

A. P. Dempster, N. M. Laird, and D. B. Rubin. Maximum Likelihood from Incomplete Data Via the *EM* Algorithm. *Journal of the Royal Statistical Society: Series B (Methodological)*, 39(1):1–22, Sept. 1977. ISSN 00359246. doi: 10.1111/j.2517-6161.1977.tb01600.x. URL https://onlinelibrary.wiley.com/doi/10.1111/j.2517-6161.1977.tb01600.x.

C. L. Epstein. *Introduction to the mathematics of medical imaging*. Pearson Education/Prentice Hall, Upper Saddle River, N.J, 2003. ISBN 978-0-13-067548-4.

S. Eroglu, R. F. Giehl, B. Meier, M. Takahashi, Y. Terada, K. Ignatyev, E. Andresen, H. Küpper, E. Peiter, and N. von Wirén. Metal Tolerance Protein 8 Mediates Manganese Homeostasis and Iron Reallocation during Seed Development and Germination. *Plant Physiology*, 174(3):1633–1647, July 2017. ISSN 0032-0889. doi: 10.1104/pp.16.01646. URL https://doi.org/10.1104/pp.16.01646.

M. Ge, H. Yan, X. Huang, and Y. S. Chu. Self-absorption correction on 2D X-ray fluorescence maps. *Sci Rep*, 13(1):7271, May 2023. ISSN 2045-2322. doi: 10.1038/s41598-023-33383-w. URL https://www.nature.com/articles/s41598-023-33383-w.

Gerhard Leubner Lab. The Seed Biology Place - Antje Voegele, accessed 16 Sept. 2023. URL http://www.seedbiology.de/voegele.asp.

R. Guo, A. Somogyi, D. Bazin, E. Bouderlique, E. Letavernier, C. Curie, M.-P. Isaure, and K. Medjoubi. Towards routine 3D characterization of intact mesoscale samples by multi-scale and multimodal scanning X-ray tomography. *Sci Rep*, 12 (1):16924, Oct. 2022. ISSN 2045-2322. doi: 10.1038/s41598-022-21368-0. URL https://www.nature.com/articles/s41598-022-21368-0.

D. R. Hunter and K. Lange. A Tutorial on MM Algorithms. *The American Statistician*, 58(1):30–37, Feb. 2004. ISSN 0003-1305, 1537-2731. doi: 10.1198/0003130042836. URL http://www.tandfonline.com/doi/abs/10.1198/0003130042836.

D. Kazantsev, E. Guo, A. B. Phillion, P. J. Withers, and P. D. Lee. Model-based iterative reconstruction using higher-order regularization of dynamic synchrotron data. *Meas. Sci. Technol.*, 28(9):094004, Sept. 2017. ISSN 0957-0233, 1361-6501. doi: 10.1088/1361-6501/aa7fa8. URL https://iopscience.iop.org/article/10.1088/1361-6501/aa7fa8.

S. A. Kim, T. Punshon, A. Lanzirotti, L. Li, J. M. Alonso, J. R. Ecker, J. Kaplan, and M. L. Guerinot. Localization of Iron in *Arabidopsis* Seed Requires the Vacuolar Membrane Transporter VIT1. *Science*, 314(5803):1295–1298, Nov. 2006. ISSN 0036-8075, 1095-9203. doi: 10.1126/science.1132563. URL https://www.science.org/doi/10.1126/science.1132563.

S. Koho, G. Tortarolo, M. Castello, T. Deguchi, A. Diaspro, and G. Vicidomini. Fourier ring correlation simplifies image restoration in fluorescence microscopy. *Nat Commun*, 10(1):3103, Dec. 2019. ISSN 2041-1723. doi: 10.1038/s41467-019-11024-z. URL http://www.nature.com/articles/s41467-019-11024-z.

C. Pafilis, A. Gaitanis, C. Gatis, G. Kontaxakis, G. Spyrou, G. Panayiotakis, and G. Tzanakos. A methodology for the estimation of the optimal iteration in MLEM-based image reconstruction in PET. In *2011 10th International Workshop on Biomedical Engineering*, pages 1–4, Kos, Greece, Oct. 2011. IEEE. ISBN 978-1-4577-0553-3. doi: 10.1109/IWBE.2011.6079046. URL http://ieeexplore.ieee.org/document/6079046/.

E. F. Pettersen, T. D. Goddard, C. C. Huang, G. S. Couch, D. M. Greenblatt, E. C. Meng, and T. E. Ferrin. UCSF Chimera?A visualization system for exploratory research and analysis. *J. Comput. Chem.*, 25(13):1605–1612, Oct. 2004. ISSN 0192-8651, 1096-987X. doi: 10.1002/jcc.20084. URL https://onlinelibrary.wiley.com/doi/10.1002/jcc.20084.

T. Punshon, K. Hirschi, J. Yang, A. Lanzirotti, B. Lai, and M. L. Guerinot. The Role of CAX1 and CAX3 in Elemental Distribution and Abundance in Arabidopsis Seed. *Plant Physiology*, 158(1):352–362, Jan. 2012. ISSN 1532-2548. doi: 10.1104/pp.111.184812. URL https://academic.oup.com/plphys/article/158/1/352/6109135.

J. Schindelin, I. Arganda-Carreras, E. Frise, V. Kaynig, M. Longair, T. Pietzsch, S. Preibisch, C. Rueden, S. Saalfeld, B. Schmid, J.-Y. Tinevez, D. J. White, V. Hartenstein, K. Eliceiri, P. Tomancak, and A. Cardona. Fiji: an open-source platform for biological-image analysis. *Nat Methods*, 9(7):676–682, July 2012. ISSN 1548-7091, 1548-7105. doi: 10.1038/nmeth.2019. URL http://www.nature.com/articles/nmeth.2019.

M. Schnell Ramos, H. Khodja, V. Mary, and S. Thomine. Using µpixe for quantitative mapping of metal concentration in arabidopsis thaliana seeds. *Frontiers in Plant Science*, 4, 2013. ISSN 1664-462X. doi: 10.3389/fpls.2013.00168. URL https://www.frontiersin.org/articles/10.3389/fpls.2013.00168.

V. A. Solé, E. Papillon, M. Cotte, P. Walter, and J. Susini. A multiplatform code for the analysis of energy-dispersive X-ray fluorescence spectra. *Spectrochimica Acta Part B: Atomic Spectroscopy*, 62(1):63–68, Jan. 2007. ISSN 0584-8547. doi: 10.1016/j.sab.2006.12.002. URL https://www.sciencedirect.com/science/article/pii/S0584854706003764.

M. van Heel and M. Schatz. Fourier shell correlation threshold criteria. *J Struct Biol*, 151(3):250–262, Sept. 2005. ISSN 1047-8477. doi: 10.1016/j.jsb.2005.05.009.

B. M. West, M. Stuckelberger, A. Jeffries, S. Gangam, B. Lai, B. Stripe, J. Maser, V. Rose, S. Vogt, and M. I. Bertoni. X-ray fluorescence at nanoscale resolution for multicomponent layered structures: a solar cell case study. *J Synchrotron Radiat*, 24(Pt 1):288–295, Jan. 2017. ISSN 1600-5775. doi: 10.1107/S1600577516015721.

CHAPTER 5

APPLICATIONS IN PATHOLOGICAL CALCIFICATIONS: RANDALL'S PLAQUE FORMATION

5.1. Characteristics of Randall's plaque

In this section, we aim to investigate the initial stages of Randall's plaque (RP) formation at the nanometer scale using the established scanning X-ray fluorescence imaging and tomography methods.

Our investigation centers on the potential role of trace elements in the context of pathological calcification. By combining synchrotron-based quantitative XRF with tomography techniques, we can gain insights into the high-resolution spatial distribution of elements with high analytical sensitivity.

5.1.1. Some physicochemical characteristics

It is widely observed that a majority (~75%) of calcium oxalate stones appear to develop on a subepithelial calcium phosphate plaque, referred to as Randall's plaque, located at the tip of the renal papilla (see Figure 5.1) (Daudon et al., 2007; Daudon and Bazin, 2013; Chung, 2014).

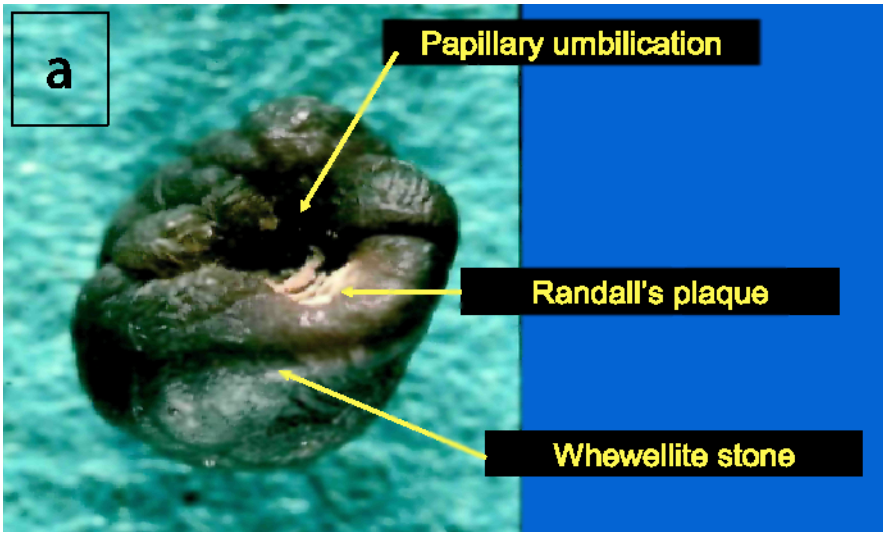

Figure 5.1: Typical aspect of calcium oxalate papillary stones (Daudon et al., 2007).

At the micrometer scale, the plaque appears as a complex structure containing calcified tubules and vessels (see Figure 5.2).

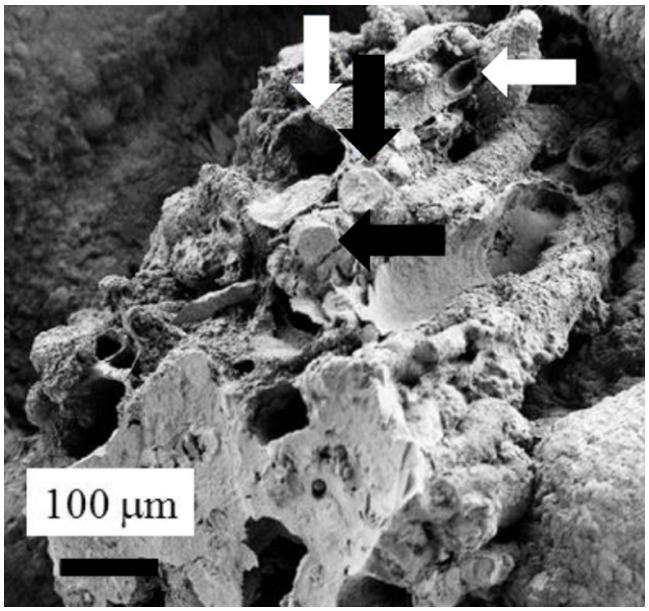

Figure 5.2: Randall's plaque at the micrometer scale by SEM. Calcified tubules and vessels (white arrows) and tubules filled by carbapatite plugs (black arrows). (Bazin and Daudon, 2012)

The presence of microcalcifications and individual nano-calcifications in the formation of Randall's plaque has been underlined by (Gay et al., 2020). Figure 5.3 shows some of these micro and nanocalcifications.

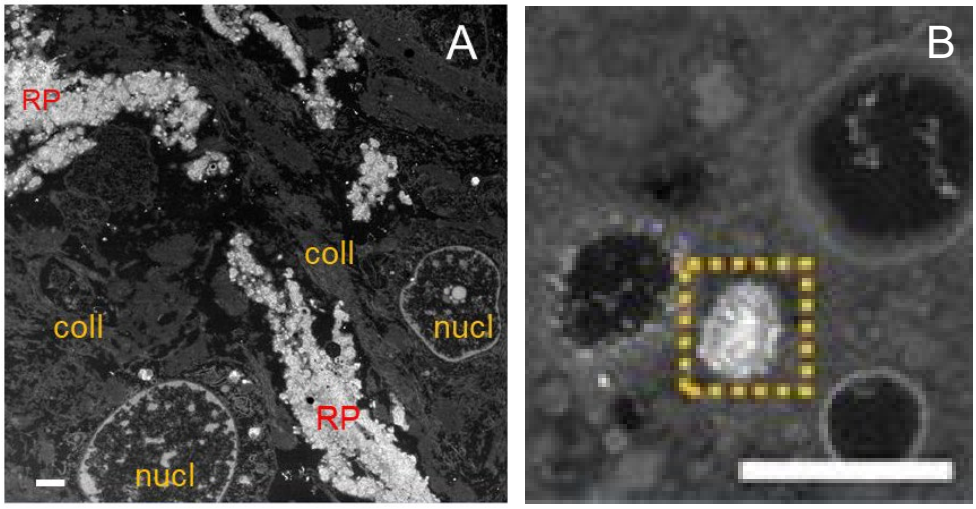

Figure 5.3: STEM-HAADF image of (**A**) micro-calcifications shows that RPs are mainly formed by electron-dense objects with rounded shapes connected together by a lower contrast fibrillary network (scale bar = 1 µm). **B**: STEM images for nanocalcifications (scale bar = 500 nm) (Gay et al., 2020).

5.1.2. Chemical composition of Randall's plaque

Randall's plaque is mainly composed of calcium phosphate apatite (Daudon et al., 2007). In addition, other mineral phases, including amorphous carbonated calcium phosphate (ACCP), and less commonly, whitlockite or brushite, are also identified in Randall's plaque. The presence of chemical species like sodium hydrogen urate and uric acid has also been documented. This chemical diversity indicates that RP can have various origins (Daudon et al., 2011). According to research by (Carpentier et al., 2010), the amorphous carbonated calcium phosphate is typically found at the center of the plaque, indicating that it forms the first chemical phase. The stable apatite then forms on the surface of the plaque. It is important to note that the mineral part and the organic matrix overlay each other in Randall's plaque. The organic matrix is composed of macromolecules produced by epithelial cells in response to exposure to the tubular deposition of crystals.

5.1.3. Trace elements in Randall's plaque

The literature concerning the interaction between trace elements and the formation of Randall's plaque is quite limited. In a previous investigation, (Carpentier et al., 2010) used X-ray fluorescence to explore the possible role of trace elements in the pathogenesis of RP. Figure 5.4 displays the X-ray fluorescence emission spectra of the different Randall's plaques. The contributions of Ca as well as trace elements like Zn, Pb and Sr are clearly identified by the presence of two main peaks characteristic of each of these elements.

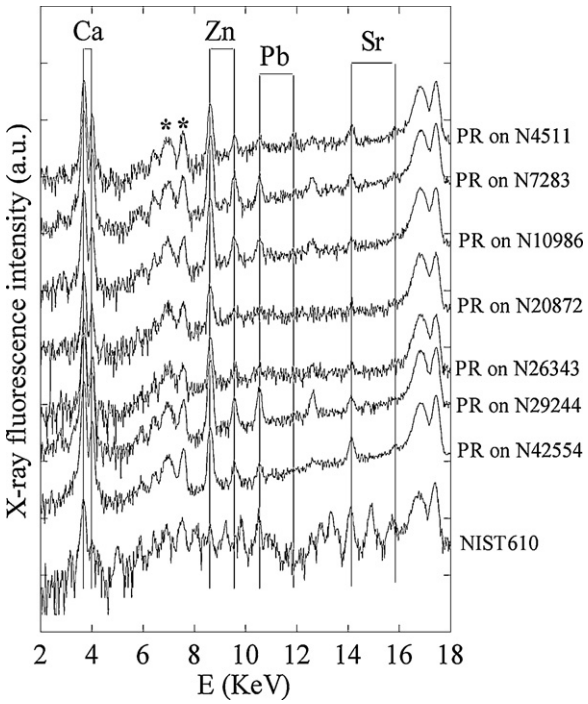

Figure 5.4: Typical X-ray fluorescence spectra collected for RP and calibration compound NIST610. For RP, we can clearly see the contribution of Ca (EK_α = 3691 eV, EK_β = 4012 eV), Zn (EK_α = 8638 eV, EK_β = 9572 eV), Pb (EL_α = 10,551 eV, EL_β = 12,613 eV) and Sr (EK_α = 14,165 eV, EK_β = 15,835 eV). ∗Peaks corresponding to absorption by the germanium detector of the Compton and Mo Ka elastic peak. Adapted from (Carpentier et al., 2011).

As observed in Table 5.1, the content of heavy elements is about 30-1000 times higher in RP than in urine or kidney tissue.

	Zn (μg/g)	Sr (μg/g)	Pb (μg/g)
CAKS[a]	1059 ± 1056	349 ± 181	62 ± 39
RP	5665 ± 490*	22 ± 13*	NA
Kidney tissue[b]	15 - 32	0.04 - 0.12	0.1 - 0.4
Urine[b]	0.002 - 0.1	0.2	0.012 - 0.030
Urine[c]	0.3 ± 0.2	0.14 ± 0.076	0.0013 ± 0.014

Table 5.1: Amount of Zn, Sr and Pb in kidney stones (CAKS), Randall's plaque (RP), kidney tissue, and urine (Carpentier et al., 2010).

However, the knowledge of trace element spatial distribution in Randall's plaque, specifically Zn and Ca, was limited to the micrometer scale (Bazin et al., 2012). Yet there is a lack of data regarding the nanometer-scale spatial distribution of trace elements. Figure 5.5-A shows a typical Particle-Induced X-ray emission (PIXE) spectrum from Randall's plaque, indicating the presence of various elements. Figure 5.5-B, C, D, and E offer more detailed views of Ca and Zn distributions at this micrometer scale.

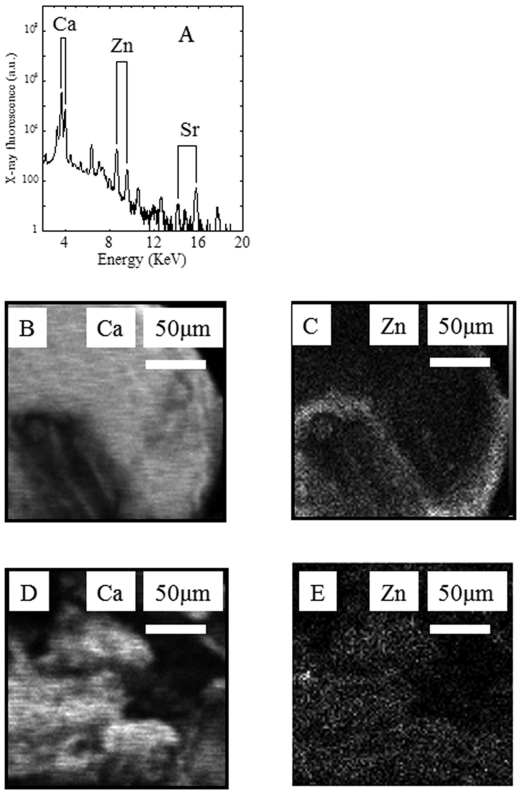

Figure 5.5: Elemental analysis of Randall's plaques in two biopsies.(**A**) Typical PIXE spectrum collected for a Randall's plaque. (**B**, **C**) Elemental distribution maps of RP in biopsy 1: Ca (**B**) and Zn (**C**). Lighter regions indicate a higher concentration of the element (scale bar: 50 μm). Total beam charge collected: 0.7 μC. (**D** and **E**) Elemental distribution maps of RP in biopsy 2: Ca (**D**) and Zn (**E**)(scale bar: 50 μm). Adapted from (Bazin et al., 2012).

5.2. Case studies: application of developed techniques

5.2.1. Sample preparation

The studied renal papillae were collected from an animal genetic model known as Abcc6$^{-/-}$ mice. The ABCC6 gene plays a crucial role as a calcification inhibitor by regulating the concentration of pyrophosphate (PPi) in the body. A deficiency in PPi can lead to increased calcium phosphate (CaP) precipitation. In the case of ABCC6 deficiency, it can potentially enhance CaP crystallization, electively at the tips of renal papillae (see Figure 5.6). This process can therefore promote the formation of Randall plaques (Letavernier et al., 2018).

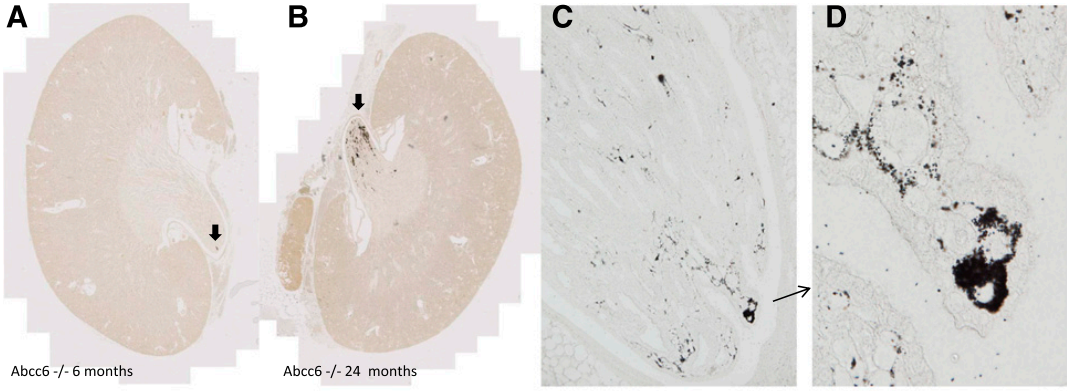

Figure 5.6: Calcifications were specifically observed at the papilla's tip in Abcc6$^{-/-}$ mice, as indicated by digital slide scanning (highlighted by arrows in **A** and **B**). **C**: Papilla slices have round-shaped and circular structures surrounding tubules (Magnification = 3200 and zoomed view in **D**). Adapted from (Letavernier et al., 2018).

The Abcc6$^{-/-}$ mouse model is a useful tool for our application study because it effectively mimics human diseases associated with calcification disorders. This animal model allows us to effectively reduce or even eliminate the potential impact of biological variability that may arise from factors like tumors or other diseases, which could otherwise complicate investigations if using human kidney samples. The presence of trace elements in the papilla is influenced by various factors, including diet, metabolism, and environmental conditions. This animal model provides a controlled and consistent experimental system, as all the mice used in the study have the same genetic mutation, thus facilitating further study of the formation of Randall's plaque in the renal papillae.

As shown in Figure 5.7, the papillae were then preserved in a 4% formaldehyde solution and embedded in paraffin. To facilitate scanning, sections with a thickness ranging from 4 µm to 50 µm were performed with a microtome (Microm HM340E, Thermo Scientific) and placed on silicon nitride membranes (frame size: 7.5 mm × 7.5 mm, membrane size: 3 mm × 3 mm). To ensure proper sample spreading, a drop of reverse osmosis water was applied to the membrane. The prepared sections were heated at 37 °C for 10 to 20 minutes in an oven. Excess water was removed using a pipette.

All studies were performed in accordance with the European Union, NIH guidelines (Comité d'Ethique en Experimentation Charles Darwin C2EA-05) and all our methods are reported as recommended by ARRIVE guidelines. The project was authorized by the Health Ministry and local Ethics Committee (authorization 11420 2017092015335292) (Guo et al., 2022).

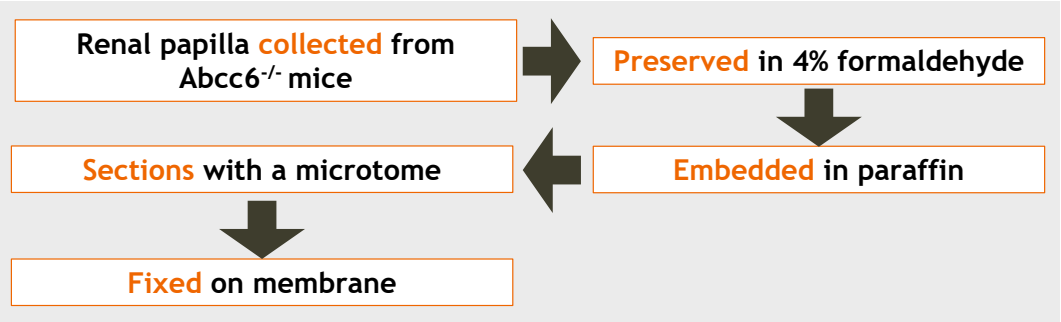

Figure 5.7: Renal sample preparation workflow.

5.2.2. Experimental: Data acquisition, processing, and data reconstruction

5.2.2.1. Data acquisition

The experiment was performed at the NANOSCOPIUM beamline of the Soleil synchrotron.

Full-field tomography

A total of 3600 projection images were taken with an exposure time of 50 ms per projection at the CX2 experimental station.

Sparse tomography

Sparse tomography was carried out at the CX3 experimental station with a focused beam energy of 12 keV. A $586 \times 272\,\mu m^2$ region of the sample was mapped at 21 angular positions over 360 ° with a lateral step size of 2 µm and an exposure time of 20 ms/pixel, with a total measurement time of 5 h (Guo et al., 2022).

High-resolution 2D tomography

High-resolution 2D tomography was performed at various altitudes of the sample. The scans were carried out using an angular step of 1 °, a dwell time of 40 ms/pixel, and a pixel size of 2 µm.

High-resolution 2D imaging

We conducted high-resolution 2D imaging for various regions to meet investigation requirements. The scans had pixel sizes of 0.4/0.5 µm with a 40 ms/pixel dwell time.

High-resolution local tomography

High-resolution local tomography was performed on a small volume of interest. This local tomography comprised 65 angular positions spanning a full 360 ° rotation, with a dwell time of 40 ms/pixel and a uniform lateral step size of 500 nm (Guo et al., 2022). The area covered by this local tomography was $67 \times 16\,\mu m^2$, and the total acquisition time took 3 hours.

5.2.2.2. Data processing

1. Full-field tomography data processing

For full-field X-ray tomography at the NANOSCOPIUM beamline (Medjoubi et al., 2018), the dataset was first flat-field corrected. The transmitted intensity I_{obj} needs to be normalized by a dark image I_{dark} and white field image I_{ref} (image taken without sample) using the following formula:

$$I_{cor} = \frac{I_{obj} - I_{dark}}{I_{ref} - I_{dark}} \tag{5.1}$$

where I_{cor} is the final corrected image, I_{obj} is the image of the sample with beam, I_{dark} is the image under the dark environment, and I_{ref} is the image without sample under beam illumination.

Following the flat-field correction, the Paganin filter was applied to the dataset (Paganin et al., 2002). This filter can enhance the phase contrast in the projection images. This filter is useful for weakly absorbing biological tissues.

The full-field tomography reconstruction was realized by a GPU-based filtered back-projection (FBP) algorithm. This algorithm was selected for its fast and user-friendly reconstruction capabilities suitable for full-field imaging.

2. XRF mapping and XRF tomography

For XRF mapping and XRF tomography, the raw summed spectra were fitted first to identify the peak areas of the elements present in the sample under investigation. The distribution maps and the sinograms of these elements were then extracted from the raw dataset using an in-house MATLAB code. The obtained XRF tomography datasets were reconstructed with the MLEM algorithm. The overall reduction process is integrated automatically in a robust in-house MATLAB code (Guo et al., 2022). The reconstructed volumetric data were exported as 16-bit z-stacks and imported either to ImageJ for analysis or to Chimera for 3D visualization. Moreover, the transmitted and incident beam intensity ratio at each pixel gave access to the sample transmission maps.

3. Pearson correlation factor

To quantify the correlation in 2D/3D between elements, we used the Pearson correlation coefficient, a common metric in X-ray microscopy dataset analysis. The Pearson correlation coefficient is defined as:

$$r = \frac{\sum(x_i - \bar{x})(y_i - \bar{y})}{\sqrt{\sum(x_i - \bar{x})^2 \sum(y_i - \bar{y})^2}} \tag{5.2}$$

where x_i and y_i are the individual data points, $\bar{x}$ and $\bar{y}$ are the means of x_i and y_i, respectively.

4. Quantitative analysis

For quantitative analysis, the 2D XRF maps were calibrated by a reference standard. This was achieved by first fitting the raw X-ray fluorescence spectra of the sample, and then the elemental contents were calibrated against a homogeneous multi-element AXO standard thin film RF7-200-S2372(AXO DRESDEN GmbH, Dresden, SN, Germany). The standard was scanned with the beam energy of 12 keV with a pixel size of 1 μm and a dwell time of 50 ms per pixel.

All data were normalized to 1 second integration time per pixel, and the incident photon intensity was recorded by the intensity monitor which is positioned before the KB mirrors. After elemental quantification, threshold masks might be performed for scans of interest in order to achieve the elemental concentrations in different identified features.

5.2.3. Results and analysis

Our investigations started by using the phase-contrast full-field technique for the renal papilla. The result of the full-field tomography is presented in Figure 5.8, showing a detailed view of the papilla's morphology with a spatial resolution of 1.6 μm.

In the figure, high-contrast zones (depicted in white) indicate regions where variations in refractive indices or densities within the renal papilla are pronounced. Notably, this technique allows for the distinction of boundaries between calcification sites and the surrounding tissues within the sample.

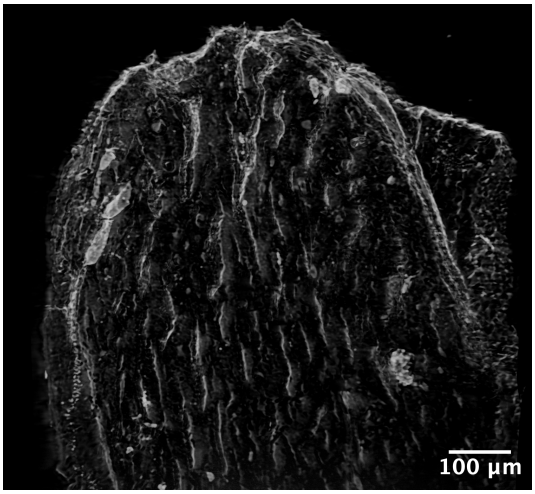

Figure 5.8: Full-field phase contrast X-ray tomography reconstruction of a longitudinally sectioned mice renal papilla, showing the 3D morphology of the sample.

Further experimental investigations were dedicated to the analysis of the elemental distribution in 2D & 3D using scanning XRF techniques. As the etiology of the stones frequently begins at the tip of the papilla, we performed further scanning X-ray fluorescence imaging at the tip of the renal papilla.

The elemental distribution of calcium (Ca), zinc (Zn), and phosphorus (P) in the indicated region (highlighted in white in Figure 5.9-A) was determined using micro-XRF imaging with a pixel size of 1 μm. The elemental maps in Figure 5.9-B-D show varying levels of co-localization between Ca, Zn, and P. Different sizes of interstitial calcifications were observed. The quantitative Ca map indicates an average calcium concentration of 300 pg/μm^2 within this area. Figure 5.9-E displays the 2D transmission image of this region. Given the sample's thickness is uniform (50 μm), the image contrast is influenced by chemical composition or density variation within the sample. The areas rich in calcium also exhibit the highest X-ray absorption.

As shown in Figure 5.9-F, the distribution maps of Ca and Zn within the same interstitial regions are overlapped. In this analysis, we found a Pearson correlation coefficient of 0.73 for Ca and Zn, indicating a positive correlated relationship between these two elements (Ratner, 2009).

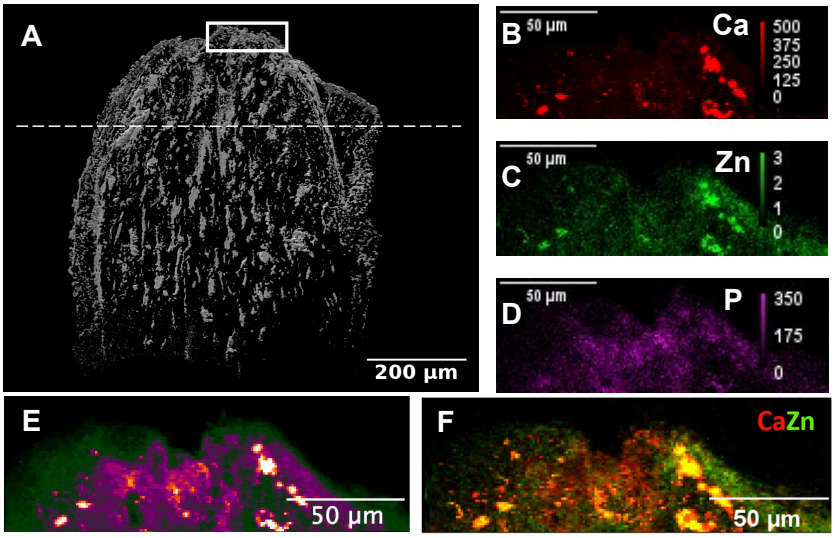

Figure 5.9: Localization of nanometer scale calcifications at the tip of the papilla. The scan area in **B** is indicated in a white rectangle in **A**. **B**-**D**: Elemental concentration maps of calcium, zinc and phosphorus distribution at the tip of the papilla (Unit: pg/µm^2). **E**: 2D scanning transmission image of the same area. **F**: Overlapped elemental distribution maps of Ca and Zn of the same region.

Our decision to further investigate Zn is driven by its abundance as a trace element present in the papilla. This initiative also builds on a previous mesoscale study that employed the 2D XRF technique to investigate Randall's plaque, which offered initial evidence of a possible correlation between trace elements, particularly zinc, and the formation of Randall's plaque (Carpentier et al., 2011).

Zinc is one of the essential trace elements in the human body, participating as a vital co-factor in over 300 enzymatic processes (Zastrow and Pecoraro, 2014). Notably, it plays a significant role in mammalian biomineralization, particularly in the formation of apatite. Despite its importance, the precise functions of zinc in various biomineralization processes, including those related to kidney stone formation, remain poorly understood. The role of zinc in Randall's plaque formation process is a subject of ongoing debate, with ambiguous results.

Regarding pathological soft tissue calcification, especially kidney papillary calcification like Randall's plaque, as well as vascular calcification, studies suggest that zinc supplementation can inhibit phosphate-induced osteo-/chondrogenic transdifferentiation of vascular smooth muscle cells and vascular calcification through an active cellular mechanism. Consequently, zinc supplementation has been proposed as a potential intervention to reduce pathological calcification in patients with chronic kidney disease (Voelkl et al., 2018). In other *in vitro* studies, Zn is considered an inhibitor of calcium phosphate mineralization (Rao and Choudhary, 2009; Atakan et al., 2007).

In this case, zinc should predominantly appear in the outer part of incipient calcifications. However, conventional 2D XRF images, which provide average information across the entire measured sample thickness, do not offer conclusive depth-resolved insight into the precise elemental colocalization and correlation within heterogeneous micrometer-sized features.

Thus, as a next step, we conducted 3D scanning sparse XRF tomography at the top of the sample, in the region shown in Figure 5.10-A. The reconstructed Ca and Zn tomograms illustrate the calcification of varying sizes and morphologies. Within these structures, we observed a high degree of spatial colocation between calcium and zinc in different features, such as tubular plugs and interstitial calcifications (Figure 5.11-A). The Pearson correlation factor calculated for calcium and zinc across the entire volume of the measured papilla sample region is 0.67.

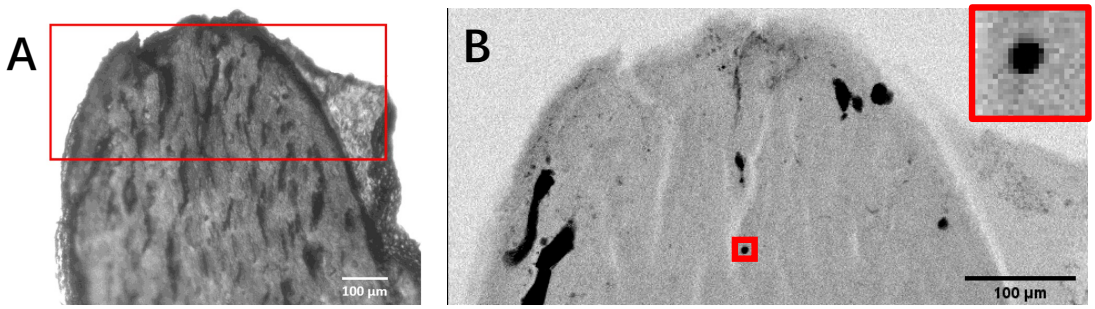

Figure 5.10: Region selection for sparse scanning tomography (Guo et al., 2022). (**A**) Optical microscope image of the mouse papilla sample, mimicking human kidney calcifications. The scanned region is marked in red. (**B**) Transmission image of the tip of the sample. The small red rectangle in the middle marks the sample region chosen for local tomography. The zoom-in image of this region is inserted into the upper-right corner.

In Figure 5.11-B, the reconstructed tomogram of calcium and zinc at the altitude marked by the dashed line in Figure 5.11-A is presented. Zinc is predominantly distributed around calcium, evident in both the tubular plug and the calcified sphere positioned in the middle.

To gain deeper insights into the elemental distribution within micron-scale calcium and zinc structures during the early stages of calcification, we conducted 3D local tomography focused on a small calcification sphere, as indicated by the white circle in Figure 5.11-A.

Considering its small size, this sphere can be viewed as representative of the early stages of Randall's plaque formation. Throughout the volume of this sphere, a Pearson correlation coefficient of 0.72 was calculated for calcium and zinc. The reconstructed local tomograms reveal that Ca is primarily concentrated in the core region of the calcification sphere. As the radius extends outward, Zn is enriched within a few micrometers thick rim on the surface of the calcification micro-sphere, as shown in the cut-off view of the 3D volume rendering in Figure 5.11-C&D. Interestingly, similar structures were observed in other smaller nano-calcifications (Figure 5.11-C), where zinc coats the surface of interstitial calcification spheres.

Furthermore, we noted that the surface morphology becomes less regular as Zn accumulates. Supported by findings from studies such as (Fujii et al., 2006; Ren et al., 2009), this suggests that Zn might play a role in altering the structure and stability of calcifications as they grow.

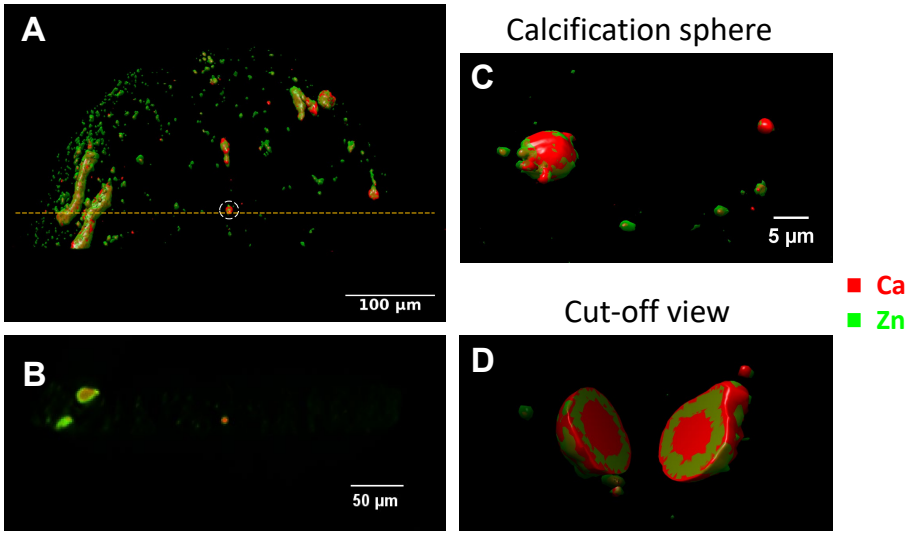

Figure 5.11: Sparse and local scanning X-ray tomography of a renal papilla sample (Guo et al., 2022). (**A**) Sparse tomography reconstruction of Zn and Ca. The small circle in the middle marks the sample region chosen for local tomography. (**B**) Reconstructed single sinogram of Ca and Zn at the altitude of the calcification sphere indicated in dashed line in **A**. (**C**) Reconstructed 3D local tomogram of Ca and Zn of the calcification micro-sphere. (**D**) Cut-off view at the middle of the calcification micro-sphere.

In the quantitative analysis, as depicted in Figure 5.12-A, we constructed a series of 1-pixel-thick shells within the tomogram of the calcification sphere, each shell representing a different depth from the surface, with color coding indicating their specific positions. Figure 5.12-B demonstrates the variation in Ca and Zn intensity within the sum spectra of the outer and inner shells. These spectra were normalized by their respective voxel numbers. Notably, Zn intensity is high in the surface shell and low in the core, while Ca intensity shows the opposite trend, being reduced at the surface shell and enriched at the core. This observation is further supported by the changes in Ca and Zn concentrations throughout the calcification sphere, as shown in Figure 5.12-C. The increasing trend in the difference between Zn and Ca concentration with the radius confirms that Zn is predominantly distributed on the outer layer of the calcification sphere.

In some kidney stone studies, it has been proposed that the presence of trace elements is often not indicative of an active catalyst role in stone formation. Instead, it is more likely a consequence of passive processes involving the adsorption and/or absorption of these elements onto and/or into stones (Bazin et al., 2009, 2007, 2008; Carpentier et al., 2011). This is primarily attributed to the similarities in charge and size between these elements and calcium, such as Zn (Joost and Tessadri, 1987). If this passive process were the case, we would expect to observe a homogeneous spatial distribution of these elements within Randall's plaque.

Nevertheless, our observations suggest a different scenario. We observed an element gradient within the calcification sphere, which raises questions about the idea that zinc is a direct factor inducing (hydroxy) apatite crystallization. If zinc were indeed responsible for this process, we would expect to find it concentrated in the core of calcifications.

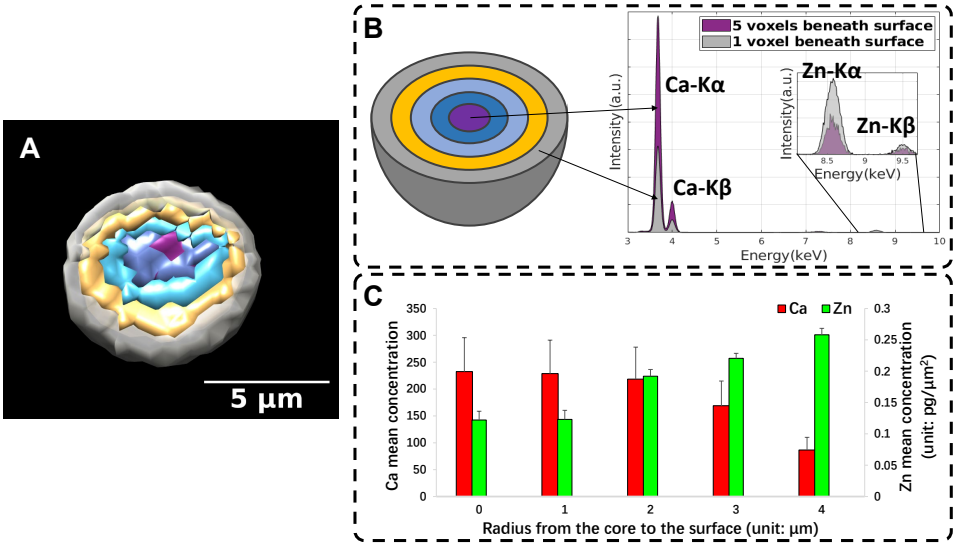

Figure 5.12: Elemental variation throughout the calcification sphere. **A**: Cut-off view of the shells extracted from the calcification sphere. **B**: Sum-spectra of the shell 1 pixel beneath the surface of the calcification sphere and of the shell 5 pixels beneath the surface. **C**: Ca and Zn mean concentration variation with the calcification sphere radius (unit: $pg/\mu m^2$).

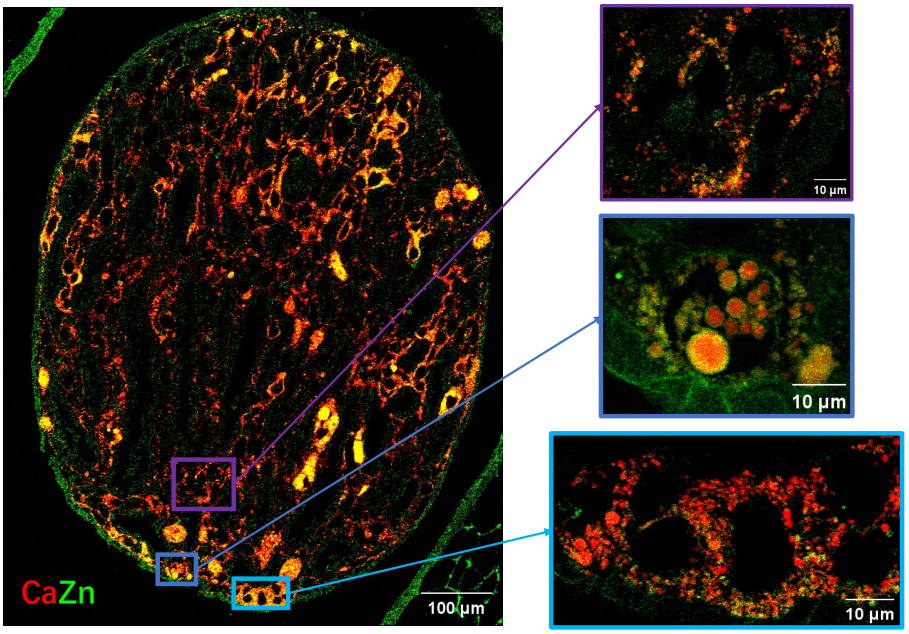

Figure 5.13: Ca-Zn correlation found in the transverse section of a different renal papilla sample. The colored boxed regions in the left panels represent areas that were scanned at a higher resolution (pixel size = 0.15 µm), as displayed in the right column panels.

To enhance the statistical significance and further observe the spatial distribution relationship between Zn and Ca, we performed further 2D scanning XRF imaging scans on 4 samples from the 2-year-old mouse model (see Figure A.1). As one of the examples, Figure 5.13 presents consistent evidence of the correlation between Ca and Zn in both tubular plugs and interstitial calcifications. Mean values of elemental concentrations were obtained in 135 regions with different features. The results reported in Table 5.2 show that the concentrations of Zn and Ca are significantly different in the tubular plugs and interstitial calcifications. In addition to Zn, tubular plugs have higher concentrations of trace elements such as S and Fe.

	Interstitial calcifications	**Tubular plugs**
Origin	At the papillary tip as a mineral overgrowth	Kidney stones developed under the tubular surface
Element concentrations (mean values, unit: $pg/\mu m^2$)		
Ca	92.37	672.99
P	71.49	348.18
S	3.03	13.11
Zn	0.22	0.89
Fe	0.03	0.12

Table 5.2: Comparison of two different types of calcifications.

It is crucial to compare the zinc proportions and spatial distribution with respect to calcium in tubular plugs. The Pearson correlation ratio between Zn and Ca was calculated for 135 regions of interest in interstitial calcifications and tubular plugs. This ratio in the interstitial calcifications (with a mean value of 0.71) did not differ from that in the tubular plugs (with a mean value of 0.68). This implies that the presence of Zn is likely not due to its existence in nanoparticles from osteoblast-like cells (Voelkl et al., 2018), as these particles are identified in the tissue and not in tubules. Additionally, it's probably not due to a tissular reaction to limit crystallization.

5.2.3.1. Comparison to previous studies and conclusion

Previous studies using a rotating anode X-ray generator observed a higher concentration of zinc in Randall's plaque compared to urine or kidney tissue. This led to the hypothesis that zinc could serve as a marker for tissue inflammatory reactions in pathological calcification (Carpentier et al., 2011). This idea drew inspiration from earlier reports indicating the uniform distribution of trace elements within kidney stones (Grases et al., 1989).

Furthermore, a study conducted by (Durak et al., 1992), utilizing atomic absorption spectroscopy (AAS), revealed higher concentrations of zinc, as well as iron and copper, in the interior rather than the crust of stones. This suggested a potential role for zinc and other metals in the early stages of stone formation. However, it's important to note that AAS, as an elemental analysis technique, requires sample dissolution or digestion, which can introduce inaccuracies due to incomplete dissolution and significant dilutions.

Additionally, some studies have explored the impact of zinc on calcium apatite crystal growth (Kanzaki et al., 2000; Wu et al., 2009). At low concentrations, Zn^{2+} ions were found to impede calcium apatite crystal growth, while elevated concentrations fostered the creation of amorphous calcium phosphate or zinc-substituted calcium phosphate (LeGeros et al., 1999). Substituting calcium with zinc was observed to reduce the propensity of apatites to crystallize, resulting in smaller and more irregularly shaped calcium apatite crystals due to higher Zn^{2+} concentrations (Fujii et al., 2006; Ren et al., 2009).

In our investigation, we employed scanning 2D mapping and multi-scale 3D tomography techniques using a synchrotron-based X-ray beam, to explore high spatial distribution trace element distribution within Randall's plaques. Our study revealed a non-uniform spatial distribution of zinc, where its concentration progressively rises as the calcification radius expands. This suggests that zinc may not act as an inhibitor in the growth of Randall's plaque. This study represents an advancement beyond the findings reported at the micrometer scale (Khan, 2022; Perre et al., 2022).

The rapid and robust workflow that has been implemented opens up the possibility of conducting systematic investigations involving a larger number of samples in future research. This approach promises to enhance our understanding of the early-stage processes of crystal nucleation, growth, and aggregation, offering new possibilities for both accurate diagnoses and preventive treatments in the field of pathological calcifications.

5.2.3.2. Dose estimation

As discussed in Section 4.3.3.7, we calculated the absorbed dose in air for dose estimation. Table 5.3 presents a comparison of dose rates and integrated doses associated with different scans in our study. Standard 2D XRF scanning, sparse and local tomography shows a dose rate of ~10^5 Gy/s, while high-resolution (HR) 2D XRF scanning exhibits substantially higher dose rates, ranging from 3.0×10^7 to 3.2×10^7 Gy/s and corresponding integrated doses of ~10^6 Gy. It is notable that sparse tomography has an integrated dose of 3.2×10^4 Gy, which is 100 times lower than the doses associated with local tomography or high-resolution 2D XRF scanning. These values provide a quantitative measure of the radiation exposure for each scan type, which is crucial for optimizing the balance between image quality and sample preservation.

	Scan type	**Dose rate (Gy/s)**	**Integrated dose (Gy)**
Figure 5.9	2D XRF scanning	2.9×10^5	1.1×10^4
Figure 5.11	Sparse tomography	8.0×10^5	3.2×10^4
	Local tomography	8.5×10^5	2.2×10^6
Figure 5.13	2D XRF scanning	6.7×10^5	3.4×10^4
	HR 2D XRF scanning (top)	3.0×10^7	1.2×10^6
	HR 2D XRF scanning (middle)	3.2×10^7	1.3×10^6
	HR 2D XRF scanning (bottom)	3.0×10^7	1.2×10^6

Table 5.3: Dose estimation for different scans in this chapter.

5.2.3.3. Discussion of the limitations of the current study

The number of specimens investigated in our study was small (<10), which limits the generalizability of our findings. Our study also raises the question for future studies about the chemical form of Zn in kidney stone formation. Of note, none of the clinical studies determined the form in which zinc was present in the urine samples (Ramaswamy et al., 2015). For example, Zn^{2+} can bind directly to oxalates and phosphates (Chou et al., 2007) or with higher binding affinity to small thiols and peptides (Winterbourn et al., 2002) which might influence the effects of zinc on stone formation. Hence, understanding the role of zinc in lithogenesis will require further analysis including the chemical forms of zinc. While our study provides insights into the spatial distribution of zinc in Randall's plaque, it does not elucidate the precise mechanisms by which zinc influences plaque formation. Future research should aim to uncover the underlying mechanisms involved in the genesis of Randall's plaque and the specific role of zinc in this process.

References

I. H. Atakan, M. Kaplan, G. Seren, T. Aktoz, H. Gül, and O. Inci. Serum, urinary and stone zinc, iron, magnesium and copper levels in idiopathic calcium oxalate stone patients. *Int Urol Nephrol*, 39(2):351–356, 2007. ISSN 0301-1623. doi: 10.1007/s11255-006-9050-4.

D. Bazin and M. Daudon. Pathological calcifications and selected examples at the medicine–solid-state physics interface. *J. Phys. D: Appl. Phys.*, 45(38):383001, Sept. 2012. ISSN 0022-3727. doi: 10.1088/0022-3727/45/38/383001. URL https://dx.doi.org/10.1088/0022-3727/45/38/383001.

D. Bazin, P. Chevallier, G. Matzen, P. Jungers, and M. Daudon. Heavy elements in urinary stones. *Urol Res*, 35(4):179–184, Aug. 2007. ISSN 1434-0879. doi: 10.1007/s00240-007-0099-z. URL https://doi.org/10.1007/s00240-007-0099-z.

D. Bazin, X. Carpentier, O. Traxer, D. Thiaudière, A. Somogyi, S. Reguer, G. Waychunas, P. Jungers, and M. Daudon. Very first tests on SOLEIL regarding the Zn environment in pathological calcifications made of apatite determined by X-ray absorption spectroscopy. *J Synchrotron Rad*, 15(5):506–509, Sept. 2008. ISSN 0909-0495. doi: 10.1107/S0909049508014556. URL https://scripts.iucr.org/cgi-bin/paper?S0909049508014556.

D. Bazin, X. Carpentier, I. Brocheriou, P. Dorfmuller, S. Aubert, C. Chappard, D. Thiaudière, S. Reguer, G. Waychunas, P. Jungers, and M. Daudon. Revisiting the localisation of zn^{2+} cations sorbed on pathological apatite calcifications made through x-ray absorption spectroscopy. *Biochimie*, 91(10):1294–1300, 2009. ISSN 0300-9084. doi: https://doi.org/10.1016/j.biochi.2009.05.009. URL https://www.sciencedirect.com/science/article/pii/S0300908409001497.

D. Bazin, M. Daudon, C. Combes, and C. Rey. Characterization and some physicochemical aspects of pathological microcalcifications. *Chem Rev*, 112(10):5092–5120, Oct. 2012. ISSN 1520-6890. doi: 10.1021/cr200068d.

X. Carpentier, D. Bazin, P. Jungers, S. Reguer, D. Thiaudière, and M. Daudon. The pathogenesis of Randall's plaque: a papilla cartography of Ca compounds through an *ex vivo* investigation based on XANES spectroscopy. *J Synchrotron Rad*, 17(3):374–379, May 2010. ISSN 0909-0495. doi: 10.1107/S0909049510003791. URL https://scripts.iucr.org/cgi-bin/paper?S0909049510003791.

X. Carpentier, D. Bazin, C. Combes, A. Mazouyes, S. Rouzière, P. A. Albouy, E. Foy, and M. Daudon. High Zn content of Randall's plaque: A -X-ray fluorescence investigation. *Journal of Trace Elements in Medicine and Biology*, 25(3):160–165, July 2011. ISSN 0946672X. doi: 10.1016/j.jtemb.2011.05.004. URL https://linkinghub.elsevier.com/retrieve/pii/S0946672X11000769.

A. H. K. Chou, R. Z. LeGeros, Z. Chen, and Y. Li. Antibacterial effect of zinc phosphate mineralized guided bone regeneration membranes. *Implant Dent*, 16(1):89–100, Mar. 2007. ISSN 1056-6163. doi: 10.1097/ID.0b013e318031224a.

H.-J. Chung. The role of Randall plaques on kidney stone formation. *Transl Androl Urol*, 3(3):251–254, Sept. 2014. ISSN 2223-4691. doi: 10.3978/j.issn.2223-4683.2014.07.03. URL https://www.ncbi.nlm.nih.gov/pmc/articles/PMC4708577/.

M. Daudon and D. Bazin. When the Synchrotron radiations highlight the Randall's plaques and kidney concretions. *J. Phys.: Conf. Ser.*, 425(2):022006, Mar. 2013. ISSN 1742-6596. doi: 10.1088/1742-6596/425/2/022006. URL https://dx.doi.org/10.1088/1742-6596/425/2/022006.

M. Daudon, O. Traxer, P. Jungers, and D. Bazin. Stone Morphology Suggestive of Randall's Plaque. *AIP Conference Proceedings*, 900(1):26–34, Apr. 2007. ISSN 0094-243X. doi: 10.1063/1.2723556. URL https://doi.org/10.1063/1.2723556.

M. Daudon, O. Traxer, J. C. Williams, and D. C. Bazin. *Randall's Plaques*, pages 103–112. Springer London, London, Jan. 2011. doi: 10.1007/978-1-84800-362-0_7. URL https://doi.org/10.1007/978-1-84800-362-0_7.

I. Durak, Z. Kilic, A. Sahin, and M. Akpoyraz. Analysis of calcium, iron, copper and zinc contents of nucleus and crust parts of urinary calculi. *Urol Res*, 20(1):23–26, 1992. ISSN 0300-5623. doi: 10.1007/BF00294330.

E. Fujii, M. Ohkubo, K. Tsuru, S. Hayakawa, A. Osaka, K. Kawabata, C. Bonhomme, and F. Babonneau. Selective protein adsorption property and characterization of nano-crystalline zinc-containing hydroxyapatite. *Acta Biomater*, 2(1):69–74, Jan. 2006. ISSN 1742-7061. doi: 10.1016/j.actbio.2005.09.002.

C. Gay, E. Letavernier, M.-C. Verpont, M. Walls, D. Bazin, M. Daudon, N. Nassif, O. Stéphan, and M. de Frutos. Nanoscale Analysis of Randall's Plaques by Electron Energy Loss Spectromicroscopy: Insight in Early Biomineral Formation in Human Kidney. *ACS Nano*, 14(2):1823–1836, Feb. 2020. ISSN 1936-0851. doi: 10.1021/acsnano.9b07664. URL https://doi.org/10.1021/acsnano.9b07664.

F. Grases, C. Genestar, and A. Millán. The influence of some metallic ions and their complexes on the kinetics of crystal growth of calcium oxalate. *Journal of Crystal Growth*, 94(2):507–512, Feb. 1989. ISSN 0022-0248. doi: 10.1016/0022-0248(89)90028-6. URL https://www.sciencedirect.com/science/article/pii/0022024889900286.

R. Guo, A. Somogyi, D. Bazin, E. Bouderlique, E. Letavernier, C. Curie, M.-P. Isaure, and K. Medjoubi. Towards routine 3D characterization of intact mesoscale samples by multi-scale and multimodal scanning X-ray tomography. *Sci Rep*, 12(1):16924, Oct. 2022. ISSN 2045-2322. doi: 10.1038/s41598-022-21368-0. URL https://www.nature.com/articles/s41598-022-21368-0.

J. Joost and R. Tessadri. Trace element investigations in kidney stone patients. *Eur Urol*, 13(4):264–270, 1987. ISSN 0302-2838. doi: 10.1159/000472792.

N. Kanzaki, K. Onuma, G. Treboux, S. Tsutsumi, and A. Ito. Inhibitory Effect of Magnesium and Zinc on Crystallization Kinetics of Hydroxyapatite (0001) Face. *J. Phys. Chem. B*, 104(17):4189–4194, May 2000. ISSN 1520-6106. doi: 10.1021/jp9939726. URL https://doi.org/10.1021/jp9939726.

S. R. Khan. Inflammation and injury: what role do they play in the development of Randall's plaques and formation of calcium oxalate kidney stones? *Comptes Rendus. Chimie*, 25(S1):355–372, 2022. ISSN 1878-1543. doi: 10.5802/crchim.93. URL https://comptes-rendus.academie-sciences.fr/chimie/articles/10.5802/crchim.93/.

R. Z. LeGeros, C. B. Bleiwas, M. Retino, R. Rohanizadeh, and J. P. LeGeros. Zinc effect on the in vitro formation of calcium phosphates: relevance to clinical inhibition of calculus formation. *Am J Dent*, 12(2):65–71, Apr. 1999. ISSN 0894-8275.

E. Letavernier, G. Kauffenstein, L. Huguet, N. Navasiolava, E. Bouderlique, E. Tang, L. Delaitre, D. Bazin, M. de Frutos, C. Gay, J. Perez, M.-C. Verpont, J.-P. Haymann, V. Pomozi, J. Zoll, O. Le Saux, M. Daudon, G. Leftheriotis, and L. Martin. ABCC6 Deficiency Promotes Development of Randall Plaque. *JASN*, 29(9):2337–2347, Sept. 2018. ISSN 1046-6673, 1533-3450. doi: 10.1681/ASN.2017101148. URL https://jasn.asnjournals.org/lookup/doi/10.1681/ASN.2017101148.

K. Medjoubi, G. Baranton, and A. Somogyi. Fast full-field micro-tomography at the Nanoscopium multitechnique nanoprobe beamline of Synchrotron Soleil. *Microscopy and Microanalysis*, 24(S2):252–253, Aug. 2018. ISSN 1431-9276, 1435-8115. doi: 10.1017/S1431927618013612.

D. Paganin, S. C. Mayo, T. E. Gureyev, P. R. Miller, and S. W. Wilkins. Simultaneous phase and amplitude extraction from a single defocused image of a homogeneous object. *Journal of Microscopy*, 206(1):33–40, 2002. ISSN 1365-2818. doi: 10.1046/j.1365-2818.2002.01010.x. URL https://onlinelibrary.wiley.com/doi/abs/10.1046/j.1365-2818.2002.01010.x.

E. V. d. Perre, D. Bazin, V. Estrade, E. Bouderlique, K. M. Wissing, M. Daudon, and E. Letavernier. Randall's plaque as the origin of idiopathic calcium oxalate stone formation: an update. *Comptes Rendus. Chimie*, 25(S1):373–391, 2022. ISSN 1878-1543. doi: 10.5802/crchim.102. URL https://comptes-rendus.academie-sciences.fr/chimie/articles/10.5802/crchim.102/.

K. Ramaswamy, D. W. Killilea, P. Kapahi, A. J. Kahn, T. Chi, and M. L. Stoller. The elementome of calcium-based urinary stones and its role in urolithiasis. *Nat Rev Urol*, 12(10):543–557, Oct. 2015. ISSN 1759-4812, 1759-4820. doi: 10.1038/nrurol.2015.208. URL https://www.nature.com/articles/nrurol.2015.208.

T. Rao and V. Choudhary. Chemoinhibition of mineralization of urinary stone forming minerals by magnesium and zinc ions in aqueous and urinary milieu. *Asian Journal of Chemistry*, 21(3):1730–1738, 2009. ISSN 0970-7077.

B. Ratner. The correlation coefficient: Its values range between +1/-1, or do they? *J Target Meas Anal Mark*, 17(2):139–142, June 2009. ISSN 1479-1862. doi: 10.1057/jt.2009.5. URL https://doi.org/10.1057/jt.2009.5.

F. Ren, R. Xin, X. Ge, and Y. Leng. Characterization and structural analysis of zinc-substituted hydroxyapatites. *Acta Biomater*, 5(8):3141–3149, Oct. 2009. ISSN 1878-7568. doi: 10.1016/j.actbio.2009.04.014.

J. Voelkl, R. Tuffaha, T. T. D. Luong, D. Zickler, J. Masyout, M. Feger, N. Verheyen, F. Blaschke, M. Kuro-O, A. Tomaschitz, S. Pilz, A. Pasch, K.-U. Eckardt, J. E. Scherberich, F. Lang, B. Pieske, and I. Alesutan. Zinc Inhibits Phosphate-Induced Vascular Calcification through TNFAIP3-Mediated Suppression of NF- B. *J Am Soc Nephrol*, 29(6):1636–1648, June 2018. ISSN 1533-3450. doi: 10.1681/ASN.2017050492.

C. C. Winterbourn, A. V. Peskin, and H. N. Parsons-Mair. Thiol oxidase activity of copper, zinc superoxide dismutase. *J Biol Chem*, 277(3):1906–1911, Jan. 2002. ISSN 0021-9258. doi: 10.1074/jbc.M107256200.

L. N. Y. Wu, B. R. Genge, and R. E. Wuthier. Differential effects of zinc and magnesium ions on mineralization activity of phosphatidylserine calcium phosphate complexes. *J Inorg Biochem*, 103(7):948–962, July 2009. ISSN 1873-3344. doi: 10.1016/j.jinorgbio.2009.04.004.

M. L. Zastrow and V. L. Pecoraro. Designing Hydrolytic Zinc Metalloenzymes. *Biochemistry*, 53(6):957–978, Feb. 2014. ISSN 0006-2960. doi: 10.1021/bi4016617. URL https://www.ncbi.nlm.nih.gov/pmc/articles/PMC3985962/.

CHAPTER 6
CONCLUSION

In conclusion, this thesis has fulfilled two main objectives: the development of a quantitative scanning sparse XRF tomography method at the NANOSCOPIUM beamline and its application in the investigation of trace element spatial distribution in Randall's plaque.

Throughout this research, the implementation of adaptive algorithms is essential for sparse tomography. Specifically, I optimized the MLEM reconstruction algorithm to facilitate the integration of XRF tomography into the multi-scale scanning XRF tomography workflow. This process involved the exploration of various reconstruction algorithms, from traditional analytical techniques like Filtered Back Projection (FBP) to iterative methods like MLEM. Furthermore, I incorporated quantitative methods into the workflow, enabling element concentration calculations in both 2D and 3D.

Despite these achievements, there remain avenues for further improvement. Firstly, there's potential for further improvement by implementing advanced algorithms such as Ordered Subset Expectation Maximization (OSEM) to expedite the reconstruction process. Regularized iterative methods can also be powerful tools by introducing additional constraints or penalties into the problem.

Secondly, data acquisition procedures could be optimized further by adopting an innovative spiral scanning configuration for XRF tomography, thereby mitigating both data acquisition time and potential radiation exposure.

The third improvement entails the implementation of self-absorption correction mechanisms in XRF imaging and tomography. Correcting the XRF intensity received in each voxel of the tomogram for each reconstructed element is crucial for accurate XRF analysis, since the XRF signals may be absorbed when passing through a complex structure in the sample.

Last but not least, a promising avenue involves enhancing the automation of our data processing pipeline. Currently, data processing consists of distinct blocks, including data reduction, correction, and reconstruction, which are executed sequentially. However, streamlining these processes could be achieved through the development of a more integrated and automated system, thereby minimizing the necessity for manual intervention and potentially accelerating the entire workflow.

The second major focus of my work involved applying the developed methodology to the characterization of Randall's plaque. This application study highlighted the utility of the developed workflow in biomedical research. Our findings revealed a high correlation between zinc and calcium present in both interstitial calcifications and tubular plugs in the renal papilla.

As discussed in Chapter 5, future research directions include augmenting our data statistics through increased sample numbers and investigating further the chemical forms of zinc within Randall's plaque. These efforts will provide deeper insights into the roles that trace elements play in the processes of Randall's plaque formation.

While the primary focus has been on medical applications, the workflow demonstrated its efficacy in the study of planktic foraminifera at the beamline. We conducted high-resolution single-slice tomography and 2D high-resolution XRF imaging experiments on foraminifera samples. These experiments revealed variations in major, minor, and trace elements during their ontogenetic development, underscoring the versatility of our approach for geological and paleoceanographic applications.

Beyond these specific examples, this robust and flexible workflow hold promise of broader applications across a multitude of scientific disciplines, capable of exploring a multitude of sample characteristics at hierarchical length-scales in a statistically significant manner.

APPENDIX A

Colocalization between calcium (Ca) and zinc (Zn) observed in other renal papilla samples

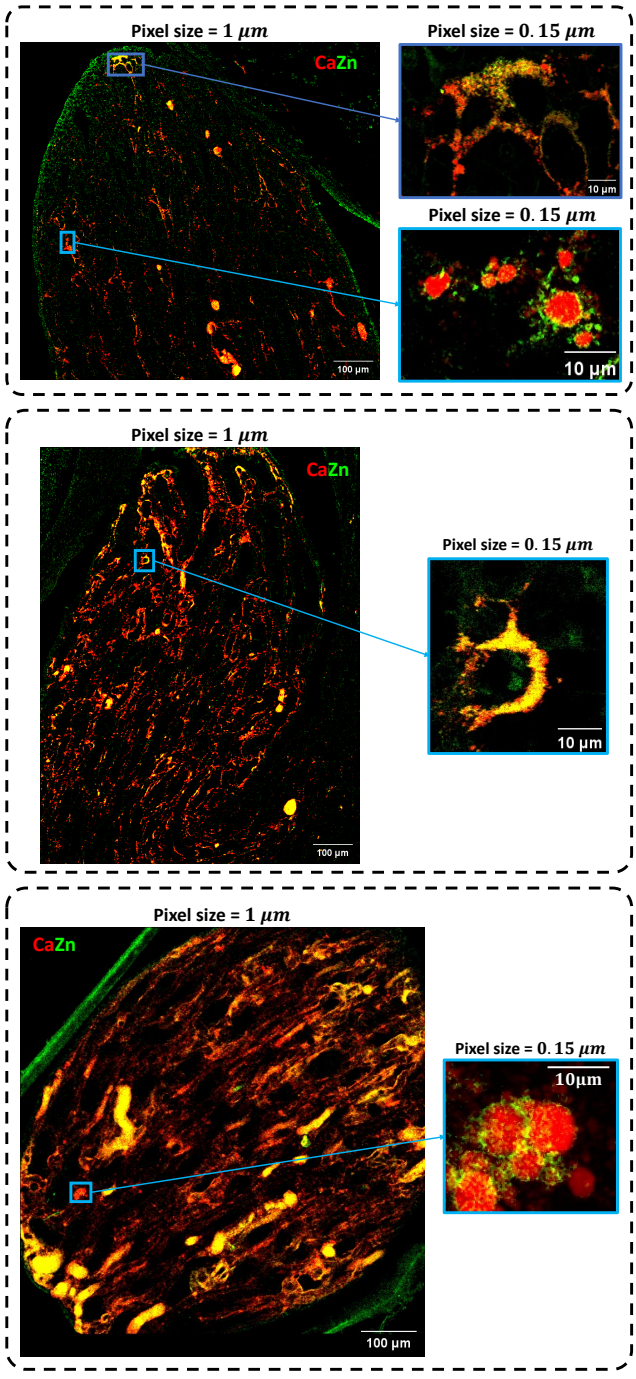

Figure A.1: 2D XRF scanning images of overlapped Ca and Zn maps in other renal papilla samples. Varied degrees of colocalization were observed. The merged image highlights regions of Ca and Zn colocalization (appearing yellow), along with the observation of Zn surrounding Ca features.

APPENDIX B

List of publication

R. Guo, A. Somogyi, D. Bazin, E. Bouderlique, E. Letavernier, C. Curie, M.-P. Isaure, and K. Medjoubi. Towards routine 3D characterization of intact mesoscale samples by multi-scale and multimodal scanning X-ray tomography. *Sci Rep*, 12 (1):16924, Oct. 2022. ISSN 2045-2322. doi: 10.1038/s41598-022-21368-0. URL https://www.nature.com/articles/s41598-022-21368-0.

scientific reports

Check for updates

OPEN

Towards routine 3D characterization of intact mesoscale samples by multi-scale and multimodal scanning X-ray tomography

Ruiqiao Guo[1,2], Andrea Somogyi[1]✉, Dominique Bazin[3], Elise Bouderlique[4,5], Emmanuel Letavernier[4,5,6], Catherine Curie[7], Marie-Pierre Isaure[8] & Kadda Medjoubi[1]✉

Non-invasive multi-scale and multimodal 3D characterization of heterogeneous or hierarchically structured intact mesoscale samples is of paramount importance in tackling challenging scientific problems. Scanning hard X-ray tomography techniques providing simultaneous complementary 3D information are ideally suited to such studies. However, the implementation of a robust on-site workflow remains the bottleneck for the widespread application of these powerful multimodal tomography methods. In this paper, we describe the development and implementation of such a robust, holistic workflow, including semi-automatic data reconstruction. Due to its flexibility, our approach is especially well suited for on-the-fly tuning of the experiments to study features of interest progressively at different length scales. To demonstrate the performance of the method, we studied, across multiple length scales, the elemental abundances and morphology of two complex biological systems, Arabidopsis plant seeds and mouse renal papilla samples. The proposed approach opens the way towards routine multimodal 3D characterization of intact samples by providing relevant information from pertinent sample regions in a wide range of scientific fields such as biology, geology, and material sciences.

Complex scientific problems in biology, earth-, environmental, and material sciences are inherently multi-scale. This requires the investigation of nanoscale features and functionalities within system-representative mesoscale samples to link those to emergent properties and functionalities at larger scales. This triggers an ever-increasing demand for new analytical tools capable of providing spatially resolved multi-scale information on intact, highly heterogeneous, or hierarchically structured samples in situ or *in operando*. Scanning hard X-ray imaging and tomography techniques are ideally suited to tackle this challenge due to their large penetration depth and inherently multimodal nature, where complementary information on the elemental distribution, morphology, crystalline structure, and chemical speciation can be obtained simultaneously. Moreover, these non-invasive scanning techniques provide straightforward access to multiple-length scale experiments. Recent developments in fast continuous scanning, data acquisition[1–4], and the high flux obtained at modern synchrotron-based hard X-ray nanoprobes have opened routine access to scanning 2D multimodal imaging. Amongst the scanning techniques, the high analytical sensitivity of X-ray Fluorescence (XRF) imaging provides unique possibilities in several scientific fields to study the role and fate of trace elements[5–13]. However, the unambiguous interpretation of 2D elemental distribution maps is not always straightforward or feasible and is especially problematic in the case of thick, complex samples. As such, the scientific community is highly demanding the extension of XRF imaging and other complementary scanning techniques to 3D tomography. Scanning XRF and multimodal tomography, where measuring projection images at different projection angles permits the reconstruction of the internal

[1]Synchrotron SOLEIL, 91190 Saint-Aubin, France. [2]Université Paris-Saclay, 91190 Gif-sur-Yvette, France. [3]Institut de Chimie Physique, Université Paris-Saclay, CNRS, 91405 Orsay, France. [4]UMR S 1155, Sorbonne Université, 75020 Paris, France. [5]Institut National de la Santé et de la Recherche Médicale (INSERM), Sorbonne Université, 75013 Paris, France. [6]Physiology Unit, Hôpital Tenon, AP-HP, 75020 Paris, France. [7]IPSiM, Univ Montpellier, CNRS, INRAE, Institut Agro, 34000 Montpellier, France. [8]IPREM, Université de Pau Et Pays de l'Adour, E2S UPPA, CNRS, 64053 Pau, France. ✉email: andrea.somogyi@synchrotron-soleil.fr; kadda.medjoubi@synchrotron-soleil.fr

features by adapted reconstruction methods, provides unambiguous information about the internal elemental distributions in the context of sample morphology, crystalline structure, chemical speciation, etc.[2,14–21]. Up to now, the lengthy acquisition time necessary for these experiments[2] at 3rd generation synchrotrons has been one of the practical difficulties to its comprehensive utilization. Indeed, even if emerging sparse tomography techniques permit boosting the measurement throughput[15,22,23] by compromising spatial resolution, overcoming the time constraint remains a challenge at 3rd generation synchrotrons.

Meanwhile, at the dawn of 4th generation synchrotron sources, routine 3D scanning X-ray tomography is becoming within reach. Indeed, the two orders of magnitude larger flux available at 4th generation hard X-ray nanoprobes boosts the speed of scanning tomography measurements proportionally, paving the way towards high-throughput scanning X-ray tomography of mesoscale samples[24]. Hence, the implementation of robust, user-friendly scanning tomography workflow is crucial for the routine application of these techniques, similarly as has been published recently for high-throughput electron tomography[25]. Such workflow imposes flexible and fast on-site data processing and tomographic reconstruction adapted to the different number of projections (sparse and high-resolution tomography), diverse data quality (e.g., high and low-level elemental abundances, missing wedge), different imaging modalities (e.g., XRF, X-ray absorption, X-ray diffraction), and the possibility of adapting the field of view and spatial resolution to the examined phenomenon by using multi-scale or local tomography. Some recent developments tackle part of these requirements by sample-type specific processing of multimodal tomography data sets[15,18], also in a semi-automatic way in the case of similar processing requirements[17,26]. A sparse sampling approach followed by sophisticated data processing has also been reported[15,27]. However, according to our knowledge, a robust, holistic approach addressing all requirements of flexible multi-scale and multimodal scanning 2D/3D X-ray tomography does not exist yet.

In the present paper, we introduce such a robust workflow for scanning multi-length scale XRF-tomography and complementary modalities. The presented workflow has been developed and implemented at the Nanoscopium beamline[21] of SOLEIL Synchrotron and includes semi-automatic data reconstruction. The proposed reconstruction algorithm yields good reconstruction data quality for diverse scientific fields with no need for parameter readjustment depending on the sample type. As the first step of this approach, sparse tomography provides a 3D overview of the entire meso- or microscale sample. The reconstructed sparse tomograms, containing relevant information to the investigated scientific problem, are used to choose pertinent regions for high spatial resolution single slice tomography, projection imaging, and local tomography. This approach permits optimizing the scanning tomography experiments and obtaining relevant information from pertinent sample regions in 2D or 3D during a user project. Thanks to recent developments[3,22,28,29], this method paves the way towards statistically significant 3D studies, similar to those already available in full-field X-ray tomography[30], and electron tomography[25].

The performance of the workflow is demonstrated through the study of two highly heterogeneous mesoscale samples. A 700 µm thick wild-type *Arabidopsis thaliana* seed, widely used as a model organism for plant biology studies, has been measured by sparse XRF tomography followed by high-resolution 2D tomography of some virtual slices and 2D projection imaging. The multi-length scale study of mesoscale renal papilla samples is crucial to investigating pathological calcification[31]. This study highly profited from high-resolution local XRF tomography of a micron-sized calcification sphere chosen from the reconstructed sparse tomograms.

Results

Multi-length scale scanning X-ray imaging/tomography workflow. The workflow implemented at Nanoscopium for multi-length scale and multimodal scanning X-ray imaging and tomography experiments is presented in Fig. 1: the sample mounting and alignment are followed by sparse tomography of the whole sample, and then the visualization of the volume rendering of the reconstructed tomograms. The strategy of high-resolution (HR) measurements is based on these medium-resolution results. This workflow permits even users who are new to X-ray imaging and tomography, to accomplish all measurement and data reconstruction steps during their experiment. At Nanoscopium all user projects apply for XRF multi-scale imaging or tomography, which is often complemented by other modalities (absorption- or phase-contrast imaging/tomography, XANES, or XRD) to best tackle the actual scientific question. As such, in this paper, we have chosen scanning XRF tomography to demonstrate our approach.

As a first step, a sparse XRF/multimodal tomography measurement with 20 projection angles (see details in "Data acquisition" section) is followed by semi-automatic on-site tomography reconstruction. Direct visualization of a specimen's reconstructed medium-resolution 3D elemental distribution and morphology enables immediate identification of information pertinent to the research project. This permits users to choose the strategy for succeeding in high-resolution (HR) measurements for studying the smallest sample features crucial to tackling the scientific problem[32]. This HR measurement can be 2D projection imaging, 2D single slice tomography, local scanning 3D tomography, or any combination of these. Notably, a reasonable trade-off must be made during a tomography experiment regarding acquisition time, spatial resolution, and the number of samples wished to be investigated. After the high-resolution experiment, an estimate of the spatial resolution achievable by different projection numbers can be obtained by the Fourier ring correlation (FRC) calculation (detailed in the "Methods" section). If the resolution of the first sparse tomography results does not meet the user's requirements, then a second sparse tomography measurement can be performed. This will start with an angular offset equal to the half angular step of the first sparse tomography experiment. The second optional sparse tomography, having the same projection numbers as the first, results in doubling the total number of projections and hence improving the spatial resolution. As demonstrated in Fig. 1, all these modalities can be reconstructed semi-automatically on-site during the experiment using predefined and pre-parameterized reconstruction algorithms with no need for interaction from the users. Hence, users can guide their experiments and redefine the scientific objectives on-the-fly depending on the results obtained on-site.

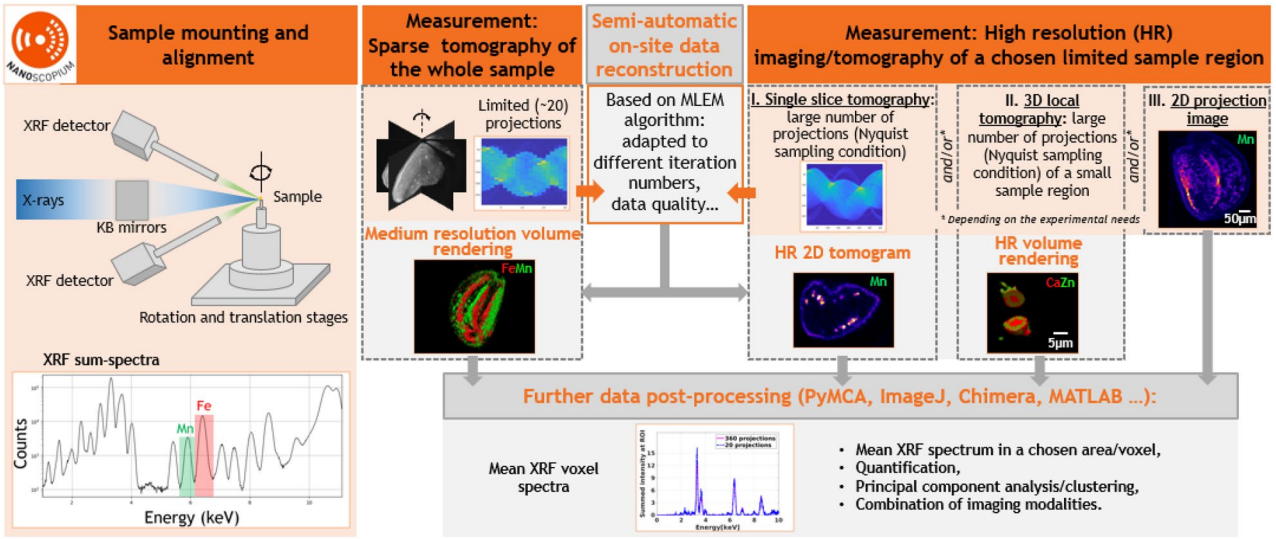

Figure 1. Semi-automatic multi-scale XRF and multimodal scanning imaging and tomography workflow implemented at Nanoscopium. After sample mounting and alignment, sparse scanning tomography is performed on the whole sample. Some minutes after the experiment, medium resolution volume rendering is available for data interpretation by the proposed semi-automatic on-site data reconstruction. This permits optimizing the strategy of successive high-resolution (HR) measurements. The on-site reconstruction algorithm provides HR tomograms for data interpretation and further data processing some minutes after the HR experiments. The measurement and data reconstruction steps are included in orange and grey rectangles, respectively.

Moreover, the HDF5 data format of the reconstructed tomograms is fully compatible with widely used cross-platform freewares and open-source data analysis tools, such as PyMCA (XRF data processing), ImageJ, Chimera (imaging/tomography data processing), etc. As such, further on-site or post-experiment processing, such as extraction of mean XRF spectra, quantification, combined treatment of different imaging modalities, and multivariate statistical analysis (Principal Component Analysis, Cluster Analysis, etc.)[33], can be obtained straightforwardly in any 2D/3D feature identified from the projection images or the reconstructed 2D/3D tomograms.

Proof of principle test measurements: Wild-type *Arabidopsis thaliana* seeds. *Arabidopsis thaliana* is a weed native to Eurasia and Africa with a short life cycle (≥ 6 weeks). This annual plant is a popular model organism in plant biology due to the knowledge of its genome and the availability of numerous mutants. The wild type (Col-0) is commonly used in plant biological laboratory experiments and even in Space experiments to study genetics, evolution, and development of flowering plants. As a model plant, *Arabidopsis thaliana* is also a powerful tool to investigate metal homeostasis and nutrient distribution, relevant questions about the world's food production and the agriculture industry. In this context, essential elements Fe and Mn in the plant seed are crucial for plant germination. Mn, involved in the photosystem II in chloroplasts, is needed for the vigour of germinating plants, and Fe is involved in various metabolic processes (respiration, photosynthesis…). These two elements have different physiological functions and different transporter pathways. Thus, differences are expected in their distribution and concentration within the seed. 2D XRF imaging is a powerful tool for locating trace elements in plants. However, assigning the measured metal distribution unambiguously to the grain's ultrastructure can be challenging due to the several hundreds of microns information depth of Mn and Fe. Moreover, sample sectioning, required to study the internal elemental distribution by 2D scanning XRF imaging, can be intricate for small and hard samples such as *A. thaliana* seeds and can induce tissue alteration and artifacts.

XRF and multimodal tomography are useful complementary tools for determining metal concentrations and distribution in intact seeds with minimal sample preparation[16,34,35].

Sparse scanning X-ray tomography of a whole seed. We tested the performance of our tomography approach on wild-type *Arabidopsis thaliana* seeds. One advantage of using seeds, in general, is their low water content, resulting in lower amounts of radiation damage than more hydrated tissues. In order to obtain an overview of the elemental distribution of a whole mesoscale seed of 700 µm dimensions, we performed simultaneous sparse XRF (see Fig. 2) and absorption (Fig. S1) micro-tomography. The figure of merit of measuring a limited number of projections is to identify, within acceptable measurement times, the features of interest, in our case the distribution of Mn and Fe within different seed compartments. Since the total measurement time of a tomography experiment scales proportionally with the number of projections, it can be drastically reduced by measuring only a few angular projections. This also reduces the eventual radiation damage of the sample, which might be important in the case of scanning imaging of larger samples. However, the reduced number of projections should be chosen without significantly compromising the quality of the obtained 3D mesoscale tomograms. The reconstructed sparse 3D tomograms of Mn and Fe can be seen in Fig. 2A, B. It comprises 223 virtual slices

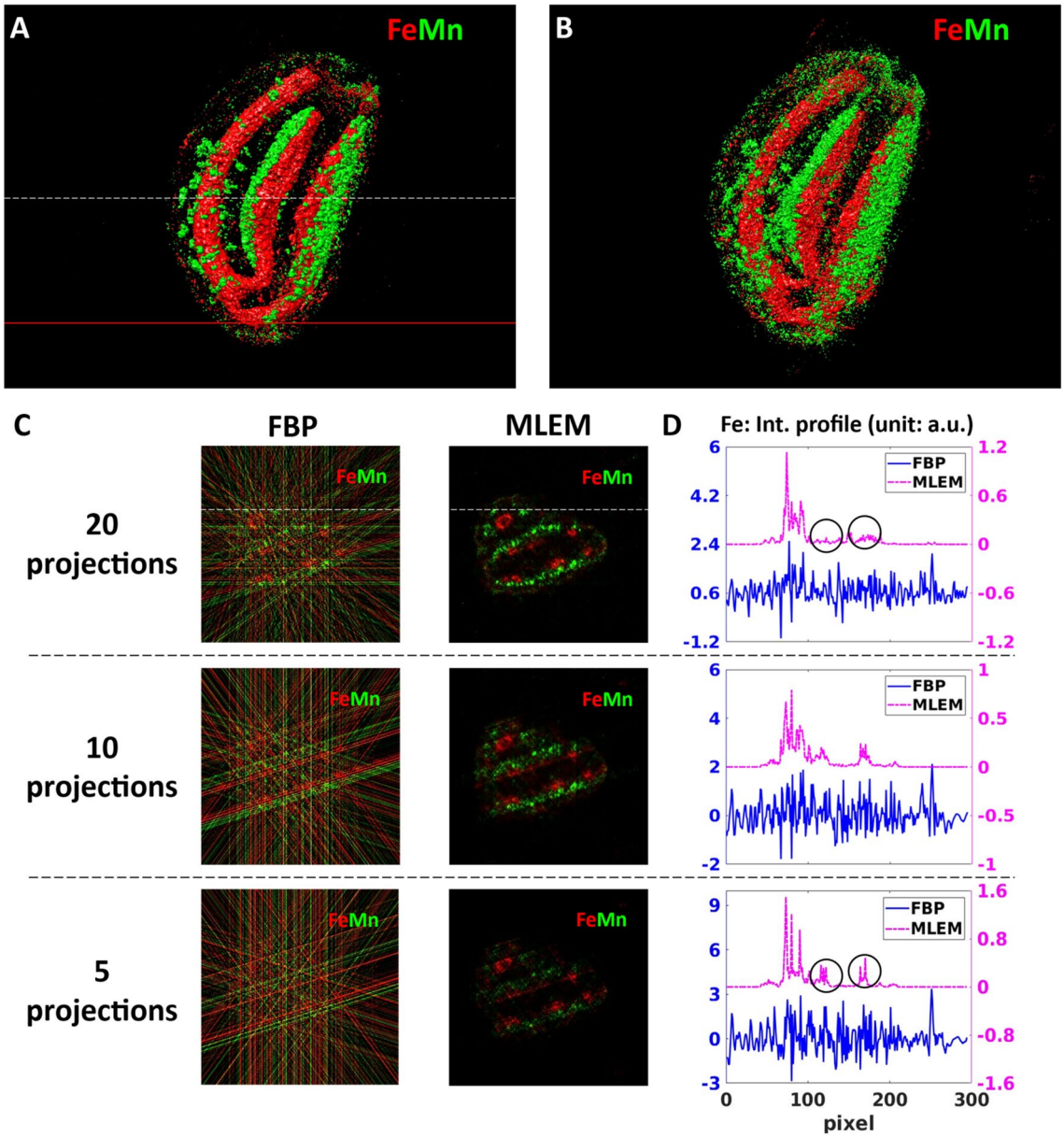

Figure 2. Reconstructed sparse 3D Fe and Mn tomograms and a virtual slice showing the internal Fe and Mn distributions. (**A**,**B**) volume rendering of the Fe and Mn tomograms reconstructed by MLEM from 20 (**A**) and 5 angular projections (**B**). The white dashed line indicates the altitude of the virtual slice shown in (**C**). The red line marks the altitude of the high-resolution single slice tomography shown in Fig. 3. (**C**) Comparison of the reconstructed results obtained by the FBP and MLEM algorithms in the function of the measured number of angular projections. The columns correspond to two different algorithms: filtered back-projection (FBP) and maximum likelihood expectation maximization (MLEM). The lines correspond to 20, 10, and 5 angular projections, respectively. (**D**) Comparison of the intensity profiles of Fe obtained by FBP and MLEM. The Fe intensity profiles were extracted along the white straight line indicated in (**C**).

and is calculated from 20 measured angular projections by the maximum-likelihood expectation–maximization (MLEM) algorithm (described in "Methods" section). It is clear from the reconstructed sparse tomograms that Fe is preferentially located in the provascular systems of the seed, and that Mn is mainly distributed in the abaxial area of both cotyledons, at the subepidermal level, as well as in the cortex area of the hypocotyl. These observations are in agreement with the results published in the literature[34,35].

To optimize the measurement conditions and the corresponding reconstruction parameters of sparse tomography, we compared two different reconstruction algorithms, Filtered back- projection (FBP) and MLEM, in the function of the number of measured angular projections (5, 10, and 20). The comparison is demonstrated in Fig. 2C, D using the virtual slice marked by a white dashed line in Fig. 2A.

FBP algorithm is the standard solution for 3D tomography reconstruction due to its fast reconstruction time and easy implementation. However, because of the intrinsic nature of the algorithm, FBP has severe limitations

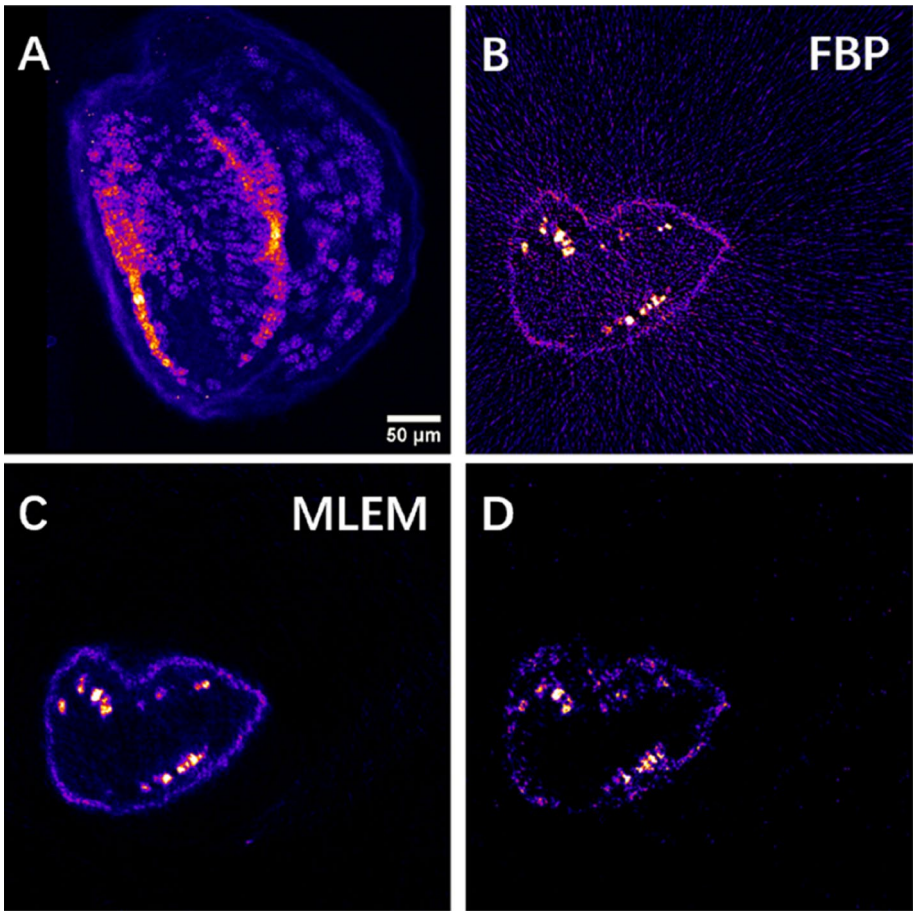

Figure 3. High-resolution 2D scanning XRF imaging and tomography of the Arabidopsis seed. (**A**) High-resolution 2D projection image of the Mn distribution at an appropriate angle chosen from the 3D sparse tomograms. (**B**,**C**) Reconstructed HR single slice of the Mn tomogram obtained by the FBP algorithm (**B**) and by the MLEM algorithm (**C**) measured at the altitude marked by the red line in Fig. 2A. (**D**) Mn sparse tomography reconstruction at the same slice obtained by MLEM.

in the case of noisy datasets and highly under-determined measurement conditions with a small number of projections[36]. This can be clearly seen in the first column in Fig. 2C, where the signal-to-noise ratio of all sparse tomograms obtained from 5, 10, and 20 projections is very low. Indeed, the strong streak artifacts of FBP, caused by the small number of projections, shadow the elemental distributions: the Mn and Fe distributions are hardly visible even in the case of 20 angular projections. In effect, as shown by the Fe intensity profiles (shown in Fig. 2D by the blue curves), these strong artifacts, resulting also in negative intensity values, are hiding the information on the Fe variation within the sample. As such, since FBP cannot significantly reduce streak artifacts at low number of projections, it is not adapted to sparse tomography reconstruction.

MLEM algorithm (second column of Fig. 2C) is superior to FBP in handling noisy datasets. Moreover, it includes the non-negativity constraint assumption. In our workflow, we included a simple automatic stopping criterion for the MLEM algorithm with the smallest possible noise as a figure of merit (as detailed in "Methods" section). This choice results in terminating the reconstruction process at small number of iterations (thus with short reconstruction time) introducing only a few, weak artifacts in the reconstructed tomograms. The reconstructed tomograms in Fig. 2C illustrate the robustness of this algorithm in treating limited number of projections. Moreover, with increasing number of projections the reconstruction artifacts of MLEM are becoming weaker. This is illustrated by the purple Fe profiles in Fig. 2D, where the strongest reconstruction artifacts marked by the black circles in the 5-projection tomogram (last line in D) diminished in the 20-projection tomogram (first line of D).

High-resolution single slice tomography. The above-described 3D sparse tomography permits choosing the best angular position for high-resolution 2D projection imaging, as shown in Fig. 3A for Mn distribution. It also allows choosing the altitude(s) for high-resolution single slice tomography (Fig. 3B, C). This provides insight into the internal Mn and Fe distributions of subcellular features within intact seeds. We performed HR single slice XRF tomography at the altitude shown by the red line in Fig. 2A. The FBP and MLEM reconstructions of the internal 2D Mn distribution can be seen in Fig. 3B, C. We included for comparison the sparse tomogram of Mn obtained by MLEM in the very same virtual slice (Fig. 3D). The reconstructed features are in

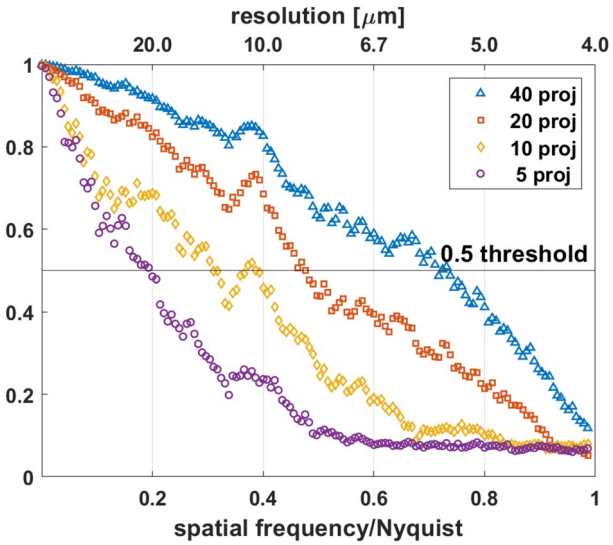

Figure 4. Spatial resolution estimation by Fourier ring correlation (FRC) method. Estimation of spatial resolution for tomograms reconstructed by MLEM from different numbers of projections chosen from the measured 360 angular projection dataset. The fixed 0.5 threshold was used for FRC analysis. The Nyquist frequency is 0.25 μm^{-1}.

Number of projections	FRC analysis: Resolution (μm)	Nyquist sampling condition: resolution (μm)
5	20.5	184.7
10	12.9	92.4
20	8.4	46.2
40	5.6	23.1

Table 1. Estimation of the spatial resolution of sparse tomograms (reconstructed by the MLEM algorithm) by FRC analysis in the function of the measured number of projections. The spatial resolution defined by the Nyquist sampling condition is included in the 3rd column for comparison.

good agreement between the sparse (Fig. 3D) and high-resolution tomography (Fig. 3B, C) results. However, as expected, high-resolution tomography reveals fine details with improved spatial resolution, which are non-detectable or hardly identifiable by sparse tomography. For such HR tomography, the use of FBP (Fig. 3B) is straightforward and is the fastest reconstruction algorithm, where the computation time is proportional to the registered number of projections. However, even with 360 angular positions, there are non-negligible streak artifacts due to insufficient angular projections compared to the number of scanned pixels in this mesoscale sample (see Nyquist sampling condition in Eq. 3). The reconstruction result of the MLEM algorithm (Fig. 3C) provides better contrast. Moreover, the computation time of < 2 s/sinogram is significantly faster than the measurement time of some hours (and will be comparable with the measurement time of some minutes/sparse tomography at a 4th generation synchrotron). As such, the MLEM algorithm proved to be the best compromise for semi-automatic image reconstruction for both 3D sparse tomography and 2D high-resolution single slice tomography experiments.

Spatial resolution of the tomograms reconstructed by MLEM. To estimate the spatial resolution of the tomograms reconstructed by the MLEM algorithm, we extracted two subsets with uniform angular sampling from the 2D high-resolution dataset. Taking the 2D high-resolution sinogram of 360 projections as an example, the full projection dataset was divided into two subsets, both having the same projection numbers. These two subsets were reconstructed independently by MLEM with the automatically determined iteration numbers. The two independent tomograms were then used for FRC analysis.

Figure 4 shows the FRC curves between the two tomograms reconstructed using a different number of projections from the same 2D high-resolution sinogram. The spatial resolution was determined at the intersection of the FRC curve and the fixed 0.5 threshold[37]. Table 1 shows the spatial resolution determined by the 0.5 threshold criterion in the function of the number of projections. The spatial resolution improves with the number of projections as expected (see Figs. S1, C and E). A resolution estimate of 8.4 μm was obtained for the 20-projection tomogram. The MLEM iterative method has resulted in a significant resolution improvement compared to the spatial resolution given by the Nyquist sampling condition.

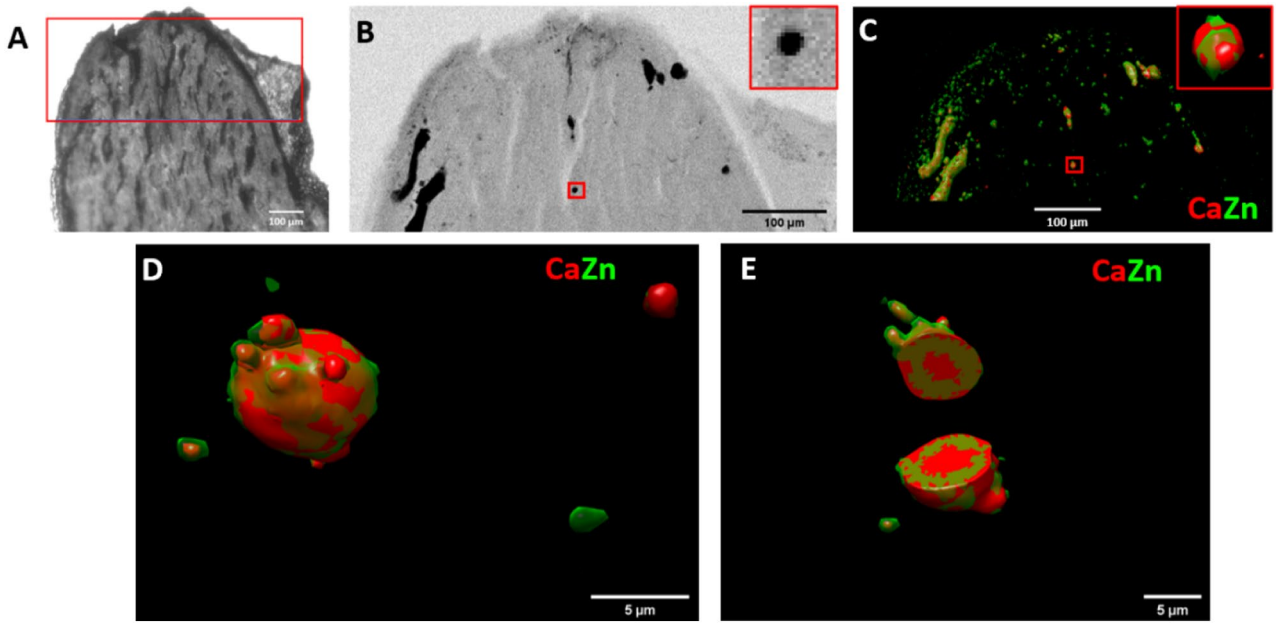

Figure 5. Sparse and local scanning X-ray tomography of a renal papilla sample. (**A**) Optical microscope image of the mouse papilla sample, mimicking human kidney calcifications. The scanned region is marked in red. (**B**) Transmission image of the tip of the sample. The small red rectangle in the middle marks the sample region chosen for local tomography. The zoom-in image of this region is inserted into the upper-right corner. (**C**) Sparse tomography reconstruction of Zn and Ca. The small red rectangle in the middle marks the sample region chosen for local tomography. The zoom-in image of this region is inserted into the upper-right corner. (**D**) Reconstructed 3D local tomogram of Ca and Zn of the calcification micro-sphere marked by the red rectangles in (**B**,**C**). (**E**) Cut-off view at the middle of the calcification micro-sphere presented in (**D**).

Renal papilla sample. In order to test the performance of our workflow in missing wedge measurement conditions and for HR 3D local tomography, we investigated mouse renal papilla samples. Nowadays, the formation of renal stones affects 10% of the global population[38]. Most of the stones develop on Randall's Plaque, a mineral deposit at the tip of renal papillae[39]. The major components of Randall's Plaque are calcium phosphate apatite and amorphous carbonated calcium phosphate[40]. Therefore, the distribution of Ca indicates the position of calcification in the renal papilla sample. Studying the correlation and colocalization between Ca and other major and trace components permits to reveal those trace elements, that are involved in early-stage calcification processes. Understanding their role in the pathological process opens the way toward efficient prevention and treatment of the renal stone formation. The sample we used in the present study is a mouse papilla affected by calcium phosphate deposits similar to the human Randall's plaque (see[41] for more details on the sample preparation).

Sparse and high-resolution XRF tomography of renal papilla. The semi-automatic workflow has been used to study the elemental abundancies within 50 µm thick slices of renal papilla samples (Fig. 5A, B). In this case, the fixation of the thin biological sample of ~ 500 µm lateral dimensions on a Si_3N_4 membrane caused a missing wedge of $2 \times 28°$ in the tomography measurement. This poses a specific challenge to tomographic reconstruction[42]. This was successfully tackled by the MLEM algorithm, which proved to be the best compromise also for missing wedge tomography. 3D sparse tomography performed on the top of the sample showed substantial colocalizations between Zn and Ca (Fig. 5C) within dense sample regions revealed by simultaneous transmission imaging (Fig. 5B). However, the ~ 8.5 µm medium spatial resolution of sparse tomography does not permit to reveal the details of micrometer-sized Ca- and Zn-rich features, that are related to early-stage calcification process. Gaining insight, with high spatial resolution, into the elemental distribution of these micrometer-sized Ca and Zn containing spherical structures is crucial. We performed 3D local tomography around a chosen micro-sphere (red rectangles in Fig. 5B, C). The angular projection images were measured with 500 nm pixel size. Figure 5D, E show the volume rendering of Zn and Ca within the measured micrometer-scale calcification sphere. In the cut-off view of the 3D volume rendering in Fig. 5E the internal distribution of Zn and Ca is shown within the ~ 10 µm dimension calcification sphere. These results reveal that Zn is enriched within a few micrometers thick rim on the surface of the calcification micro-sphere. Since Zn is considered to be a marker of inflammation[43], this result also indicates that the calcium phosphate deposition in the medullary interstitial is a pathological process.

Mean XRF voxel-spectrum. Next to the elemental distribution maps, complete local XRF spectral information is necessary to obtain detailed information on the chemical composition of local features. This might reveal rare characteristics appearing only in particular sample locations/voxels ("needle in the haystack prob-

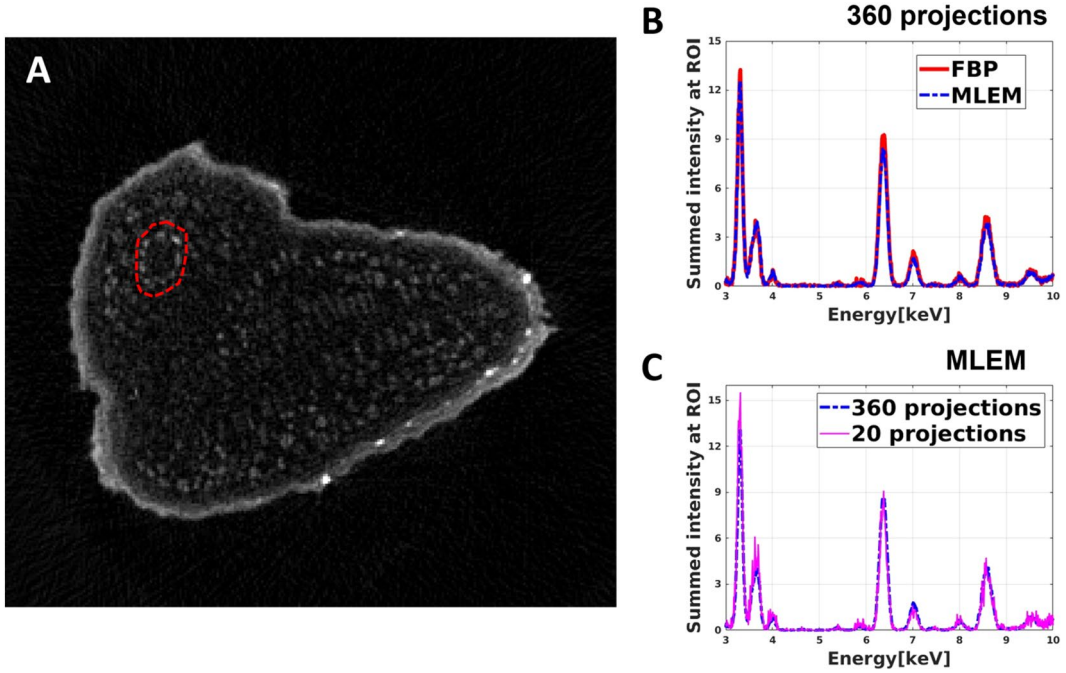

Figure 6. Extraction of the mean XRF spectra of a chosen area in a virtual slice of the Arabidopsis seed. (**A**) Reconstructed high-resolution virtual slice of the sum XRF spectra of the Arabidopsis seed. (**B**) Comparison of the mean XRF spectra of the selected area, marked by a red dashed circle in (**A**), obtained by FBP (red curve) and MLEM (blue curve) algorithm. (**C**) The mean XRF spectra of the selected area obtained by MLEM from 360 projections (blue curve) and from 20 projections (fuchsine curve).

lem"). Since we collect the full XRF spectrum in each measured pixel during data collection, next to the tomograms of the predefined elements, it is also possible to reconstruct the full XRF spectrum in each voxel of the tomogram. In other words, we can include a spectral dimension to the reconstructed dataset, which can be used to extract the mean XRF spectrum of any chosen sample area or volume. Such complete hyperspectral tomography reconstruction was realized for each energy channel of the measured XRF spectra. At 10 keV excitation energy, this results in 1000 sinograms for each virtual slice, and the reconstruction process, even with the MLEM iterative method and multi-core, is becoming quite time-consuming. For example, the reconstruction of the high-resolution 3D hyperspectral XRF tomogram (with the energy as the 3rd dimension) took ~ 1 h by MLEM for the Arabidopsis seed.

Figure 6A shows the virtual slice of the Arabidopsis seed reconstructed from the sum-XRF spectra of the dataset containing 360 projections. The mean XRF spectra extracted from the area marked by a red circle in Fig. 6A by FBP and MLEM can be seen in Fig. 6B, C. The mean XRF spectra of the chosen region obtained by FBP and MLEM do not show a significant difference; the total intensities of the XRF spectra agree within 5%. As such, in the case of high-resolution tomography, FBP is a good compromise to obtain local spectral information within a limited reconstruction time.

As the next step, we selected equiangularly 20 projections out of the 360 ones to simulate a sparse tomography in identical experimental conditions. This allows comparing the mean XRF spectra obtained by sparse and high-resolution tomographies. In the case of sparse tomography, FBP cannot be used for data reconstruction due to the low number of projections. As such, we reconstructed the sparse tomogram for each energy channel by MLEM. The mean XRF spectrum of the same region as before (red circle in Fig. 6A) was calculated from this sparse tomography dataset. Figure 6C shows that the two mean XRF spectra agree well, which illustrates that the MLEM algorithm provides reliable hyperspectral tomograms and mean XRF spectra even for a severely limited number of projections.

The mean XRF spectrum within a selected volume of interest of the calcification sphere (shown in Fig. 5D) of the renal papilla is demonstrated in Fig. 7. The reconstruction process for the 4D hyperspectral tomography dataset (with the energy as the 4th dimension) took around 1 h by the MLEM algorithm. To obtain the mean XRF spectra within a volume of interest, we selected the 3D volumes of interest by ImageJ, a freeware frequently used by our users. We applied this mask to each energy channel in the reconstructed 4D dataset. The extracted mean XRF spectra shown in Fig. 7B reveal that Ca is the dominant element in the core of the calcification microsphere (red XRF spectrum), which also contains Zn. Within the surface rim (indicated by green in Fig. 7A and green XRF spectrum in Fig. 7B), the increased Zn to Ca ratio, due to the threefold larger Zn and ~ 20% smaller Ca content, provides evidence of the association of Zn to the pathological process.

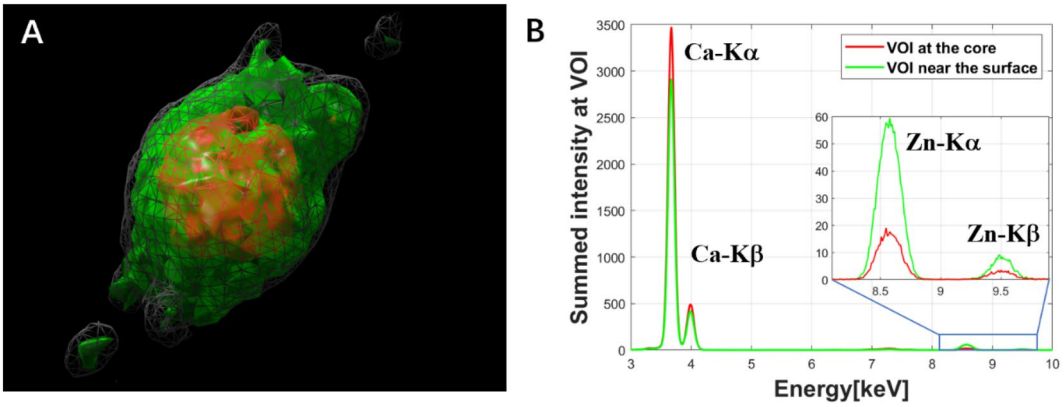

Figure 7. Extraction of the mean XRF spectra within the volume of interest of the reconstructed calcification micro-sphere shown in Fig. 5D,E. (**A**) Reconstructed result by MLEM algorithm from the total intensity of the XRF spectra, grey volume: reconstructed total sphere volume, red and green volumes: core and surface rim regions, respectively. (**B**) Comparison of the mean XRF spectra of the core (red) and surface rim (green) volumes.

Discussion

The proposed holistic multi-scale and multimodal scanning X-ray tomography workflow, implemented at Nanoscopium, was tested on mesoscale samples. To tackle the scientific problems presented in the recent paper, multi-scale XRF- and scanning absorption contrast tomography were the best-adapted imaging modalities.

The best compromise for semi-automatic on-site tomography reconstruction for sparse-, local- and high-resolution scanning X-ray tomography is proved to be the MLEM algorithm if it is benefited from the apt early stopping strategy. This algorithm also efficiently handles the missing wedge sampling conditions. The FBP algorithm is, in general, not adapted for the reconstruction of sparse and missing wedge tomographies since the measured dataset does not fulfill the optimal Nyquist sampling criterion. In the case of high-resolution hyperspectral tomography, which results in large 3D/4D datasets, the figure of merit is a compromise between the reconstructed data quality and the reconstruction time. Here, FBP is the best compromise to obtain, within a limited reconstruction time, reliable mean XRF-spectra from regions/volumes chosen from the reconstructed XRF hyper-spectral tomograms. The semi-automatic use of these two algorithms according to the above-detailed conditions permits obtaining a flexible semi-automatic workflow providing good quality on-site reconstruction for various samples in diverse experimental conditions. Due to its flexibility, our approach is especially well suited for on-the-fly tuning of the experiments to study features of interest progressively at different length scales.

We must note that scanning XRF imaging is generally a semi-quantitative approach. However, in the present paper, we presented the 2D and 3D elemental intensity distributions (number of characteristic X-ray Fluorescence photons per given dwell time). As the next step, we intend to fully integrate the quantification method in the semi-automatic user-friendly data-processing pipeline and to provide it for all scanning XRF tomography experiments as an option. For this, the measurement conditions will be calibrated by an adequate reference sample, and simultaneous scanning X-ray absorption tomography will be used for self-absorption correction in each voxel of the tomogram for each reconstructed element.

The robust scanning tomography method implemented at the Nanoscopium beamline opens the way for non-expert users towards routine non-destructive multi-length-scale characterization of complex samples during a standard beam-time of 3–5 days. The reconstructed tomograms can be treated by widely used freewares such as ImageJ, Chimera, etc. This allows straightforward data handling for users during and after their experiments. The workflow provides the possibility to study relevant 3D micro-features of several mesoscale samples during a routine user experiment, even at 3rd generation synchrotrons. Next to XRF and scanning absorption tomography, we have also extensively tested the workflow for scanning phase contrast- and X-ray diffraction tomography studying perovskite samples and bio-mineralization. These results will be presented in a separate paper. Moreover, the application of our approach for XANES tomography, which can be considered as a variant of hyperspectral tomography[44], is straightforward.

Such a robust semi-automatic flexible scanning multimodal tomography workflow will be a scientific game-changer at emerging 4th generation synchrotron sources, where data throughput of scanning hard X-ray techniques is boosted by ~ two orders of magnitude. The new possibility to explore a multitude of sample characteristics simultaneously, with high analytical sensitivity, at hierarchical length-scales in 3D, in a statistically significant manner in meso- and micro-scale samples, will revolutionize a wide range of scientific fields in ways that we can currently only dream of and will provide a unique complement to already existing state-of-the-art multi-scale and fast full-field X-ray tomography techniques[45–47]. These high through-put scanning X-ray imaging techniques will also complement emerging state-of-the-art laboratory scanning charged-particle microscopy and tomography and other conventional laboratory microscopy techniques providing 2D/3D elemental and morphology information with nanometer resolution. For example, scanning electron microscopy[48] has limited analytical sensitivity (~ 0.1–1%) for the analysis of heavy elements, and its small depth of information (a few microns) limits its non-invasive (without sample sectioning) application to surface studies of large samples or the 3D study of

light, major, and minor components of tiny, micrometer-sized samples. Due to sample radiation damage caused by charged-particle microscopies, multiple measurement on the very same sample region is often problematic. Scanning hard XRF imaging and tomography has high analytical sensitivity (with trace, ≤ ppm detection limit) for transition metals and heavier elements. Moreover, their large information depth of several tens/hundreds of microns permits the non-invasive multilength-scale 3D study of mesoscale samples. Multiple measurements and hence, multi-scale and local tomography is readily available by scanning X-ray imaging techniques, where radiation damage is smaller than by charged particle microscopies.

Methods

Data acquisition. The experiments were performed at the KB-based nanoprobe station of the Nanoscopium beamline of Synchrotron Soleil[21]. Two energy-dispersive silicon drift detectors, placed at 120° to the incident beam path, collected the X-ray fluorescence (XRF) spectra. The intensity of the incident and the transmitted beam has been collected in each pixel by two Si diodes placed before and behind the sample, respectively. An RT100 air-bearing rotation stage has been used for tomography measurements. The experiments have been performed by the Flyscan architecture[1].

In the case of scanning X-ray single slice tomography, the number of angular projections has been chosen according to the Nyquist sampling condition (see Eq. 3) in order to preserve the spatial resolution along the horizontal direction in the reconstructed tomograms.

The medium resolution 3D elemental distribution of the Arabidopsis seed has been obtained by sparse XRF tomography at 11 keV excitation X-ray energy. We collected 20 projections at 18 degrees angular intervals over 360°. These scanning parameters are proposed by default for sparse tomography by our workflow since, according to our experience with multiple samples and imaging modalities, they are proved to be the best-balanced parameters for almost all experimental conditions. At each projection angle, a total area of $581 \times 445\ \mu m^2$ has been scanned with 2 µm pixel size and 20 ms dwell time in continuous scanning mode. The collection of the full XRF sparse tomography dataset of this mesoscale sample took 8 h 40 min. For high-resolution single slice tomography, we measured 360 angular projections over 360° with a lateral step size of 2 µm and a dwell time of 20 ms/pixel, with a total measurement time of 35 min. For high-resolution 2D projection imaging, a field of view of $375 \times 434\ \mu m^2$ was scanned with a step of 500 nm and a dwell time of 40 ms per pixel. The total acquisition time was 7 h 30 min.

In the case of the mouse renal papilla sample, the sparse tomography was performed at 12 keV. A $586 \times 272\ \mu m^2$ region of the sample was mapped at 22 angular positions over 360° with a lateral step size of 2 µm and an exposure time of 20 ms/pixel, with a total measurement time of 5 h. This is followed by a high-resolution local tomography of a local sample volume with 65 angular positions over 360° with a dwell time of 40 ms/pixel and a uniform lateral step size of 500 nm, covering a total area of $67 \times 16\ \mu m^2$. The total acquisition time was 3 h.

Data processing. The elements present in the investigated samples were identified from the sum-spectra of all angular projections. The sum XRF spectra were fitted by the PyMCA software[49] for the identification of the elements present in the sample. The elemental distribution maps and sinograms were then extracted from the raw dataset by integrating pre-selected spectral regions of interest corresponding to the detected elements. The transmitted and incident beam intensity ratio at each pixel gives access to the sample absorption maps and sinograms. The sinograms were then reconstructed either by the MLEM or FBP algorithms. The overall reduction process is performed automatically with a robust in-house MATLAB code. The reconstructed volumetric data were exported from MATLAB as 16-bit z-stacks and imported either to ImageJ[50] for analysis or to Chimera[51] for 3D visualization.

The overall data processing is performed on a workstation with an Intel® Xeon® Processor E5-2630 v3 @ 2.40 GHz × 32 CPU with 125.8 GB of system RAM.

Reconstruction algorithms. Two different tomography reconstruction algorithms have been integrated into the workflow: the FBP[42,52,53] and MLEM[54] methods. The first, which is an analytical filtering inversion technique, is the most commonly used method in routine tomography reconstruction. It is the fastest method, exploiting fast Fourier transforms. However, FBP suffers from a lack of robustness when the measurements are sparse, of low contrast, or noisy[55,56], which is often the case in XRF tomography. MLEM is an iterative algorithm that explicitly accounts for the noise affecting the data and imposes positivity on the estimated pixels. MLEM was initially developed for the analysis of positron emission tomography (PET) data. It assumes a Poisson distribution of the acquired photon statistics and thus might be more noise-tolerant than FBP[22]. MLEM belongs to the class of majorization-minimization algorithms[57]. By construction, it decreases the negative log-likelihood of the estimated image of the given data monotonically. Moreover, it involves only simple multiplicative updates in such a way that the estimated image has positive pixel values, if all the pixels of the starting assumption image are positive. The MLEM algorithm provides good performance with sparse datasets, and the streak artifacts can be reduced as long as it is combined with an appropriate early stopping strategy, as is described hereafter.

Determination of the number of iterations: automatic early stopping strategy for MLEM. Although the loss of the MLEM algorithm decreases along with iterations, there is also an increase in the noise amplitude, which significantly impacts the final reconstruction results. This is typical for non-regularized reconstruction methods. Therefore a so-called early stopping strategy with a well-tuned criterion is crucial and must be integrated into the workflow[58]. We implemented the figure of merit about the Normalized Root Mean Square Error Deviation (NRMSED) as an indicator:

$$NRMSED = \sqrt{\frac{\sum_{i=1}^{N}(x(i)-\tilde{x}(i))^2}{\sum_{i=1}^{N}x(i)^2}} \quad (1)$$

where $x(i)$ is the sinogram of the measured data, $\tilde{x}(i)$ is the estimated sinogram by MLEM and N is the pixel number in the sinogram. NRMSED indicates the accordance between the reconstructed and measured data. In addition to this, information about the derivative of NRMSED between two successive iterations should also be considered, and the ratio R is therefore defined as:

$$R = \frac{\Delta NRMSED}{NRMSED} \quad (2)$$

where $\Delta NRMSED = NRMSED^{(i)} - NRMSED^{(i-1)}$ is the derivative of NRMSED. This similarity increases monotonically with the number of iterations. A threshold is set to terminate the algorithm when the evolution curve of R is close to zero: $R \geq threshold$. We have chosen − 0.15% as *threshold*, since this value, obtained as average over numerous test data sets, gave robust and rapid results for all tested data sets and imaging modalities.

In the implementation of our workflow, a relatively large number (~ e.g., 200) of iterations is preset to limit the maximum reconstruction time. The reconstruction of the tomograms using the MLEM algorithm is performed slice by slice, and the ratio R is calculated for each slice after each iteration. The algorithm terminates automatically for a given virtual slice after reaching the threshold and proceeds to reconstruct the next slice. Optionally, the reconstruction could perform a few additional iterations after reaching the R threshold. According to our experience, the algorithm generally reaches the $R \geq threshold$ condition around 20 iterations, well before 200 iteration steps.

The process of the optimization of the iteration number can be summarized as follows:

(1) For all the slices, set the *threshold* to − 0.15% and the initial number of iterations to a relatively large value (~ 200);
(2) Start the reconstruction for the first slice using the MLEM algorithm while calculating the ratio R for each iteration;
(3) Stop the iteration when the condition $R \geq threshold$ is reached;
(4) Repeat (2)–(3) for all slices.

This robust automatic reconstruction process provides exploitable results even for 5 angular projections, and it assures that even inexperienced users in synchrotron-based imaging/tomography can reconstruct their tomographic dataset on-site.

Spatial resolution evaluation. *Nyquist angular sampling condition.* During the experiment, a reasonable trade-off must be reached between the acquisition time and spatial resolution. For the analytical reconstruction methods, the number of projections has to satisfy the Nyquist angular sampling condition[59] in order to preserve the spatial resolution along the horizontal direction in the reconstructed tomogram:

$$n_{proj} = \frac{\pi}{2}N \quad (3)$$

where n_{proj} is the number of projections over 180°, and N is the number of pixels along the scanning direction.

The corresponding maximum resolvable spatial frequency f_{res} in the Fourier domain can be written as:

$$f_{res} = \frac{1}{\pi}\frac{n_{proj}}{PN} \quad (4)$$

where P is the pixel size.

The resolution limit R in direct space is then:

$$R = \frac{\pi}{2}\frac{PN}{n_{proj}} \quad (5)$$

This resolution limit decreases with increasing number of projections.

Fourier ring correlation for spatial resolution estimation. The most common method to estimate spatial resolution is the knife-edge technique. However, in the case of sparse tomography of highly heterogeneous samples, it can be challenging to find a sharp edge for the knife-edge method. To overcome this difficulty, the Fourier ring correlation (FRC)[60–62] method can be used as a general approach.

For the iterative reconstruction methods, the estimation of the achievable spatial resolution in the function of the number of projections can be described by the Fourier ring correlation approach. FRC estimates this by measuring the normalized cross-correlation of two independent datasets of the sample. The spatial frequency elements at different radii can be integrated circularly in the frequency domain:

$$FRC_{12}(r) = \frac{\sum_{r_i \in r} F_1(r_i)\cdot F_2(r_i)^*}{\sqrt{\sum_{r_i \in r}|F_1(r_i)|^2 \cdot \sum_{r_i \in r}|F_2(r_i)|^2}} \quad (6)$$

where r_i is the ith frequency element at radius r, F_1 and F_2 denote the Fourier transform of the two reconstructed tomograms.

At a specified cut-off threshold, the FRC curve drops below the threshold, indicating an indistinguishable signal-to-noise ratio. This defines the spatial resolution.

Theoretically, the two data sets used in FRC calculation should be formed by independent measurement[63], but this can be impractical, especially in the high-resolution scanning experiments, where the acquisition time is generally several hours at 3rd generation synchrotrons. To overcome this problem, the two subsets used for FRC calculation were extracted from the high-resolution tomography sinogram, from which independent tomographic images of the same slice were reconstructed. This resolution estimation method is mostly applied to 2D high-resolution datasets.

Ethics approval

Arabidopsis thaliana seeds: The research on the wild-type Col0 seed *Arabidopsis Thaliana* seed complies with relevant institutional, national, and international guidelines and legislation. The wild-type *Arabidopsis thaliana* seeds had been provided by C. Curie, and is the same as described by Carrió-Seguí, À., Romero, P., Curie, C. et al. "Copper transporter COPT5 participates in the crosstalk between vacuolar copper and iron pools mobilization." In *Sci Rep 9, 4648 (2019)* https://rdcu.be/cROAu. Renal papilla samples: All studies were performed in accordance with the European Union, NIH guidelines (Comité d'Ethique en Experimentation Charles Darwin C2EA-05) and all of our methods are reported as recommended by ARRIVE guidelines as previously described. The project was authorized by the Health Ministry and local Ethics Committee (authorization 11420 2017092015335292).

Data availability

All data needed to evaluate the conclusions in the paper are present in the paper and/or the Supplementary Materials. Additional data related to this paper will be available from the authors upon reasonable request and in accordance with the Journal policy described in the Instructions for Authors (Availability of materials and data).

Received: 5 July 2022; Accepted: 26 September 2022
Published online: 08 October 2022

References

1. Medjoubi, K. *et al.* Development of fast, simultaneous and multi-technique scanning hard X-ray microscopy at Synchrotron Soleil. *J. Synchrotron. Rad.* **20**, 293–299 (2013).
2. Deng, J. *et al.* Correlative 3D x-ray fluorescence and ptychographic tomography of frozen-hydrated green algae. *Sci. Adv.* **4**, eaau4548 (2018).
3. Kopittke, P. M. *et al.* Synchrotron-based X-ray fluorescence microscopy as a technique for imaging of elements in plants. *Plant Physiol.* **178**, 507–523 (2018).
4. Wang, Y. *et al.* A high-throughput x-ray microtomography system at the Advanced Photon Source. *Rev. Sci. Instrum.* **72**, 2062–2068 (2001).
5. Figon, F. *et al.* Catabolism of lysosome-related organelles in color-changing spiders supports intracellular turnover of pigments. *Proc. Natl. Acad. Sci. USA* **118**, e2103020118 (2021).
6. Wolf, M., May, B. M. & Cabana, J. Visualization of electrochemical reactions in battery materials with X-ray microscopy and mapping. *Chem. Mater.* **29**, 3347–3362 (2017).
7. Dean, C., Le Cabec, A., Spiers, K., Zhang, Y. & Garrevoet, J. Incremental distribution of strontium and zinc in great ape and fossil hominin cementum using synchrotron X-ray fluorescence mapping. *J. R. Soc. Interface* **15**, 20170626 (2018).
8. Xie, R. *et al.* Seasonal zinc storage and a strategy for its use in buds of fruit trees. *Plant Physiol.* **183**, 1200–1212 (2020).
9. Yan, H. *et al.* Multimodality hard-x-ray imaging of a chromosome with nanoscale spatial resolution. *Sci. Rep.* **6**, 20112 (2016).
10. Kosior, E. *et al.* Combined use of hard X-ray phase contrast imaging and X-ray fluorescence microscopy for sub-cellular metal quantification. *J. Struct. Biol.* **177**, 239–247 (2012).
11. Sforna, M. C. *et al.* Evidence for arsenic metabolism and cycling by microorganisms 2.7 billion years ago. *Nature Geosci.* **7**, 811–815 (2014).
12. Chaurand, P. *et al.* Multi-scale X-ray computed tomography to detect and localize metal-based nanomaterials in lung tissues of in vivo exposed mice. *Sci. Rep.* **8**, 4408 (2018).
13. Serpell, C. J. *et al.* Carbon nanotubes allow capture of krypton, barium and lead for multichannel biological X-ray fluorescence imaging. *Nat. Commun.* **7**, 13118 (2016).
14. Helliwell, J. R. *et al.* Applications of X-ray computed tomography for examining biophysical interactions and structural development in soil systems: A review: X-ray computed tomography for soil physical properties. *Eur. J. Soil Sci.* **64**, 279–297 (2013).
15. Gao, X., Yang, Y., Yang, S., Ma, Y. & Chen, M. Microstructure evolution of chalcopyrite agglomerates during leaching—A synchrotron-based X-ray CT approach combined with a data-constrained modelling (DCM). *Hydrometallurgy* **201**, 105586 (2021).
16. Punshon, T. *et al.* The Role of CAX1 and CAX3 in elemental distribution and abundance in Arabidopsis seed. *Plant Physiol.* **158**, 352–362 (2012).
17. Parsons, A. D. *et al.* Automatic processing of multimodal tomography datasets. *J. Synchrotron. Rad.* **24**, 248–256 (2017).
18. Suuronen, J.-P. & Sayab, M. 3D nanopetrography and chemical imaging of datable zircons by synchrotron multimodal X-ray tomography. *Sci. Rep.* **8**, 4747 (2018).
19. Hong, Y. P., Chen, S. & Jacobsen, C. A new workflow for X-ray fluorescence tomography: MAPStoTomoPy. In: (ed. Lai, B.) 95920W (2015). https://doi.org/10.1117/12.2194162
20. Gürsoy, D., Biçer, T., Lanzirotti, A., Newville, M. G. & De Carlo, F. Hyperspectral image reconstruction for X-ray fluorescence tomography. *Opt. Express* **23**, 9014 (2015).
21. Somogyi, A. *et al.* Optical design and multi-length-scale scanning spectro-microscopy possibilities at the Nanoscopium beamline of synchrotron soleil. *J. Synchrotron. Radiat.* **22**, 1118–1129 (2015).
22. Bourassa, D., Gleber, S.-C., Vogt, S., Shin, C. H. & Fahrni, C. J. MicroXRF tomographic visualization of zinc and iron in the zebrafish embryo at the onset of the hatching period. *Metallomics* **8**, 1122–1130 (2016).
23. Villarraga-Gómez, H. & Smith, S. T. Effect of the number of projections on dimensional measurements with X-ray computed tomography. *Precis. Eng.* **66**, 445–456 (2020).
24. Li, P. *et al.* 4th generation synchrotron source boosts crystalline imaging at the nanoscale. *Light Sci. Appl.* **11**, 73 (2022).
25. Schwartz, J. *et al.* Real-time 3D analysis during electron tomography using tomviz. *Nat. Commun.* **13**, 4458 (2022).
26. Atwood, R. C., Bodey, A. J., Price, S. W. T., Basham, M. & Drakopoulos, M. A high-throughput system for high-quality tomographic reconstruction of large datasets at Diamond Light Source. *Phil. Trans. R. Soc. A.* **373**, 20140398 (2015).
27. Liu, Z. *et al.* TomoGAN: Low-dose synchrotron x-ray tomography with generative adversarial networks: Discussion. *J. Opt. Soc. Am. A* **37**, 422 (2020).

28. Somogyi, A. & Mocuta, C. Possibilities and challenges of scanning hard X-ray spectro-microscopy techniques in material sciences. *AIMS Mater. Sci.* **2**, 122–162 (2015).
29. Chu, Y. S. *et al.* Multimodal, multidimensional, and multiscale X-ray imaging at the national synchrotron light source II. *Synchrotron Radiat. News* **33**, 29–36 (2020).
30. Odstrcil, M. *et al.* Ab initio nonrigid X-ray nanotomography. *Nat. Commun.* **10**, 2600 (2019).
31. Bazin, D., Daudon, M., Combes, C. & Rey, C. Characterization and some physicochemical aspects of pathological microcalcifications. *Chem. Rev.* **112**, 5092–5120 (2012).
32. de Jonge, M. D. & Vogt, S. Hard X-ray fluorescence tomography—An emerging tool for structural visualization. *Curr. Opin. Struct. Biol.* **20**, 606–614 (2010).
33. Johnson, R. A. & Wichern, D. W. *Applied Multivariate Statistical Analysis* (Pearson Prentice Hall, 2007).
34. Kim, S. A. *et al.* Localization of iron in *Arabidopsis* seed requires the vacuolar membrane transporter VIT1. *Science* **314**, 1295–1298 (2006).
35. Eroglu, S. *et al.* Metal tolerance protein 8 mediates manganese homeostasis and iron reallocation during seed development and germination. *Plant Physiol.* **174**, 1633–1647 (2017).
36. Schofield, R. *et al.* Image reconstruction: Part 1—Understanding filtered back projection, noise and image acquisition. *J. Cardiovasc. Comput. Tomogr.* **14**, 219–225 (2020).
37. Sorzano, C. O. S. *et al.* A review of resolution measures and related aspects in 3D electron microscopy. *Prog. Biophys. Mol. Biol.* **124**, 1–30 (2017).
38. Trinchieri, A. Epidemiology of urolithiasis: An update. *Clin. Cases Miner. Bone Metab.* **5**, 101–106 (2008).
39. Randall, A. An hypothesis for the origin of renal calculus. *N. Engl. J. Med.* **214**, 234–242 (1936).
40. Van de Perre, E. *et al.* Randall's plaque as the origin of idiopathic calcium oxalate stone formation: an update. *C. R. Chim.* **24**, 1–19 (2022).
41. Letavernier, E. *et al.* ABCC6 deficiency promotes development of Randall plaque. *JASN* **29**, 2337–2347 (2018).
42. Kak, A. C. & Slaney, M. *Principles of Computerized Tomographic Imaging* (Society for Industrial and Applied Mathematics, 2001).
43. Carpentier, X. *et al.* High Zn content of Randall's plaque: A μ-X-ray fluorescence investigation. *J. Trace Elem. Med Biol.* **25**, 160–165 (2011).
44. Dong, X. *et al.* A review of hyperspectral imaging for nanoscale materials research. *Appl. Spectrosc. Rev.* **54**, 285–305 (2019).
45. Duncan, K. E., Czymmek, K. J., Jiang, N., Thies, A. C. & Topp, C. N. X-ray microscopy enables multiscale high-resolution 3D imaging of plant cells, tissues, and organs. *Plant Physiol.* **188**, 831–845 (2022).
46. Marone, F., Studer, A., Billich, H., Sala, L. & Stampanoni, M. Towards on-the-fly data post-processing for real-time tomographic imaging at TOMCAT. *Adv. Struct. Chem. Imag.* **3**, 1 (2017).
47. Walsh, C. L. *et al.* Imaging intact human organs with local resolution of cellular structures using hierarchical phase-contrast tomography. *Nat. Methods* **18**, 1532–1541 (2021).
48. Goldstein, J. *Scanning Electron Microscopy and X-ray Microanalysis* (Springer, 2017).
49. Solé, V. A., Papillon, E., Cotte, M., Walter, Ph. & Susini, J. A multiplatform code for the analysis of energy-dispersive X-ray fluorescence spectra. *Spectrochim. Acta Part B* **62**, 63–68 (2007).
50. Schindelin, J. *et al.* Fiji: An open-source platform for biological-image analysis. *Nat. Methods* **9**, 676–682 (2012).
51. Pettersen, E. F. *et al.* UCSF Chimera: A visualization system for exploratory research and analysis. *J. Comput. Chem.* **25**, 1605–1612 (2004).
52. Zeng, G. L. *Medical Image Reconstruction: A Conceptual Tutorial* (Springer, 2010).
53. Hsieh, J. *Computed Tomography* 2nd edn. (SPIE, 2009). https://doi.org/10.1117/3.817303.
54. Dempster, A. P., Laird, N. M. & Rubin, D. B. Maximum likelihood from incomplete data via the *EM* algorithm. *J. R. Stat. Soc.: Ser. B (Methodol.)* **39**, 1–22 (1977).
55. Kazantsev, D., Guo, E., Phillion, A. B., Withers, P. J. & Lee, P. D. Model-based iterative reconstruction using higher-order regularization of dynamic synchrotron data. *Meas. Sci. Technol.* **28**, 094004 (2017).
56. Bergamaschi, A., Medjoubi, K., Messaoudi, C., Marco, S. & Somogyi, A. *MMX-I*: Data-processing software for multimodal X-ray imaging and tomography. *J. Synchrotron. Rad* **23**, 783–794 (2016).
57. Hunter, D. R. & Lange, K. A tutorial on MM algorithms. *Am. Stat.* **58**, 30–37 (2004).
58. Pafilis, C. *et al.* A methodology for the estimation of the optimal iteration in MLEM-based image reconstruction in PET. In *2011 10th International Workshop on Biomedical Engineering* 1–4 (IEEE, 2011). https://doi.org/10.1109/IWBE.2011.6079046.
59. Epstein, C. L. *Introduction to the Mathematics of Medical Imaging* (Pearson Education/Prentice Hall, 2003).
60. Koho, S. *et al.* Fourier ring correlation simplifies image restoration in fluorescence microscopy. *Nat. Commun.* **10**, 3103 (2019).
61. van Heel, M. & Schatz, M. Fourier shell correlation threshold criteria. *J. Struct. Biol.* **151**, 250–262 (2005).
62. Banterle, N., Bui, K. H., Lemke, E. A. & Beck, M. Fourier ring correlation as a resolution criterion for super-resolution microscopy. *J. Struct. Biol.* **183**, 363–367 (2013).
63. de Jonge, M. D. *et al.* Spiral scanning X-ray fluorescence computed tomography. *Opt. Express* **25**, 23424 (2017).

Acknowledgements

The authors wish to thank E. Chouzenoux (Centre de Vision Numerique, CentraleSupélec, 91190 Gif-sur-Yvette, France) for her help in the validation process of the reconstruction algorithm and G. Correc (Synchrotron Soleil) for his help during the X-ray experiments. The measurements have been performed at the Nanoscopium beamline of Synchrotron Soleil during consecutive in-house research projects and user experiments (20201481 and 20191993).

Author contributions

Supervision of the project: K.M. Sample preparation: E.B., E.L., M.P.I. Synchrotron measurements, design, preparation, and participation: R.G., D.B., E.B., E.L., M.P.I., K.M., A.S. Development and integration of tomography reconstruction algorithms: R.G., K.M. Provision of the wild-type *Arabidopsis thaliana* seeds: C.C. Validation of the reconstruction algorithms: R.G., K.M. Writing—original draft: R.G., K.M., A.S. with discussion and comments from the other authors.

Funding

Agence Nationale de la Recherche (Project 'DEFIMAN', ANR-19-CE20-0009-02). French Society of Nephrology (SFNDT) financial support for the research dedicated to kidney calcifications.

Competing interests

The authors declare no competing interests.

Additional information

Supplementary Information The online version contains supplementary material available at https://doi.org/10.1038/s41598-022-21368-0.

Correspondence and requests for materials should be addressed to A.S. or K.M.

Reprints and permissions information is available at www.nature.com/reprints.

Publisher's note Springer Nature remains neutral with regard to jurisdictional claims in published maps and institutional affiliations.